VARIATIONS OF OPTICAL AND RADIO LIGHTNING CHARACTERISTICS AND THE RELATIONSHIP BETWEEN STORM CONVECTIVE INTENSITY AND ABOVE-CLOUD ELECTRIC FIELDS

by

Michael Jay Peterson

A dissertation submitted to the faculty of
The University of Utah
in partial fulfillment of the requirements for the degree of

Doctor of Philosophy

Department of Atmospheric Sciences

The University of Utah

August 2014

The University of Utah Graduate School

STATEMENT OF DISSERTATION APPROVAL

The dissertation of **Michael Jay Peterson**

has been approved by the following supervisory committee members:

Chun Tao Liu	, Chair	**Mar 7, 2014** Date Approved
Edward J. Zipser	, Member	**Mar 7, 2014** Date Approved
Gerald G. Mace	, Member	**Mar 7, 2014** Date Approved
Kevin D. Perry	, Member	**Mar 7, 2014** Date Approved
Douglas M. Mach	, Member	**Mar 7, 2014** Date Approved

and by **Kevin D. Perry**, Chair of the Department of **Atmospheric Sciences**

and by David B. Keida, Dean of The Graduate School.

ABSTRACT

The optical properties of lightning observed by the Lightning Imaging Sensor (LIS) aboard the Tropical Rainfall Measuring Mission (TRMM) satellite between 1998 and 2010 are described and examined in the context of how they interrelate, when and where they occur globally, the nature of the cloud environment they illuminate, and the properties of the parent thunderstorm. Daytime (nighttime) flashes that occur over the open ocean are shown to be 31.7% (39.8%) larger and 55.2% (75.1%) brighter than flashes over land. Three factors are proposed that determine the size of the illuminated region: the brightness of the flash, the scattering properties of the cloud medium, and the structure of the electrical breakdown. Some of these results are explored using a Monte-Carlo radiative transfer model.

The properties of TRMM Radar Precipitation Features (RPFs) that produce exceptionally large, long-lasting, and optically bright lightning flashes are compared to typical storms. RPFs over land with exceptionally large lightning flashes are up to three times larger than typical RPF thunderstorms and are considerably stronger. Coastal and oceanic RPFs with exceptionally large lightning flashes, as well as RPFs with exceptionally long lasting or bright flashes are also considerably larger and stronger than typical thunderstorms.

Finally, high-altitude aircraft passive microwave and electric field observations taken by the NASA ER-2 over the course of multiple field campaigns are used to

examine relationships between the properties of electrified clouds and above-cloud electric fields. A retrieval algorithm is created that is capable of estimating above-cloud electric fields from 85 GHz or 37 GHz passive microwave observations. The 37 GHz estimates are only valid over land since the ocean surface appears "cold" at 37 GHz and can reproduce the observed electric fields to within a factor of two 60% of the time. By comparison, the 85 GHz estimates fall within a factor of two of observations more than 70% of the time over land, but the 85 GHz routine is valid for both land and ocean cases. Individual cases are examined, and methods for improving the routine before applying it to satellite observations to study the Global Electric Circuit are discussed.

For Mieko

TABLE OF CONTENTS

LIST OF TABLES

ACKNOWLEDGEMENTS

This research was supported by NASA PMM grant NNX13AQ70G under the direction of Dr. Ramesh Kakar and NASA Grant NNX08AK28G under the direction of Dr. Erich Stocker. AMPR data were obtained from the NASA EOSDIS Global Hydrology Resource Center DAAC, Huntsville, AL. LIP data were obtained from the NASA EOSDIS Global Hydrology Resource Center and from Dr. Douglas Mach. Portions of this research were in collaboration with Dr. Weibke Deierling and Tina Kalb of the National Center for Atmospheric Research (NCAR).

CHAPTER 1

INTRODUCTION

Few forces of nature are as common and powerful as lightning. With billions of flashes occurring each year, lightning is also an important part of the global electric circuit, helping to neutralize electrical potential differences in the atmosphere. Lightning is an important part of life as we know it on Earth (Miller and Urey, 1959), but it can also be dangerous. Outdoors enthusiasts, the aviation industry, electric utilities, and many other spheres of the general public are particularly interested in whether lightning may affect their activities. For this reason, lightning detection and monitoring is an important undertaking.

Lightning is a tremendously complex natural phenomena that relies on many different physical processes from microphysical mixed phase charge generation to storm dynamics in charge advection to electrical dynamics and thermodynamics in the discharges themselves. There is no shortage of ways to look at lightning because fulminology relates to so many different fields, each with its own unique way of approaching lightning. In this study, lightning activity is examined from observations taken by three different types of sensors: orbital optical observations of lightning flashes from the Tropical Rainfall Measuring Mission (TRMM) Lightning Imaging Sensor (LIS), ground based electromagnetic pulses of strokes in the Low Frequency (LF) radio band

from the National Lightning Detection Network (NLDN), and airborne electric field values from the Lightning Instrument Package (LIP) aboard the NASA ER-2 and other aircraft during various field campaigns.

1.1 Charge Generation and Lightning Initiation

Lightning is an electrostatic discharge between two charged cloud regions or one charged cloud region and the ground that serves to neutralize electrical imbalances in charged thunderclouds. Lightning is an important part of the global electric circuit. Our understanding of storm electrical structure and electrification processes has advanced greatly in the past century. In first part of the twentieth century, it was thought that clouds would collect negative ions in their lowest regions in response to the polarization of the Earth's electric field, which would be intensified when these negative ions would collide with the updraft (Wilson 1929). Early cloud models and measurements pointed to a dipole moment scheme for electrification with a lower negative charge layer and an upper positive charge layer (Wilson 1920; Wilson 1929), resulting in a vertical electric field. The presence of these broad regions of significant charge would then, result in a buildup of opposite polarity charge along the periphery of the cloud, which could then be entrained into the cloud and contribute to the charge buildup by convective processes (Grenet 1973; Vonnegut 1953; Vonnegut 1982). There have been a number of theories introduced that attempt to identify and explain electrification processes (Saunders 1993); however, many have been disproven over the years.

Two competing schools of thought on storm electrification that persist today are convective charging and charging by hydrometeor particle interactions. Each theory has

its fair share of defenders and critics, and charging mechanism has been a relatively contentious area of the field in the past half century. According to convective charging theories (Vonnegut 1963; Vonnegut 1982; Moore 1977; summarized by Saunders 1993), a developing cloud becomes electrified by ingesting positive ions in its updraft from beneath the cloud, where they are trapped by water droplets as modeled by Brown et al. (1971) and advected upward. The creation of a positively charged layer near the top of the cloud attracts negative ions to the cloud top, forming a negative screening layer. This screening layer then descends through entrainment and downdrafts (Winn et al. 1986; Jonas 1990). Similar processes also bring in negative ions from the cloud edges, which further develop the charge structure of the electrified storm.

Originally, Grenet (1947) proposed that the initial source of positive ions was a natural excess of positive charge near the surface of the Earth. This excess of positive charge was initially thought to be produced by atmospheric interactions with cosmic rays, but it was soon realized that these processes could not produce nearly enough positive ions to electrify storms to the extent observed in nature (Wormell 1953). Other sources have since been proposed, including the decay of radioactive isotopes in the ground (Martell 1984). Vonnegut (1953) also suggested that convective ingestion of positive ions could be a self-feeding process, whereby the descending negative charge layer would increase and cause positive point charges to be released from the ground, increasing the rate of ingestion.

The other school of thought is that storm clouds become electrified via particle interactions. There are two mechanisms that lead to electrification under this theory: inductive and noninductive charging. Inductive means that charging takes place with an

already-existing vertical electric field that induces hydrometeors to become charged. This mechanism was originally proposed by Elster and Geitel in 1913 for collisions involving falling droplets of different sizes. When a small droplet collides with a larger drop under the presence of an electric field, charge is transferred from one drop to the other, resulting in each gaining an opposite charge. This enhances the electric field, leading to more charging. The major drawback to the inductive charging mechanism is that it would be more likely to lead to coalescence (Jennings 1975), and the scale of electrification seen in thunderstorms would never occur. The more accepted particle-based charging mechanism is through noninductive charging. Generally, it includes any process that transfers charge from one particle to another, regardless of the electric field involved. More specifically, the most important noninductive charging mechanism involves the collision of vapor-grown ice crystals with graupel pellets in the presence of supercooled liquid water (Saunders 1993). Simulations by Reynolds et al. (1957) first showed that this mechanism could account for the amount of charging observed in thunderstorms and that falling graupel pellets would become negatively charged while colliding ice crystals would become positively charged. Given the mass and fall speed differences between graupel and ice crystals, this would lead to the observed dipole charge structure of typical thunderstorms. Further studies found that the sign of the charge on the graupel was dependent on temperature and the abundance of supercooled liquid water (Church 1966; Takahashi 1978; Jayaratne 1983). The amount of charge transfer was also found to depend on the size of the colliding ice crystals and the impact velocity (Jayaratne 1983) and liquid water content (Saunders et al. 1991).

While the noninductive charging mechanism has been supported by numerous

laboratory, computer simulation, and real world observation studies, the role of convective charging has been hotly debated. Still, there have been a number of studies supporting convective origins of charged storm clouds. Latham (1991) noted positively charged smoke from a forest fire, which can cause lightning. Moore et al. (1960) observed clouds over the Bahamas that seemed to be capable of producing lightning despite occurring completely below the freezing level, where noninductive charging would be impossible due to a complete absence of graupel and supercooled liquid water. However, Goodman et al. (1989) showed using a polarized (horizontal and vertical polarization) radar that lightning did not occur until after solid-phase hydrometeors were observed in a storm over Alabama. Dye et al. (2007) also postulated that charging in anvil clouds without the presence of supercooled liquid water is the result of ice-ice particle collisions involving either an inductive or noninductive charging mechanism.

Storm regions outside the main convective area may also become electrified through the convective transport of charged particles and in situ charge generation. Lightning flashes have been observed in both the leading anvil ahead of a convective system and trailing stratiform regions behind mature mesoscale convective systems (MCSs). Leading anvils typically are characterized as a horizontally expansive, yet vertically thin cloud layer near the level of neutral buoyancy. Most anvil clouds are too cold for mixed-phase particles to exist, which are a required component for the in situ generation of charge through the noninductive charging mechanism. Therefore, anvil clouds are thought to become electrified by means of convective properties, primarily through the advection of ice crystals from the convective core, though the possibility of in situ generation cannot be discounted. Advection of positive charge into the anvil leads

to the creation of negative screening layers both above and below the cloud (Marshall et al. 1989); however, they are not always observed. Charge advection into the anvil has also been shown to be more like a broken sprinkler than a steady faucet and is neither constant in time or extent (Dye et al. 2007), leading to complex charge structures. Charged anvils may interact with each other or with the storm core, leading to lightning flashes that are initiated up to 100 km away from strong convection (Kuhlman et al. 2009).

The stratiform region of a mature, organized MCS is very different from that of the leading anvil. Stratiform radar profiles are characterized by low echo top heights, low-to-moderate radar reflectivities, and the presence of a local reflectivity maximum below the freezing level. This signature reflectivity maximum is known as the bright band and is caused by melting solid precipitation. This structure allows for a substantial amount of charging from both the advection of charged hydrometeors from the convective core and local charging processes (Rutledge and MacGorman 1988). The stratiform region can also feature mesoscale updrafts, which can serve to invigorate the rates of in situ charge generation (Ely et al. 2008; Lang and Rutledge 2008). These competing sources of charge buildup result in a horizontally stacked charge structure within the stratiform region. As many as six vertically stacked charge layers of alternating polarity have been observed in nature. They are often expansive: stretching more than 100 km from end to end (Marshall and Rust 1993; Stolzenburg 1994; Lang et al. 2004; Marshall et al. 2009). Based on computer simulations, the uppermost layers are thought to be the result of charge advection from the convective region of the storm, while the lowest layers are primarily created by local in-situ processes (Schuur and

Rutledge 2000). In a real-world example, Carey et al. (2005) noted the presence of a positive charge layer that penetrated the transition zone between the convective and stratiform regions of a storm near Dallas, TX, that sloped rearwards following hypothetical trajectories of snow particles. Like anvil flashes, stratiform cloud to ground lightning strokes (CGs) are typically positive polarity, and their frequency can sometimes be related to the areal integration of stratiform rainfall (Rutledge and MacGorman 1988).

Both convective and noninductive charging theories suggest that the updraft controls both lightning production and precipitation, and this was a major topic in the early days of radar meteorology (Battan 1964). In 1960, Shackford determined that the rate of lightning production correlated well with both the radar reflectivity maximum above the freezing level and the particular reflectivity profile for a particular storm. Since then, a number of empirical studies have determined relationships between mixed phase reflectivity thresholds and lightning activity (e.g., Larsen and Stansbury 1974; Marshall and Radhakant 1978). Rutledge and MacGorman (1988) examined a storm in which the peak flash rate of negative CGs was coincident with the peak rainfall intensity of the system. Keighton et al. (1991) studied a tornadic supercell that merged with ordinary cells and formed a squall line with a significant trailing stratiform region and found that CG flash rates in the system were indeed related to the updraft strength.

These studies alone would not necessarily discount the convective charging theory. Strong updrafts would lead to more advection under this model, but would also lead to more ice aloft and higher reflectivities above the freezing level. A number of studies have also focused on ice-related parameters. Carey and Rutledge (2000) examined a tropical system over the Tiwi Islands in 1995 and noted that after the system reached

maturity, not only lightning but also surface electric fields were highly dependent on mixed-phase ice mass and rainfall. Later, Deierling et al. (2008) studied 11 storms representing a variety of different types in two different climates and found correlation coefficients of 0.8 and 0.9 between ice mass estimates above the freezing level and total lightning activity. Lund et al. (2009) also examined the locations of lightning relative to hydrometeor properties taken from polarimetric radar observations and found that lightning in this particular storm system occurred in or near regions that contained graupel, consistent with what one would expect with noninductive charging taking place.

Satellite studies have also linked lightning production with precipitation radar maximum reflectivity and minimum observed microwave brightness temperatures (Toracinta et al. 2002; Cecil et al. 2005), precipitation radar derived ice water path (Petersen et al. 2005), total rain yield for storms over the tropics (Takayabu et al. 2006), and the volume of intense convection in storms over southeast Asia (Xu et al. 2010) and entire tropics and subtropics (Liu et al. 2012). Various convective proxies for lightning flash rate have been evaluated globally, and the strongest relationship between radar observations and lightning activity was found to be the area of 35 dBZ at -10° C (Liu et al. 2012).

1.2 Methods of Lightning Detection

Lightning can be detected and observed in many ways. Some of the earliest platforms for detecting lightning at a considerable distance were simple direction-finding radios. When a lightning discharge occurs, it emits radiation across nearly the whole electromagnetic spectrum. Strokes produce strong radio impulses, known as sferics,

which can be detected by anyone listening to an AM radio. The only question is which frequency to use to listen for lightning. The radio section of the electromagnetic spectrum is broken down into a number of frequency ranges, or bands, ranging from very low frequency radio waves beginning at 3 kHz to microwaves going up to 1 THz. Each band has its own, unique properties and is used in a different way. The lowest frequency bands refract off the ionosphere, allowing for long-range transmission. For this reason, the Very Low Frequency (VLF: 3–30 kHz), Low Frequency (LF: 30–300 kHz), and Medium Frequency (MF: 300–3000 kHz) bands are often used for maritime navigation signals. Traditional AM radio falls between the MF band and High Frequency (HF: 3–30 MHz) band, while FM radio is broadcast in the Very High Frequency (VHF: 30–300 MHz) range. Wireless television signals are broadcast in the VHF and Ultra High Frequency (UHF: 300–3000 MHz) bands, and space and satellite communications occur at Super High Frequency (SHF: 3–30 GHz) frequencies, at the beginning of the microwave end of the spectrum. Lightning detection is typically done with sensors listening in the VLF, LF, and VHF bands, with each having their own set of advantages and drawbacks.

The oldest lightning sferics detectors operated in the VLF band. With multiple radio receivers, it was possible for early meteorologists to triangulate the positions of thunderstorms and reliably track their movements over considerable distances. However, VLF and LF sferics detection also has a major drawback: since cloud-to-ground (CG) strokes are much more powerful than intracloud (IC) strokes at these frequencies, as well as due to the polarization of their impulses, they have a much higher detection efficiency than IC strokes.

The VLF and LF method for locating and tracking storms was common as early

as the 1920s (Norinder 1952), before even radar technology became commonplace (though the principles of radio detection and ranging were first discovered back in 1904, only just about a decade after Marconi first demonstrated wireless telegraphy by sending and receiving his first radio signal). An early type of VLF direction finding radio receiver was the Watson-Watt design (Watson-Watt and Herd 1926), which was made of perpendicular loop antennas connected to a cathode ray tube screen. These early detectors were capable of real time observations of the electromagnetic components of lightning sferics, though they were also quite inaccurate and were frequently subject to polarization errors caused by the very effect that made them useful at long distances: reflection off the ionosphere. These polarization errors often resulted in phantom storms being detected by the sensors that were not actually there (Watson-Watt et al. 1933).

Eventually these early direction finders were replaced as computing and timing techniques improved. In 1960, the first time-of-arrival system for sferic detection was introduced by Lewis et al. (Lewis et al. 1960). Much like today's VLF/LF systems, Lewis et al. developed an array of sferic detectors that observed stroke sferics from all sensors in the network. Then, knowing the spatial layout of the network and the delay between each sensor in detecting each pulse, the locations of individual lightning strokes could then be determined. Unlike the previous electromagnetic component method for determining stroke locations, this method completely eliminated the polarization error issue and is still used today to detect lightning strokes in modern networks. One of the key advancements used in modern direction finders, first developed by Krider et al. in 1975, is the use of only the first few microseconds of the return stroke waveform to estimate stroke location (Krider et al. 1975). Only looking at the initial part of the signal

allowed for much more accurate estimates of where CG flashes actually struck the ground while simultaneously reducing direction errors from lightning channels with significant horizontal components and other in-cloud processes. Over the next few years, advancements in radio detection and geolocation of lightning sferics sources and breakthroughs in automatic computer-based signal processing and networking technologies led to the development of the Bureau of Land Management (BLM) lightning network in the western United States, including Alaska, as described in Krider et al. (1980). The BLM network proved itself to be invaluable in the detection and fighting of range and forest fires in these more isolated parts of the country. However, others were interested in these data. Researchers began installing direction finders in other parts of the country, which they used in a number of field campaigns including the Severe Environmental Storm and Mesoscale Experiment (SESAME; Brown 1992)), and the Cooperative Convective Precipitation Experiment (CCOPE; Biter and Johnson 1982). By the early 1980s, these individual projects led to the creation of a number of small, regional lighting networks across the United States. These networks, however, lacked the ability to track very large storms that covered thousands of kilometers. Eventually, an agreement was reached to combine observations from the BLM network, the SUNY Albany network, and the National Severe Storms Laboratory network, forming the foundation of the modern National Lightning Detection Network (NLDN; Orville et al. 2008), which has served the community ever since. The first complete year with complete network coverage over the entire United States was 1989, and that year the network recorded 13.4 million flashes and led to many scientific achievements. The NLDN has been upgraded a number of times since 1989 and now features Improved

Accuracy from Combined Technology (IMPACT) sensors, which combine traditional direction finding and time of arrival techniques to detect lightning.

Meanwhile, in Germany, scientists at the University of Munich developed a VLF/LF lightning detection network called the Lightning Location Network (LINET; Betz et al. 2008) that is used both operationally and for research with 65 sensors deployed in Europe as of 2006. LINET boasts a number of improvements over traditional direction finding techniques. Unlike other networks like the NLDN described previously, LINET claims to provide information of total lightning, not just powerful CG flashes. In fact, low amplitude flashes down to 5 kA were detected within the center of the network. LINET also uses advanced time of arrival methods to estimate the height of the center of the lightning channel in addition to the location of the stroke. LINET has been used extensively for lightning research and has collected data in not just Europe, but also on missions in Brazil, Australia, and Benin, in central Africa. LINET is able to use low amplitude signals by monitoring noise levels in the network as a function of the number of sensors reporting. By fine-tuning the sensor baselines of each station, Betz et al. have greatly improved the detection rate of low-amplitude flashes in regions where the network is considerably dense (250 km spacing between sensors) and as a result, the tendency for "outlier locations," or single locations where a large number of noise flashes tend to occur, are not observed in their results. However, even though they have effectively eliminated one type of systematic artifact, their observations are not by any means free of outliers (Peterson 2011).

While LINET aims to detect more flashes over a small area, another relatively new network, the World Wide Lightning Location Network (WWLLN; Jacobson et al.

2006), attempts to do the opposite: complete global coverage, though with low detection efficiencies and location accuracies. WWLLN takes advantage of the Earth-ionosphere waveguide to detect VLF signals from strong discharges over a range of 10^4 km (Lay et al. 2008). Using sensors distributed across the globe, the goal of the WWLLN is to provide global CG lightning with detection rates theoretically as high as 50%, but more realistically less than 1% overall and 4% for flashes with high current amplitudes (> 30 kA) and location accuracies within 20 km (Jacobson et al. 2006). This kind of network could compliment satellite coverage of visible, infrared, and water vapor imagery in real time, making it incredibly useful for broad thunderstorm identification and tracking purposes and regional studies in less developed areas or over the open ocean. Ideally, this scale of a network would be created with about 500 sensors spaced roughly 1000 km apart; however, the early network consisted of just 11 VLF receivers, which has now increased to 40 stations with 60 more planned according to the WWLLN website. The detection efficiency of WWLLN has increased along with the number of stations. More recent advertised detection efficiencies relative to LIS are as high as 6% in 2009 and 9% in 2012 (Rudlosky and Shea 2013). Detection efficiencies relative to NLDN were found to be highly dependent on peak current and polarity, ranging from less than 2% for currents between 0 and 10 kA, 10% for currents greater than +35 kA, and 35% for currents stronger than -130 kA, resulting in a 2008–2009 detection efficiency of 10% overall (Abarca et al. 2010).

With such a sparse network, great care was taken from the early days to reduce the effects of noise. Stations were mounted on steel and concrete buildings that remained at ground potential, and only the vertical electric field components were considered in

order to reduce the effect of power line noise (Lay et al. 2008). In order for an event to be considered, no less than four (later increased for five) stations must register the pulse. Then, a time of arrival technique is applied to determine the location of the stroke. Data are available every 10 minutes and include not only lightning locations, but also accuracy estimates of each lightning event (Lay et al. 2008). Early results examined a "worse case" scenario, examining lightning in Brazil, where WWLLN stations were most sparse at 7000 km apart. Overall, only 0.3% of lightning strokes were picked up by WWLLN, and the probability of detection was determined to be a strong function of peak return stroke current (Lay et al. 2004). Location accuracies and detection efficiencies have since increased with the number of stations and are highly dependent on region and breakdown strength considered, though detection efficiencies between land and ocean appear to be similar (Lay et al. 2008).

VLF receivers are not the only method for using sferics to observe lightning. In 1973, Murty and MacClement used some of the latest advancements in the VLF/LF techniques, including modern time of arrival techniques developed by Oetzel and Pierce and Time Interval Meters (TIM) with time accuracies of just 10 ns, and developed a direction finder that operated at much higher frequencies, in the VHF band of the radio spectrum (Oetzel and Pierce 1969). VHF sensors are able to detect much more than just the return stroke, as VLF/LF sensors do. VHF signals, or sources, are formed every time a new stepped leader formed along the breakdown channel, allowing VHF observers to chart the evolution of individual lightning flashes in fine detail. They can also detect total lightning, not just CG flashes, since the amplitudes of radio impulses in the VHF band for CG and IC strokes are roughly the same. Murty and MacClement also added a third

antenna to their design in the late 1970's in order to remove ambiguity in the measured azimuth angle and also to add the capability of measuring the elevation angle of individual sources as well, allowing them to be measured in three-dimensions (Murty and MacClement 1978). There are some issues with VHF sensors, however. First, CG/IC discrimination is not always straightforward. Although VLF/LF signals from CG flashes are quite strong, CG flashes may not always emit VHF radiation near the surface, making CG flashes appear as IC flashes. Furthermore, the VHF band operates at a high enough frequency that does not refract off the ionosphere. This means that VHF sensors are limited to line-of-sight observations and have considerably limited ranges (Oetzel and Pierce 1969). The original VHF sensor developed by Murty and MacClement had an effective range of only 100 km, compared to thousands of kilometers for VLF sensors. Furthermore, even modern networks suffer from exceptional amounts of interference from other sources of VHF radiation than lightning activity (e.g., Murty and MacClementt 1973; noted in Thomas et al. 2001). Unlike the VLF band, which is primarily used for long-range beacons and maritime communications, the VHF band is much more crowded than the VLF/LF bands, particularly with television signals, resulting in significant amounts of noise. It is therefore essential for VHF networks to first determine which sources come from actual atmospheric lightning activity and which are artifacts. After removing as much of this noise as possible, sources are grouped into separate flashes in order to determine flash rates in thunderstorms. This is not always straightforward, however, as often thunderstorms have such high flash rates and flash densities that it becomes difficult to reliably separate sources into individual flashes (Koshak et al. 2004). A number of different VHF networks have been deployed across

the United States in locals that include northern Alabama, Houston, New Mexico, Oklahoma, Washington DC, and the Kennedy Space Center.

One method of combining the detail of VLF networks with the range of VLF networks is to create a network that incorporates both types of receivers. Such a network has been built in Belgium by the Royal Meteorological Institute. This network consists of four Surveillance et Alerte Foudre par Interférométrie Radioélectrique (SAFIR) sensors located across the country that operate primarily as VHF instruments tracking VHF sources, but also include a LF antenna that adds the ability to discriminate between CG and IC flashes more reliably than typical VHF sensors (Poleman et al. 2013).

Just as radio detection systems have become increasingly sophisticated over the years, optical instruments have progressed from the naked eye to cameras, then to specialized instruments recording the optical characteristics of lightning discharges and the corresponding illuminated cloud area. Researchers began to build optical lightning detectors to mount on high-altitude aircraft and satellites to observe the optical footprints of lightning on surrounding cloud regions from above. Some of the first optical instruments that featured lightning detection were launched as part of the Defense Meteorological Satellite Program (DMSP; Orville and Spencer 1979) during the 1970s. These satellites featured onboard cameras that were built for other purposes, but were able to detect lightning activity from space. However, since the DMSP was a military program, the data from these scanners were often classified. Still, Orville and Spencer were able to obtain some data from the sensors onboard two different satellites (Orville and Spencer 1979). These cameras had spatial resolutions of 3.8 km across, and images from each individual scan were compiled into a mosaic that corresponded to lightning

activity below the satellite. The major drawback to this technique was that satellites could only detect lightning that occurred at night since that was when the contrast between lightning flashes and the surrounding environment was sufficient for consistent detection. For this reason, these early satellites were launched into sun-synchronous orbits. One of the satellites used in the 1979 study was positioned to always be at midnight, while the other was always at dusk. Their observations allowed them to update Brooks' 1925 estimate of global lightning frequency, now putting it at 123 s^{-1} on average. They also determined that the ratio of land to ocean flashes was between 8 to 20 at dusk.

Being able to observe lightning only at night turned out to be a serious problem for early studies as most lightning is known to occur during the day following well-established diurnal cycles of convection (Hendon and Woodberry 1993; Nesbitt and Zipser 2003; Liu and Zipser 2008; Lay et al. 2007). There was a substantial demand for a satellite that could provide continuous observations of lightning, regardless of the local solar zenith. During the 1980s, the Lightning Mapper Sensor (LMS) project was introduced. With a launch date scheduled closer to the end of the decade, the LMS system was developed to be mounted to a geostationary satellite to observe lightning flashes at all times of day (Davis et al. 1983).

Meanwhile, a number of studies relating to optical observations of lightning were conducted. Vonnegut et al. flew high-altitude aircraft with open shutter cameras (Vonnegut et al. 1989) and captured videos of lightning flashes from above, including from the space shuttle (Vonnegut et al. 1985; Vaughan 1990). Christian and Goodman (1987) also observed lightning in the near-infrared at 777.4 nm in order to compare the optical properties of CG and IC flashes. These studies paved the way for modern

lightning imaging platforms. In 1995, the Optical Transient Detector (OTD; Boccippio et al. 2000) was launched. The OTD was a staring lightning imager that was put onboard the Microlab-1 satellite in a low Earth orbit at 735 km altitude and 70° inclination with an operating range spanning both the tropics and the subtropics past 70° latitude. Since the orbit was not geostationary, the OTD only detected snapshots of lightning activity in the storms it passed over. The sensor is comprised of a charge-coupled device (CCD) array of 128 x 128 pixels with a readout rate of once per 2 ms and a pixel size of 10 km. A filter limits the optical frequency to 777.4 nm—the 0_2 emission line for lightning—allowing the sensor to detect CG and IC flashes both during the day and at night with a detection efficiency that ranges between 46–69% for CG flashes, and spatial and temporal accuracies of 20–40 km and 100 ms, respectively (Boccippio et al. 2000). Lightning flashes are identified from OTD observations at different scales. The basic measurement is the OTD event, which is a single pixel that exceeds the set radiance threshold during a 2 ms integration window. Events that are at the same time frame and in adjacent pixel locations are clustered into groups. Lastly, groups that occur within 330 ms and 16.5 km of each other are clustered into flashes (Christian et al. 1994; Mach et al. 2007).

A more advanced version of the OTD, the Lightning Imaging Sensor (LIS), was flown on the Tropical Rainfall Measuring Mission (TRMM) satellite launched in late 1997 as a joint venture between the National Aeronautics and Space Administration (NASA) and National Space Development Agency (NASDA) of Japan. The goal of the TRMM mission, which was originally slated to last just 3 years, was to measure the rainfall and energy exchange of the tropics and subtropics (Kummerow et al. 1998).

However, the value of this satellite was realized shortly thereafter and as of 2014, it is still in orbit collecting data. The LIS is still collecting data along with the other TRMM instruments including the Precipitation Radar (PR), TRMM Microwave Imager (TMI), and Visible and Infrared Scanner (VIRS). Since much of the LIS domain can incorporate collocated information from all of these other instruments, the LIS platform has a considerable advantage in examining lightning activity in relation to storm properties. The LIS instrument has a smaller global coverage compared to the OTD and can only detect flashes within 38° latitude of the equator (Cecil et al. 2014). After the TRMM launch, a second flight of the LIS instrument was planned for the International Space Station (ISS), which has an orbital inclination of 51.6°, allowing for the detection of lightning well into the midlatitudes (Christian et al. 2000).

Perhaps the greatest improvement in the LIS aboard TRMM over the OTD is the detection efficiency. Unlike the OTD, which could only see half of the lightning flashes it flew over, the LIS has a detection efficiency of 73 ± 11% at noon and 93 ± 4% at night (Boccippio et al. 2002). The LIS has a shorter view time than the OTD (~80 s as compared to ~180 s) as well as a finer pixel size (~5 km compared to 10 km). However, both platforms are subject to certain limitations. Perhaps the most important of these is that these satellites are moving at high speed along their orbits around the planet. On one hand, this allows for global coverage at very high detection efficiencies compared to ground networks like WWLLN, but on the other hand it makes it impossible to track and study individual storms with these platforms.

A more direct approach for detecting lightning is to use electric field mills. Field mills positioned directly above, below, or within electrified clouds observe the strength of

the atmospheric electric field wherever it is deployed. Lightning flashes cause a sudden change in electric potential, often many orders of magnitude greater than the background field strength of the electrified cloud before the lightning event. As charge is neutralized by lightning, electric fields are weaker after lightning discharges. While field mills can be used for lightning detection, they are typically used for studying the electric field structure of thunderstorms. They can be deployed at ground level for continuous operation (Marshall et al. 2009), in balloons to provide soundings of storm electrical structure (e.g., Sonnenfeld et al. 2006; Bruning et al. 2007; MacGorman et al. 2008; Marshall et al. 2009; Stolzenburg et al. 2010), or on aircraft flying at various altitudes above target storms (e.g., Bateman et al. 2007; Mach et al. 2009).

Aircraft observations are particularly useful in locations where ground sensors would be impractical, such as over the ocean or in missions with large domains that could not be practically covered by a field mill network. One airborne field mill platform that has been extensively used is the Lightning Instrument Package (LIP). When it was first deployed in 1991, the LIP platform consisted of two field mills—mounted on the top and bottom of the aircraft—and an air conductivity probe. The original LIP field mill configuration could only directly measure the vertical component of the electric field, but given certain assumptions, could also detect the nose-tail (Ex) component of the external electric field (Mach et al. 2009). Subsequent deployments of the LIP have utilized six or more field mills allowing for the measurement of the full three-dimensional electric field (Mach et al. 2009). Lightning flashes are detected by looking for rapid changes in LIP electric field data consistent with lighting discharges.

Since the LIP sensor package observes total electricity above thunderstorms, it is

well suited for studying the Global Electric Circuit (GEC; Williams et al. 2009). When neutrally charged ice particles and larger graupel pellets collide in the presence of supercooled liquid water, there is often a net transfer of electrons from the ice particles to the graupel (Takahashi 1978). Convective updrafts within thunderstorms enhance the frequencies of these collisions—and therefore the amount of charge transfer—and then stratify charged particles by mass, creating a predictable net charge distribution within ordinary thunderstorms that is often described as having a tripole structure with a positive charge region near the cloud top, a negative charge region in the midlevels, and another positive charge region near the cloud base (Williams et al. 1989). Alternating concentrations of opposing charge produce currents that attempt to destroy the charge imbalance within the Earth's electrical system. From an electrical engineering perspective, cloud charge can be thought of as a battery with positive upward currents (Wilson currents; Wilson 1920) between the top of the cloud and the ionosphere and a negative return current between the negative charge region and the ground (Wilson 1924). Equations describing the average contribution of thunderstorms to the global electric circuit have also been derived from the Maxwell continuity equation of electric current (Driscoll et al. 1992) and applied to thunderstorms over Florida (Driscoll et al. 1994). Upward electrical currents from thunderstorms are then counterbalanced by fair-weather return currents across the globe, completing the quasi-steady state DC circuit.

This view of atmospheric electricity where thunderstorms generate the fair-weather electric field was first postulated by Wilson in 1920. Early support for this theory came from the voyages of two research vessels, the Carnegie and Maud, which traveled the world taking measurements of the fair-weather electric field. These electric field

records were found to correspond to the reported number of thunder days (Whipple and Scrase 1936). More recent endeavors have compared the diurnal oscillation of fair-weather electric fields observed by the Carnegie with the diurnal cycle of lightning activity (Blakeslee et al. 1999; Bailey et al. 2007; Williams 2009; Liu et al. 2010). These results, however, did not completely match observations. Electrified Shower Clouds (also coined by Wilson) and differences between the electrical properties of land and ocean storms were thought to be the cause of this discrepancy. Even though they do not produce any lightning activity, relatively weakly charged clouds contribute significantly to the GEC (Mach et al. 2009, 2010), yet since they do not produce lightning, their contributions cannot be properly characterized by lightning observations alone. To this aim, recent work by Mach et al. used ER-2 observations to "correct" the lightning flash-rate-based approximation of the Carnegie curve, substantially improving the agreement with direct observations (Mach et al. 2011).

1.3 Motivation and Objectives of This Study

The goal of this study is to examine the properties of lightning flashes and electrified clouds and then explore what factors contribute to these characteristics. The next chapter (Chapter 2) describes the datasets and instruments used in this study. Scientific results, then, are separated into three separate chapters organized by the primary type of observations involved. While each chapter section stands alone, subsequent sections and chapters build on one another to help develop the ideas that are presented throughout the study, culminating in a general theory of flash illumination (Chapter 3 and Chapter 4) and a computer model for recreating the observed electrical

fields above electrified clouds (Chapter 5).

Chapter 3 examines optical observations of lightning flashes from space courtesy of the LIS instrument aboard the TRMM satellite. Key questions that are addressed include why is there so much variation in LIS-observed optical characteristics of lightning? What factors contribute to these variations? What is special about particularly large, long-lasting, or bright flashes and the storms that produce them? First, the statistics of lightning flash optical properties are reviewed to establish a basis for comparison. Next, relationships between different optical properties of lightning are examined. Then, the characteristics of the cloud region illuminated by lightning flashes are inspected. A computer radiative transfer model, then, is used to explore some of these trends. Lastly, the properties of parent storms that produce exceptional flashes are compared with those that only produce "typical" flashes.

Chapter 4 looks at the properties of LF radio impulses from lightning observed by NLDN. NLDN strokes are collocated with LIS optical flashes in order to compare both radio and optical aspects of the lightning event. First, the properties of the collocated NLDN strokes and LIS optical flashes are examined side-by-side to see how they are related. Then, NLDN observations are used to provide additional insights into the nature of exceptionally bright flashes observed by LIS.

Chapter 5 combines passive microwave and electric field measurements taken above electrified clouds by the NASA ER-2 aircraft and attempts to relate electric field strength with microwave ice scattering signals. The goal of this chapter is to construct a computer algorithm that can recreate electric fields above arbitrary electrified clouds from just passive microwave observations. The theoretical basis for this algorithm and

the assumptions that go into it are described in Chapter 5. Should this method prove successful and be applied to global passive microwave observations such as those available from the TMI aboard TRMM, it will be possible to characterize electrified cloud contributions to the Global Electric Circuit from across the globe in a level of detail that has never before been possible. Finally, Chapter 6 summarizes the most significant findings of this study.

CHAPTER 2

DATA AND METHODOLOGY

Observations from four different platforms are utilized in this study: the Tropical Rainfall Measuring Mission (TRMM), the National Lighting Detection Network (NLDN), the National Aeronautics and Space Administration (NASA) ER-2 high-altitude aircraft, and the World Wide Lightning Location Network (WWLLN). These platforms were chosen due to either the level of detail they provide or their superior coverage area.

2.1 LIS Observations of Lightning Flashes

The TRMM satellite is particularly well suited for studying lightning in the context of storm structure, given its global coverage of up to 38° latitude, long record from December, 1997, to the present, and the multitude of instruments onboard. In this study, 12 years of Tropical Rainfall Measuring Mission (TRMM) observations are considered: 1998–2010, during which time more than 6 million flashes have been observed within the union of the fields of view of all sensors of interest (Lightning Imaging Sensor: LIS, Visual and Infrared Scanner: VIRS, TRMM Microwave Imager: TMI, Precipitation Radar: PR). Since the LIS is an optical instrument, certain technical limitations much be taken into account.

As described in the previous chapter, the LIS is a staring imager that operates at

777.4 nm with a spatial resolution of 4–5 km, a temporal resolution of 2 ms, and an average view time over a particular region of around 80 s leading to a minimum detectable flash rate of 0.7 flashes per second (Cecil et al. 2005). The LIS can detect lightning against a bright background during the day by using sophisticated algorithms to separate the individual lightning flashes from the bright background. This is accomplished with a combination of a narrowband filter, background subtraction, and software filtering. The resultant data are clustered by the LIS ground software into a tree structure with four levels. Only three of those levels will be used in this analysis: events, groups, and flashes. Events are the smallest, most basic elements of LIS observations and are defined as a single pixel of the LIS array exceeding the background threshold during a single integration period. Contiguous events during the same 2 ms time frame are then combined into features known as groups. Groups are simply an amalgamation of adjacent individual events observed during the same 2 ms time frame. Finally, flashes are defined from LIS observations as a collection of groups in time. Groups are combined into flashes using a weighted Euclidean distance routine that is carried out using distance thresholds of 5.5 km and a time threshold of 330 ms (Mach et al. 2007).

It is possible that one or more luminous events would occur within a shorter time frame than the 2 ms integration period of the sensor, resulting in a lightning flash that consists of only 1 group. Typically, flash duration is computed by calculating the time difference between the first and last observed groups in a particular flash, but for these one group flashes, which comprise 7.6% of the overall sample, this methodology would not work. Since it is impossible to determine their true durations with any sort of accuracy, these flashes have durations arbitrarily defined as 0 s and may be omitted

where required. In these cases, their omission and the reasons for it will be explicitly stated.

Although LIS can detect flashes at all times of day, it does not do so with a constant efficiency. The LIS instrument works by observing rapid changes in the background illumination level at 777.4 nm. However, some flashes will be too dim to be detected above the background illumination level. The background radiance, however, is far from constant, ranging from almost zero when the sun is below the horizon to considerable values when the sun is above the horizon. Therefore, the LIS has a substantial diurnal sensitivity dependence, as noted by Boccippio et al. (2002) and Peterson and Liu (2013). This sensitivity fluctuation leads to not just an increased ability to detect nocturnal flashes as a whole, but also an increased ability to observe areas that are dimly illuminated from any flash at night, making it difficult to compare the optical properties of daytime and nocturnal flashes. For this reason it is necessary to divide the 24-hour day-night cycle into regimes of nearly constant sensitivity when examining the optical properties of LIS flashes. As was done in Peterson and Liu (2013), the day has been broken up into four temporal regions: night (20:00–5:00 local time), transition 1 (T1; 5:00–10:00 local time), day (10:00–15:00 local time), and transition 2 (T2; 15:00–20:00 local time). The two transition zones correspond to time periods of changing sensitivity, corresponding to sunrise, sunset, and the changing day length with the seasons. This division of the day treatment is only required when discussing the optical properties of lightning flashes and, as it turns out, is done out of precaution more than necessity, as explained in Peterson and Liu (2013).

When it is applied, however, it imposes substantial restrictions on the resulting

diurnally partitioned samples. The first effect associated with it is on sample size. Most lightning globally occurs following the typical diurnal cycles of convection (e.g., Hendon and Woodberry 1993; Nesbitt and Zipser 2003; Lay et al. 2007; Liu and Zipser 2008). As seen in Peterson et al. (2011, 2013) and others, the maximum in lightning activity over land falls within the duration of the T2 transition zone described above and would not be included in the daytime sample. The effect of losing the most common time for the most common location for lightning production (land) is an overall reduction of the sample size by nearly half. Moreover, while much of the common time frame for land-based lightning is omitted in this way, the most frequent period of oceanic lightning production falls nicely within the nighttime sensitivity regime (Peterson and Liu 2013). This means that oceanic flashes are much more likely to be included in this partitioning scheme than typical flashes over land, which could introduce bias. For this reason, a terrain partitioning must also be employed. Figure 2.1 shows the terrain-based partitioning scheme employed in this study. As in Peterson and Liu (2013), terrain type is determined using 1-degree boxes, resulting in some coastal land regions appearing smaller than they should and some islands being classified as coastal or even oceanic, based on their size.

Three terrain categories are employed: land, coastal waters (within 1000 km of major continents), and open ocean. The boundary between land and offshore coastal regions is fixed at the shoreline, but subject to the resolution of the algorithm. A case could be made for improving the resolution of the classification routine, but there are two issues for why this study elects to maintain the current resolution. First, coastal effects do not begin immediately at the shoreline, and costal land regions—particularly islands—may be different from continental landmasses. Second, increasing the resolution greatly

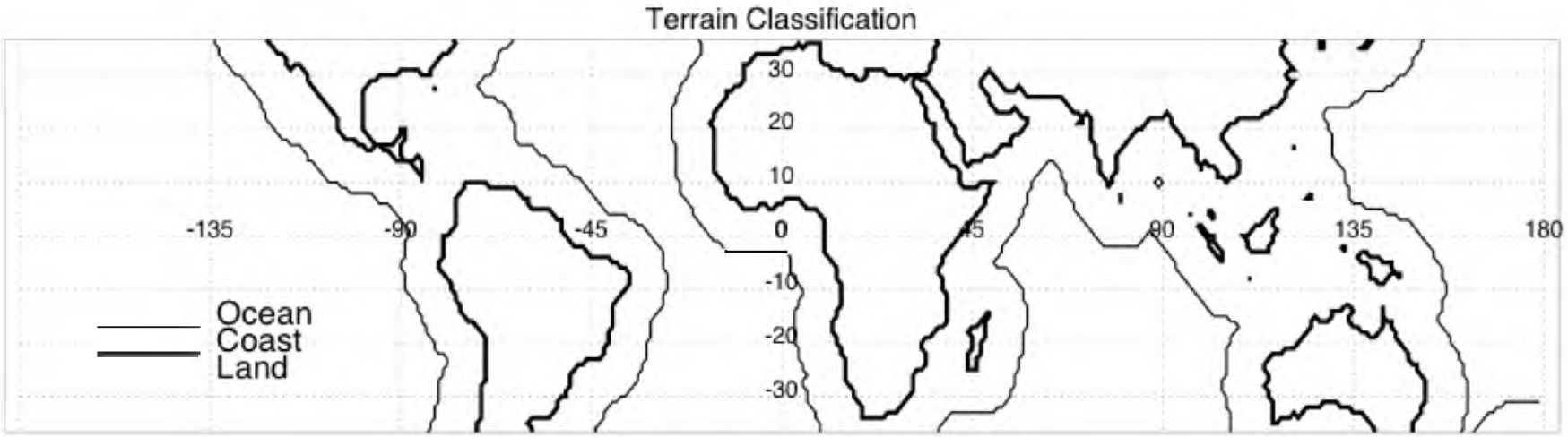

Fig. 2.1. Terrain type classification scheme dividing land, coastal, and open ocean regions.

increases the required computational time. Alternatively, the border between the coastal and ocean terrain types is completely arbitrary and is chosen because it is more than sufficient to remove any sea breeze storms from the open ocean sample. The concept is to differentiate between oceanic flashes that happen close to shore and may be the result of continental storms that form on land and move offshore versus storm systems that have been under the influence of the oceanic environment throughout their entire lives.

Another potential source of error in LIS observations is interference from the South Atlantic Anomaly (SAA). The SAA is a region where the Van Allen belt reaches anomalously low altitudes—less than 200 km in some areas. When low orbiting satellites, such as TRMM, pass through the SAA as part of their regular orbits, they are bombarded by a large amount of energetic charged particles captured from the solar wind by the Van Allen belts, which can cause issues with electrical systems and lead to premature deterioration of spacecraft systems. As the TRMM satellite passes over this region, which includes parts of Brazil, Argentina, Uruguay, and Paraguay, as well as adjacent regions offshore, substantial levels of LIS noise are produced, leading to a substantial cluster of LIS/OTD pixel rejection rates centered near Florianopolis, Brazil (Boccippio et al. 2002). While quality control filters are able to remove much of this noise, there are still some erroneous flashes in the LIS sample that typically show up as single-pixel, 0 s-duration LIS flashes, often over a clear ocean or warm rain events. Still, these artifacts are small in number and, for most purposes, have insignificant effects on the overall statistics.

The cloud medium itself can also influence what the LIS sees. Since the LIS can only see the radiance emitted from the top of the cloud, scattering can significantly affect

how much radiance actually reaches the sensor. Consider two optically concentrated flashes of identical properties: one within a region of stratiform precipitation, and the other embedded deep within a convective tower. If the stratiform region is sufficiently homogeneous and expansive, the radiance from the stratiform flash may illuminate a pristine disc as viewed from above, with a radiative density similar to a Gaussian distribution radially outward from a bright center. Of course, real-world stratiform flashes would not look like this except in perhaps very rare cases. Flashes with expansive horizontal extents (spider lightning) are common in the stratiform region and would likely look different than a single point source of radiance. Also, obscuration from intervening cloud layers would undoubtedly alter the radiance perceived by the LIS.

Still, flashes within the convective region are subject to additional factors that would alter its radiative footprint as seen from above. Significant amounts of rain, graupel, ice crystals, and even hail would undoubtedly lead to much of the radiance emitted by the flash being scattered in an inhomogeneous manner. The resulting picture would look less like a flashlight shining on a glass of Valencian horchata and more like a flashlight shining on a cup of bubble tea, with pockets of light and dark radiance dispersed throughout, dependent on the spatial distribution and optical properties of the various hydrometeors present.

Moreover, if the flash is large enough or positioned close to the edge of the cell, the region under the thicker, more convective cloud layer would be severely affected by scattering, while the part of the flash closer to the edge of the cell may be only slightly affected, resulting in very different optical properties compared to the original flash. Fortunately, there is a way to differentiate between convective and stratiform rain types.

The 2A23 TRMM algorithm classifies precipitation types at each PR pixel based on horizontal and vertical gradients in PR reflectivity (Awaka et al. 1998). Peterson and Liu (2010) used 2A23 rain types along with derived near surface rain rates (Iguchi et al. 2000) in order to arrive at three primary classifications of the storm environment: raining convective, defined as storm regions with convective precipitation types in the 2A23 algorithm and nonzero near surface rain rates, corresponding to rainfall above the minimum detectable rain rate of 0.1 mm hr^{-1} (Iguchi et al. 2000); raining anvil (stratiform), defined as storm regions with stratiform 2A23 rain types and nonzero detected near surface rain rates; and nonraining anvil, defined as any storm region with no rain detected near the surface by the PR. This convention will be used in this study as well, in particular when addressing the potential for the cloud medium to affect the observed optical properties of lightning flashes, which is discussed in Chapter 3.

In order to describe how a lightning flash is detected by LIS, a sample flash is chosen and displayed in Fig. 2.2 overlain on plots of TMI 85 GHz PCT (Fig. 2.2a), VIRS infrared brightness temperature (Fig. 2.2b), PR-derived storm height (Fig. 2.2c), and PR-derived precipitation type (Fig. 2.2d). The last two parameters are calculated using the PR 2A23 algorithm described in Awaka et al. (1998, 2009). This flash, which was observed during TRMM's 59 297th orbit at 10:36:40 UTC over the West Irian Jaya province of Indonesia, is one of the largest lightning flashes ever observed, consisting of 1,739 individual event pixels with an illuminated footprint area spanning more than 9,000 km^2 and a duration of 1.38 seconds.

The various components of the flash described earlier are shown in the figure. Individual illuminated (event) pixels are shown as yellow plus signs, where coincident

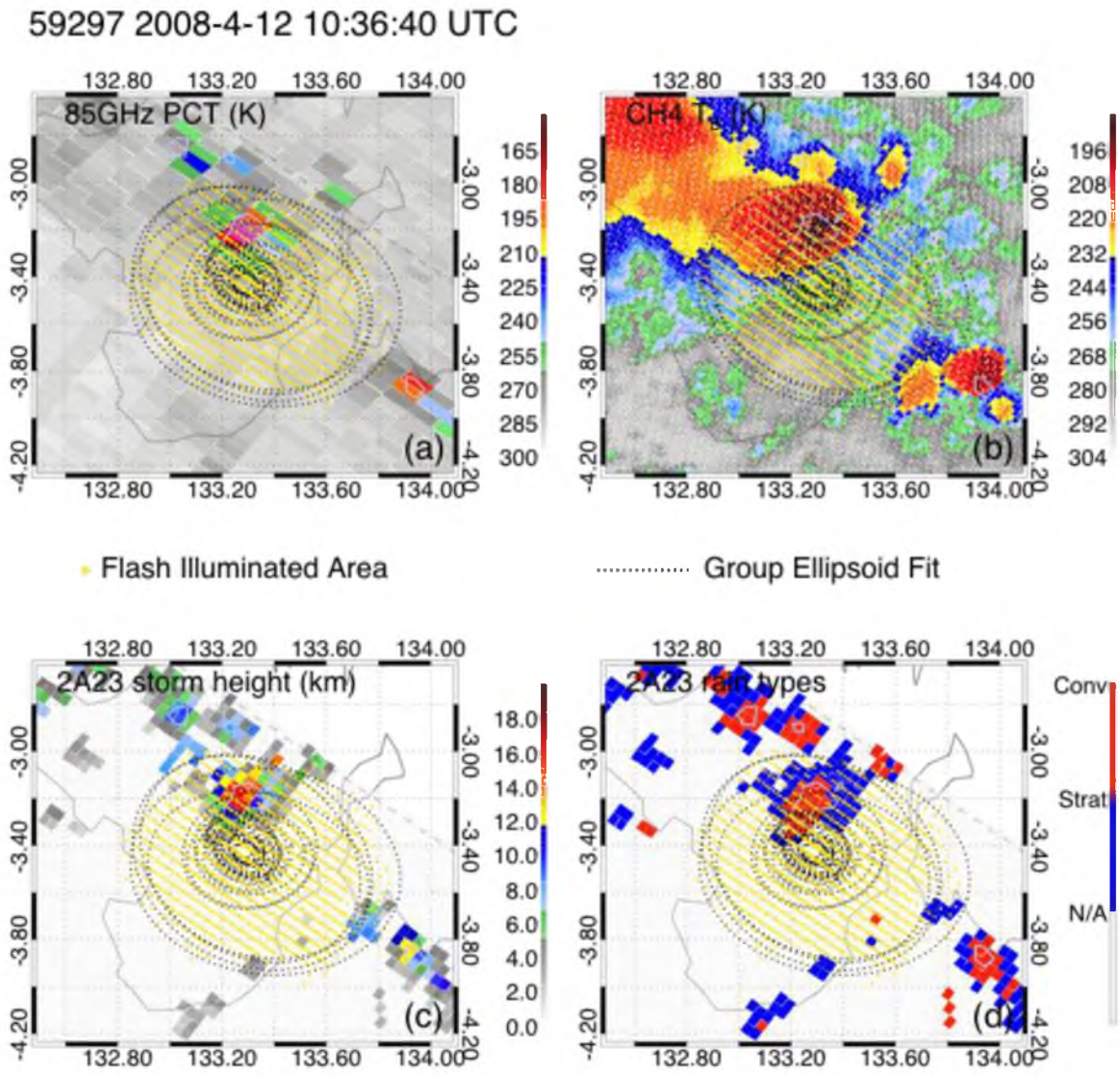

Fig. 2.2. An example of a lightning flash that illuminates a large area. The centers of illuminated pixels are indicated by yellow cross signs, and dotted lines separate groups of event pixels at a particular observation time. TMI 85 GHz PCTs (a), VIRS CH4 IR brightness temperatures (b), 2A23 storm heights (~18 dBZ echo top height) (c), and 2A23 rain types (Awaka et al. 1998) (d) are also shown.

observations at different times are overlain. This study considers the overall illuminated area to be the illuminated footprint area, or the area of the yellow region in Fig. 2.2. Like most flashes observed by LIS, this particular flash is roughly elliptical in shape and consists of 37 separate groups. Since flash and group footprints are roughly elliptical in nature, ellipsoid fits are shown for each of these groups in Fig. 2.2 as dotted contours. Most groups that make up this flash are much smaller than its overall footprint area, with only four of the 37 encompassing most of the yellow region in the figure. The flash, itself is centered at the southern edge of a convective cell and a large fraction of the illuminated footprint area occurs outside raining areas (Fig. 2.2d), though not necessarily regions free of cloud cover as seen in infrared brightness temperatures (Fig. 2.2b).

The geometric center of a lightning flash is a particularly important parameter that is used in a number of ways in this study, including for collocating LIS lightning flashes to the coordinate systems of the PR and TMI and as a representative property of the environment lightning flashes propagate through. There are many ways to determine the center of a flash, but in this study it is calculated as the arithmetic mean of the location coordinates of all of the event pixels that comprise a given flash. The arithmetic mean is not weighted by the flash amplitude as the flash centroid is. Since most groups (and consequently most events) in this flash occur to the northwest of the true center location based on the footprint shown in Fig. 2.2, the centroid of interest is displaced along that vector and occurs right in the center of the cluster of groups at 133.3° E, 3.43° S. LIS flashes, such as this, are first collocated to the TMI coordinate system since the LIS and TMI have similar swath widths and then to the other sensors from there, where defined. This is, of course, not as straightforward as just identifying a common sample volume

and recording the relevant coordinates. TMI collocation introduces one of the first important caveats of this methodology: scale uncertainty. At 85 GHz, the effective cross-track field of view of the TMI was 4.6 km at launch (Kummerow et al. 1998). For flashes with major radii smaller than 4.6 km, it should be clear which TMI sample volume the flash corresponds to, only being off by a pixel at most. However, as the size of the flash increases and surpasses the scale of the horizontal resolution of the TMI, the centroid location and the corresponding collocation becomes more and more arbitrary. Particularly in large flashes, such as the one shown in Fig. 2.2, which is centered along an 85 GHz PCT gradient (Fig. 2.2a), it becomes unclear whether the flash is a product of the convective cell just to the north that just so happens to radiate into the surrounding regions or whether this flash could actually be an anvil flash, perhaps interacting with a charged anvil corresponding to the cell to the southeast similar to the lightning flash observed by Kuhlman et al. (2009). This is particularly a problem for the TMI 85 GHz channel since it has nearly twice the horizontal resolution of the other channels. The median estimated radius of all LIS lightning flashes is 7.6 km, which is smaller than the effective cross track field (EFOV) of view at launch of all of the TMI channels. Since cross-track EFOVs correspond to the minor axis diameters of ellipse-shaped TMI scans, this means that more than half of all LIS flashes illuminate areas that can be contained by 2 low-resolution (low frequency) TMI pixels.

After a LIS lightning flash is bound to the TMI coordinate system, its PR and VIRS coordinates are determined by precalculated conversions between the three coordinate systems. PR and VIRS pixels are much smaller than the low-resolution TMI coordinates used by the lower-frequency bands on the TMI. PR and VIRS pixels are

collocated with TMI pixels using the nearest neighbor method (Nesbitt et al. 2000; Liu et al. 2008). Since the TMI resolution is typically lower than the other sensors, determining which TMI coordinate a PR or VIRS pixel belongs to is not difficult, but going the other direction can return no pixels (since the PR swath width is much smaller than that of the TMI) or multiple pixels (Liu et al. 2008). Aside from footprint size, another technical consideration that must be made when collocating LIS, VIRS, and PR observations to TMI coordinates is the TMI scan angle. The TMI scans at a 52° incident angle, so elevated hydrometeors result in some parallax uncertainty in true-Earth coordinates. Additionally, the LIS can also have parallax issues for storms that are not at the assumed cloud height of 12.5 km. In order to compensate for TMI parallax and improve the agreement between the sensors for strong convection, TMI coordinates are displaced backwards or forwards by one scan depending on the orientation of the satellite when the scan was made. This improves the agreement in locating tall, strong convective systems, but at the expense of increasing parallax errors when observing shallow precipitation systems (Liu et al. 2008).

2.2 LIS Flashes and Radar Precipitation Features

LIS optical characteristics may also be dependent on the properties of the parent thunderstorm. For this reason, a consistent approach must be applied in order to examine the properties of larger precipitation features (Liu et al. 2008) that lightning flashes may be embedded in. There are a number of precipitation feature definitions to choose from, each with their own use and ranging in size from the scale of convective cells to entire precipitating systems. The properties of all of these precipitation features are summarized

in the University of Utah precipitation Feature database (Liu et al. 2008). The most important consideration that must be made for the purpose of this study when choosing which feature definition that should be used should be scale. Whatever precipitation feature is chosen should at least be the size of the lightning flashes considered or else problems arise such as ambiguity in the assignment of flash to feature or the assigned feature may not be large enough with enough ice to really contribute to the charge separation that culminated in the occurrence of the flash.

In this study, Radar Precipitation Features (RPFs) are chosen. RPFs are defined as contiguous areas of raining pixels determined from PR observations. Since they encompass the entire raining region of a precipitating system, they can range in size dramatically, depending on the nature of the precipitation system. Overall, RPFs are typically small in size with a mean area of 240 km^2. RPF thunderstorms (RPFs with LIS flash centers embedded within them) are usually much larger, with a mean area of 5,518 km^2 and are often on the same scale of the overall system. In each RPF, the properties of the feature are summarized, including maximum radar echo top, minimum 85 and 37 GHz PCT, overall area, and the amount of volumetric rainfall, flash rate, etc. For details see Liu et al. (2008).

Lightning flashes are assigned to RPFs using index masks produced when RPFs are defined. The index at the PR collocated centroid location of each flash is compared with the unique RPF number and assigned to that RPF. This method reduces some of the uncertainty introduced in the nearest neighbor method when a single flash occurs near multiple potential parent features. However, it does introduce another important caveat: only flashes that are centered in raining areas are assigned to RPFs. Because of this,

nearly half a million flashes are removed from the sample, bringing the new total to 5.5 million flashes.

2.3 LIS and NLDN Observations of Lightning

The National Lightning Detection Network (NLDN) is an important tool to use alongside LIS observations over the southern United States. Like TRMM, the NLDN has a long data record and also provides continuous observations with sufficient accuracy to allow for a high number of successful collocations, even with considerably strict prerequisites. By combining the LIS and NLDN datasets, it is possible to examine the optical properties of lightning flashes in the context of the characteristics of the electrical breakdown, including its strength, multiplicity, whether the stroke has positive or negative polarity, and whether the stroke is intracloud (IC) or cloud-to-ground (CG) in nature, though the NLDN has a difficult time detecting IC flashes.

The collocation routine is quite complex, relying on multiple scales of LIS observations to determine which LIS flash is the best fit for a particular NLDN stroke. It is described as a schematic diagram in Fig. 2.3. The routine starts out with two primary sources of data: LIS level 1 orbit files and NLDN stroke observations. LIS level 1 data is an elementary dataset containing the optical properties of LIS events, groups, and flashes, among other sensor-specific parameters. It is organized in a hierarchy, with each element linked to each of its related elements. For example, a group is considered the parent of an individual event, and a flash is considered the parent of a group and the grandparent of an event. It is possible to move up the hierarchy and get the flash that a particular event belongs to or down to get all of the groups or events for a particular flash.

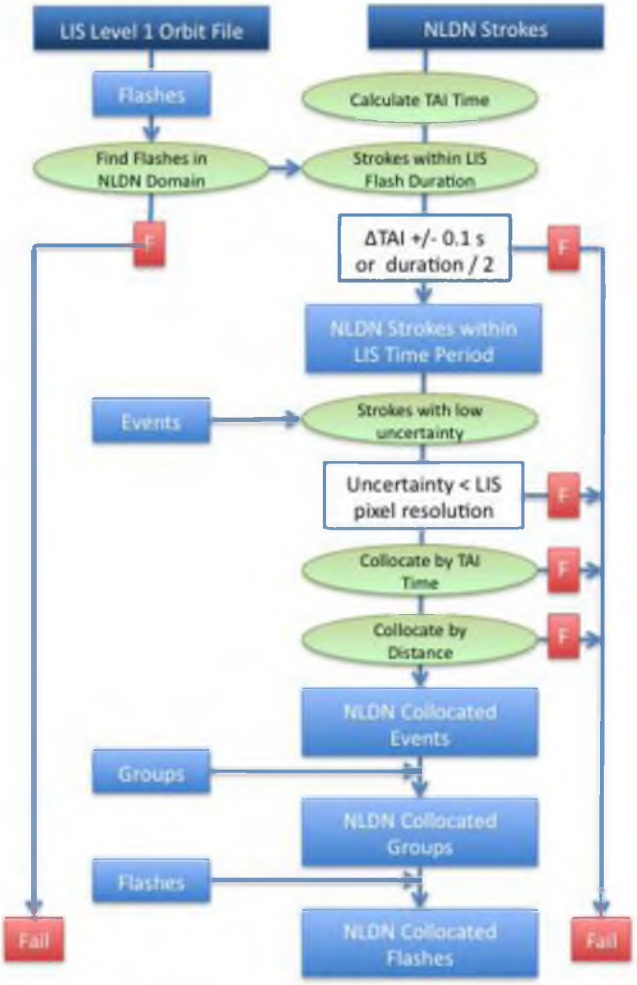

Fig. 2.3. Schematic diagram of the LIS/NLDN collocation routine.

Since the LIS has a much larger spatial domain than the NLDN, while the NLDN has a much larger temporal domain over a particular area than the LIS, one of the main concerns of the collocation routine is to remove unnecessary data. To do this, the collocation routine first looks at flash-level data and removes all LIS flashes that do not occur within the common LIS/NLDN spatial and temporal domain. At the same time, the routine works on the NLDN sample calculating the atomic time coordinates (TAI93 times, or number of seconds from January 1, 1993) of NLDN flashes.

Then, the routine looks for flashes that are potential candidates for collocation by time coordinates, alone. This process requires very little computation time, but drastically reduces the work load of the collocation routine by quickly eliminating flashes that could not possibly be collocated. This phase of processing looks for NLDN flashes that occur within one-half of the flash recorded duration (or 0.1 ms, whichever is larger) of the recorded time of the flash observation, which corresponds to the time of the first event within the group. At this point, the routine has lists of LIS and NLDN flashes that occur simultaneously that are much smaller than the original sample.

Before the collocations are performed, however, one last round of quality control removes NLDN flashes that have a greater location uncertainty than the LIS pixel size. This should remove most NLDN strokes far from the network, or those that are detected by only one or two stations. After uncertain strokes are removed, the remaining NLDN strokes are compared to the LIS events for a given flash both in space and time to determine which LIS event pixel is most likely caused by the NLDN stroke. Events are used instead of flashes or groups because the triangulated center positions recorded by NLDN are likely caused by discharge events that take place over a considerable area.

Using all LIS events increases the odds of a collocation for a given NLDN stroke by increasing the size of the target. If a flash or group spans a large area, there is no way of determining where in that illuminated region the NLDN sees the stroke, and so previous methods that collocated by flash or group center location may not work for all flashes. Once the collocated event pixel is found, the LIS level 1 data structure makes it easy to link the corresponding collocated LIS group and flash, which are then recorded. Once the collocated flashes have been identified, additional TRMM parameters are collected from the main TRMM dataset, including flash center TMI and PR properties, whole flash region TMI and PR properties, indexes of nearby precipitation features, and others.

One of the chief challenges of using this method to collocate NLDN strokes first to events and then to groups and flashes is the question of how to handle multiple collocations. On one hand, it is possible for multiple NLDN strokes to be registered within the duration of a single LIS flash and within its illuminated area. This is particularly likely in cases where the illuminated LIS region may contain actually multiple flashes that are impossible to separate optically or where a single discharge strikes the ground at multiple locations. On the other hand, it is also possible to imagine a case where a short-lived LIS flash occurs in the same region as a long-lived LIS flash when the long-lived flash is not sufficiently illuminating that particular part of the cloud, causing ambiguity as to which LIS flash the NLDN flash belongs. The first scenario is very likely, while the second may be possible, but it is hard to imagine as a common issue.

Nonetheless, the collocation routine has logic to handle both scenarios. For the first case, this could actually be an interesting phenomenon to study, particularly since

the issue of amalgamated LIS flashes is important elsewhere. For this reason, these flashes are retained, and the number of NLDN strokes per LIS flash and multistroke parameters are created (e.g., mean NLDN strength, percent CG, percent negative strokes). The second scenario, featuring a NLDN flash collocated to two different LIS flashes is not allowed. If this were to ever happen, the routine would skip the NLDN stroke.

The sample sizes of the input datasets and results of the collocation routine are shown in Table 2.1. Eleven years of TRMM and NLDN observations over the southern United States are used in this study, resulting in a sample of 4.6×10^8 NLDN strokes and over 700 000 LIS lightning flashes. Of course, the NLDN sample size is orders of magnitude greater than the LIS sample size due to the fact that the NLDN is a continuous network, while the LIS is only over the region periodically. Regardless, both systems show a land:coastal ocean lightning ratio of between 2–3. Though LIS flashes over the open ocean account for a higher fraction of all lightning by two orders of magnitude compared to the NLDN (0.6% versus 0.006%). This is likely due to the fact that there are no sensors offshore, making it very difficult for the NLDN to detect all but the strongest flashes over the open ocean.

One of the issues with the current NLDN dataset is that it is comprised of a mixture of version 2 and version 3 data due to the lack of availability of version 3 data for some years. One of the key improvements of version 3 to version 2 NLDN data is the introduction of CG/IC separation, (e.g., Wacker and Orville 1999a; Wacker and Orville 1999b), which would be quite helpful to this research. Table 2.1 also shows the size of the version 3 sample with CG/IC differentiation compared to the overall sample size.

Table 2.1. Sizes of the NLDN and LIS datasets over the common domain overall and for each terrain type.

	Total	Land	Coast	Ocean
NLDN Strokes	4.61×10^8	3.53×10^8	1.08×10^8	29 428
NLDN Strokes with IC/CG	1.14×10^8	8.97×10^7	2.4×10^7	9,600
NLDN IC Strokes	5.45×10^7	4.46×10^7	9.92×10^6	89
NLDN CG Strokes	5.94×10^7	4.51×10^7	1.42×10^7	9,511
LIS Groups	1.09×10^7	6.08×10^6	4.68×10^6	92 485
LIS Flashes	712 666	445 245	263 064	4,357

Roughly one in four NLDN strokes has CG/IC separation information, with a similar land/coastal ocean distribution to all strokes. Despite the fact that the NLDN is much more sensitive to strong CG strokes than IC discharges, IC and CG strokes each account for about half of the overall sample. Land and coastal terrains also show similar abundances, but that changes far offshore, where all but 89 of the 9,600 total open ocean flashes are stronger CG strokes and are subject to significant amounts of uncertainty. IC flashes over the open ocean are much too weak to be detected by the NLDN in most cases, though they would likely still be detected by the LIS since it observes total lightning.

The uncertainty introduced with such distant triangulations of NLDN stroke locations also hinders the collocation of NLDN strokes over the open ocean, defined as further than 1,000 km offshore. Table 2.2 shows distributions of the various elements of the collocated sample over each terrain type. Of the original 8th order of magnitude NLDN stroke sample, only nearly 99 000 can be successfully collocated to LIS flashes, and only 16 000 of these have CG/IC information available. Interestingly, the collocation routine seems to prefer IC flashes to CG. Where the original sample had a nearly equal quantity of each, 3,000 more IC flashes were successfully collocated than CG flashes, or 47% more. These NLDN flashes correspond to nearly 90 000 LIS flashes, or 12% of observed LIS flashes over the region. However, due to poor detection efficiency offshore and the uncertainty in the observed NLDN strokes observed offshore and outside of the network, not a single LIS flash over the open ocean could be successfully collocated with a NLDN stroke, and the land:coast ratio is significantly higher in the collocated dataset than in the LIS dataset.

Table 2.2. Size collocated NLDN/LIS dataset overall and for each terrain type.

	Total	Land	Coast	Ocean
Collocated NLDN Strokes	98 870	71 687	27 183	0
Collocated NLDN Strokes with IC/CG	16 819	13 633	3,186	0
Collocated IC NLDN Strokes	10 016	8,450	1,566	0
Collocated CG NLDN Strokes	6,803	5,183	1,620	0
Collocated LIS Groups	96 186	69 485	26 701	0
Collocated LIS Flashes	89 998	64 801	25 197	0

Indeed, some of these fundamental differences between the NLDN and LIS create the potential for characteristic oddities to be present in the statistics of the collocated sample. Figure 2.4 shows the distribution of NLDN strokes in the common NLD/LIS domain. Florida stands out as the lightning capitol of the region, with the southern Midwest not too far behind and local maxima over northern Mexico and immediately offshore of the Atlantic coast. On the low side, the sample size drops off very quickly offshore and over central Mexico, which are too far away from the network for most lightning to be detected. There is also a minimum in lightning activity over southern California and western Arizona.

These patterns lead to some pretty interesting regional statistics. Figure 2.5 shows the average strength of NLDN discharges, region by region, as well as the regional fractions of negative flashes and CG flashes. NLDN strengths for land regions tend to be lower than those for coastal regions, with mean strengths increasing with distance from the network. For the furthest regions, this is likely only the result of detection efficiency declining offshore. Low-amplitude IC flashes cannot be resolved across large distances, so the sample becomes dominated by stronger-amplitude CG flashes with increasing distance from the shoreline. This can be verified by looking at Fig. 2.5c, which shows that CG fractions in these distant areas are 90%, even 100% comprised of CG flashes. These regions generally lie well outside the contoured region in Fig. 2.4 and therefore correspond to a very small fraction of the total sample of coastal oceanic flashes.

The local maximum flash density in Fig. 2.4 lies at around 150 km offshore of South Carolina. Flashes shoreward of this maximum are no further from the NLDN stations near Savannah, Georgia or Wilmington, North Carolina than flashes onshore

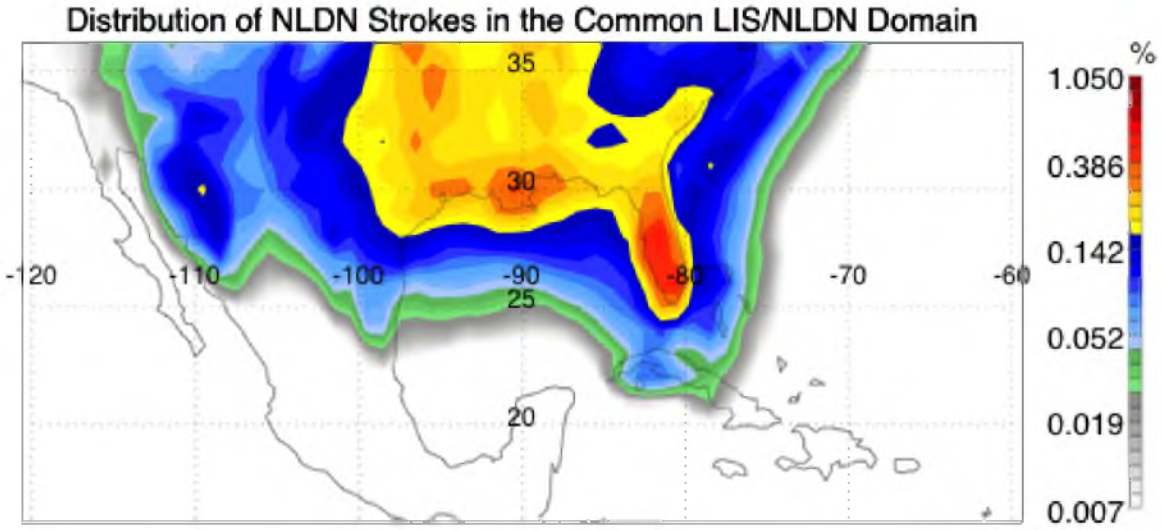

Fig. 2.4. Distribution of NLDN strokes in the common LIS/NLDN domain.

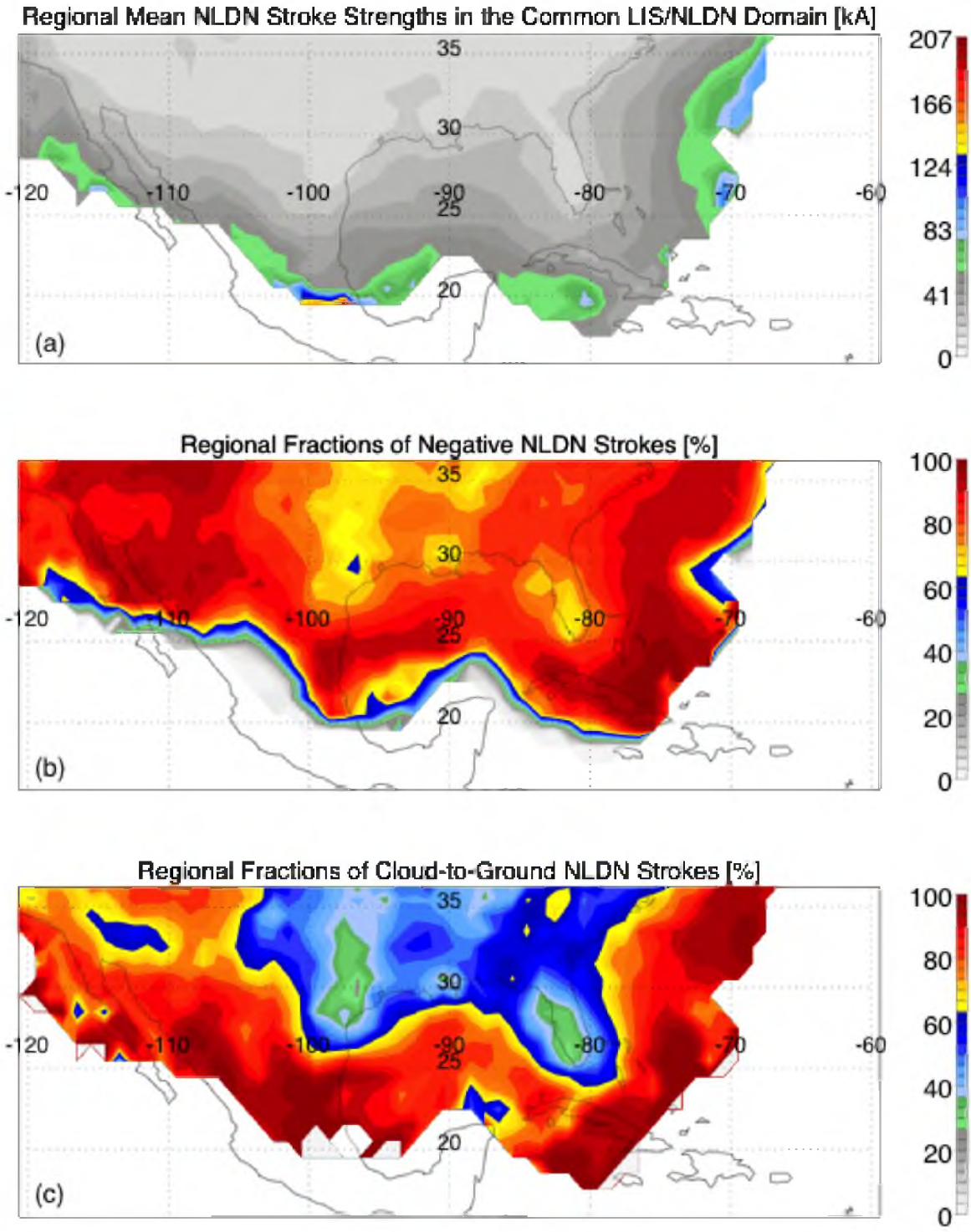

Fig. 2.5. Regional mean NLDN stroke strength (a), and regional fractions of negative NLDN lightning (b), and CG strokes (c).

between those stations and would likely be just as easily detected, though may still have a decreased location accuracy than flashes over land. This maximum is centered in the middle of the gradient between an average 20 kA, 50–60% CG flashes and 80% negative flashes onshore and an average 50 kA, 70–80% CG flashes, and 90% negative flashes further offshore. The fact that these gradients are present throughout the entire region offshore—and not just at extreme distances where the detection efficiency of the NLDN drops off, biasing observations towards stronger CG flashes—lends credibility to the idea that oceanic flashes are, indeed, stronger and more likely to be negative and CG flashes.

East of the Rockies and onshore, significant regional fractions of CG and IC flashes can be observed. In fact, some regions such as Florida and Texas see more IC flashes than they do CG flashes, more closely resembling reality despite NLDN's difficulties detecting IC flashes. These regions are also home to a higher fraction of positive lightning strokes (Fig. 2.5b). These regional statistics come together to produce the overall statistics in Fig. 2.6. Taken as a whole, coastal flashes are slightly more likely to be negative flashes (83% versus 79%) and tend to be significantly stronger than strokes over land (twice as strong at median), though no notable differences in the multiplicity statistics are observed. NLDN sensitivity alone does not explain how coastal flashes are stronger than flashes over land since the sample size decreases drastically with offshore distance, and the frequency of very strong distant offshore flashes is much lower than the frequency of lightning within the typical NLDN sensor spacing from the shoreline, where there should not be any reductions in NLDN sensitivity due to a lack of sensors. Regional differences such as these have been examined in literature (Zajac and Rutledge 2001).

Another interesting trend in this figure lies in the differences between CG and IC

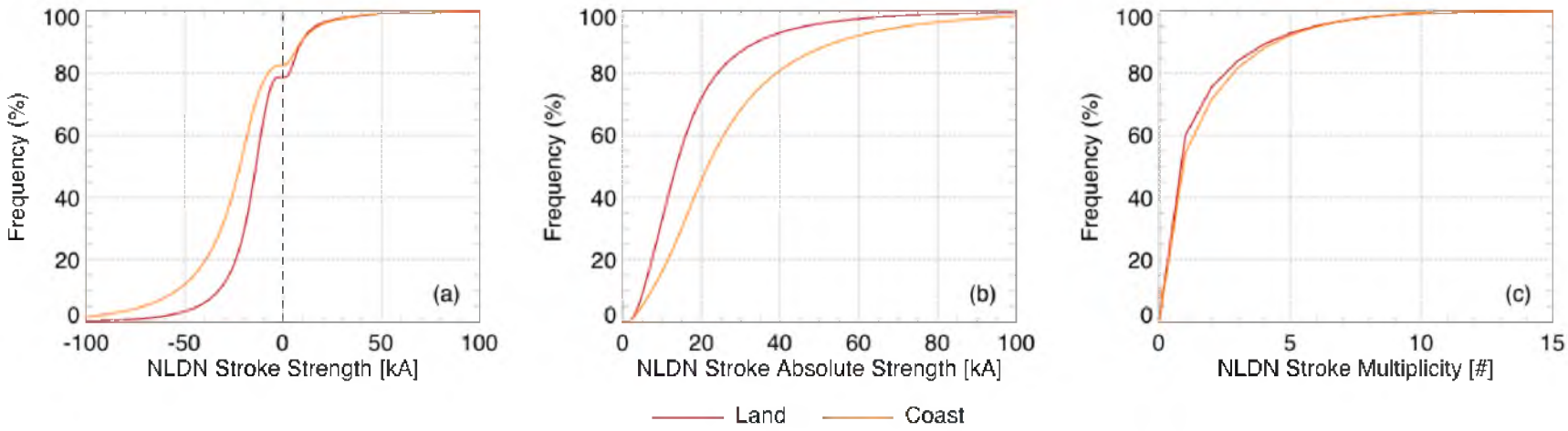

Fig. 2.6. Cumulative Distribution Functions (CDFs) of NLDN polarized stroke strength, absolute strength, and multiplicity for all NLDN strokes.

flashes. Nearly 90% of CG flashes are negative polarity over land and coast, while only 15–20% of IC flashes are negative (Fig. 2.7a). This is important because the number of collocated NLDN strokes with CG/IC separation is too small for use with the LIS collocations, which further reduces the amount of data with IC/CG separation by removing flashes with significant location uncertainties such as flashes far offshore. On the other hand, polarity is defined for all flashes. Therefore, looking at the polarity of lightning flashes, in some specific cases, may be used as a crude, first guess proxy to try to identify CG flashes in the collocated dataset where CG/IC identification is not available. However, this guess would not be valid for storms that produce primarily positive cloud-to-ground flashes such as the stratiform regions of mature MCSs. Another difference between CG and IC flashes is that while CG flashes can have multiplicities greater than 1, IC flashes are always a single-stroke event. This difference is not as useful as polarity differences for guessing whether a flash is a CG or IC flash since 60% of CG flashes also have singular multiplicities.

The distribution for LIS lightning flashes in Fig. 2.8 looks quite different compared to the NLDN distribution in Fig. 2.4. The lightning maximum is not located in Florida in this figure, but rather in the Midwest. Those offshore regions that the NLDN could not see are now filled in, with the Atlantic maximum extending far offshore over the Gulf Stream, a notable maximum along the western Mexican coast, and a signature of island convection over Cuba, Hispaniola, and Puerto Rico. There is also a sharp drop-off in sample density at the north extreme of the LIS domain. The reason this distribution is different from the NLDN distribution is not just that it is more complete or that the LIS observes total lightning without a strong preference to CG flashes. Due to the nature of

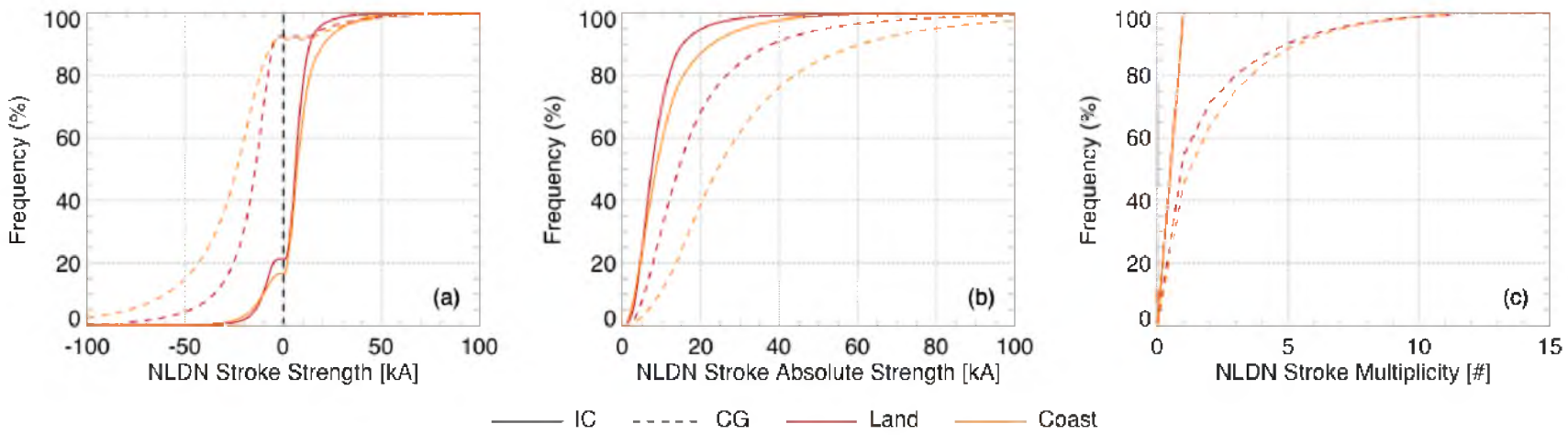

Fig. 2.7. CDFs of NLDN polarized stroke strength, absolute strength, and multiplicity for all NLDN strokes with CG/IC differentiation.

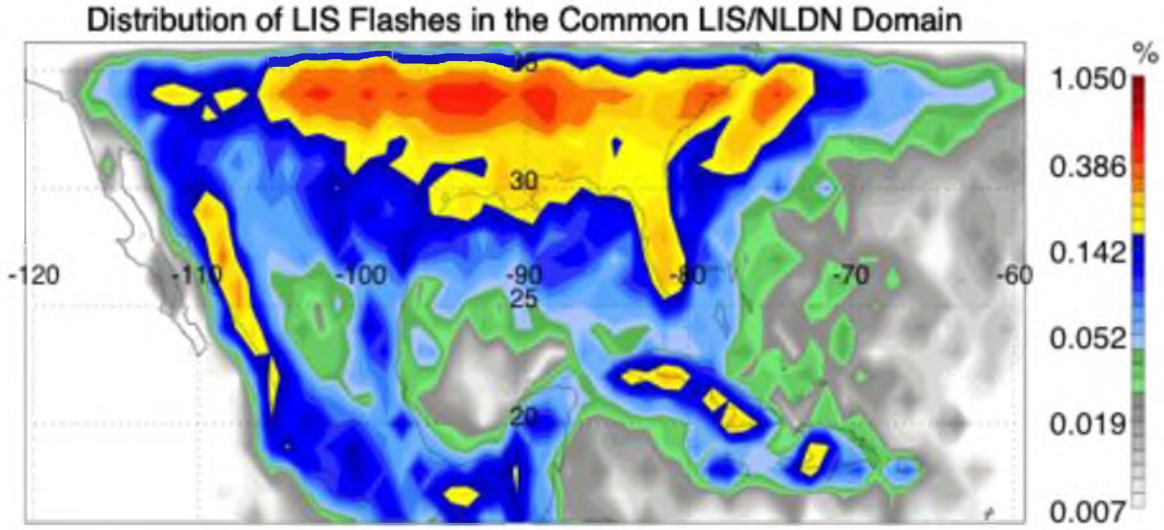

Fig. 2.8. Distribution of LIS flashes in the common LIS/NLDN domain.

the TRMM orbit, the LIS actually spends significantly more time looking at the higher latitudes near 30–33°N than it does at lower latitudes. The orbit track "turns" when it gets close to 36 degrees north or south, allowing the LIS to sample these latitudes for a longer interval.

The result of these factors is the distribution of the collocated sample in Fig. 2.9. The high latitude maximum of Fig. 2.8 and the Florida maximum in Fig. 2.4 are both present in the combined distribution. With the exception of the coastal Atlantic immediately offshore, the oceanic and much of the coastal flashes seen by LIS are all but nonexistent. Since these flashes are collocated, they are subject to the restrictions and quality control measures described in the collocation routine, greatly reducing the potential for artificial bias. Figure 2.10 shows the resulting NLDN statistics from the collocated sample, similar to Fig. 2.6 for all NLDN flashes. Despite the different distributions between the collocated sample and only NLDN and other than the slightly greater disparity in the negative fractions between land and ocean flashes, the statistics compare nicely with those for all NLDN flashes.

2.4 LIS and WWLLN Observations of Lightning

One of the shortcomings of the NLDN is that it overlaps only a small portion of the TRMM domain. It would therefore be ideal to collocate LIS observations with a lightning network that has global coverage. One of these networks is the World Wide Lightning Network (WWLLN). The WWLLN uses a similar system to the NLDN to detect lightning, except relying on the Very Low Frequency (VLF) band. Due to this, it has a very low detection efficiency, even compared to LF networks. This is just one of

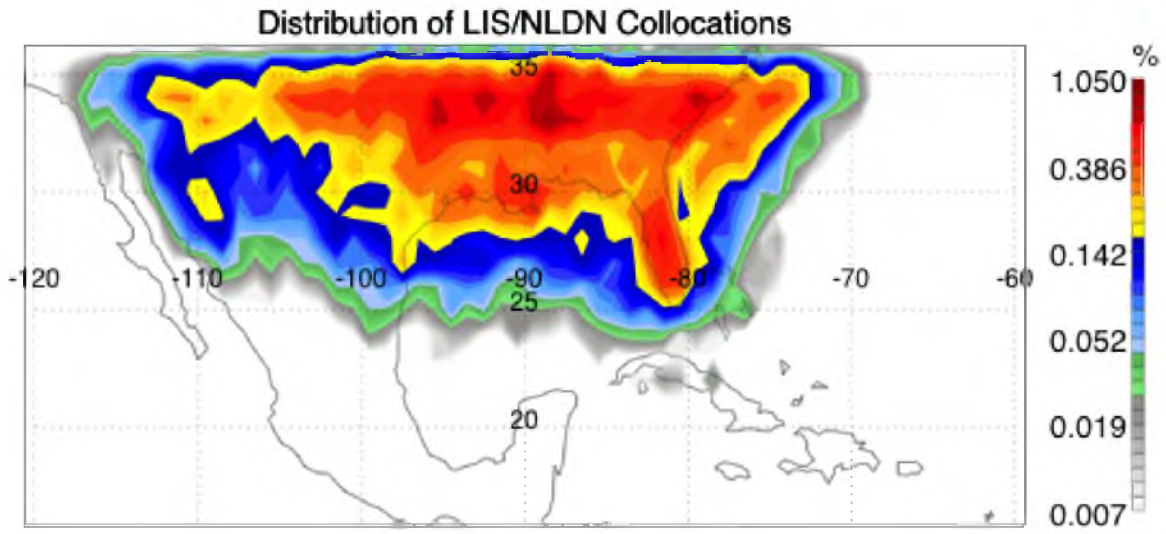

Fig. 2.9. Distribution of collocated LIS/NLDN flashes.

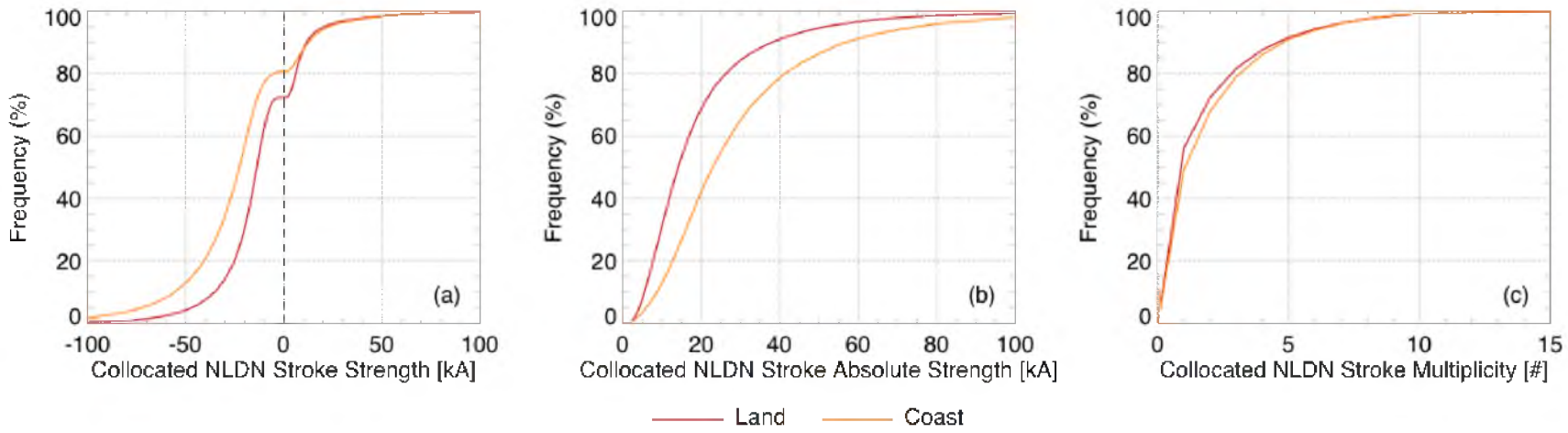

Fig. 2.10. CDFs of NLDN polarized stroke strength, absolute stroke strength, and multiplicity for collocated LIS/NLDN flashes.

a number of caveats that hamper attempts to collocate WWLLN with LIS. Additionally, only a small amount of WWLLN data are available, there are greater location uncertainties associated with WWLLN observations, and the data that are available show a clear regional bias of lightning detection based on the density of WWLLN sensors. This bias will decrease as more sensors come online in different regions of the world. Even since the data were first obtained, the sensor list on the WWLLN website has already grown substantially to even include the Universitat de València in Spain, their newest station. Furthermore, the WWLLN does not report many of the same parameters as NLDN such as the polarity of the flash or whether it is a CG or IC event, limiting the potential usefulness of the dataset in this line of research.

Fig. 2.11 shows a schematic diagram representing the program used for collocating WWLLN and LIS observations. The collocation routine created for use with WWLLN is nearly functionally equivalent to that used with the NLDN, but applicable to the entire LIS domain. Early tests included a much more generous time interval for the collocations, but those runs resulted in too much uncertainty and too many cases of WWLLN strokes being associated with multiple LIS flashes. Using the NLDN thresholds of half flash duration or 0.1 s seems to resolve this issue at the expense of the size of the collocated sample.

Table 2.3 shows the distributions of collocated elements for each terrain type and how the sample of collocated WWLLN strokes is spread out on each side of the equator and prime meridian. As before, most collocations occur over land, but the small sample sizes are problematic, with just on the order of 10 000 successful collocations across the globe. Similar to NLDN, it may be possible to create some meaningful statistics of land

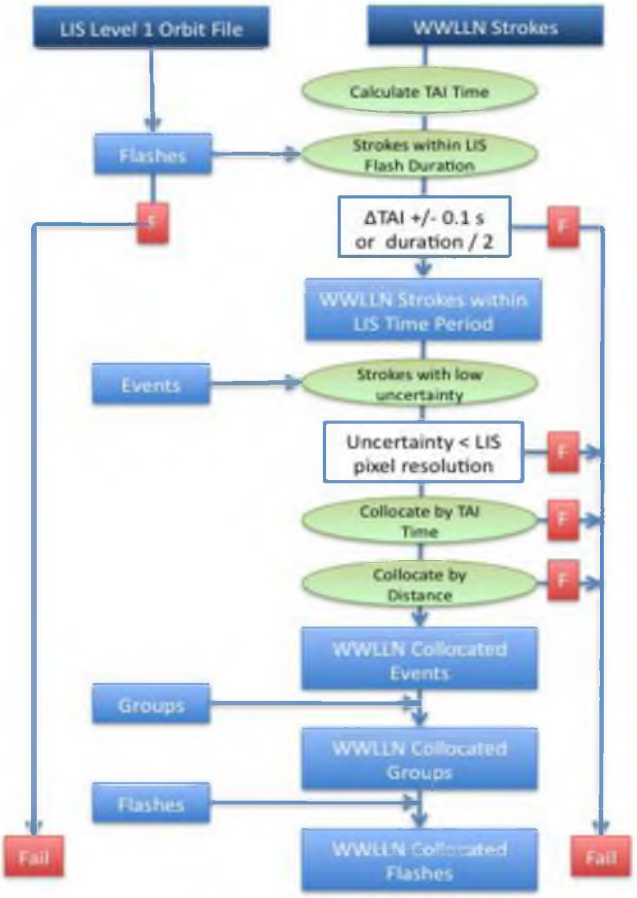

Fig. 2.11. Schematic diagram of the process of collocating WWLLN and LIS observations.

Table 2.3. Size of the collocated LIS/WWLLN dataset overall and for each terrain type and quarter-sphere.

	Total	Land	Coast	Ocean
Collocated LIS Groups	11 731	6,617	4,498	616
Collocated LIS Flashes	10 207	5,876	3,815	516
Collocated WWLLN Strokes	13 438	7,463	5,268	707
- NH West	7,485	3,996	3,156	333
- NH East	1,191	918	127	146
- SH West	2,200	1,117	1,010	73
- SH East	2,562	1,432	975	155

and coastal flashes, but there are too few oceanic flashes to compare coastal lightning, which may be produced by sea breeze convection with lightning from storms over the open ocean.

This shortcoming is exacerbated by the fact that the collocations are not distributed evenly around the world. Of the 13 000 independent WWLLN collocations, more than half occur over the western Northern Hemisphere. This can be seen clearly in the global distribution in Fig. 2.12. Significant contours in the distribution are almost entirely clustered over the southern United States, with smaller concentrations showing up in Colombia and Venezuela, the Maritime Continent, and northern Australia. Some of the world's premier lightning hotspots like Argentina and the Congo basin are almost completely devoid of collocated lightning flashes. This is different from what WWLLN climatology shows (Virts et al. 2013). The primary reason for this is the comparably poor detection efficiency of WWLLN compared to the NLDN. Even though LIS detects a high percentage of the flashes that it flies over, since it only sees snapshots of lightning activity, the overall probability of detection of a particular flash anywhere in the world is actually very small. For a flash to be collocated it must be observed by both sensors. Therefore, the probability of collocation for a given flash can be calculated by combining the probabilities of detection of each. For LIS and WWLLN, both of these probabilities are very small, and the product of two very small probabilities is an even smaller probability, resulting in a miniscule amount of successful collocations. NLDN on the other hand has a much higher probability of detection, resulting in a higher probability of finding collocated flashes within the common domain. Because of this and because of the inferior location accuracies of the WWLLN and the short record available, the WWLN is

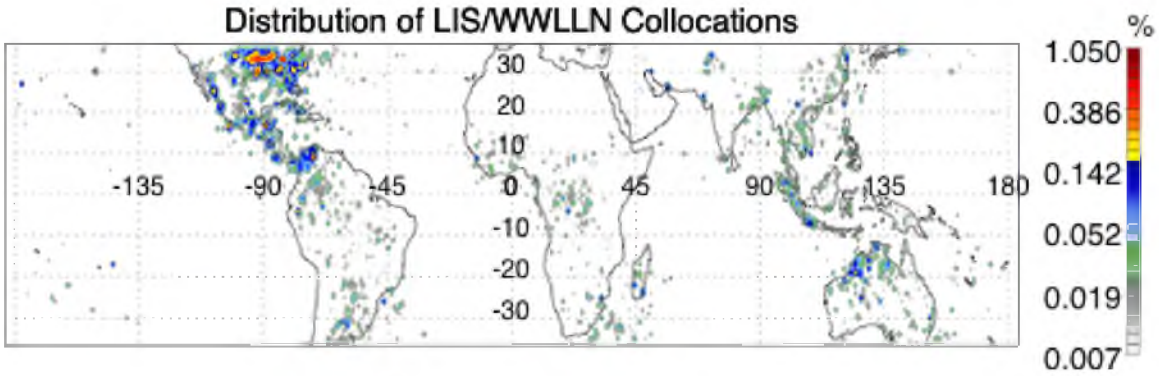

Fig. 2.12. Global distribution of LIS/WWLLN collocations.

not well suited for the purposes of this study after all. For this reason, only LIS and NLDN collocations will be used in the forthcoming analysis.

2.5 LIP Electric Field Observations

In this section, electric field measurements above storms taken by the Lightning Instrument Package (LIP) are compared to microwave brightness temperatures observed by the Advanced Microwave Precipitation Radiometer (AMPR) onboard the NASA ER-2 aircraft in order to find relationships between passive microwave observations and electric field strengths above thunderstorms and electrified storms without lightning. AMPR observations of brightness temperature provide estimates of convective strength and rain rates, though, unlike the TMI, the sensor only observed total power, not individual observations of the horizontal and vertical polarizations in each channel. Because of this, it is impossible to compute polarization corrected temperatures (PCTs; Spencer et al. 1989), which are corrected with surface background radiances.

Similar to satellite platforms, aircraft platforms such as the ER-2 only provide snapshots of individual storms at particular times. However, they also have an additional caveat: aircraft are not steady platforms and can change altitude, pitch, roll, and yaw. For this reason, it is crucial when working with airborne data to take into account the attitude and orientation of the aircraft. Still, aircraft can be much cheaper to operate and can be relatively easily fitted with new or different sensors depending on the needs of the mission, making them much more versatile than any satellite platform. The ER-2 flies at a nominal altitude of 20 km and speed of 210 m s^{-1} (Mach et al. 2009). Observations from multiple field campaigns are used in order to create a robust sample for examining these

relationships. The four different field campaigns that are used include: the Third and the Fourth Convection and Moisture Experiments (CAMEX-3, CAMEX-4; Kakar et al. 2006), the Tropical Cloud Systems and Processes mission (TCSP; Halverson et al. 2007), and the Tropical Rainfall Measuring Mission Large-scale Biosphere Atmosphere field campaign (TRMM-LBA; Halverson and Rickenbach 2002).

These field campaigns were chosen, in part, because they share the modern configuration of the LIP sensor package and also because each has a different focus and collection of different types of storm overflown. CAMEX-3 and CAMEX-4 took place over the Atlantic hurricane domain in the summers of 1998 and 2001, respectively. CAMEX-3 includes overflights of hurricanes Bonnie, Danielle, Earl, and George at different stages of development, while CAMEX-4 sampled hurricanes (including Erin, Gabrielle, and Humberto). Both field campaigns also overflew some nonhurricane convective storms. TCSP took place around Costa Rica in 2005. TCSP includes overflights of hurricanes and tropical storms Dennis, Emily, and Gert. Lastly, TRMM-LBA took place over the Brazilian Amazon from November, 1998, to February, 1999. TRMM-LBA was a ground validation mission for the Tropical Rainfall Measuring Mission (TRMM; Kummerow et al. 1998) with a focus on characterizing the dynamical, microphysical, electrical, and diabatic heating characteristics of Amazonian tropical convection.

Two ER-2 products are used in this study: LIP electric fields and AMPR passive microwave brightness temperatures. The LIP consists of several high-precision field mills that map the three-dimensions of the electric field vectors at the aircraft location as well as the charge on the aircraft and a Gerdien conductivity probe that measures air

conductivity. The LIP has seen service in many regions of the globe, from the FIRE-ACE field campaign (1998) in the far west through no less than 10 field campaigns in the Americas and then to the KWAJEX field campaign (1999) in the far east and spanning more than a decade of use since its maiden flight in 1990. The field mills are not only high-precision, but are also sensitive across a large dynamic range of electric field strengths, ranging from 1.9 V m^{-1} (which might be observed at altitude during fair weather flights) to 1.1 MV m^{-1} (which might be observed inside a strong thunderstorm) (Bateman et al. 2007; Mach and Koshak 2007).

Due to this wide range of observable electric fields, the LIP can observe numerous electrical phenomenon, including electric fields from electrified clouds and, as its name implies, lightning discharges. It may also be possible to differentiate between intracloud and cloud-to-ground discharges based on the characteristics of electric field changes; however, the instrument documentation does not go into detail. This information, as well as much of the following technical analysis of the sensor package, is partially a synthesis of information taken from the LIP instrument description page on the TEFLUN field campaign website, which seems to be one of the most detailed and complete sources of technical information about the LIP sensor package in print or online media (Lightning Instrument Package; Bateman et al. 2007). Identifying lightning flash locations from LIP data would not be straightforward without the help of some other ground-based network. Most lightning networks find the location of lightning based on triangulation techniques, either by comparing the arrival time of the lightning signal at multiple stations or the magnetic direction. Since the LIP is basically one moving station, it would seem that the only information it can provide by itself for lightning detection in

the conventional sense is the observation time of a lightning flash and the current at the location of the aircraft.

The other half of the LIP platform is the Gerdien conductivity probe mounted on the nose cone of one of the ER-2 superpods. The conductivity probe is made up of two Gerdien capacitor-type sensors, which allow for the measurement of conductivity due to positive and negative ions simultaneously. Using these observations of electric field and conductivity together, it is possible to estimate the strength of storm generator currents (Wilson currents), which make up an important part of the global electric circuit.

When the LIP was first flown, it consisted of only two electric field mills, mounted on the top and bottom of the aircraft's fuselage, just behind the cockpit. Under this original configuration, it was only possible to measure the vertical component of the electric field, but around the time of the TEFLUN and CAMEX-3 field campaigns (1998) the LIP expanded to as many as 8 field mills, depending on the availability of space on the aircraft. Typical mounting locations include the two superpods, which can accommodate 3 field mills each and the two on the main fuselage. Raw field mill output is converted to the actual atmospheric eclectic field vectors using an iterative matrix calibration process described in Mach and Koshak (2003).

The AMPR observes microwave emissions at wavelengths characteristic of precipitation: 10.7, 19.35, 37.1, and 85.5 GHz, similar to the TMI. Unlike the TMI, however, the AMPR is a total power passive microwave radiometer. It does not provide separate observations of horizontal and vertical polarizations, but rather reports a combination of both, simultaneously in the same reading. While this is not an issue for storms with strong microwave signals, clear air observations can look completely

different and even resemble strong convection in some situations. According to Spencer et al. (1994), the basic philosophy for the development of AMPR was to balance the "trade-offs between limited aircraft accommodation space and the need for multiple frequencies in a scanning instrument." The AMPR was mounted in the Q-bay of the ER-2 aircraft and observes microwave brightness temperatures at each of its four frequencies through a 90 degree scan angle centered at aircraft nadir. The polarization of the sensor is a function of scan angle, varying from completely vertical at -45 degrees, 50% of each polarity at aircraft nadir, and completely horizontal polarization at 45 degrees. The actual function of polarization with scan angle is of the form of $\sin^2$ rather than a first-power sin function (Hood et al. 2006).

Each scan consists of 50 bins within a common measurement grid for each frequency. Due to the AMPR scan geometry and assuming a mean flight altitude of 20 km, the footprint sizes for each frequency vary from 640 m at ground level for 85.5 GHz to 2.8 km at ground level for 10.7 GHz. The scan grid is completely filled by 85.5 GHz observations, giving a typical grid width of 32 km at ground level, and significant oversampling occurs for the lower frequencies. In reality, the average AMPR swath width varies between 30 km to 40 km at ground level, depending on the aircraft orientation and altitude.

AMPR and LIP observations are ideal for intercomparison between the electrical and precipitation properties of storms since they fly aboard the same aircraft and can be collocated into a common observation space. AMPR and LIP observations from each of the four of these field campaigns used in this study come courtesy of the Global Hydrology Resource Center (GHRC; http://ghrc.msfc.nasa.gov/) and Dr. Douglas Mach

(Mach et al. 2009, 2010, 2011). The distribution of AMPR observations by field campaign and terrain type is shown in Table 2.4. Since the LIP field mills operate at a higher temporal resolution than the AMPR (1 s^{-1} for LIP, 0.33 s^{-1} for AMPR), LIP observations are degraded to the AMPR sampling interval in this table. The combined sample includes more than 250 000 datapoints, with nearly 40% coming from CAMEX-3 alone. However, just over 200 000 of these datapoints have both valid coincident AMPR and LIP observations. Most of the reduction comes from CAMEX-3, which loses nearly 40 000 of its 100 000 datapoints to bad data, making the subset of good data from each campaign comparable in size. Based on the previous terrain-partitioning scheme, it is clear that most datapoints come from coastal oceanic regions, particularly in CAMEX-3, CAMEX-4, and TCSP. Only two field campaigns observed data over the open ocean: nearly 7,000 datapoints from CAMEX-4 and just 16 datapoints from TCSP. On the other hand, most land observations came from TRMM-LBA over Brazil.

Before LIP electric fields and AMPR brightness temperatures can be compared, a few quality control procedures must be performed on the LIP sample. Not only must the LIP data be degraded to match the AMPR temporal resolution, but since electric fields from electrified clouds make up the primary focus of this study, electric fields induced by lightning discharges, aircraft charging, and any other sources must first be removed. Figure 2.13 shows the LIP quality control and LIP/AMPR collocation routines employed in this study for most datapoints. There are too many special cases to be described in one simple schematic diagram, but the vast majority of ER-2 observations follow this branch, resulting in a refined collocated AMPR/LIP dataset.

The data processing starts by removing signatures of lightning flashes. This is an

Table 2.4. Distribution of collocated AMPR-LIP datapoints by field campaign and terrain type.

Field Campaign	Total	With Valid AMPR & LIP Observations			
		Total	Land	Ocean	Coast
CAMEX 3	101 684	64 152	6,972	0	57 180
CAMEX 4	47 396	45 699	1,122	6,743	37 834
TCSP	50 914	48 850	7,057	16	41 777
TRMM LBA	55 826	49 849	49 840	0	9
Total	255 820	208 550	64 991	6,759	136 800

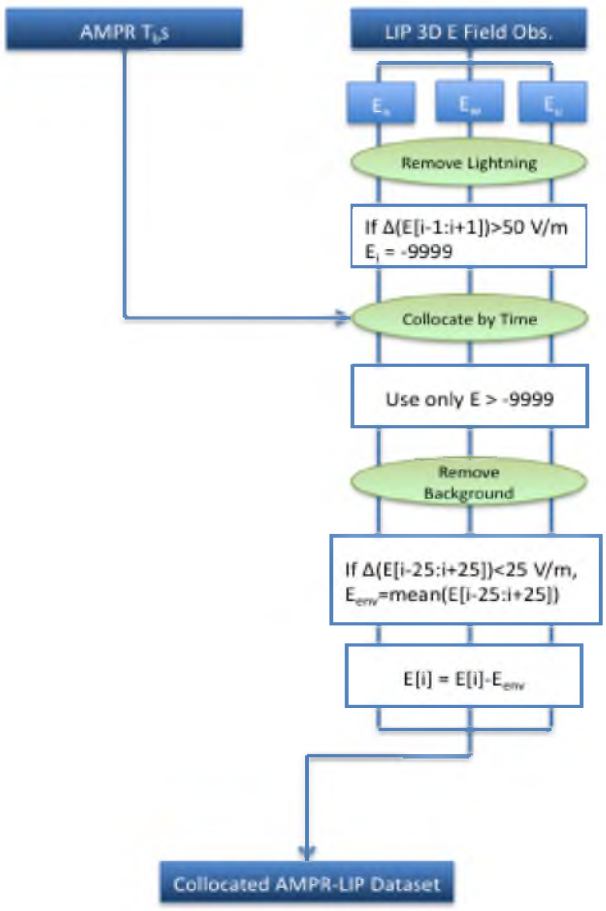

Fig. 2.13. Schematic diagram of the AMPR/LIP quality control and collocation routines.

important step since lightning flashes, while short in duration, often induce electric fields an order of magnitude greater than the relatively steady-state electric fields by comparison induced by electrified clouds. The lightning removal algorithm looks through the LIP record and picks out any datapoint associated with a sudden change of electric field between datapoints. Each datapoint in the record corresponds to roughly one second of observations, so most lightning events are almost completely contained within two datapoints. The algorithm uses not just the datapoint of interest but also the two surrounding datapoints to look for suspicious data. If any of these three datapoints have rapid increases or decreases in electric field (by more than 50 V m^{-1}, determined analytically to be a good threshold), the datapoint of interest is omitted (assigned a value of -9999). This process is done separately for each LIP component of the electric field in earth-relative coordinates (E_n: north, E_w: west, and E_u: up) rather than aircraft-relative coordinates (E_x, E_y, E_z), which are also reported. This algorithm does not always work, however. If lightning events induce electric field oscillations of a small amplitude, for instance, or if lightning flashes occur in rapid succession over a significant length of time, they may appear to be electrified clouds rather than lightning activity. By reviewing the output, this scenario appears to be rare, but not negligible, and will be discussed further by looking at some cases where this occurs.

After removing most lightning activity from the sample, the next step is to collocate AMPR and LIP observations by time. Only valid, nonlightning LIP datapoints are used for the collocation. The collocation routine takes all datapoints that fall within the AMPR observation window not associated with an error code and takes the median of their electric field strength rather than the mean to further limit the effect of lightning

contamination.

To emphasize electric fields contributed by electrified clouds, the last step of AMPR/LIP processing is to remove the contributions from background sources to the observed electric field, such as from aircraft charging. Background electric fields are not insignificant: they can often approach the amplitude of strong electrified clouds and even thunderstorms. They also have the potential to vary greatly between days, flights, and even throughout the duration of a single flight, not to mention in space in addition to time. The challenge, then, becomes separating out the effect of background electric fields so that the electric fields above different storms can be compared from one hour/flight/day/place to another. For most datapoints, the procedure is simple: sift through the data, recording the long-term mean electric field, and then subtract this mean value from the entire record. However, this becomes more difficult in situations where the electric field may be changing significantly throughout a large portion of the sampling interval, such as when the aircraft is passing over a large MCS or hurricane or when there is a lot of lightning. For this reason, the background electric field removal algorithm imposes a fluctuation criterion on calculating the long-term average electric field value: a new value of the background electric field is only recorded when the LIP observations are not oscillating by more than a certain amount. The specific requirement, which was determined by hours of fine-tuning, is a change of 25 V m^{-1} over the course of 50 datapoints (~150 seconds). The environmental electric field is defined using the first 50 datapoints of a flight (assuming the aircraft is not flying right into a storm after takeoff) and then is updated each time this criterion is met, often when the aircraft reaches the end of a leg and begins to turn around to make another pass.

For each LIP datapoint, the instantaneous electric field is subtracted by the previously recorded background value. This is done, once again, for each component of the earth-relative electric field, separately, though this does not usually affect the horizontal components so much as it does the vertical component. This step in the data processing can lead to a significant amount of uncertainty in the case of weaker electrified clouds. Vertical electric field observations can be reduced by as much as 1,000 V m^{-1}, which might leave a weaker case with only a strength of a few dozen volts per meter or a very small percent of the original observations. For this reason, observed electric fields below 10–20 V m^{-1} are not reliable in the following results. As a general rule, the stronger the observed electric field is above the background, the less potential there is for background reductions to induce uncertainty and the more likely the results are valid.

CHAPTER 3

LIS OPTICAL OBSERVATIONS OF LIGHTNING

TRMM observations of lightning flashes and the storms that initiate them can be very useful for examining relationships between the properties of thunderstorms and the properties of lightning. Optical sensors such as LIS differ substantially from other types of lightning detecting instruments since they observe the interaction of the actual flash of light created by the electrical discharge with the surrounding cloud medium rather than radio impulses from the breakdown. Because of this, for a flash to be visible to the LIS, its radiant energy must be sufficient to penetrate the cloud top, which depends on both the optical brightness of the flash as well as the scattering properties of the cloud layers in/under which it occurs. The overarching question in this section is why LIS flashes look the way they do. Are their footprint sizes and optical energies relatively constant and any perceived difference really a viewing problem or are there basic fundamental differences in the flashes themselves that cause them to be brighter or dimmer, larger or smaller? As for flash illuminated area, one would expect some component of both.

In this chapter, first the optical properties of lightning observed by LIS are summarized. Then, possible factors that can influence these properties are explored. The central questions in this chapter include

- What are the variations in the optical properties of lightning flashes? How

are they distributed geographically?

- Are the optical properties of the perceived flashes solely dependent on the properties of the viewing medium or is there room for the electrical properties of lightning (e.g., the strength of the return stroke, expansive spider lightning, etc.) to possibly play a role?
- Can exceptionally large, long duration, and bright flashes occur in any storm or are they the product of special types of storms?

3.1 LIS Optical Flash Properties

Before addressing what may contribute to the optical properties of lightning flashes, it is first necessary to summarize what those properties actually are. Cumulative Distribution Functions (CDFs) of flash illuminated (footprint) area, duration, the maximum radiance of all of the events that comprise the flash, and overall mean optical power are shown in Fig. 3.1. Mean optical power is a measure of the temporal radiative density of LIS flashes. It is simply calculated as the mean of all of the individual event component radiances for a given flash divided by its duration. Short-lasting, bright flashes would have high radiative powers, while long-lasting, dim flashes would correspond to low values. While maximum event radiance shows the peak brightness of a flash at any moment in its lifespan, mean optical power can be thought of as the overall brightness of the flash in time. The CDFs shown in Fig. 3.1 contain separate curves for each of the categories described in Section 2, daytime and night time flashes for land, ocean, and coastal regions, resulting in six separate distributions. Looking at this figure, it is clear that daytime and nighttime flashes have substantially different ranges of sample

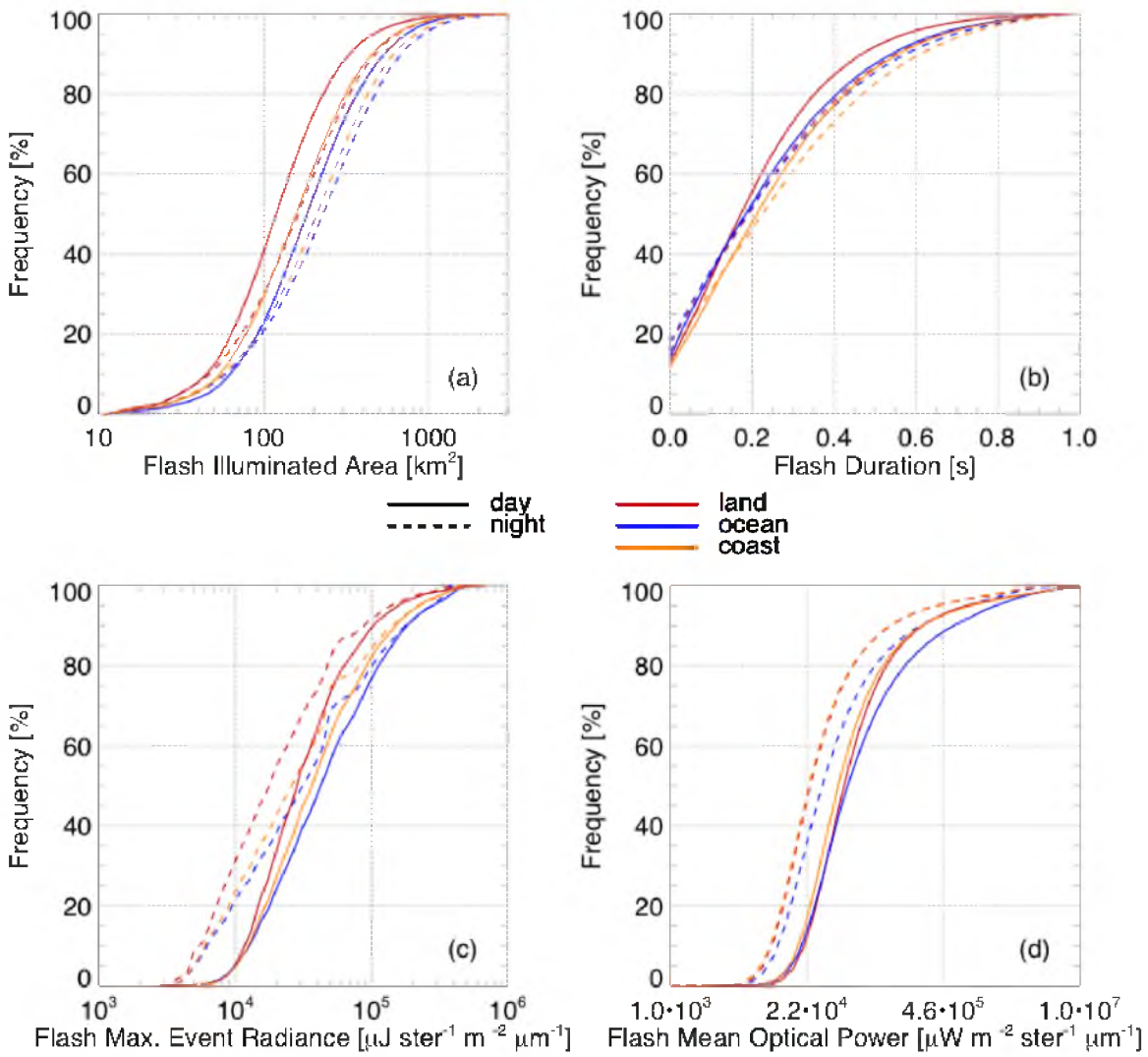

Fig. 3.1. CDFs of the properties of LIS lightning flashes categorized by terrain type and LIS sensitivity regime. Properties include flash illuminated area (a), flash duration (b), flash maximum event radiance (c), and flash mean optical power (d).

properties, particularly in maximum event radiance (Fig. 3.1c). In general, flashes that are observed during the daytime sensitivity regime are smaller than those observed at night. Daytime flashes also have higher mean optical powers than nighttime flashes and also maximum event radiances. Going from bright flashes towards dim flashes, particularly below 10^5 μJ $ster^{-1}$ m^{-2} μm^{-1}, the day and night curves in Fig. 3.1c diverge consistently, which is consistent with the LIS being more able to resolve dim flashes at night than during the day. While 20–30%of flashes observed at night have peak radiances of less than 10^4 μJ $ster^{-1}$ m^{-2} μm^{-1}, not even 5% of daytime flashes are this dim. The same argument can be made for flash mean optical power (Fig. 3.1d). Because the sensitivity of the LIS varies diurnally, it seems necessary to examine the optical properties of flashes at different times of day where the sensitivity is nearly the same to remove this potential source of bias.

In addition to the differences between sensitivity regimes discussed previously, differences between terrain types (land, ocean, coast) can also be observed. Flashes over land are typically small compared to oceanic and coastal flashes and are also relatively dim both by measure of peak brightness and areal mean power. Coastal flashes are in between the other two terrain types for flash illuminated area (Fig. 3.1a) and maximum event radiance (Fig. 3.1c). However, the distributions for flash duration (Fig. 3.1b) are significantly different from the other parameters. Flashes over land during the day are, overall, shorter duration than daytime oceanic flashes, but given the nonlogarithmic scale employed in Fig. 3.1b, the differences are much more subtle. Almost no difference can be seen between the same curves for nighttime flashes. However, in both day and night regimes, coastal flashes are longer lasting than flashes occurring over either of the other

terrain types. Because of this, flash optical powers of coastal flashes are also comparable to those of flashes over land since mean event radiance follows maximum event radiance and falls between land and ocean regions, while durations are relatively long.

The mean properties of each group are shown in Table 3.1. Not only are oceanic flashes larger, but larger by a substantial margin. Despite being less common than flashes over land, the average oceanic flash is 31.7% larger during the day and 39.8% larger at night than the average land flash. They are also brighter on average, with maximum event radiances 55.2% greater during the day and 75.1% greater at night. This is not just the case for flash peak brightness, but overall brightness as well, with mean optical powers over the ocean 24.6% higher than over land during the day and 41.2% higher at night. Flash durations between land and the open ocean are not significantly different, but coastal flashes are 22.1% longer lasting than daytime flashes over land and 15.6% longer at night. Coastal flashes also last slightly longer than oceanic flashes, on average. Coastal flashes are 7.8% longer during the day and 11.4% longer at night compared to the average oceanic flash.

One of the interesting aspects about these trends is that they hold for each sensitivity regime. Although it is justified dividing the day by LIS sensitivity, it is not entirely necessary as regional differences stand out regardless of the time of day considered. That is, unless diurnal regional differences in lightning production are concerned. Figure 3.2 shows the global distributions of lightning normalized by LIS view time for all flashes as well as the departures from this pattern for the daytime and nighttime sensitivity regimes. The global distribution of lightning (Fig. 3.2a) is dominated by a few key land regions, including the Congo Basin in Africa, the

Table 3.1. Median and 90th percentile threshold values for flash illuminated area, duration, and mean optical power for flashes in each sensitivity regime and categorized by terrain type.

		Day		Night	
	Terrain	Median	Top 10%	Median	Top 10%
Flash Area (km^2)	all	148.6	604.8	206.4	839.7
	land	137.4	533.8	189.1	751.9
	ocean	211.5	840.4	267.6	1,085.3
	coast	181.2	724.8	246.7	980.8
Flash Duration	all	0.20	0.65	0.22	0.75
(s)	land	0.19	0.61	0.21	0.73
	ocean	0.21	0.72	0.21	0.78
	coast	0.24	0.74	0.25	0.82
Flash Mean	all	62 512	1 083 060	31 440	565 709
Optical Power	land	63 893	1 000 030	30 982	523 655
(μW m^{-2} ster^{-1}	ocean	68 969	1 956 580	40 111	1 075 970
μm^{-1})	coast	57 446	1 127 510	31 132	559 729

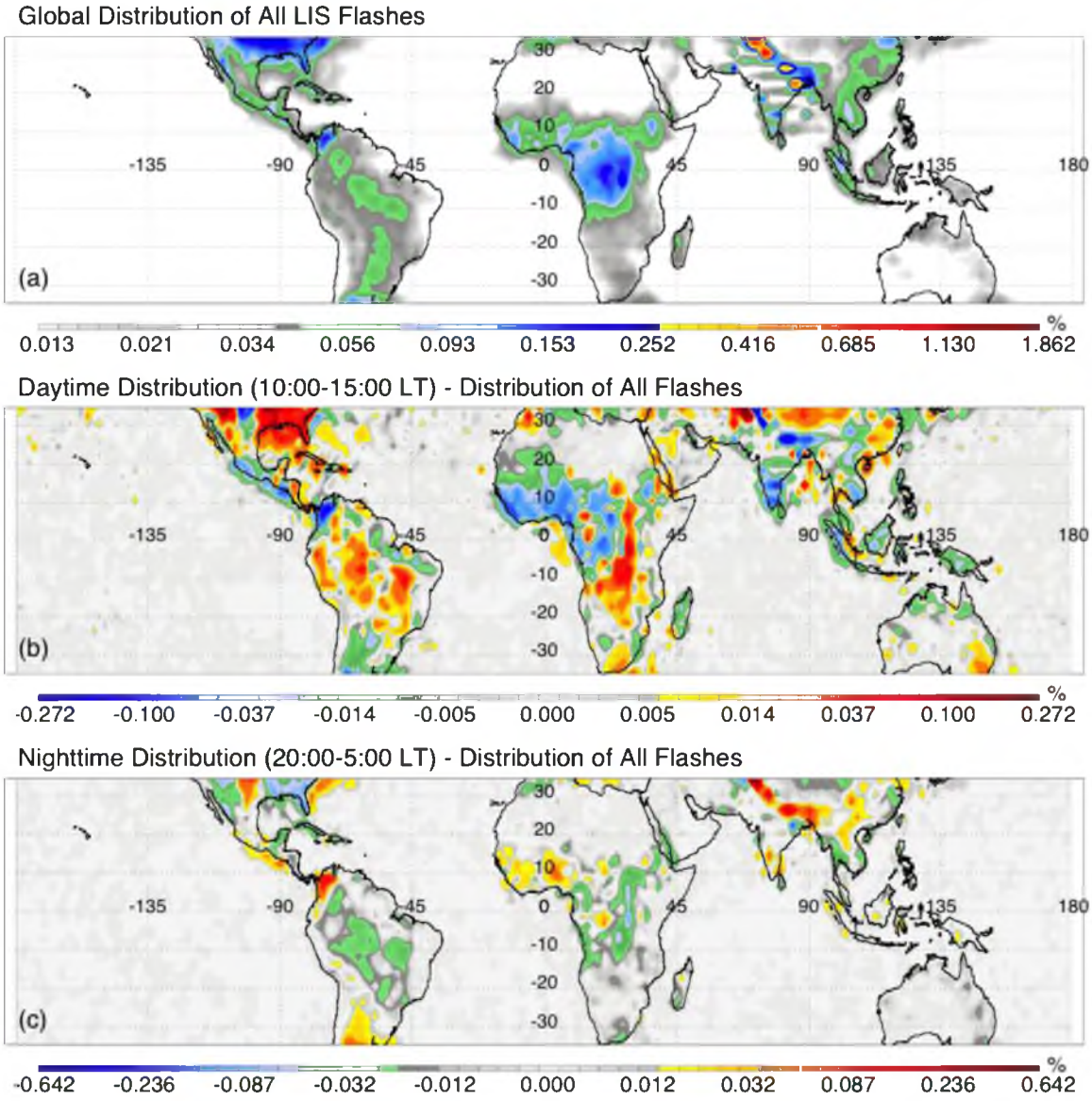

Fig. 3.2. Global distributions of LIS lightning flashes. Regional sample density of all LIS-observed lightning flashes normalized by instrument view time as a function of latitude (a), differences between the global distribution of daytime flashes from the overall distribution (b), and differences between the global distribution of nighttime flashes from the overall distribution (c).

southeastern United States, and the slopes of the Himalayas, consistent with previous research (Christian et al. 2003). Significant numbers of flashes can also be found in Argentina, throughout the "green ocean" (Williams and Satori 2004) of the Amazon, Colombia, the Sahel, parts of China, Vietnam, Thailand, and the maritime continent of Indonesia (Williams et al. 2005). Figure 3.2b shows the difference in the fractional distributions of lightning between daytime (10:00 and 15:00 local time) flashes and the global fractional distribution shown in Fig. 3.2a. Compared to the general pattern a higher daytime proportion of lightning can be found in the southeastern United States and Gulf of Mexico, Arizona and parts of Mexico, Ecuador, Peru, much of the Amazonian "green ocean," the eastern half of the Congo Basin, eastern South Africa, Tibet, parts of eastern China, and southeastern Australia. At the same time, the proportion of lightning flashes is reduced over west Texas, Colombia, Argentina, the northern coast of Brazil starting from Natal westward, the Sahel and western Congo Basin, much of India, Indochina, and the maritime continent. This pattern is largely inverted for the nighttime distribution (Fig. 3.2c). Compared to the global pattern, Arizona, the southeast United States, the "green ocean," much of the Congo Basin, eastern South Africa, and Tibet see lower proportions of lightning activity, while Texas, Colombia, Argentina, the Sahel, and the Himalayas see an increased flash proportions.

We next examine how the distributions of exceptionally large, long-lasting, and bright flashes differ from the general case. LIS sensitivity should influence these global statistics to some extent. For this reason, daytime and nighttime statistics are presented first, separately, and then, after it has been shown that these trends are apparent in both daytime and nighttime sensitivity regime (signifying that they are not merely the result of

sensitivity bias); the results are generalized for all times of day. Global distributions of the world's largest daytime flashes based on the thresholds established in Table 3.1 are shown in Fig. 3.3. By simply comparing Fig. 3.3a to Fig. 3.2a, it is clear that regions that have significant lightning activity also have large numbers of flashes with exceptional illuminated areas, leading to similar global distributions. Figure 3.3b shows the difference between global daytime flash distribution and daytime top 10% largest flash distribution using the same method employed in Fig. 3.2b for comparing the daytime and general distributions of all flashes. By pure concentrations (normalized by the total number of flashes in each distribution) it appears that most regions show little difference between these distributions. However, some regions stand out as having an increased proportion of large flashes in the daytime. These regions include the land and adjacent coastal areas of the southern United States, Panama, and parts of Indonesia as well as the waters offshore of eastern South Africa and Okinawa. Meanwhile, daytime large flash frequencies are suppressed compared to the global distribution over the western United States, most of the Congo basin, and India and Tibet.

These major differences in the global distributions indicate that some regions of the world are more susceptible to exceptionally expansive lightning flashes. Figure 3.3c shows the regional fraction of daytime lightning flashes exceeding the global 90^{th} percentile threshold described in Table 3.1. If such flashes were evenly distributed, these fractions would be 10% everywhere; however, considerable variations are observed in Fig. 3.3c. These statistics cannot be shown for every region as not every part of the world has enough lightning to produce reasonable statistics. There is very little lightning over the Sahara, and much of the world's oceans during the daytime sensitivity regime,

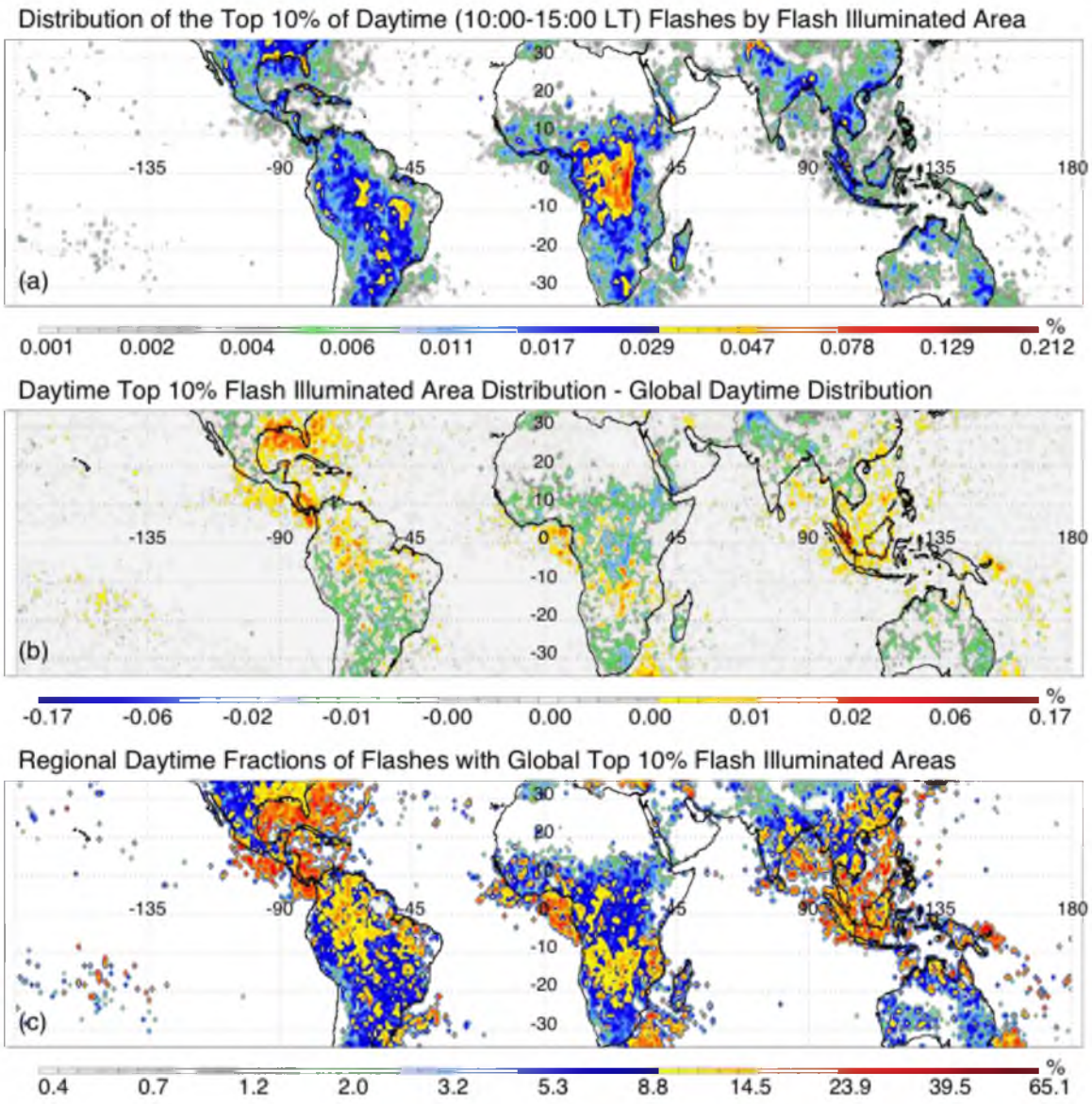

Fig. 3.3. Global regional sample density of the top 10% largest daytime flashes globally, normalized by latitude-dependent instrument view time (a), differences between the daytime top 10% largest and overall daytime distributions (b), and regional fractions of the global daytime top 10% largest flashes (c).

resulting in insufficient flashes for stable statistics. For this reason, if less than 20 flashes are observed in a 1° by 1° box, that box is omitted from the analysis. For most land regions that are defined, the frequencies of large lightning flashes fall generally between 8% and 12%, which is expected since most lightning occurs over land, so the 90th percentile of flash area should be more akin to the 90th percentile of land flashes. Frequencies higher than 15% are rarely observed over land, and where they are (e.g., Panama, southern India) it is likely due to contouring issues or boxes that straddle coastlines and include significant amounts of coastal flashes.

Typically, regions with significantly elevated daytime fractions of large flashes lie over coastal regions and the open ocean, at least where the sample is large enough to be counted (Fig. 3.3c). In these regions, flashes exceeding the global 90th percentile of flash illuminated area often account for 20%, 30%, even up to 60% of all observed flashes. Flashes over these regions are not as frequent, but when they do happen, they tend to illuminate a large area. Coastlines such as the coast of Vietnam often show sharp gradients in regional fraction of large flashes, while islands may have regional frequencies similar to either land or ocean regions.

Distributions of large flashes in the nighttime sensitivity regime are shown in Fig. 3.4. Significant differences can be observed between night and day, though much of it appears to be due to the diurnal variation of lightning in general, as most of the same regions stand out in Fig. 3.4b, though not all and not to the same extent. Some key differences between then daytime and nighttime frequencies of large flashes include the "green ocean," which has a relatively small fraction of nighttime flashes, but a large portion of those flashes illuminate large areas (Fig. 3.4b). Additionally, the Gulf of

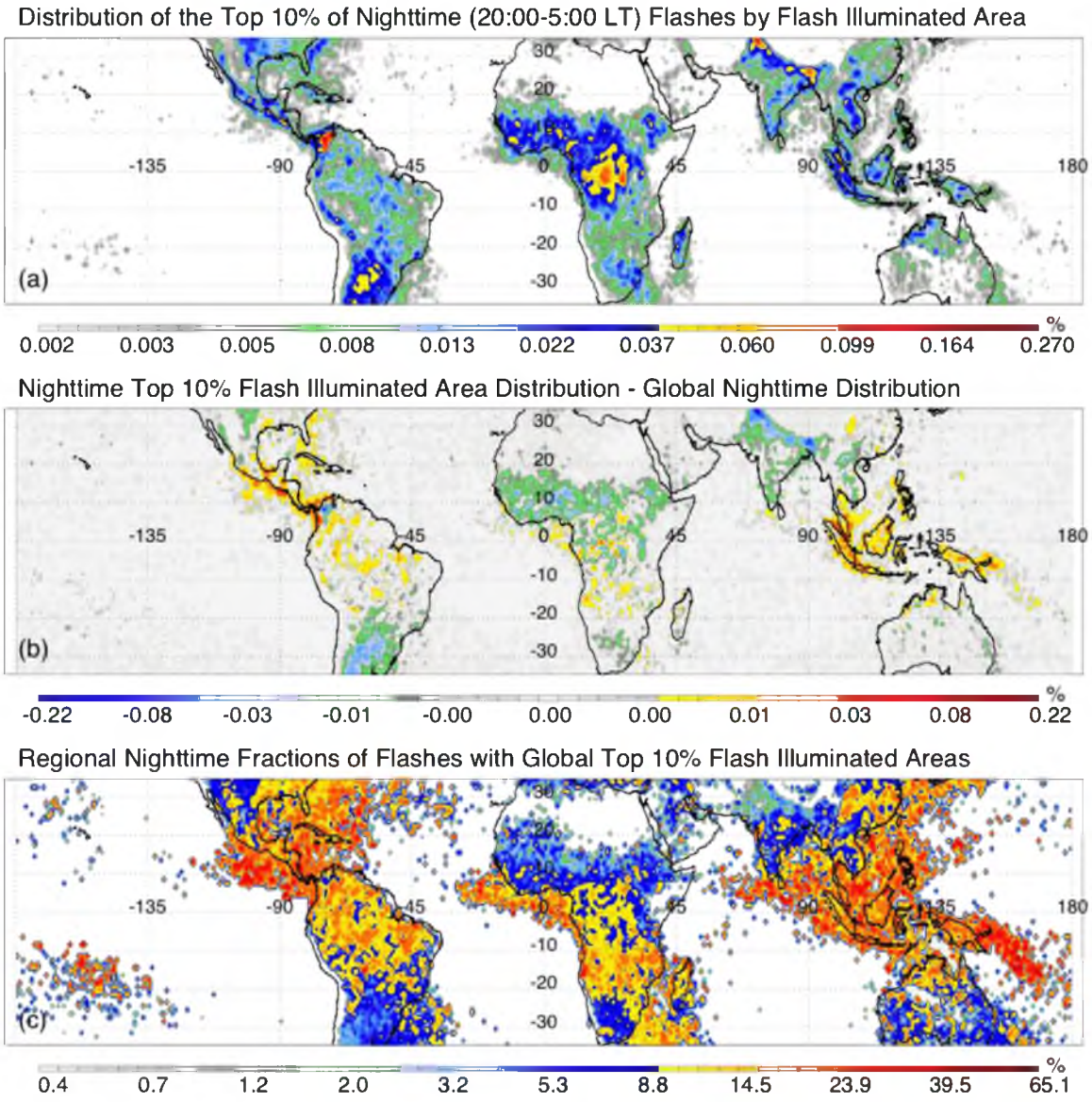

Fig. 3.4. Global regional sample density of the top 10% largest nighttime flashes globally, normalized by latitude-dependent instrument view time (a), differences between the nighttime top 10% largest and overall nighttime distributions (b), and regional fractions of the global nighttime top 10% largest flashes (c).

Mexico maximum is now considerably reduced. Despite these differences, the global pattern of the regional fractions of large flashes is similar, but more detailed due to the combined effect of most oceanic flashes occurring at night and the increased sensitivity of the LIS allowing for more flashes to be observed. Large flashes are 3–6 times more likely than over land throughout most of world's coastal and oceanic regions, far exceeding 10% of the local sample. Still, there are some significant differences between day and night. Unlike the daytime regional fraction distribution (Fig. 3.3c), the boundaries between typical land and ocean values at night do not form a sharp cutoff along all coastlines, but rather are more gradual in the subtropics, resulting in values closer to 10% to be seen far offshore of the eastern United States, South Africa, Australia, and Argentina.

While it may have appeared that terrain type alone may have been responsible for the sharp gradient between land and coastal statistics before, this diurnal difference suggests that the reason for the land versus ocean difference is primarily convective in nature, stemming from sea breeze circulation systems. Meanwhile, large tropical islands and thin columns of land surrounded by water (e.g., Central America) show large—even oceanic—regional fractions of large flashes at night. Much of the green ocean also shows regional fractions exceeding 15% at night. It is clear from these two figures that land-ocean differences in flash optical area are the result of other factors than LIS sensitivity. For this reason, while it may be beneficial to partition the lightning data into day, night, and transition periods, giving the added bonus of being able to examine diurnal trends associated with convection as well as sensitivity, the global results of the regional variation of flash properties in Fig. 3.2 are independent of LIS sensitivity.

This diurnal pattern leads to the global distribution in Fig. 3.5. Using the entire sample of LIS flashes allows for additional regions to be filled in and additional confidence in borderline regions in Fig. 3.3 and Fig. 3.4, though the effects of LIS sensitivity on perceived optical area must be kept in mind. Overall differences in land and ocean flashes are seen much more clearly in this figure than in the previous two. Most regions where the distribution of large flashes shows enhancement over the general distribution are coastal, oceanic, or island in nature. The majority of large islands and thin land regions within 15° of the equator seem to see this enhancement, while those that are poleward of 15° latitude are often more similar to land. Additional isolated regions may also show enhanced potential for large flashes, including parts of the green ocean, Colombia, Venezuela, Zambia, Angola, Mozambique, northern Australia, and central China (Fig. 3.5b). The remaining land regions either see no difference or slightly less large flashes than the general distribution would indicate. These trends lead to low-to-normal large flash fractions over land, including most of the green ocean and islands and thin land features outside the deep tropics, and consistently high fractions of large flashes over nearly every ocean region where there are enough data.

Unlike flash illuminated area, flash duration was shown in Fig. 3.1 to be shortest over land and longest in coastal regions. The global distribution of the world's top 10% longest lasting flashes is shown in Fig. 3.6. Regions with enhanced flash duration include coastal central America and the Caribbean, the southern and eastern coasts of the United States, the center of the Congo Basin, the waters off the eastern coast of South Africa, northern Australia, the maritime continent, and a few coastal regions of the South China Sea. In contrast, long duration flashes are less common in Arizona, Mexico, nearly all of

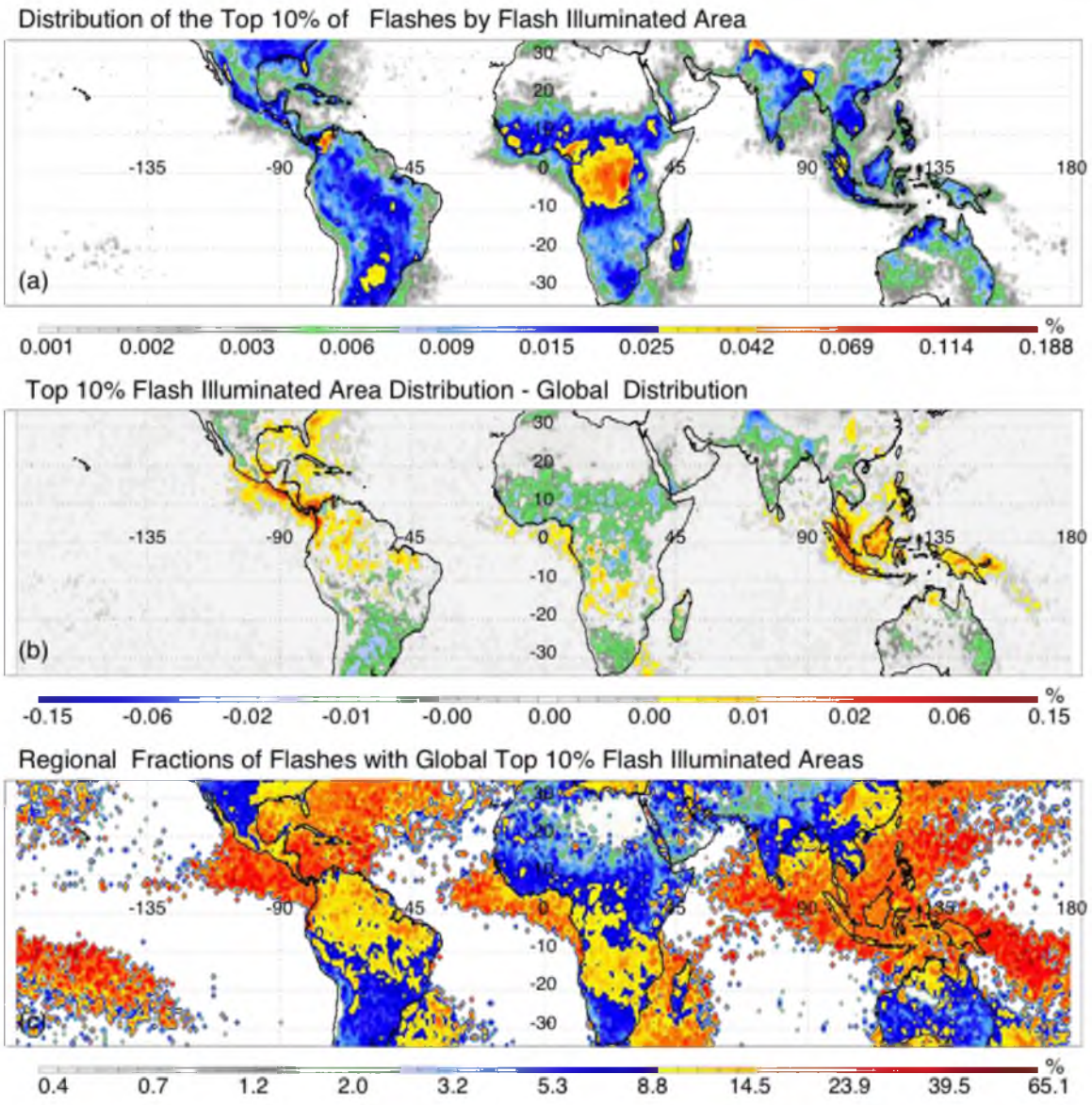

Fig. 3.5. Global regional sample density of the top 10% largest flashes globally, normalized by latitude-dependent instrument view time (a), differences between the top 10% largest and overall distributions (b), and regional fractions of the global top 10% largest flashes (c).

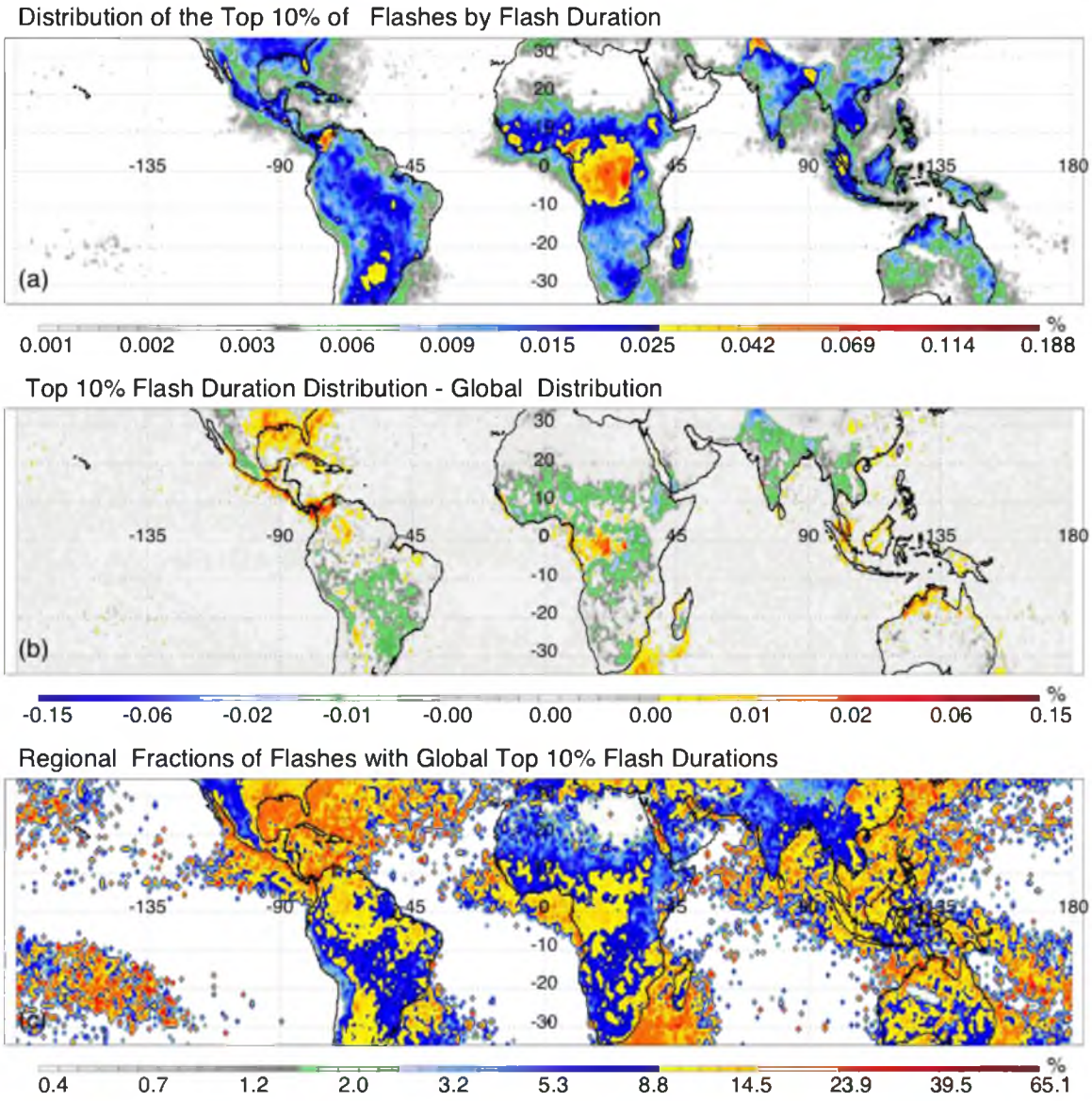

Fig. 3.6. Global regional sample density of the top 10% longest lasting flashes globally, normalized by latitude-dependent instrument view time (a), differences between the top 10% longest lasting and overall distributions (b), and regional fractions of the global top 10% longest lasting flashes (c).

South America below the equator, the remainder of sub-Saharan Africa, India, and Indochina (Fig. 3.6b). Based on these deviations from the global distribution, regional fractions of long lasting flashes (Fig. 3.6c) are significantly higher for coastal waters adjacent to the southern and eastern United States, Central America, the Caribbean, South Africa, Australia, and China as well as the South Pacific Convergence Zone (SPCZ). Long lasting flashes can also be found at disproportionate frequencies in the Red Sea and certain areas of the Pacific. Most of these regions are coastal, based on terrain type, leading to the differences noted earlier. Very few regions over land show relatively high fractions of long lasting flashes, and the majority of those are located right along a major coastline with high values. Regions that have abnormally high regional fractions that extend significantly inland include Louisiana and central China.

Separate distributions of flashes categorized by duration during daytime and nighttime sensitivity regimes are shown in Fig. 3.7 (day) and Fig. 3.8 (night). As before, the overall distributions in panel (a) of each figure are similar to the general case, with certain areas standing out in each sensitivity regime. During the day, the Congo basin maximum extends into the Sahel, the Unites States lightning maximum is well pronounced, and large amounts of lightning flashes are visible throughout most of Brazil. At night, on the other hand, many of these regions do not have nearly as much lightning, particularly Brazil and the southern United States. There are also differences in the departures from the global distribution shown in panel (b) of each figure. During the day, the southern United States is much more likely to have long lasting lightning flashes than normal compared to the global distribution. At night, the Panamanian and Grand Colombian maximum is the most prominent feature, and the local maximums

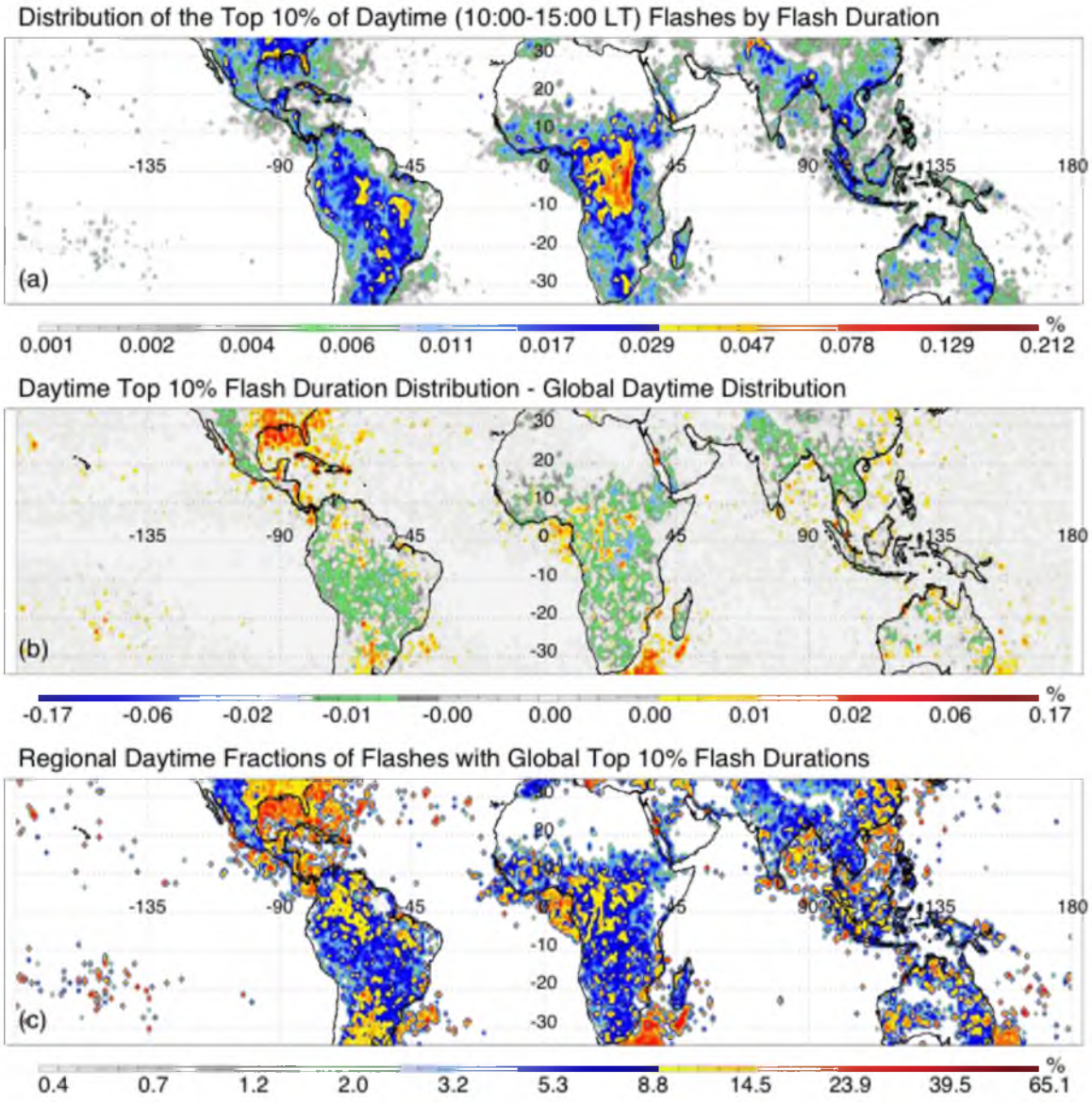

Fig. 3.7. Global regional sample density of the top 10% longest lasting daytime flashes globally, normalized by latitude-dependent instrument view time (a), differences between the top 10% longest lasting and overall daytime distributions (b), and regional fractions of the global top 10% longest lasting flashes (c).

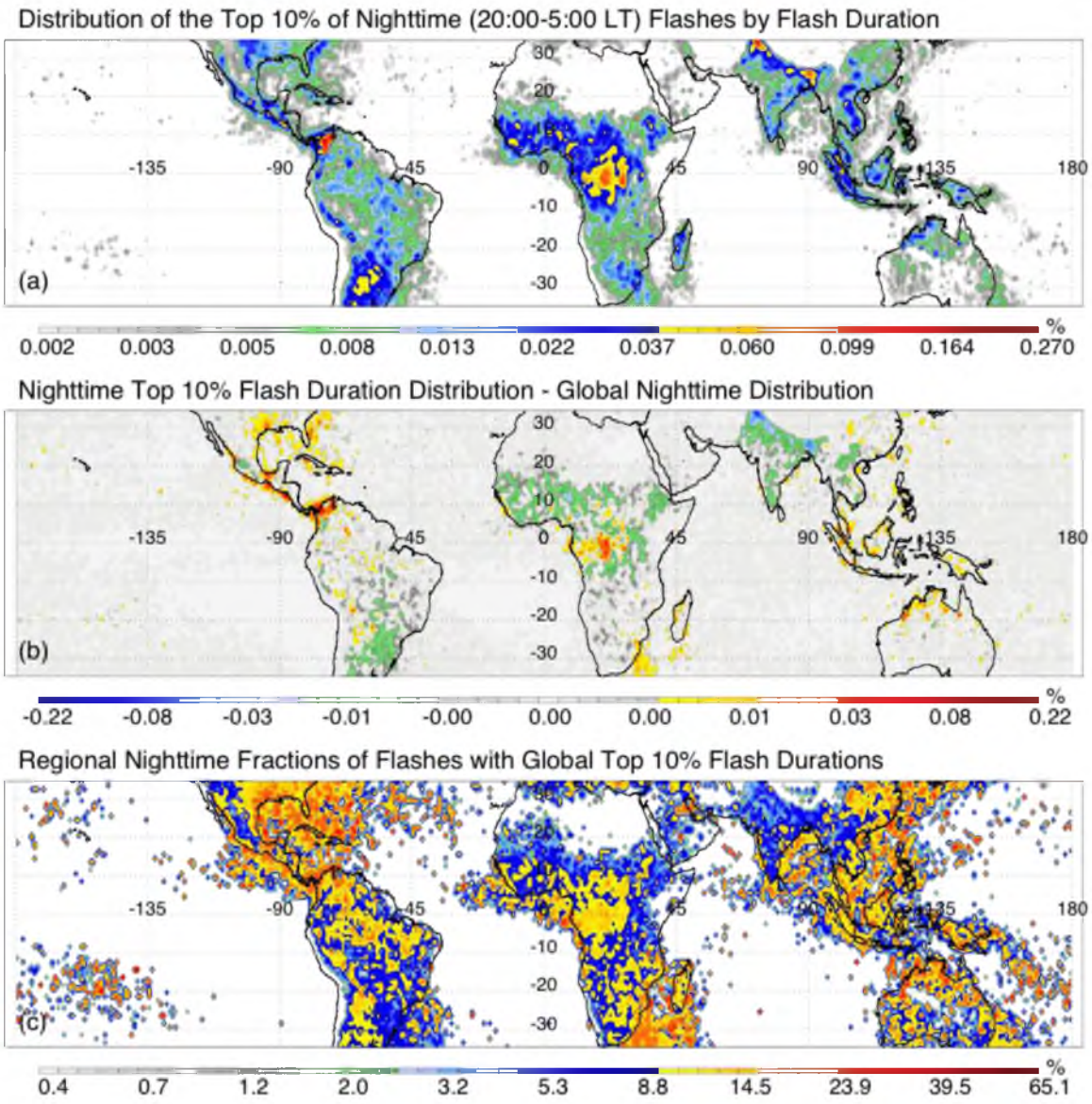

Fig. 3.8. Global regional sample density of the top 10% longest lasting nighttime flashes globally, normalized by latitude-dependent instrument view time (a), differences between the top 10% longest lasting and overall nighttime distributions (b), and regional fractions of the global top 10% longest lasting flashes (c).

downstream of major continents are not nearly as important as during the day. Despite these regional differences in the number of long lasting flashes in each region, most of the same regions show up in Fig. 3.6c, Fig. 3.7c, and Fig. 3.8c as having abnormally high regional fractions of long lasting flashes.

Global distributions for the radiance of the brightest event pixel for a given flash are shown in Fig. 3.9. The overall distribution is nearly identical (Fig. 3.9a) to that of flash illuminated area (Fig. 3.5a), yet there are still significant differences between the two that are too subtle to be seen from overall frequency distributions. Even though both large flashes and exceptionally bright flashes show enhancement over coastal regions (Fig.3.5b, Fig. 3.9b) and consequently make up exceedingly high regional fractions in coastal and oceanic regions (Fig. 3.5c, Fig. 3.9c), the regions that see the most enhancement over the global pattern are different for each parameter. While particularly large flashes see the most enhancement and are the most common in coastal and oceanic regions within 20° of the equator, particularly bright flashes account for higher fractions of flashes in regions poleward of 20° latitude, with the exception of the South Pacific Convergence Zone (SPCZ) between Australia and the Cook Islands. Furthermore, particularly bright flashes make up significantly smaller fractions of flashes over many large islands and thin land regions (e.g., Central America, Madagascar, Maritime Continent), resulting in regional fractions more similar to land regions than coastal or oceanic regions.

Based on these global distributions, high fractions of flashes with exceptional mean optical power occur in regions that typically have flashes with high powers and short durations, including much of the open ocean, particularly in the subtropics. The

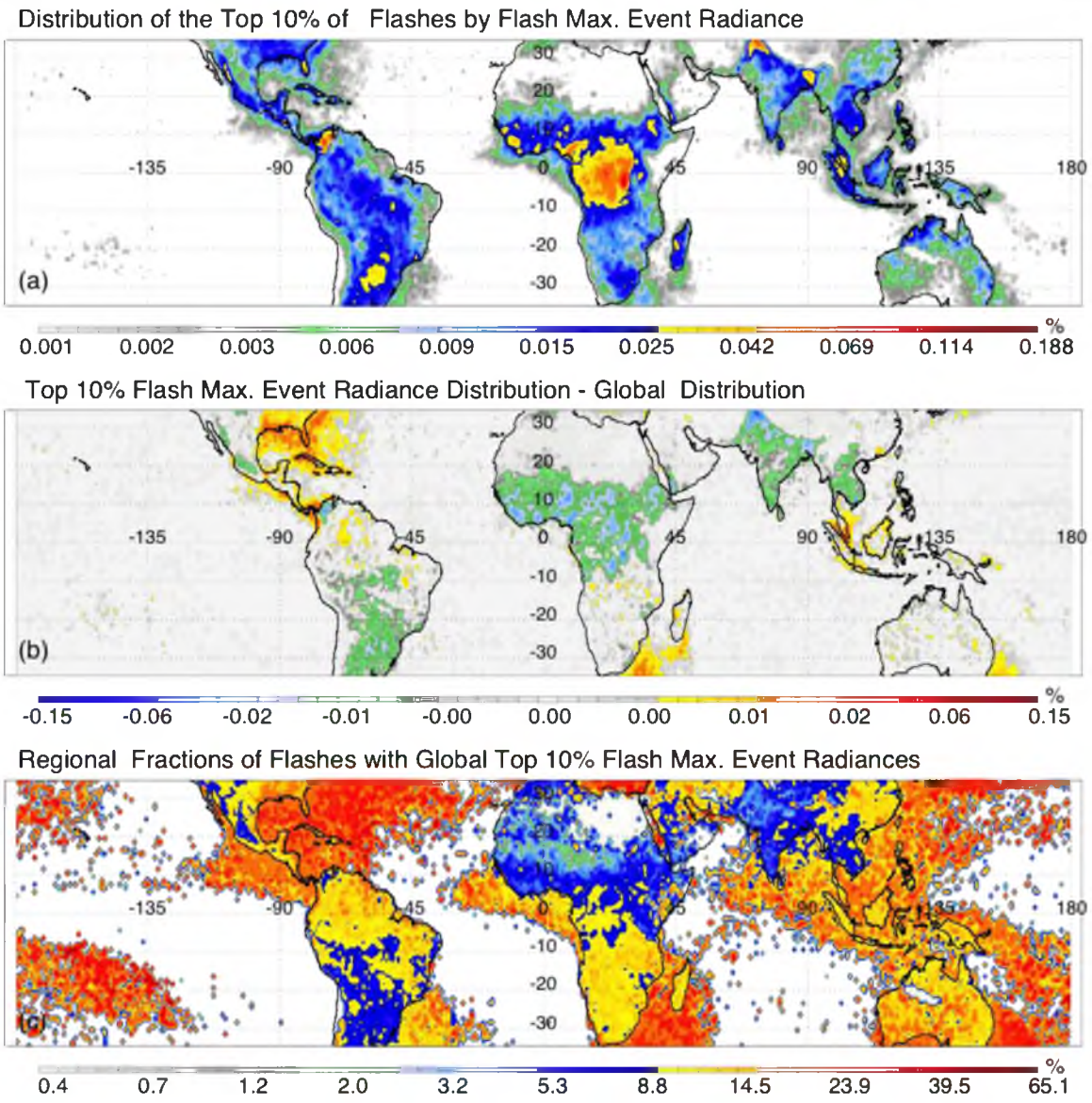

Fig. 3.9. Global regional sample density of the top 10% brightest flashes by peak event radiance globally, normalized by latitude-dependent instrument view time (a), differences between the top 10% brightest by peak event radiance and overall distributions (b), and regional fractions of the global top 10% brightest flashes by peak event radiance (c).

Mediterranean and Central Asia also stand out as regions with abnormally high fractions of optically powerful flashes. Once more, since daytime and nighttime sensitivity regimes show similar results, these are not shown.

In this section, regional variations of the optical flash properties are discussed. The observations of Boccippio et al. (2000) that oceanic flashes tend to be larger and brighter are confirmed, with much greater detail. Unlike Boccippio, this study separates oceanic regions into coastal and deep ocean for analysis. Based on this analysis, coastal regions were shown to have long lasting flashes on average compared to both land and ocean regions.

3.2 Relationships Between Flash Illuminated Area, Duration, and Brightness

In the previous section, clear regional variations of flash optical properties were shown and discussed. Care was taken to address the issue of LIS sensitivity differences between night and day; however, it still has yet to be determined whether these observed differences are the result of actual differences in lightning properties between different regions or merely differences in the observed optical flash, potentially caused by differing characteristics of the cloud viewing medium.

The first step in determining if the properties of exceptional flashes observed in the previous section are the result of the state of the viewing medium or properties of the flashes themselves is to examine whether flash illuminated area, duration, and brightness are related to one another. From a radiative standpoint, absorption and scattering from the atmosphere would reduce the radiance perceived by the satellite more with increasing

optical thickness between the flash and the sensor. For clear air, the relationship between flash perceived area and radiance is simple, stemming from the Rayleigh scattering equation shown below:

$$I(r) = I_0 \frac{1+\cos^2(\theta)}{2r^2}\left(\frac{2\pi}{\lambda}\right)^4\left(\frac{n-1}{n+2}\right)^2\left(\frac{d}{2}\right)^6 \tag{3.1}$$

where I(r) is the intensity of light at a given distance from its source, r, I_0 is the intensity of the source, λ is the light source wavelength, n is the refractive index of the scattering particle, d is the diameter of the scattering particle, and θ is the scattering angle.

Assuming a homogeneous viewing medium and a relatively stationary TRMM during the rapid scan interval between LIS observations so that the viewing angle does not change considerably, the Rayleigh scattering equation can be reduced so that the fractional radiative intensity of a flash at a particular radius is a direct function of radius squared in Eq. (3.3):

$$\frac{I(r)}{I_0} = \frac{1+\cos^2(\theta)}{2r^2}\left(\frac{2\pi}{\lambda}\right)^4\left(\frac{n-1}{n+2}\right)^2\left(\frac{d}{2}\right)^6 \tag{3.2}$$

$$\frac{I(r)}{I_0} = \frac{c}{r^2} \tag{3.3}$$

Then, assuming an approximate flash equivalent radius by dividing flash area by pi, the relationship between flash area and the ratio of the observed radiance at the flash center to the radiance observed at the flash edge is merely

$$\frac{I_0}{I(r_{eq})} \cong c \times area \tag{3.4}$$

Of course, this only holds so long as the optical scattering at the LIS observation wavelength remains within the Rayleigh regime. In the case of Mie scattering situations, such as cloud regions where lightning flashes occur, the relationship between the ratio of observed center and edge radiance and illuminated area is not so clear. Mie scattering has a high situational dependency and is typically examined through the use of complex computer simulations for particular size distributions, concentrations, and species of scattering particles. Still, real world observations indicate that there should be some reductive relationship between observed optical intensity and optical thickness. In nature, thick storm clouds are not observed to be brighter than thin altocumulus under the same lighting conditions.

In order to look for relationships between flash perceived brightness and illuminated area, an additional radiance parameter is introduced: flash radiance ratio, which is the ratio of the brightest event pixel within the flash to the dimmest event pixel within the flash. Radiance ratio can be thought of as an approximation of the center to edge radiance ratio if the flash were circular and had the greatest radiance at the center and the least radiance along the observed perimeter. Under these assumptions for conditions within the Rayleigh regime, it should correlate very well with flash illuminated area, regardless of sensitivity regime. Figure 3.10 shows two-dimensional histograms of flash duration, mean optical power and radiance ratio with flash illuminated area. Flash areas seem to increase with increasing duration (Fig. 3.10a), but the histogram is very broad and nowhere near sufficient for defining a predictive

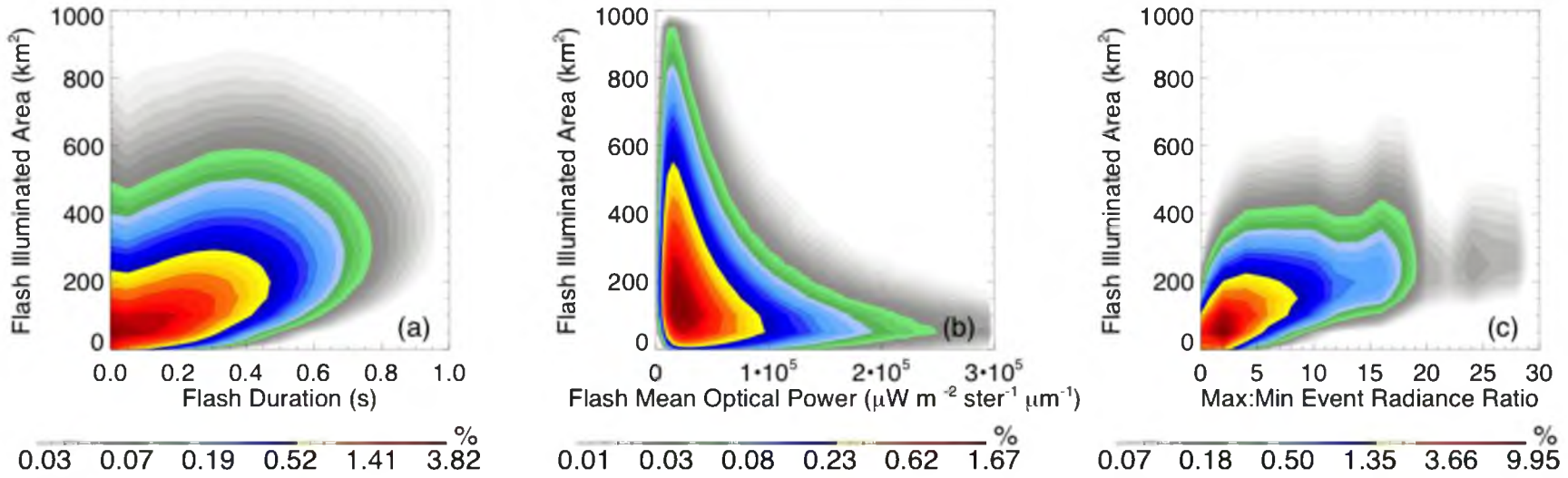

Fig. 3.10. Two-dimensional histograms of flash duration (a), flash mean optical power (b), and flash max:min radiance ratio (c) with flash illuminated area.

relationship between the two. The flash mean power histogram, meanwhile, follows the axes in a form similar to a $1/x^2$ function. The most expansive flashes have very small optical powers throughout their illuminated footprints, while very bright flashes are typically very small with radiance concentrated in a small area. However, the histogram between flash radiance ratio and flash illuminated area is much more linear in nature than any of the other optical parameters examined and may indicate a high correlation.

Actual correlation coefficients between flash radiance ratio and the optical properties examined in Fig. 3.10 are given in Table 3.2. Based on a purely linear model, flash illuminated area only correlates reasonably well (0.56, 0.60) with peak event brightness and radiance ratio, which are and should be virtually identical. Correlation coefficients between nonzero flash duration and either flash area or peak brightness show low correlations (0.36, 0.37). Also, correlations between flash mean optical power and the other parameters range from very low (-0.18) in the case of nonzero flash duration to nonexistent for the other parameters. Since flash peak radiance and flash radiance ratio correlate equally well with the other parameters, flash radiance ratio is chosen over flash maximum radiance for the remainder of this section.

Linear distributions do not adequately represent the entire distribution, however. Often what occurs at extreme values of distributions can be more interesting or telling. Switching from a linear to a log-log distribution makes it possible to examine how the brightest, dimmest, shortest duration or longest duration may be related to flash area.

Figure 3.11 shows the same distributions in Fig. 3.10, but using a log-log distribution. At a rough glance, it would appear that this logarithmic model would increase the correlation between these optical flash characteristics, especially for the

Table 3.2. Linear correlation coefficients between LIS-observed optical flash properties.

	Duration	Mean Optical Power	Maximum Event Radiance	Max:Min Radiance Ratio
Illuminated Area	0.37	0.01	0.56	0.60
Duration		-0.18	0.36	0.37
Mean Optical Power			0.04	0.02
Maximum Event Radiance				0.97

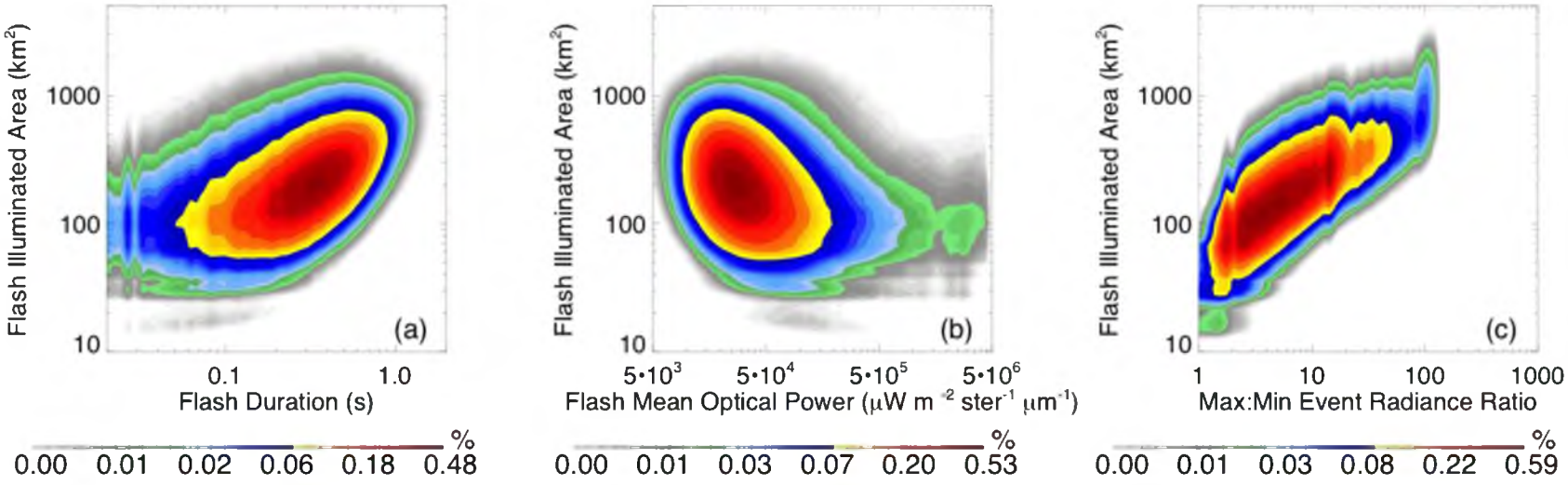

Fig. 3.11 Same as Fig. 3.10, but using logarithmic distributions instead of linear distributions.

radiance ratio and flash illuminated area distribution. Table 3.3 shows the correlation coefficients for the parameters in Fig. 3.10 and 3.11 using a log-log model for flash area and radiance and a linear-log model for flash duration and the other parameters. Flash area and radiance ratio now reach correlations exceeding 0.7, and flash mean power now correlates similarly well with flash duration. Correlations between flash optical area and duration have also improved to 0.48 under this model and are only slightly less well correlated with radiance. These general correlations hold true for flashes regardless of the diurnal sensitivity of LIS, the major concern of the previous section. Regional and terrain type variations are also a concern. Figure 3.12 shows correlation coefficients between flash area, duration, and radiance ratio region by region. Correlations between flash area and duration, mean optical power, and radiance ratio are all typically higher in the subtropics and lower in the tropics. Correlation coefficients between flash area and radiance ratio even exceed 0.8 over Argentina, the Mediterranean, and the Middle East, indicating a strong relationship between flash brightness and illuminated area over those regions.

3.3 Relationships Between Flash Optical Properties and Storm Properties Throughout the Flash Footprint Region

The prior two sections have shown that there is a strong regional variation in flash properties and the degree to which optical flash properties are interrelated. The optical characteristics of flashes observed by LIS depend on properties of the cloud that acts as a viewing medium. Thick clouds with a lot of ice, for example, could potentially scatter away much of the radiance of the flash headed for the cloud top, resulting in the flash

Table 3.3. Log-linear (for cells that include duration) and log-log (the remainder of the table) correlation coefficients between LIS-observed optical flash properties.

	Duration	Mean Optical Power	Maximum Event Radiance	Max:Min Radiance Ratio
Illuminated Area	0.48	-0.28	0.65	0.71
Duration		-0.68	0.45	0.47
Mean Optical Power			-0.07	-0.14
Maximum Event Radiance				0.96

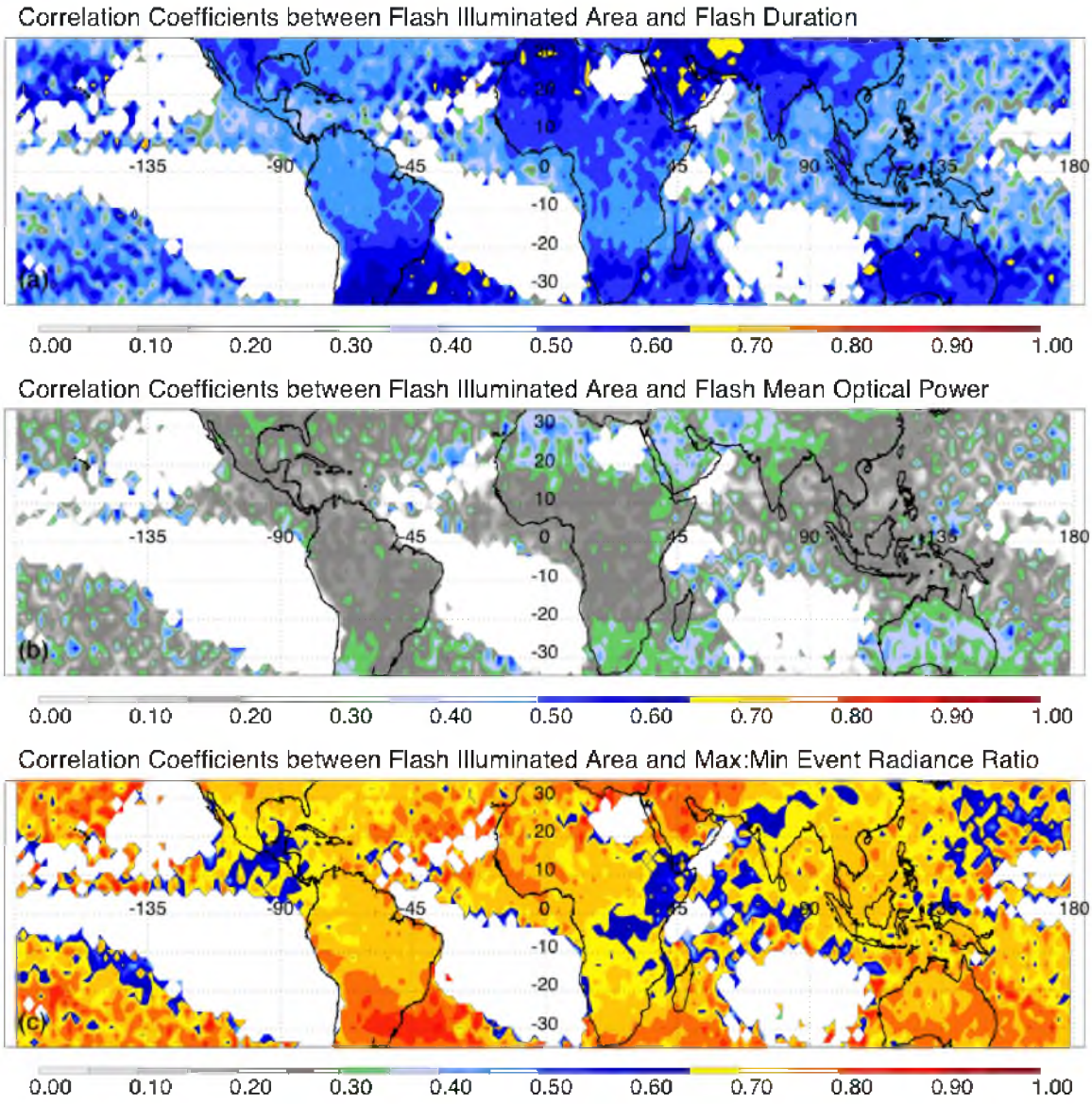

Fig. 3.12. Regional mean correlation coefficients between flash illuminated area and duration (a), mean optical power (b), and the ratio of maximum event radiance to minimum event radiance (c). (a) is based on a log-linear model, while (b) and (c) are based on a log-log model.

appearing dimmer and smaller than the original flash and having an irregular footprint when observed from above. Cloud layers between the optical flash and the observer can also affect the observed properties of the optical flash, even to the point of completely obscuring the flash when observed from above. Differences in storm structure are particularly great between land and ocean, as noted in Zipser et al., 2006. Therefore, these regional differences, particularly the variations in optical footprint area and brightness noted by Boccippio et al. (2000) and the first section of this chapter may merely be the consequence of these differences in storm structure.

3.3.1 Properties at Lightning Flash Centroid Locations

One method of examining the properties of the environment that flashes propagate through is to look at the collocated TRMM properties of the flash centroid. These coincident pixels should be representative of the environment through which the illuminated radiance traverses, except in the case of flashes that are significantly larger than the grid size of the TMI. This assumption breaks down even further for large flashes that occur along steep gradients in TMI and PR properties throughout their footprint. Figure 3.13 shows CDFs of coincident TMI 85 GHz PCT observations for flashes with various mean optical powers (a and b) and maximum event radiances (c and d). Unlike the CDFs in Fig. 3.1, only quartile and median values are shown for each bin of flash brightness so that land, ocean, and coastal curves may be overlain on the same plot. For each terrain type and LIS sensitivity, a general shift can be observed in the 85 GHz PCT statistics with increasing mean optical power. While dim flashes tend to be centered in regions with relatively cold 85 GHz PCTs with median values around 170 K, flashes with

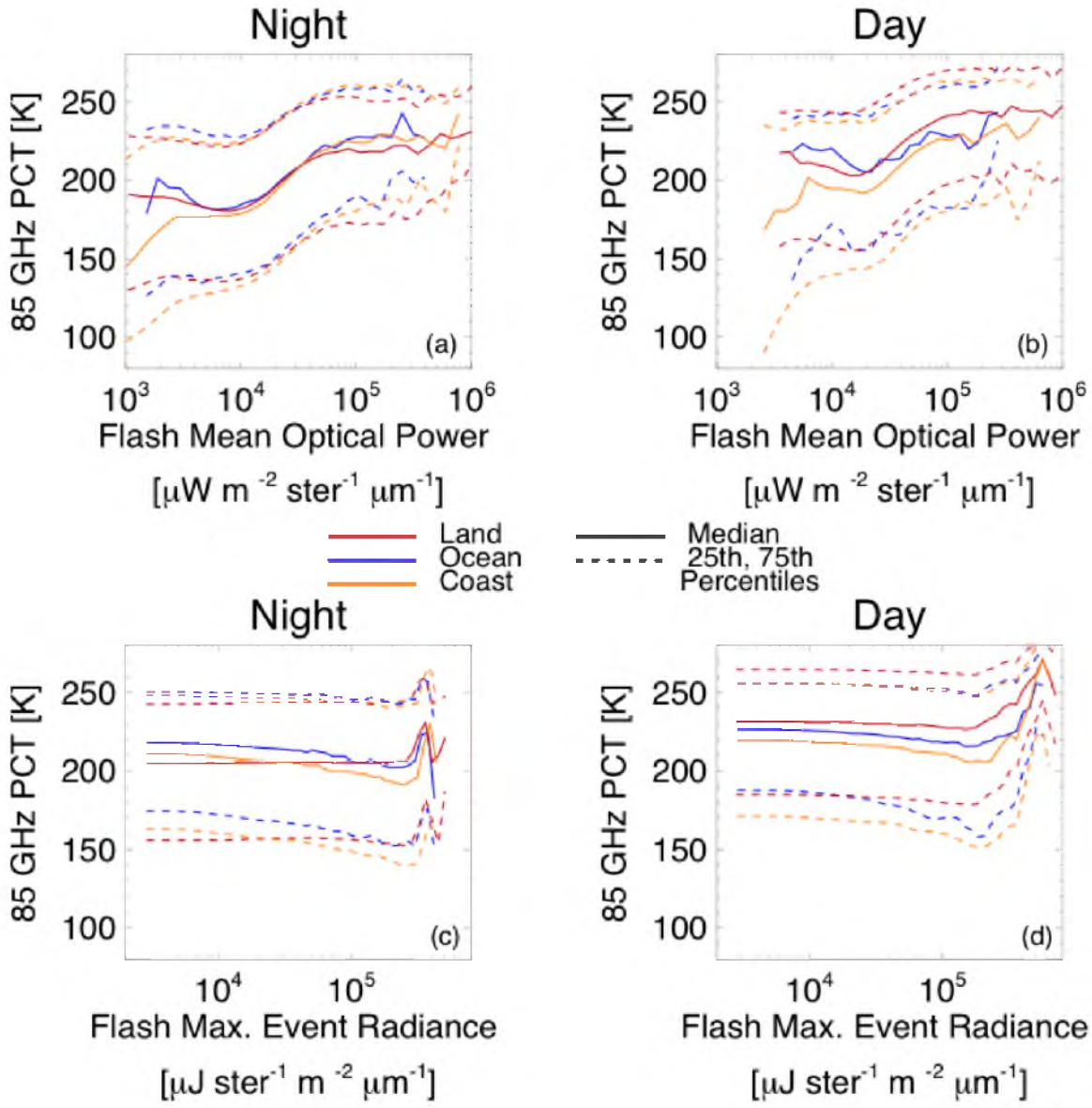

Fig. 3.13. Two-dimensional CDFs of flash centroid collocated 85 GHz PCT and flash mean power (a and b) and flash maximum event radiance (c and d) separated by LIS sensitivity regime.

high mean optical powers typically have coincident 85 GHz PCTs around 40 K warmer, with median values in the vicinity of 220 K. This trend persists for flashes observed with daytime and nighttime LIS sensitivity, and the CDFs within each regime for each terrain type are almost superimposed, indicating that these statistics are independent of terrain.

The statistics for maximum event radiance (and, by extension, flash radiance ratio) are different than those for mean optical power. Throughout most of the maximum event radiance domain, there is little change in the statistics of 85 GHz PCT. If anything, brighter flashes in terms of maximum event radiance are slightly more inclined to occur coincident with storm regions that are slightly stronger than dim flashes up until the most extreme values of maximum event radiance, where the trend reverses, tending towards weaker storm regions like mean optical power.

Even though both the maximum event radiance and the mean optical power estimate the relative brightness of a flash, there is quite a discrepancy between their statistics since they correspond to two different definitions of brightness. Maximum event radiance measures the maximum intensity of the flash, or its peak instantaneous brightness. Optical power measurements, such as mean optical power, correspond to the spatial and temporal radiative density of flash illumination. Mean optical power is not just a measure of how bright a flash is instantaneously, but how bright it is for its size and duration. Figure 3.14 shows similar statistics for flash illuminated area (a and b) and flash duration (c and d). The variations of the statistics of flash center 85 GHz PCT with increasing flash illuminated area are different between night and day. At night, for flashes with optical footprints smaller than 100–400 km^2, depending on the terrain type, coincident 85 GHz PCTs decrease with increasing flash area by around 10–20 K, and

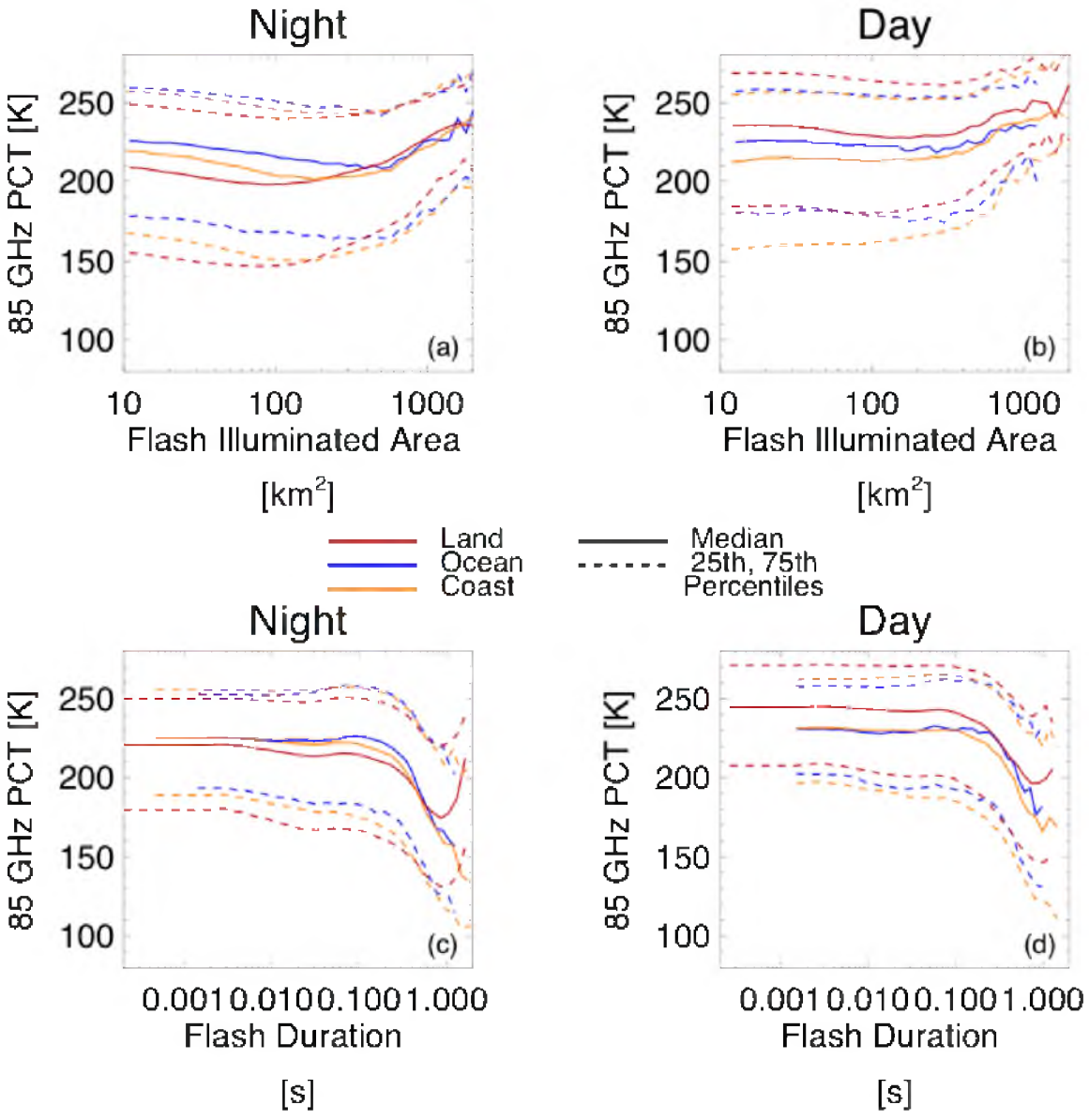

Fig. 3.14. Two-dimensional CDFs of flash centroid collocated 85 GHz PCT and flash illuminated area (a and b) and flash duration (c and d) separated by LIS sensitivity regime.

then larger flashes are associated with an increase in centroid 85 GHz PCTs up to extreme flash areas. During the day, however, the initial strengthening of the centroid microwave signal with increasing flash area for smaller flashes is not as evident, but extreme flashes are still associated with warmer 85 GHz PCTs, which is likely a consequence of the size of the flash relative to the size of cold 85 GHz PCT convective regions in storms.

At the same time, the statistics of coincident 85 GHz PCT with varying flash duration (Fig. 3.14 c and d) do not change much for flashes with nonzero durations that are shorter than 0.1 s. Longer duration flashes tend to be associated with strong storm regions. One explanation for this is that lightning flashes observed over strong storm regions with high flash counts may be more likely to be aggregated into a single observed flash. Basically, when multiple flashes occur at the same time in a geographically limited space such as a convective cell, it can become nearly impossible to tell where the illumination from one flash ends and another begins. Even though Mach et al. (2007) did not find a significant variance in the performance of the LIS grouping algorithms with flash rate, that does not necessarily discount this potential source of uncertainty for extreme cases where close flashes may be indistinguishable, increasing possibly the area or duration of the flash (or both) and simultaneously decreasing the perceived flash count.

3.3.2 Properties of Flashes Illuminating Convective, Stratiform, and Anvil Regions of Storms

A better way of characterizing the effect of the viewing medium on optical flash characteristics is to examine lightning flashes that illuminate thunderclouds with a variety

of different typical structures and then compare the results to see how changing the properties of the viewing medium affects the observations of lightning. One way of doing this is by classifying flash footprint regions as convective, stratiform, or anvil based on the definitions employed in previous work (Peterson and Liu 2011, 2013). These definitions are based on 2A23 rain types (Awaka et al.1998) and 2A25 near surface rain rates. Convective and stratiform categories are defined as PR pixels that have finite near surface rain rates and are classified as convective or stratiform by the 2A23 algorithm, while the anvil category is defined as any remaining PR pixels that have near surface rain rates that are too small to be observed by the PR (< 0.1 mm/hr).

A new approach is used here to classify lightning flashes by precipitation type category. Where before (Peterson and Liu 2011, 2013), flashes were defined as convective, stratiform, or anvil based on PR observations collocated to their centroid locations, the method used in this section examines each pixel within the flash footprint area and then computes the fractions of the storm areas illuminated by the flash that correspond to convective, stratiform, or anvil cloud types. Flashes that occur partially outside the PR swath or in a region with missing or erroneous PR data or flashes with illuminated areas smaller than 100 km^2, whose flash-footprint properties would likely not differ much from their centroid properties, are not considered. In addition to precipitation type fractions, minimum, mean, and maximum values of TRMM observations throughout the LIS flash footprint region are calculated. A full list of these new flash-footprint parameters is provided in Table 3.4.

Figure 3.15 shows a two-dimensional histogram of flashes with each possible combination of stratiform and convective fraction. Since all three fractions must sum to

Table 3.4. List of LIS flash footprint environment parameters.

Instrument	Parameter
PR	Max. Height of 15 dBZ
	Mean. 15 dBZ Echo Top Height
	Min. 15 dBZ Echo Top Height
	Max. Height of 20 dBZ
	Mean. 20 dBZ Echo Top Height
	Min. 30 dBZ Echo Top Height
	Max. Height of 40 dBZ
	Mean. 40 dBZ Echo Top Height
	Min. 40 dBZ Echo Top Height
	Max. 2A23 Storm Height
	Mean. 2A23 Storm Height
	Min. 2A23 Storm Height
	2A23 Convective Fraction
	2A23 Stratiform Fraction
	2A23 Anvil Fraction
	Max. 2A25 Rain
	Mean. 2A25 Rain
	Min. 2A25 Rain
	Total. 2A25 Rain
TMI	Max. 85 GHz PCT
	Mean. 85 GHz PCT
	Min. 85 GHz PCT
	Max. 37 GHz PCT
	Mean. 37 GHz PCT
	Min. 37 GHz PCT
	Max. 2A12 Rain
	Mean. 2A12 Rain
	Min. 2A12 Rain
	Total. 2A12 Rain
VIRS	Max. VIRS Channel 4 Tb
	Mean. VIRS Channel 4 Tb
	Min. VIRS Channel 4 Tb

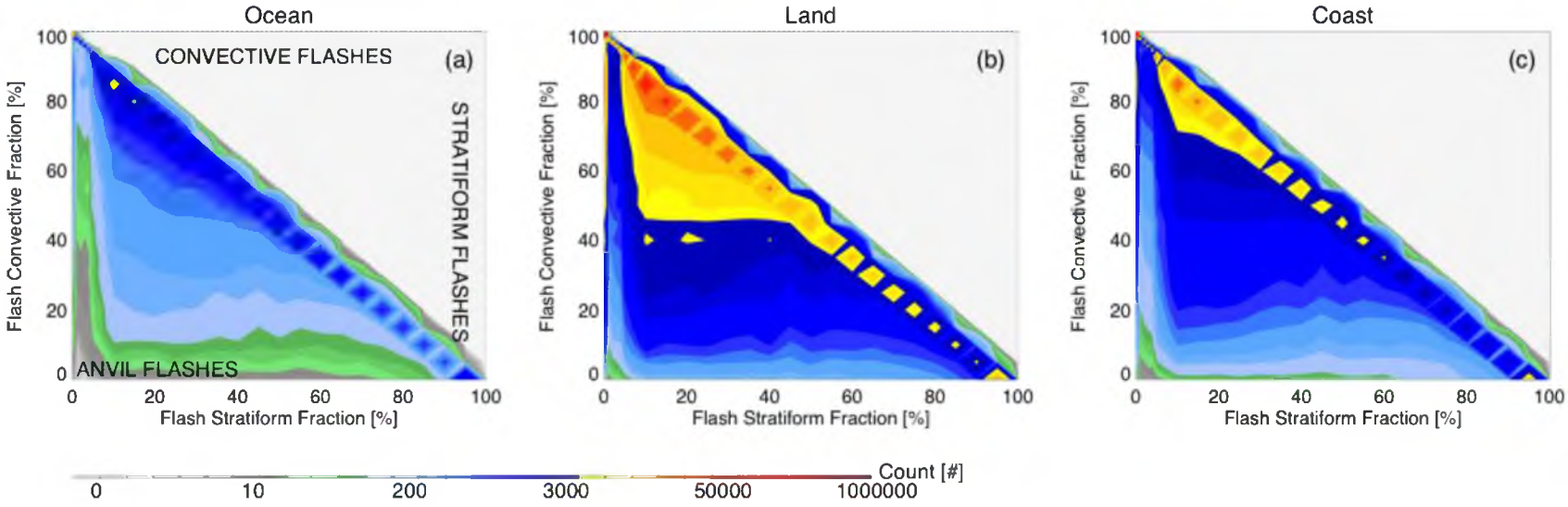

Fig. 3.15. Flash frequency categorized by flash footprint convective fraction (y axis) and flash footprint stratiform fraction (x axis) plotted for each terrain type, separately.

100%, anvil fractions of flashes can be inferred by subtracting the total of the stratiform and convective fractions from 100%. Flashes that are primarily convective are located towards the top of the figure, primarily stratiform flashes are located towards the right of the figure, and primarily anvil flashes are located near the origin. The majority of flashes in each terrain category are primarily convective, some are primarily stratiform, and only a few are primarily anvil. This is a departure from Peterson and Liu (2011), which found that centroid-based stratiform and anvil flashes accounted for a roughly equal fraction of the total sample at around 5–6%. These anvil flashes from the previous study may be centered in the anvil regions of storms, but it is very rare to find flashes that are completely encompassed by anvil pixels. Instead, many anvil flashes from the previous study illuminate anvil and convective regions, anvil and stratiform, or all three regions of storms.

Peaks in the distribution can be found where the convective and stratiform fractions are 100% in each panel. This is a mathematical issue rather than a scientific one and also accounts for the beading along the 0% anvil line between 100% convective and 100% stratiform. The reason for this is that the number of possible combinations of convective, stratiform, and anvil fractions is more limited for smaller flashes than it is for larger flashes. For example, a flash that has one pixel can either be 0% or 100% convective. Fortunately, one-pixel flashes do not exist in this sample. A more likely example is a flash with four pixels, but even these flashes can only be 0%, 25%, 50%, 75%, or 100% convective, and so forth. Since most flashes are on the small end of the spectrum, certain bins will be preferred, particularly 0% or 100%. A value of 100% convective does not say anything about the intensity of the storm or the size of the flash.

It could be a large flash in an enormous MCS convective core, or it could be a four-pixel flash occurring in a small convective cell. On the other hand, a 95% convective flash requires a large system since it would mean that 95 out of 100 observed LIS events correspond to convective pixels.

In order to examine whether the correlations between radiative ratios and flash illuminated areas of convective and nonconvective flashes are significantly different, correlation coefficients have been produced for flashes of varying convective fraction in Fig. 3.16. Flashes with no convective pixels (flashes that occur entirely in regions of stratiform precipitation or anvil clouds) have high correlations between flash area and brightness, almost reaching 0.8. At the same time, strongly convective flashes (excluding those that are 100% convective due to the permutation issue noted earlier) have much lower correlation coefficients, extending below 0.5, or explaining less than 25% of the variation in the sample. This implies that increased attenuation by thicker clouds in convective regions does, indeed, alter the relationship between radiance and the illuminated area.

Fig. 3.17 shows correlation coefficients between flash area and radiance ratio categorized by both convective and stratiform fractions. Similar to what was seen in Fig. 3.16, high correlation coefficients occur where convective fractions are close to 0%, while smaller correlation coefficients occur in primarily convective regions of the figure. At the same time, exceptionally high correlation coefficients occur not just where convective fractions are low, but also where stratiform fractions are also high, but not where anvil fractions are significant. Stratiform clouds could have a greater correlation between radiance ratio and illuminated area due to their horizontally uniform nature (the

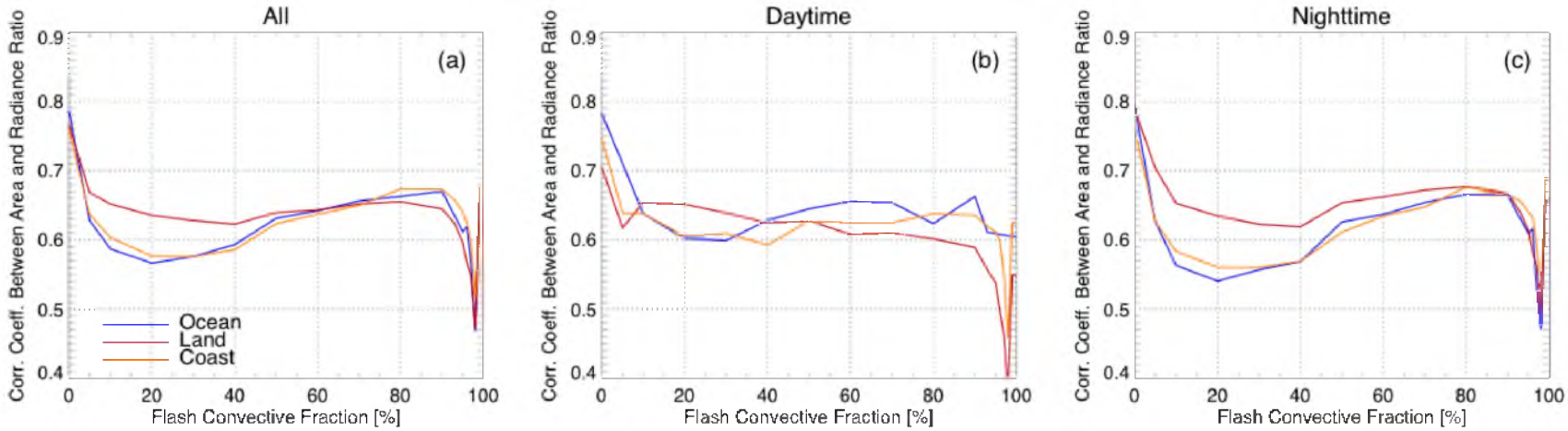

Fig. 3.16. Correlation coefficients between flash illuminated area and max:min radiance ratio categorized by flash footprint convective fraction.

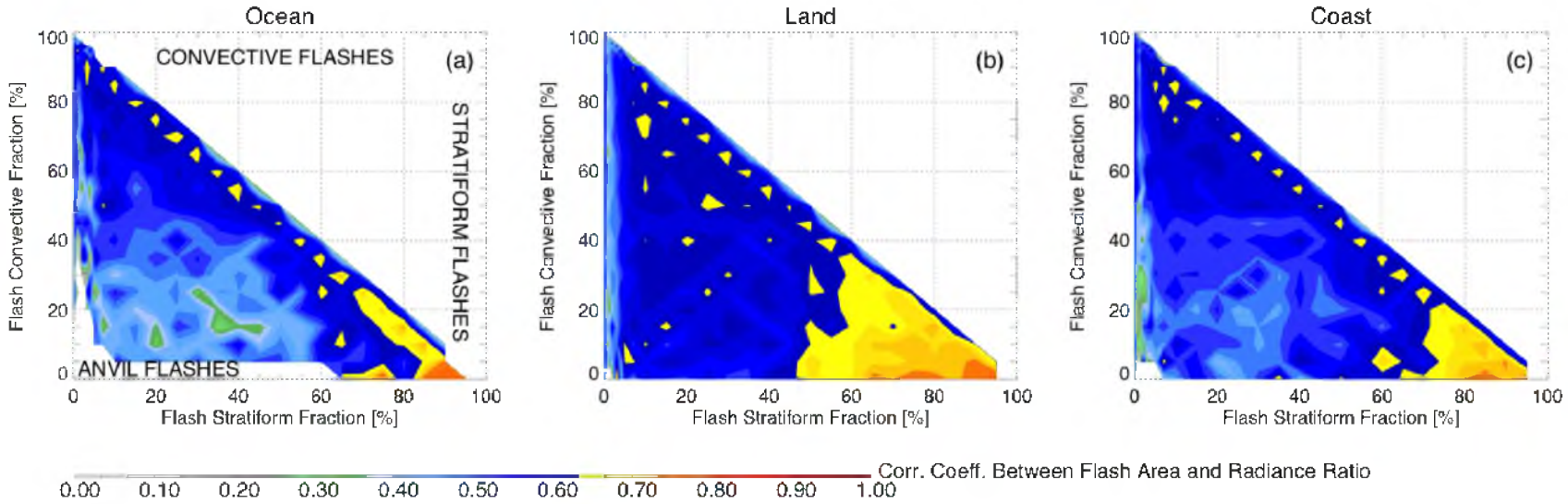

Fig. 3.17. Correlation coefficients between flash illuminated area and max:min radiance ratio categorized by flash footprint convective fraction (y axis) and flash footprint stratiform fraction (x axis) plotted for each terrain type, separately.

definition of stratiform means "to be arranged in layers") and their typically large size compared to convection. Anvil clouds, on the other hand, could have lower correlation coefficients if they are optically thin or if these statistics are biased by contamination from the SAA, which has been shown to produce unrealistic artifacts that show up as anvil flashes (Peterson and Liu 2011), but removing the affected region makes no difference in these correlation coefficients.

This leaves the optical thickness issue as a potential cause of a lack of correlation between flash radiance ratio and flash illuminated area. The anvil classification includes all pixels outside of the raining area of the storm, and traditional anvil flashes typically occur near the edge of the cloud shield. Since the optical footprint of lightning is typically much larger than the actual electrical event, anvil flashes typically illuminate storm regions that would be considered extremely weak or even not be picked up by most TRMM metrics of storm strength, regardless of the properties of the storm region where the electrical discharge took place. This effect is enhanced whenever a flash occurs close enough to the edge of the storm that the radiative footprint that would be observed is cropped by the physical cloud boundary.

To show how this issue affects anvil flashes, mean PR-derived storm heights are shown in Fig. 3.18 for flashes grouped by convective and stratiform fractions. Convective flashes correspond to high average storm heights, while primarily stratiform flashes have lower mean heights, but they are still above 6 km. Primarily anvil flashes near the origin, on the other hand, have mean storm heights well below 5 km in this figure, corresponding to large illuminated areas without substantial PR echoes that may not scatter radiance from lightning as efficiently as interior clouds.

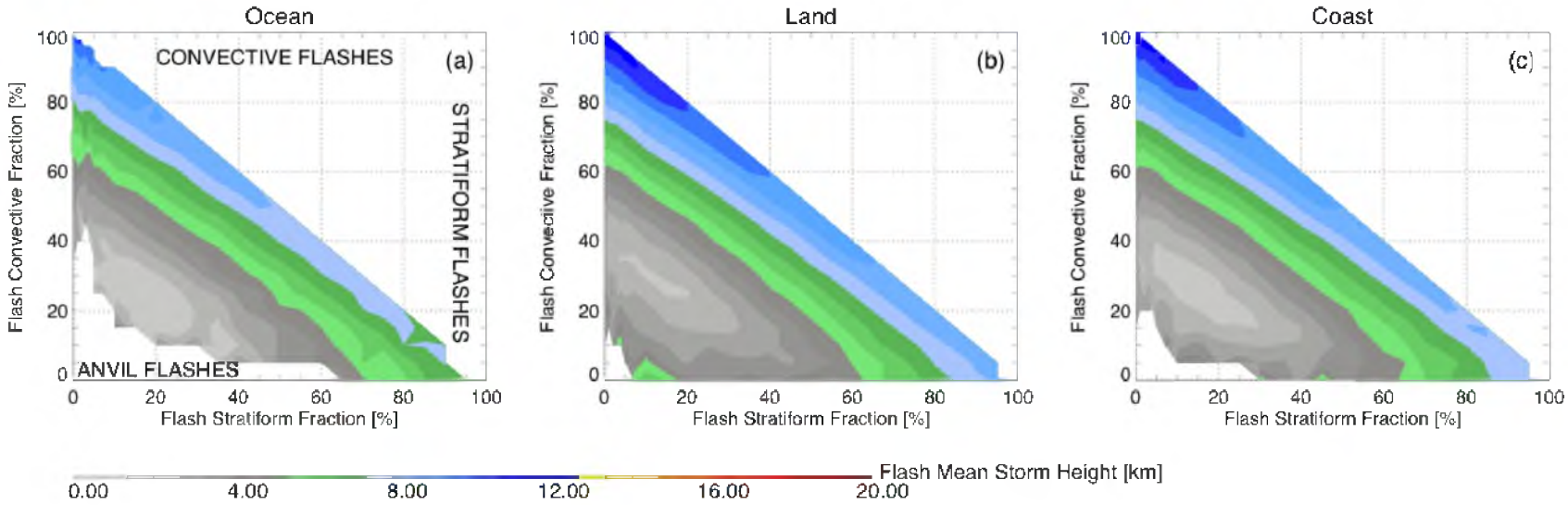

Fig. 3.18. Flash footprint mean storm height for flashes categorized by flash footprint convective fraction (y axis) and flash footprint stratiform fraction (x axis) plotted for each terrain type, separately.

Even though this is particularly an issue for anvil flashes, stratiform and convective flashes that partially illuminate outlying storm regions can suffer from this issue as well. Correlation coefficients between flash illuminated area and radiance ratio for flashes with various mean storm heights are shown in Fig. 3.19 for all precipitation types. Interior to optically thin anvils, one might expect that radiance and illuminated area should relate better for weaker convective clouds where a higher portion of the initial radiance can be observed by the LIS. However, correlation coefficients for all flashes (and all nighttime flashes) are highest for cloud layers between 13 and 15 km tall and lower both for taller, denser clouds, and shorter, thinner clouds. The lowest correlation coefficients for all flashes can be found for clouds shallower than 5 km over the ocean, just like for primarily anvil flashes.

Classifying LIS lighting flashes by convective, stratiform, and anvil fractions makes it possible to examine some of the differences between flashes that occur in each of these regions described in Peterson and Liu (2011) in a more specific manner. Figure 3.20 shows the mean peak flash event radiance for flashes categorized by convective and stratiform fraction of flashes. Over the ocean, significantly large flashes tend to be brighter on the convective side of the 1:1 convective/stratiform fraction line, while over land, anvil and mostly stratiform flashes are typically the brightest. In contrast, average flash durations, shown in Fig. 3.21, are significantly shorter for anvil flashes than for stratiform or convective flashes, with the longest mean durations occurring at high convective fractions where flash counts are higher and partitioning between individual flashes can become difficult. Mostly stratiform flashes also tend to be rather long despite the fact that flash rates over the stratiform region are significantly smaller. With

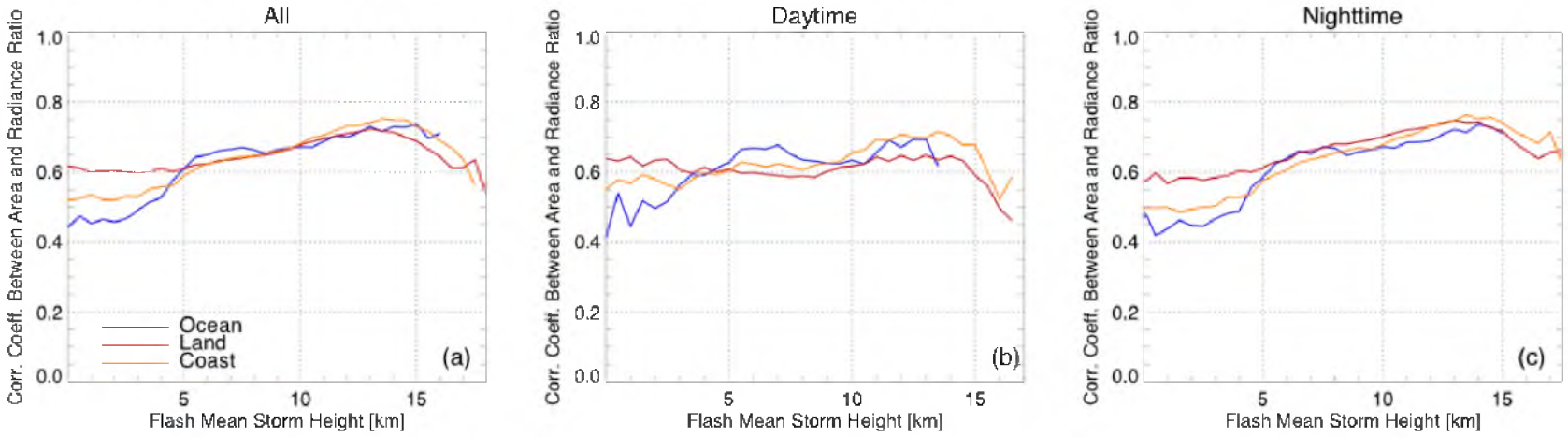

Fig. 3.19. Correlation coefficients between flash illuminated area and max:min radiance ratio categorized by flash footprint mean storm height.

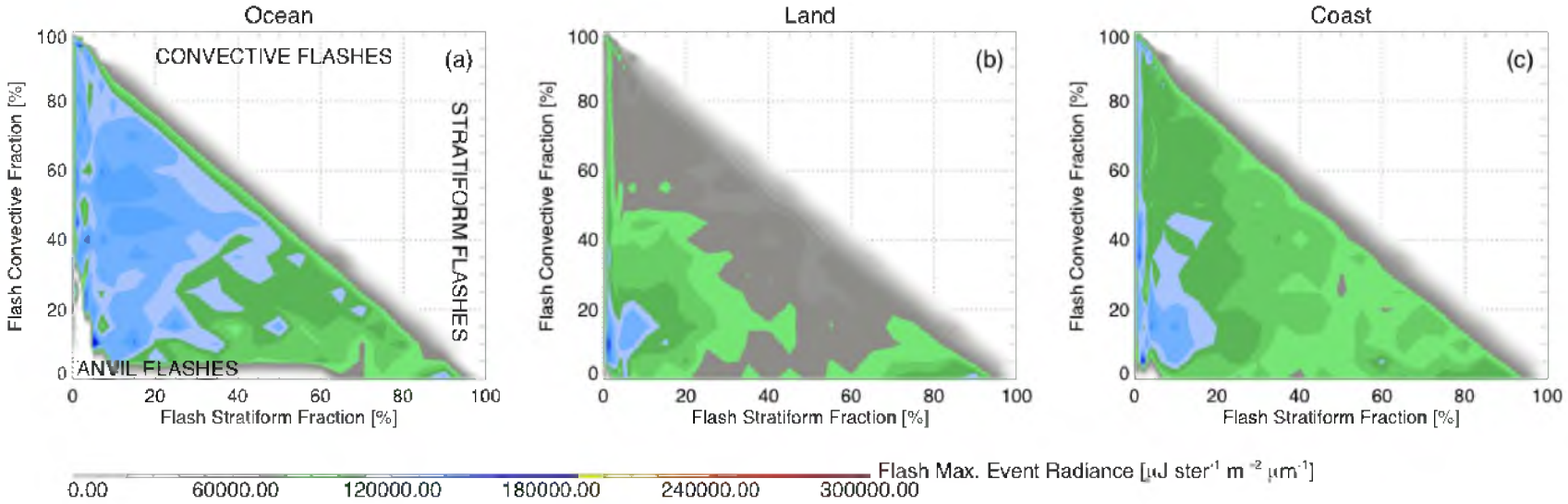

Fig. 3.20. Mean flash peak event radiance for flashes categorized by flash footprint convective fraction (y axis) and flash footprint stratiform fraction (x axis) plotted for each terrain type, separately.

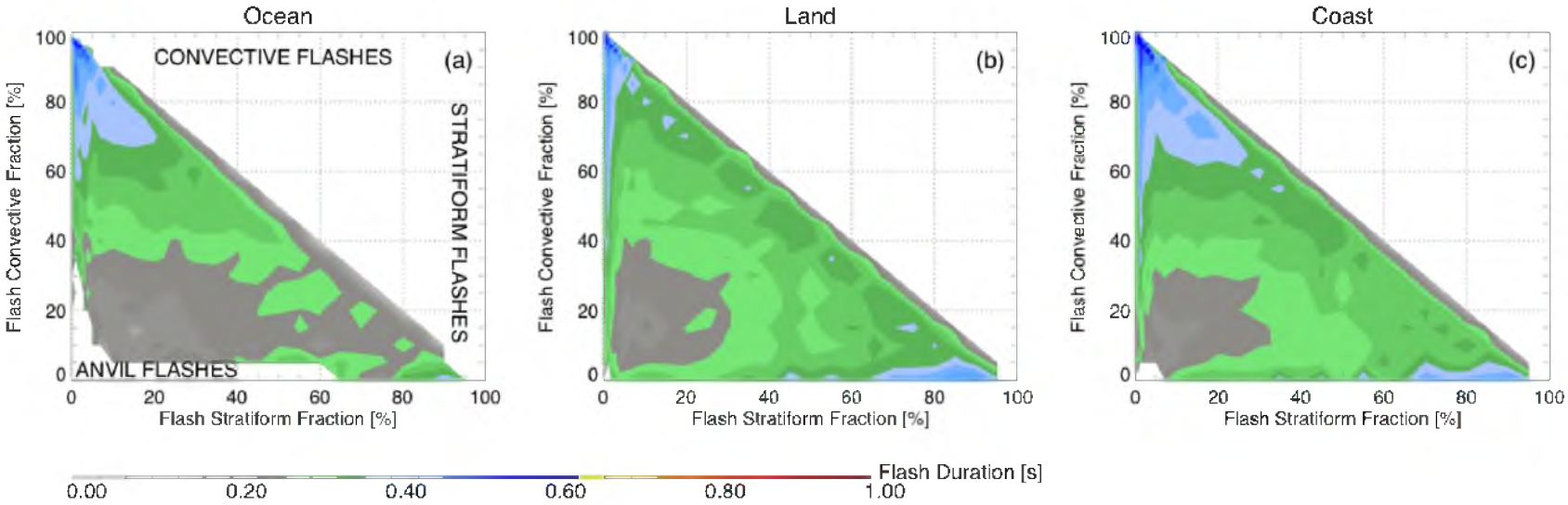

Fig. 3.21. Mean flash duration for nonzero-duration flashes categorized by flash footprint convective fraction (y axis) and flash footprint stratiform fraction (x axis) plotted for each terrain type, separately.

significant maximum event radiances and short durations, it is no surprise that average flash mean optical powers shown in Fig. 3.22 are much higher for anvil flashes than any other category. At the same time, highly convective flashes appear to be very dim overall, while stratiform flashes fall in between the two other categories.

The statistics of flash illuminated area, shown in Fig. 3.23, are also significantly higher for anvil flashes than any other type, with mean illuminated areas exceeding 800 km^2 for all three terrain types, far above the top 10% values given in Table 3.1. Mostly stratiform flashes are also considerably large on average, but are not nearly as consistently large as anvil flashes. This is likely due to the relative sizes of each of the different regions. Convective regions are often quite small, and stratiform rain regions trailing a convective storm may be many times the area of the convective region, but anvil regions incorporate the entire remainder of the cloud shield, which covers a larger area, still. Looking back at Fig. 2.2, the flash shown would be categorized as a mostly anvil flash as only one of its quadrants contains significant numbers of stratiform and convective pixels (Fig. 2.2d). Most of its illuminated area corresponds to storm heights of 0 km (Fig. 2.2c), corresponding to a cloud region that is too thin to be detected by the PR. This is consistent with the low storm heights seen for anvil flashes. In cases like this, where the flash exceeds the size of the contiguous raining region (Radar Precipitation Feature; Liu et al. 2008) that produced it, it will fall into the anvil category. Figure 2.2 also depicts a scenario that may be the reason as to why anvil flash areas and radiance ratios do not correlate well. While the PR may not be able to see echoes below 15 dBZ, infrared brightness temperatures (Fig. 2.2b) throughout the footprint area vary substantially from deep convective 196 K all the way down to near ground level 292 K.

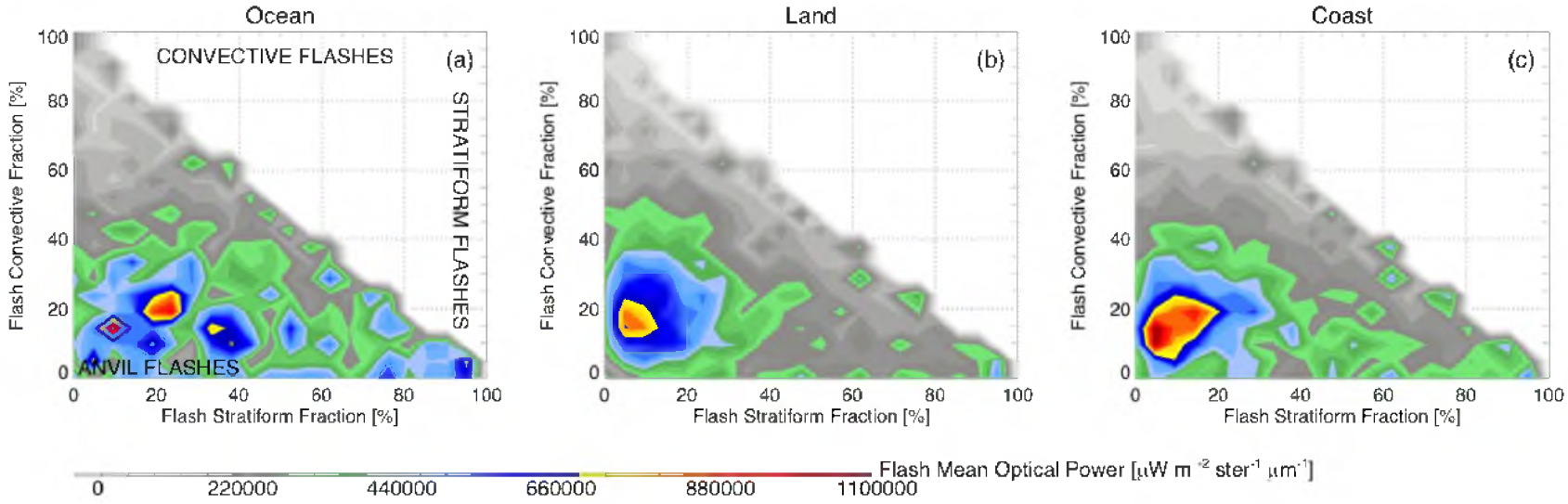

Fig. 3.22. Mean flash optical power for flashes categorized by flash footprint convective fraction (y axis) and flash footprint stratiform fraction (x axis) plotted for each terrain type, separately.

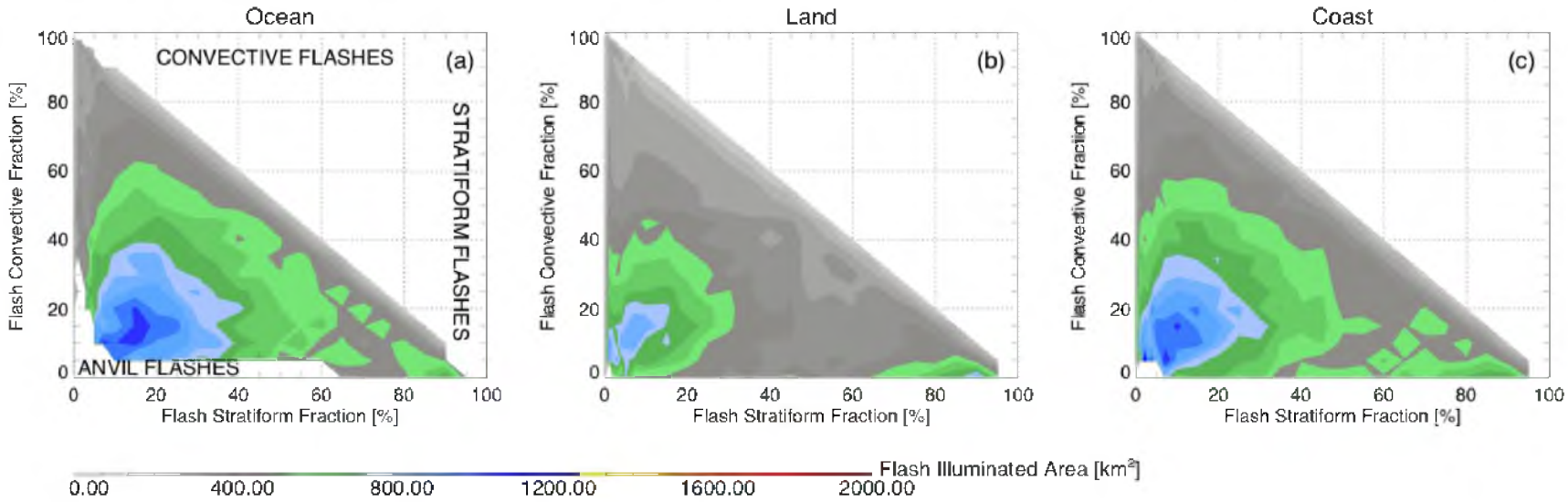

Fig. 3.23. Mean flash illuminated area for flashes categorized by flash footprint convective fraction (y axis) and flash footprint stratiform fraction (x axis) plotted for each terrain type, separately.

The area illuminated by the flash is as far from homogeneous as one can get. In fact, assuming that the mean center of the groups of the flash is more indicative of the discharge location than the overall flash centroid, the flash appears to extend further into the anvil region than into the actual storm region.

However, this does not mean that all large flashes, or even a large fraction of large flashes, are anvil flashes. Even though anvil flashes do tend to be larger than stratiform or convective flashes (Fig. 3.23), the overall totals of flashes in bins associated with predominantly anvil flashes in Fig. 3.16 are more than an order of magnitude smaller than primarily stratiform or primarily convective bins. Even for considerably large flashes with illuminated areas exceeding 500 km^2 (Fig. 3.24), large anvil flashes still are relatively rare compared to large convective and large entirely stratiform flashes. In these scenarios, the large size of the flash is still almost completely encompassed in an even larger convective or stratiform region so that almost no portion of the flash occurs in the outlying anvil region. It is not until the top couple of percent of flash illuminated area that large anvil flashes become more common than the other two categories, as seen for sample sizes of extremely large flashes exceeding 1,500 km^2 shown in Fig. 3.25. However, entirely stratiform flashes are also nearly as abundant for flashes this large.

A summary of optical characteristics of primarily (> 60%) convective, stratiform, and anvil flashes is shown in Table 3.5. Primarily convective flashes typically have the smallest illuminated areas over all three terrain types, the longest durations, and the lowest optical powers compared to the other two categories. Radiance ratios are high for primarily convective and primarily anvil flashes. Convective flashes have the highest radiance ratios of any group over the ocean. Primarily stratiform flashes have larger

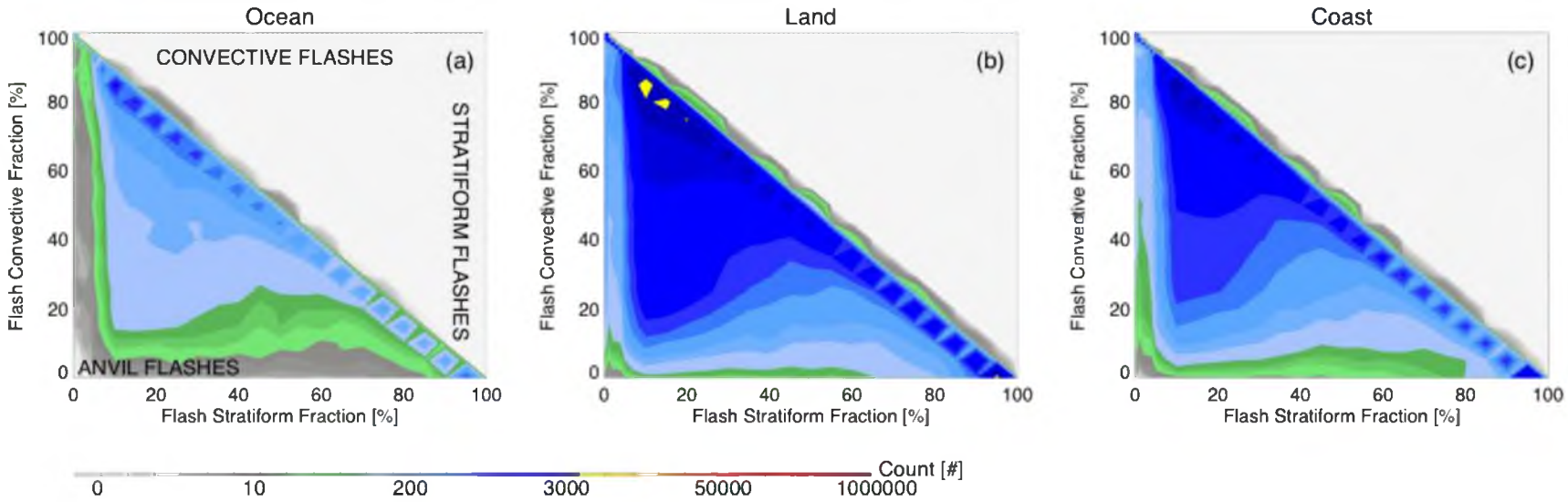

Fig. 3.24. Frequency of flashes greater than 500 km^2 in illuminated area categorized by flash footprint convective fraction (y axis) and flash footprint stratiform fraction (x axis) plotted for each terrain type, separately.

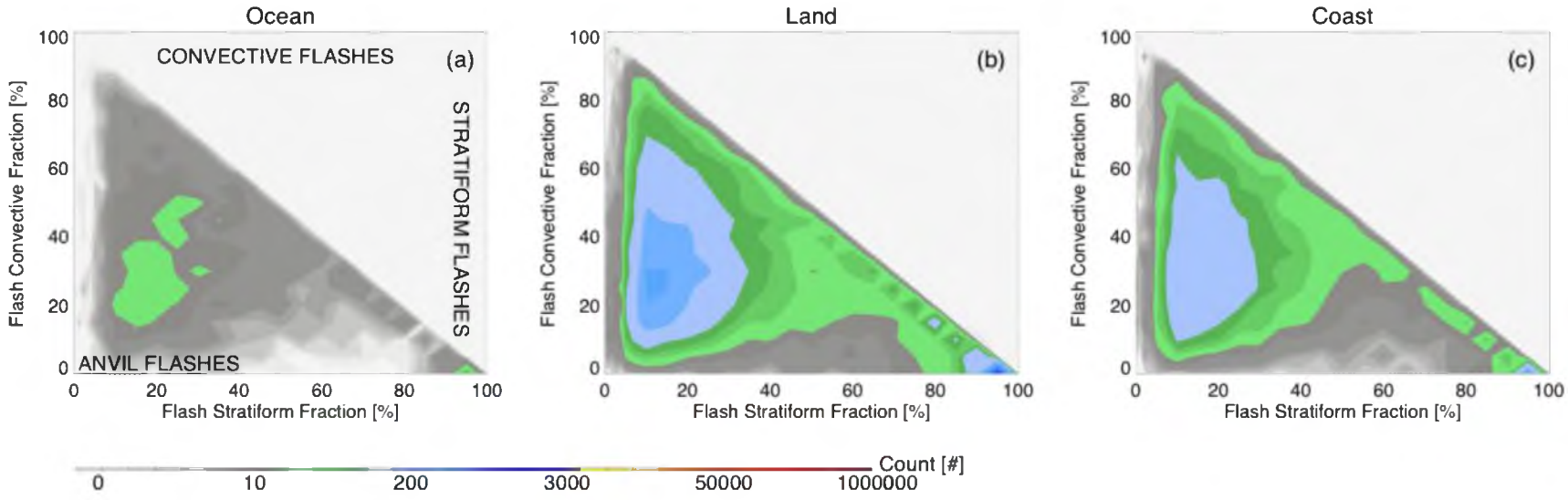

Fig. 3.25. Frequency of flashes greater than 1500 km^2 in illuminated area categorized by flash footprint convective fraction (y axis) and flash footprint stratiform fraction (x axis) plotted for each terrain type, separately.

Table 3.5. Mean flash optical properties for flashes that illuminate primarily convective, stratiform, and anvil cloud regions.

Flash Mean	Terrain	Primarily (> 60%) Convective	Primarily (> 60%) Stratiform	Primarily (> 60%) Anvil
Area (km^2)	land	205.7	271.3	310.8
	ocean	290.6	316.8	448.6
	coast	262.0	307.3	439.7
Duration	land	0.27	0.24	0.19
(s)	ocean	0.31	0.20	0.18
	coast	0.33	0.23	0.21
Optical	land	170 480	341 986	426 140
Power	ocean	209 239	489 859	449 531
(km)	coast	161 322	390 591	474 294
Max:Min	land	10.2	10.8	13.0
Radiance	ocean	20.1	13.9	19.7
Ratio (km)	coast	15.9	12.2	17.6

illuminated areas and shorter durations than convective flashes, yet have nearly twice the optical power of convective flashes. Stratiform flashes also have the lowest radiance ratios, indicating that flash radiance is distributed more evenly in space than convective or anvil flashes. Primarily anvil flashes have the largest illuminated areas and shortest durations of the three groups, resulting in much higher mean optical powers than the other categories. Primarily anvil flashes have the highest radiance ratios over land and coastal regions. These means are consistent with the two-dimensional histograms shown in this section and demonstrate that the cloud medium that is illuminated by lightning, in addition to the source structure and optical characteristics of the flash, has an impact on the flash observed by LIS.

3.3.3 On Flashes with Exceptionally Bright or Only Dim Events

It has been shown that there is a significant amount of correlation between flash max:min event radiance ratio and flash illuminated area (Table 3.3). However, the flashes that this correlation fails to explain could be more interesting. The previous subsection looked into how the properties of the cloud medium illuminated by the flash can alter this relationship. A number of scenarios can arise in real-world observations that would cause the radiance from a flash to not be distributed in a flashlight-like circular pattern with radiance decreasing from the center. Thick convective towers can scatter away significant amounts of radiance, and optically thin clouds can fail to be sufficiently illuminated, resulting in part of all of the flash to go undetected by LIS. This subsection contrasts flashes at the extremes of the two-dimensional histogram in Fig. 3.10c and uses TRMM observations throughout the entire cloud region illuminated by each flash to reveal what

makes these flashes different from typical flashes.

Figure 3.26 shows the mean optical powers of flashes categorized by illuminated area and radiance ratio for each terrain category. Bins with less than 50 flashes are omitted. The top and bottom of the resulting distribution are marked by firm linear boundaries representing the brightest and the dimmest flashes can be for a given illuminated area. These firm boundaries divide the distribution into three sections: an upper branch of extremely bright flashes, a lower branch of extremely dim flashes, and typical flashes in-between. There is no symmetry in the distribution or the locations of the upper and lower boundaries. Even though a 25 km^2 flash will never have a radiance ratio of 20, flashes ranging in size from 10 km^2 to 800 km^2 can have a radiance ratio of 5, meaning that the brightest event that makes up the flash is only 5 times more radiative than its dimmest pixel. The color contours in Fig. 3.26 indicate that the upper and lower branches of the distribution corresponding to the brightest and dimmest flashes, respectively, are more optically powerful than typical flashes in between. Upper branch flashes are by far the most radiant, but only up to 200 km^2, which makes sense because they contain the brightest pixels and are still relatively small.

But, how can a 90^{th} percentile flash be so dim or homogenous to have a radiance ratio less than 5? If peak brightness is related to flash area, the lower boundary should be further from the x-axis, like the upper boundary. The properties of the cloud medium could partially explain this. Figure 3.27 shows mean stratiform fractions throughout the distribution. Lower branch flashes have the highest illuminated stratiform cloud fractions of any region of the distribution. The stratiform region is much better suited for flashes with large illuminated areas due to its relatively weak precipitation structure yet still

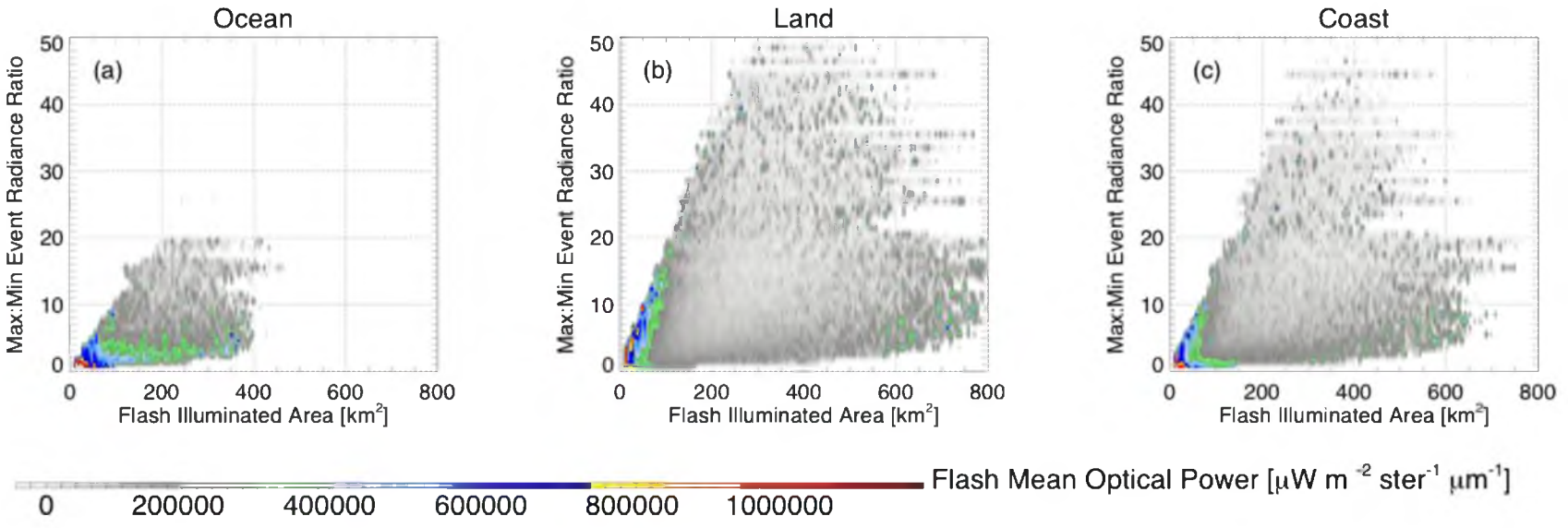

Fig. 3.26. Two-dimensional histograms of mean flash optical power categorized by flash illuminated area (x axis) and flash event max:min radiance ratio (y axis) plotted for each terrain type, separately.

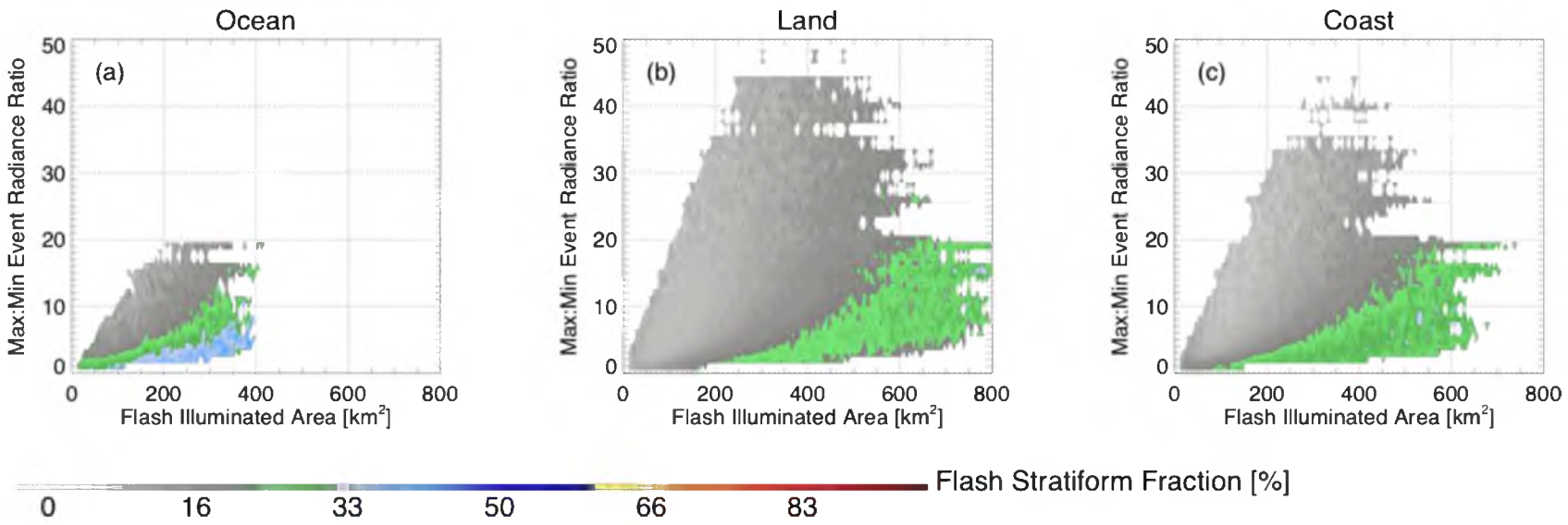

Fig. 3.27. Two-dimensional histograms of mean flash stratiform fraction categorized by flash illuminated area (x axis) and flash event max:min radiance ratio (y axis) plotted for each terrain type, separately.

optically thick clouds and its large size in many cases. However, the actual discharges of stratiform flashes are also known to occur across large distances, providing another possible explanation for why stratiform flashes are larger. Mean stratiform flashes for upper branch flashes, on the other hand, are much less likely to illuminate stratiform clouds and instead mostly illuminate convective and anvil clouds. Looking at all three fractions, together, the dimmest flashes (0–10°, treating the figure as a unit circle) are mostly stratiform/anvil flashes, with primarily stratiform flashes above that (10–20°), followed by stratiform/convective flashes (20–30°), primarily convective (30–50°), and convective/anvil flashes (50–60°).

The state of the viewing medium can also be described in terms of mean storm height throughout the flash footprint in Fig. 3.28. Lower branch flashes not only have the highest fractions of stratiform precipitation, but also the lowest mean storm heights, often below 4 km. The largest flashes with the lowest radiance ratios likely illuminate cloud regions near the edge of the storm where thin clouds prevent some of the radiance from reaching the LIS. Intermediate flashes also show an interesting trend: the smallest and least radiative flashes near the origin have high mean storm heights throughout the flash footprint, and this value decreases following the center of the histogram. In other words, flashes that are embedded within deeper convection are dimmer and smaller than those that occur in weaker cloud layers. Lastly, there is another local minimum in flash mean storm height along the upper branch where radiance ratios are less than 20 and illuminated areas are less than 100 km^2. Upper branch flashes in this region seem to occur in weaker storm regions than even other, larger and brighter, upper branch flashes and

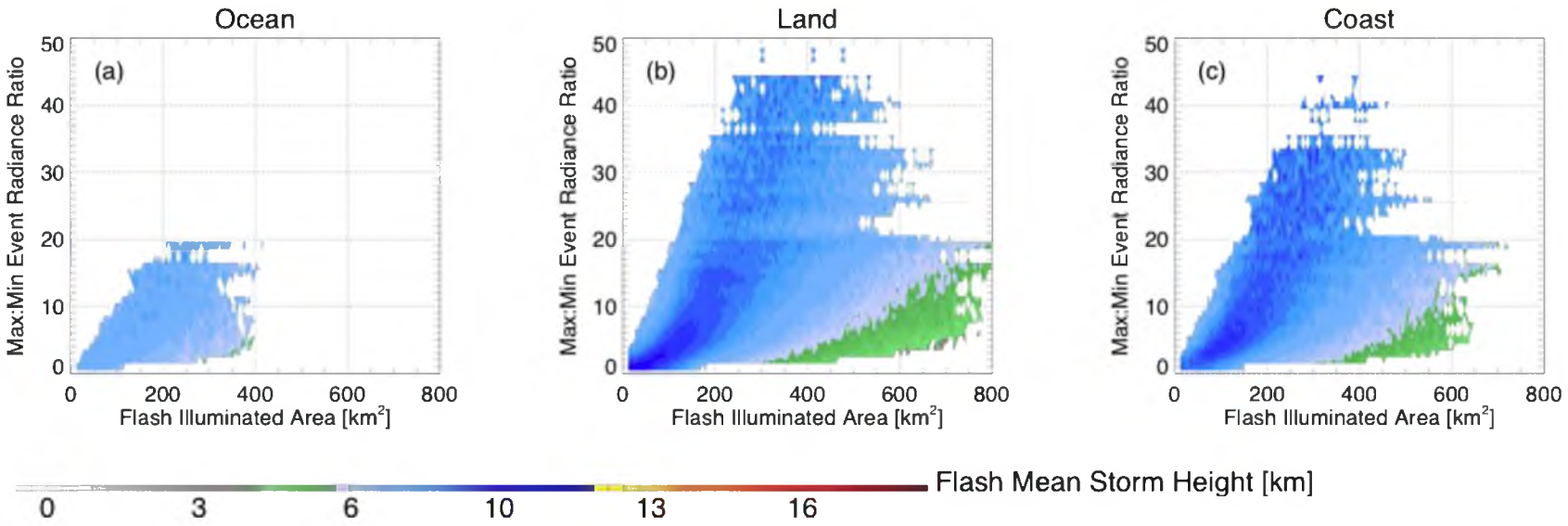

Fig. 3.28. Two-dimensional histograms of mean flash storm height categorized by flash illuminated area (x axis) and flash event max:min radiance ratio (y axis) plotted for each terrain type, separately.

even have similar mean storm heights to flashes in the middle of the lower branch. This seems odd because the peak radiance of these flashes is quite high for the relatively thin cloud layer they illuminate.

In order to examine why this may be, maximum storm heights throughout the flash footprint areas are examined in Fig. 3.29. In this particular section of the upper branch, mean storm heights and maximum storm heights are considerably low compared to other sections of the distribution, including the lower branch where mean flash heights even reach 13 km over land. While lower branch flashes occur in regions of both strong and weak storm clouds, flashes in this particular section of the upper branch only illuminate weaker cloud regions and yet are still able to produce very bright event pixels with very large optical powers.

The combination of these results paints an interesting picture of flashes in this part of the upper branch. Since these flashes illuminate weak clouds, yet are very bright, it would stand to reason that these flashes occur right at the boundaries of thick clouds, possibly convective towers. Three possible scenarios that would explain this combination of properties include anvil flashes parallel to the convective tower, convective flashes near the edge of very strong convection such that the interior of the convective cloud is not illuminated and lightning out the side or top of a thundercloud, so-called upward lightning where charge regions within a thunderstorm interact directly with upper atmosphere charge (Krehbiel et al. 2008). Regardless of what kinds of flashes cause these statistics, they certainly represent a special kind of lightning. However, a more complex approach is required to develop a better understanding of why they appear the way that they do when observed by LIS.

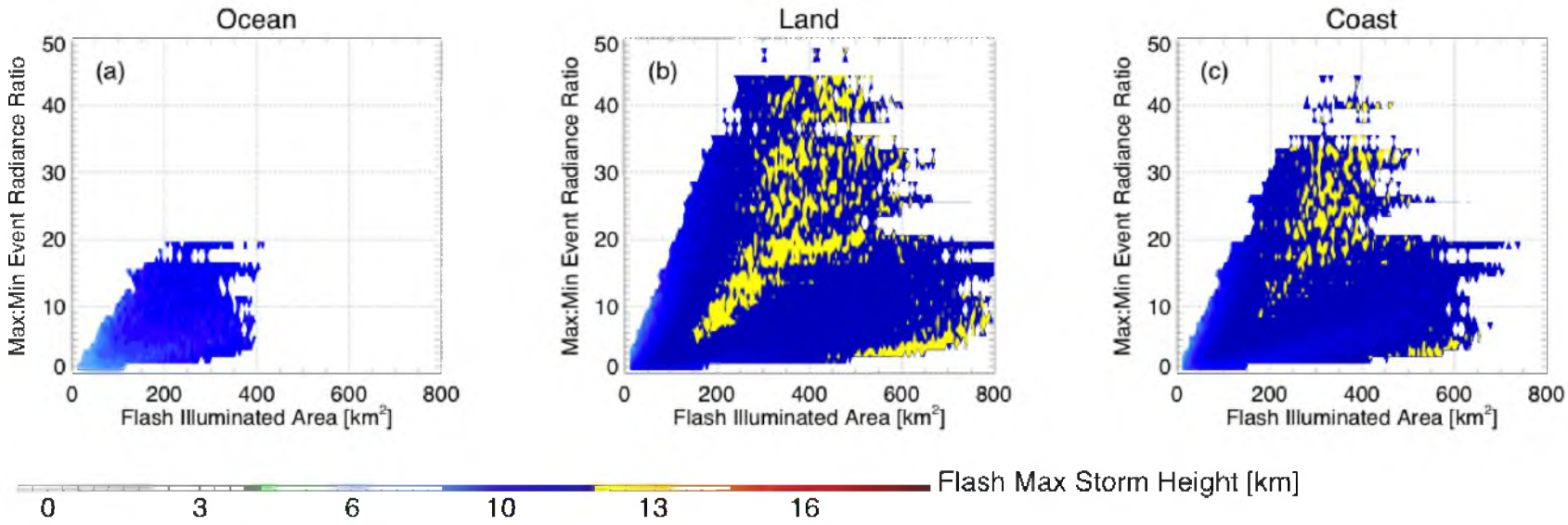

Fig. 3.29. Two-dimensional histograms of maximum flash storm height categorized by flash illuminated area (x axis) and flash event max:min radiance ratio (y axis) plotted for each terrain type, separately.

3.4 Simulated Optical Properties of Lightning Flashes

A Monte Carlo radiative transfer model is employed to examine some of the ideas of what determines the optical properties of lightning illumination from space, particularly the size of illuminated areas. Three mechanisms have been put forward that may determine the areas of illumination: the flash brightness, the cloud medium, and the flash breakdown structure (CG, IC, spider lightning). The first two mechanisms are examined in this section.

The Monte Carlo Atmospheric Radiative Transfer Simulator (MCARaTS; Iwabuchi et al. 2006) is used to simulate cloud illumination from lightning flashes embedded within a cumulus cloud layer as they would be observed at the TRMM orbit altitude. MCARaTS is a particularly useful model for studying lightning cloud illumination because it is capable of being run for homogeneous 1-D and inhomogeneous 3-D layers. Radiances are calculated by tracking photons as they bounce through the test region following specified phase functions for more than 60 species of common atmospheric aerosols and hydrometeors of various diameters and states of matter.

The model setup used in this study simulates a lightning flash embedded within a simulated cumulus cloud layer created by a large-scale eddy simulation that was included in the library that came with the MCARaTS model. This simulated cloud layer spans the entire horizontal model grid above the Lifted Condensation Level (LCL) and can be described as more horizontally stratified than vigorous convection and is free from convective towers, anvils, or other distinguishing—and complicating—features. Because of its uniform nature, it is a good candidate for studying variations in the distribution of radiance due to differences in the properties of lightning flashes.

A conceptual representation of the experimental setup is shown in Fig. 3.30. The model domain space contains 30 grid points in each horizontal direction and 41 vertical levels between the ground and 30 km. The model assumes a standard lapse rate from a surface temperature of 290 K and Lambertian surface reflectance. Lightning flashes are simulated as isotropic point sources of radiance that can be placed at any point within the model domain. For this experiment, lightning flashes will be placed in the center of the model domain at either 3 km, deep within the simulated cloud layer, or 7 km, near the top of the cloud layer, and then observed from space at 350 km altitude. Radiances observed by the sensor are then calculated by tracking 10^6 photons as they are scattered through model domain.

Fig. 3.31 shows how a simulated flash would illuminate the sample cloud layer if it occurred at 3 km altitude. Radiance ratios are contoured, and the boundary of the illuminated region detectable by LIS at night (1^{st} percentile of LIS event radiance, or 1,000 $\mu J\ m^{-2}$ ster-1 μm^{-1} per Fig. 3 in Peterson and Liu 2013) is circled. The observed flash footprint is not perfectly circular, however. In addition to concentric biases from the polar coordinate grid, the effects of small eddies within the cloud layer are visible, especially for particularly dim cloud sections (very high radiance ratios) outside the LIS-observable footprint. The LIS-observed flash would have a diameter of 6 grid points.

In order to see what would happen if the same flash occurred near the top of the cloud, as would be the case with anvil flashes and upward lightning events, the lightning point source in the simulation is moved from 3 km to 7 km without changing its radiative flux. Figure 3.32 shows how the cloud region would be illuminated. With little cloud between the flash and the sensor, the area illuminated by this flash is much more irregular

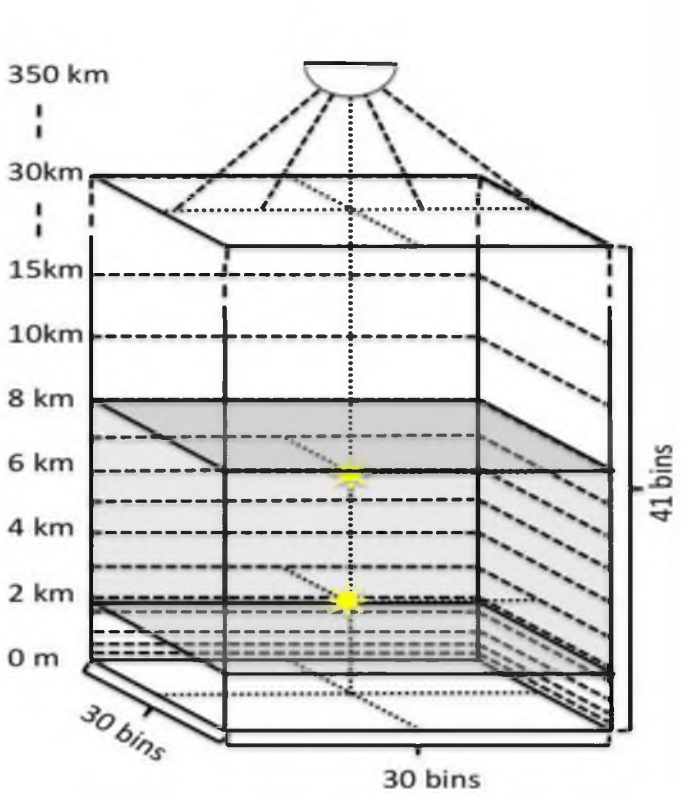

Fig. 3.30. Experimental setup of the model domain, simulated cloud layer, and the locations of the sensor and flash sources used in this study.

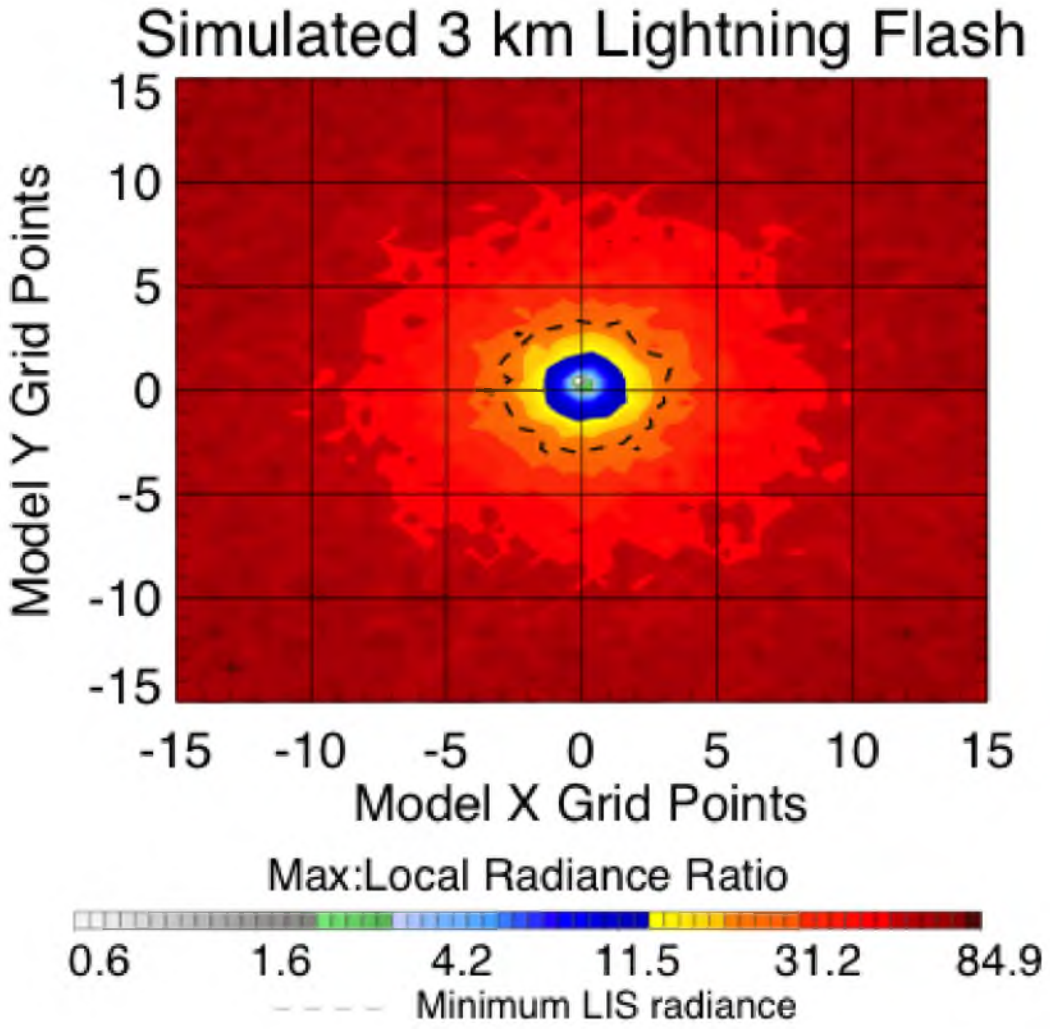

Fig. 3.31. Polar plot of simulated cloud radiance for a lightning flash at 3 km viewed from space. Horizontal coordinates represent sensor grid points. Contours represent the ratio between each pixel and the maximum radiance of the illuminated cloud. The dashed line depicts the approximate minimum nighttime observable radiance of the LIS (1,000 $\mu J\ m^{-2}\ ster^{-1}\ \mu m^{-1}$).

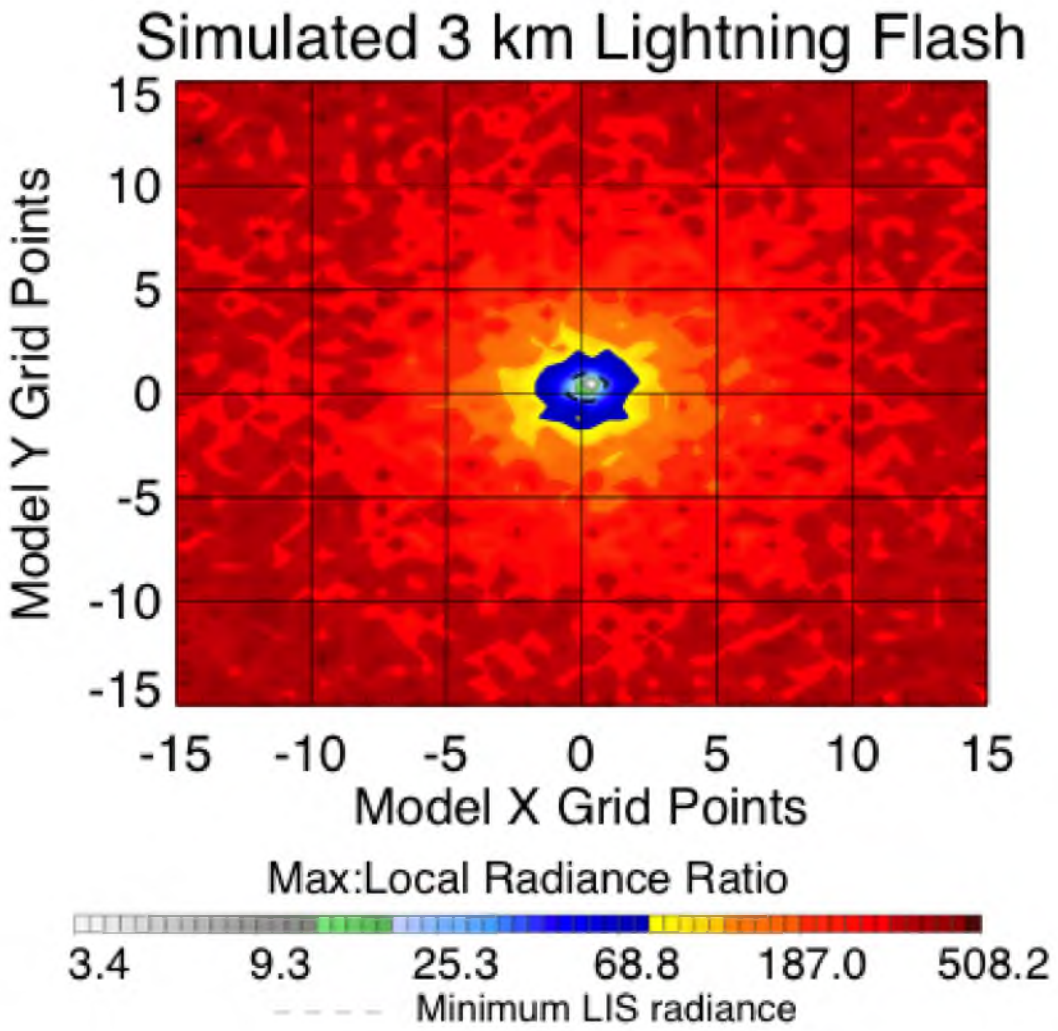

Fig. 3.32. Polar plot of simulated cloud radiance for a lightning flash at 7 km viewed from space. Horizontal coordinates represent sensor grid points. Contours represent the ratio between each pixel and the maximum radiance of the illuminated cloud. The dashed line depicts the approximate minimum nighttime observable radiance of the LIS (1,000 $\mu J\ m^{-2}\ ster^{-1}\ \mu m^{-1}$).

than the lower flash. Also, radiance ratios are more than five times greater for this flash. While the radiance of the lower flash was scattered over a large area, the radiance from this flash is mostly concentrated around the source location. This flash would be very small when viewed by LIS, but exceptionally bright. This scenario is an extreme case of what was seen in Fig. 3.19. Thinner clouds have the worst relationship between radiance ratio and illuminated area because the radiance from the flash cannot sufficiently illuminate the thin cloud layer around it.

Another way to affect flash illumination is by varying the initial radiative flux of the lightning point source. The flash at 3 km in Fig. 3.33 differs from the flash in Fig. 3.31 only in that its radiative flux has been halved. The radiance ratio contours are virtually identical, meaning that it illuminates the cloud in the same way as before, but amount of radiance at the center is only half of what it was before. As a result, the radius of the flash observed by LIS is smaller than it was in Fig. 3.31. While the first flash was 6 pixels across, this flash is only 3 pixels in diameter. On the other hand, increasing the radiative flux of the source to twice the value of the flash in Fig. 3.31 increases the diameter of the area illuminated by the flash observed by LIS, as seen in Fig. 3.34. Now, the dashed circle has a diameter of roughly 15 pixels. Figure 3.35 illustrates additional simulations of the same flash with differing source radiative fluxes and shows the illuminated areas of the flashes that would be observable by LIS. With all other factors being equal, the size of the region illuminated by a lightning flash does, indeed, depend on the radiative intensity of the flash.

Based on these simulated results, it is clear that both the brightness of the lightning flash and the properties of the viewing medium work together to determine the

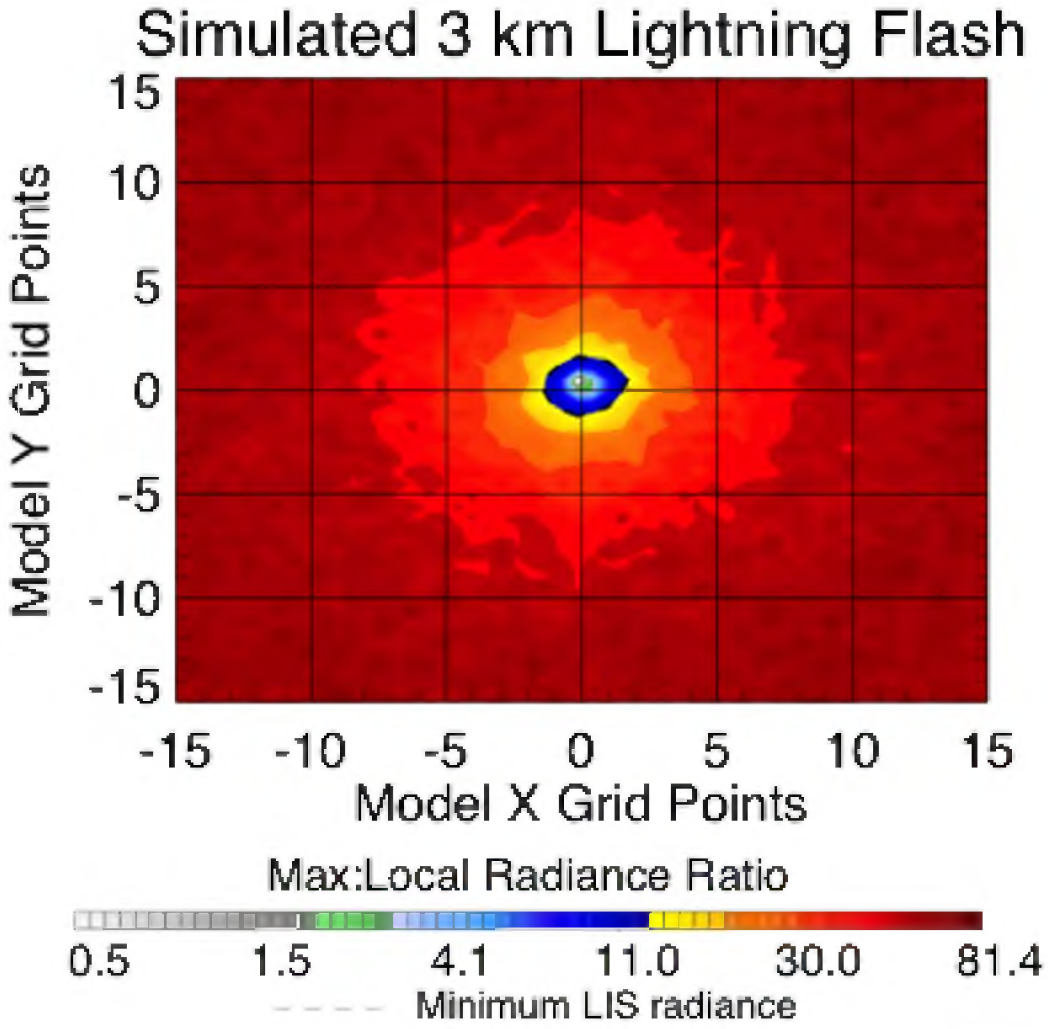

Fig. 3.33. Polar plot of simulated cloud radiance for a lightning flash at 3 km viewed from space that has half the radiative flux as the flash in Fig. 3.31. Horizontal coordinates represent sensor grid points. Contours represent the ratio between each pixel and the maximum radiance of the illuminated cloud. The dashed line depicts the approximate minimum nighttime observable radiance of the LIS (1,000 μJ m^{-2} $ster^{-1}$ μm^{-1}).

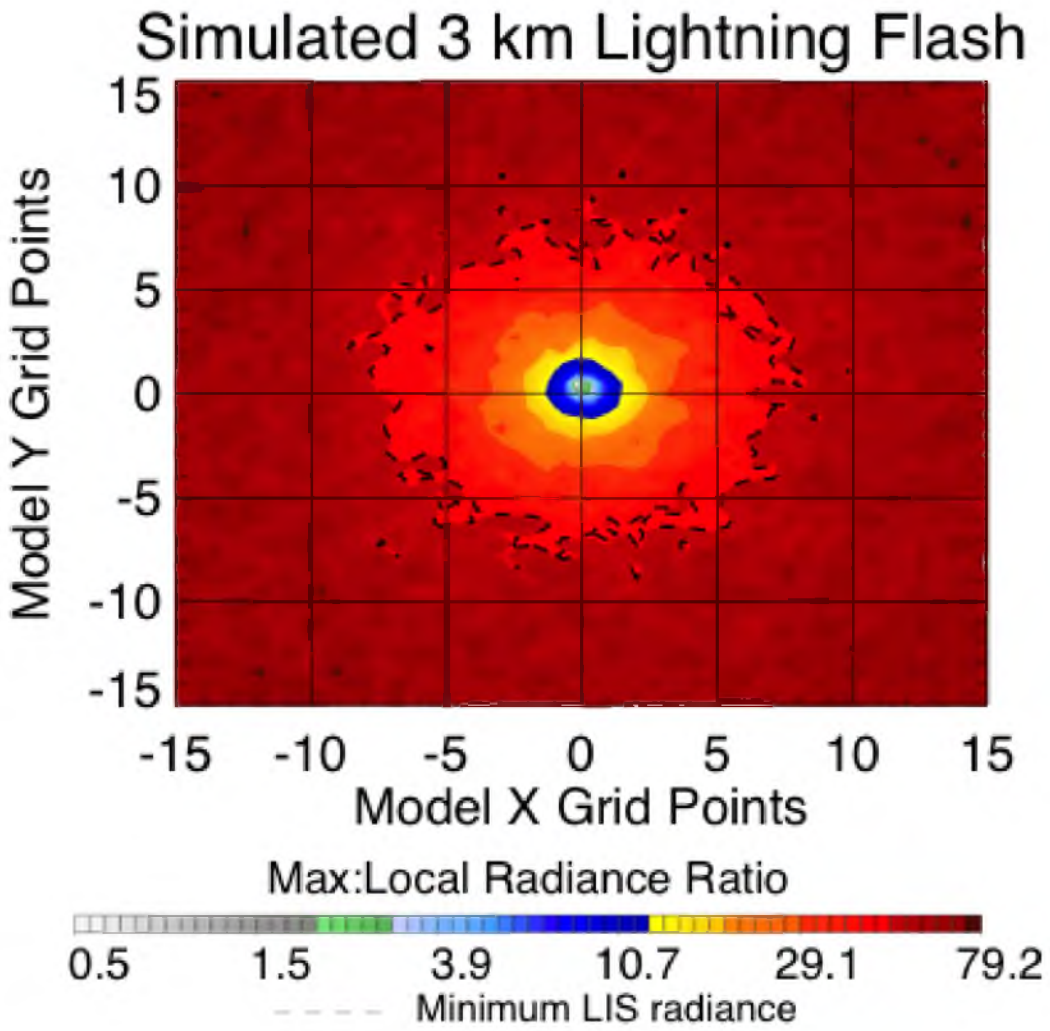

Fig. 3.34. Polar plot of simulated cloud radiance for a lightning flash at 3 km viewed from space that has twice the radiative flux as the flash in Fig. 3.31. Horizontal coordinates represent sensor grid points. Contours represent the ratio between each pixel and the maximum radiance of the illuminated cloud. The dashed line depicts the approximate minimum nighttime observable radiance of the LIS (1,000 μJ m^{-2} $ster^{-1}$ μm^{-1}).

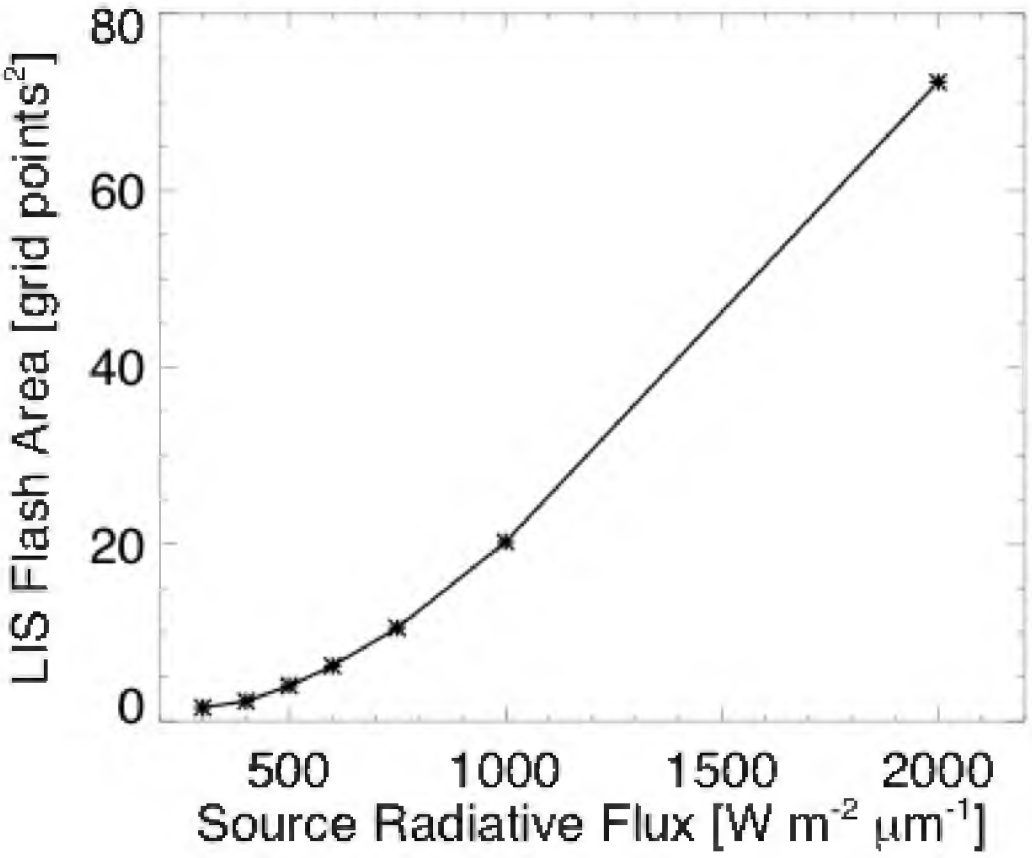

Fig. 3.35. Radiative flux of 3 km lightning flash sources and the resulting illuminated areas of the LIS-observable flash.

illuminated areas of lightning flashes. Flash area depends on the radiative flux of the lightning flash on a fundamental level. This relationship is then modified based on the optical properties of the cloud medium (thick cloud, thin cloud, no cloud) surrounding the flash. These results are consistent with the trends observed in observations in the previous section.

3.5 Properties of Parent Thunderstorms

Relationships between the optical properties observed by LIS and coincident storm properties both at the center location of the flash and throughout the footprint area have been examined. What remains is the scale of storm. It was shown that the properties of the environment through which the radiance from a lightning flash propagates affects the measured properties of the flash, but it is also possible that the properties of the storm itself play a role in determining the size, brightness, and duration of the flashes. For example, what kind of storms would have extremely large, bright, and long duration flashes? Do they have unique properties in radar or passive microwave observations?

To examine storm properties and their relationship to LIS flashes, LIS-observed lightning flashes must be associated with a consistently defined storm area. For this purpose, Radar Precipitation Features (RPFs) are chosen. LIS flashes are assigned to RPFs following the method described in Chapter 2. Then, for each RPF, the properties of the largest, longest lasting, and brightest flashes are recorded so that the maximum properties of the lightning in each storm can be compared to its own characteristics, which are stored in the University of Utah precipitation feature database (Liu et al. 2008).

Figure 3.36 shows the median values of the minimum 85 GHz PCT for the parent

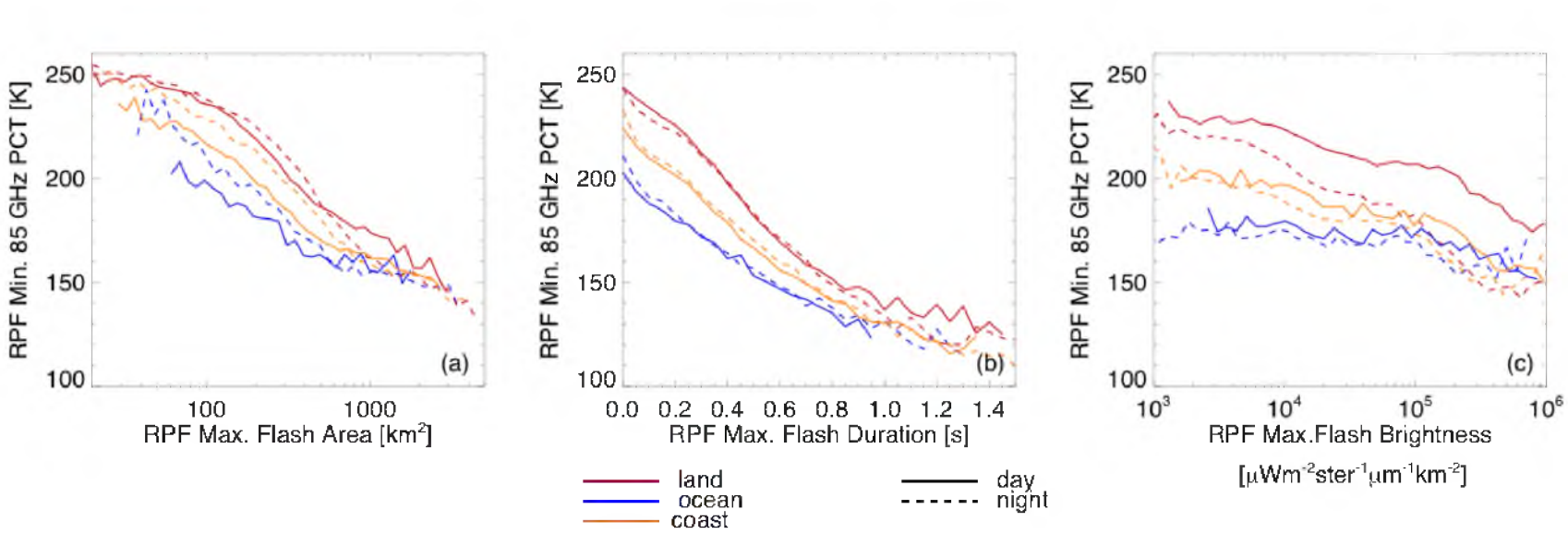

Fig. 3.36. Two-dimensional CDF medians of RPF minimum 85 GHz PCTs grouped by RPF maximum flash illuminated area (a), RPF maximum flash duration (b), and RPF maximum flash brightness by mean optical power (c).

RPFs categorized by the maximum illuminated area (a), maximum duration (b), and maximum mean optical power (c) of all of their associated child flashes. For each sample partition displayed, RPFs that produce only small, short duration, and dim flashes tend to have warm 85 GHz PCTs and are therefore relatively weak, while those that are capable of producing flashes with exceptional optical properties have much colder 85 GHz PCTs and are much stronger. Additionally, these trends depend more on terrain type than they do LIS sensitivity.

This tendency for stronger storms to produce exceptional flashes is not just the case for 85 GHz PCT. Figure 3.37 shows the same type of plot for RPF maximum 30 dBZ echo heights. Echo top heights increase dramatically with increasing RPF maximum flash area and duration. RPFs with only short and small flashes typically have maximum 30 dBZ heights below 8 km, while those with large and long lasting flashes have 30 dBZ heights between 10 km and 12 km. This trend is similar for all LIS diurnal sensitivities and terrain categories. Mean optical power statistics, however, do not show the same, strong trends. For RPFs over land and coastal regions, there is a systematic increase in maximum 30 dBZ echo top height with increasing peak flash overall brightness, but it plateaus near 10^5 μJ $ster^{-1}$ m^{-2} μm^{-1} before increasing again at higher values mean optical power. At the same time, oceanic RPF 30 dBZ echo top heights do not vary much with observed maximum flash mean optical power and even decrease around 10^5 μJ $ster^{-1}$ m^{-2} μm^{-1}. This indicates that stronger storms do tend to have larger and longer lasting lightning flashes. However, brighter flashes are not necessarily observed in stronger storms.

Table 3.6 shows a summary of the differences between RPFs with near-median

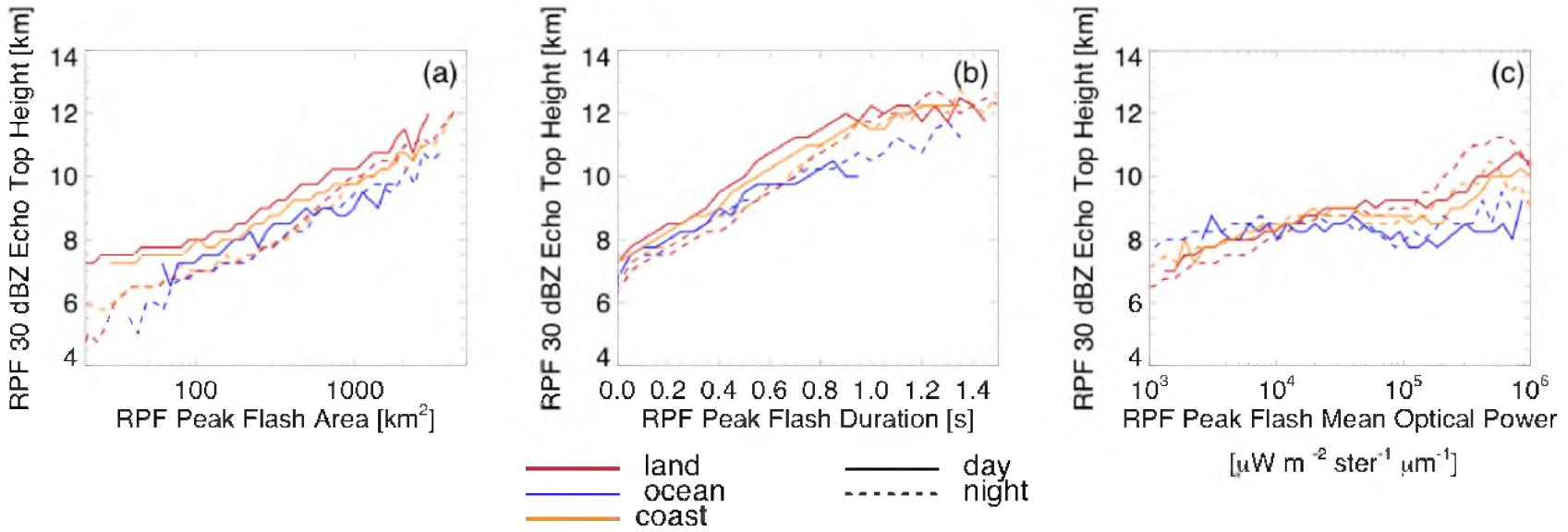

Fig. 3.37. Two-dimensional CDF medians of RPF maximum 30 dBZ echo top height grouped by RPF maximum flash illuminated area (a), RPF maximum flash duration (b), and RPF maximum flash brightness by mean optical power (c).

Table 3.6. Median properties of RPFs with flashes categorized by RPF maximum flash illuminated area, duration, and mean optical power. Near median (45th to 55th percentile) and top 10% RPF maximum flash properties are shown for land, ocean, and coastal flashes.

		RPF Max. Flash Area		RPF Max. Flash Duration		RPF Max. Flash Mean Optical Power	
RPF Mean	Terrain	Median	Top 10%	Median	Top 10%	Median	Top 10%
Area (km^2)	land	2,236	7,918	2,089	8,216	2,114	6,459
	ocean	10 528	12 614	9,537	15 543	8,883	15 373
	coast	6,110	9,182	5,161	11 400	4,444	11 227
Flash	land	7.0	23.0	4.0	35.6	5.1	24.6
Count (#)	ocean	3.6	9.8	2.3	16.7	3.0	10.3
	coast	5.6	17.5	2.9	28.6	4.5	19.3
20 dBZ	land	11.4	13.3	11.2	13.6	11.5	12.4
Echo Top	ocean	11.3	12.4	11.0	12.6	11.4	10.7
(km)	coast	11.7	13.3	11.4	13.6	11.9	12
30 dBZ	land	9.0	10.7	8.7	11.5	9.0	10.3
Echo Top	ocean	8.6	9.7	8.2	10.5	8.7	8.5
(km)	coast	8.9	10.4	8.4	11.4	9.0	9.6
Min. 85	land	199.6	162.7	208.5	146.8	202.3	177.4
GHz PCT	ocean	169.4	155.9	178.1	135.4	172.9	165.4
(K)	coast	180.9	156.7	191.3	136.5	184.5	166.4
Min. 37	land	264.4	250.4	268.6	240.0	266.3	253.0
GHz PCT	ocean	255.9	250.8	259.5	239.2	257.8	250.1
(K)	coast	259.8	250.5	264.6	238.4	262.2	250.0
Min. IR Tb	land	213.4	200.0	215.2	199.9	214.0	208.4
(K)	ocean	210.5	204.8	211.8	204.7	210.3	213.4
	coast	208.4	200.3	210.1	199.5	208.7	207.9
Volumetric	land	9,838	38 623	8,856	41 816	9,265	31 872
Rain (km^2	ocean	50 834	63 974	44 797	82 817	41 706	77 386
mm/hr)	coast	29 089	48 239	24 202	61 750	21 210	58 180

(45th to 55th percentile) peak flash characteristics and those with exceptional (top 10%) flashes for maximum flash illuminated area, duration, and mean optical power. A quick review of the table shows that RPFs with exceptionally large flashes are much larger than their counterparts with only typical-sized flashes, and also have much higher flash counts, higher echo top heights, lower PCTs at both 85 GHz as seen before and 37 GHz, somewhat colder minimum infrared brightness temperatures, and much higher rain volumes, especially over land. RPFs with particularly long lasting flashes also show elevated values in these storm properties, including the most dramatic increase in mean RPF flash rate, which is consistent with the idea that particularly long lasting flashes may be comprised of multiple individual flashes. RPFs with particularly bright flashes also show the same trend.

The previous sections in this chapter have shown that exceptionally large and bright flashes typically occur in relatively weak storm regions. These trends indicate that flash area and brightness can be described in terms of a radiative transfer photon diffusion problem sensitive to the optical intensity of the flash source and the optical properties of the cloud medium. However, this section suggests that the size of the largest flash in a storm depends on the convective intensity of the storm. Because of this, the existence of exceptionally large and bright flashes may be more than just a viewing problem, but an indication—assuming that the convective and electrical properties of thunderstorms are related—that the optical properties of lightning flashes may depend on the nature of the electrical discharges themselves.

CHAPTER 4

LIS AND NLDN COLLOCATED OBSERVATIONS OF LIGHTNING

In the previous chapter, the optical characteristics of lightning were shown to relate to the radiance of the flash and the optical properties of the viewing medium. A third mechanism that may affect the perceived illuminated area of a flash—the properties of the electrical breakdown—was theorized but not examined since no sensor aboard TRMM has the ability of characterizing the electrical properties of lightning. This chapter seeks to answer this question by collocating lightning strokes observed by the ground-based National Lightning Detection Network (NLDN) with LIS optical flash observations over the common domain of these two different platforms.

Discussion of the collocation routine and related samples can be found in Chapter 2. This chapter will continue this discussion and examine relationships between NLDN and LIS observations of lightning in the context of some of the results from the previous chapter.

4.1 Properties of Collocated NLDN and LIS Flashes

Figure 4.1 shows CDFs of LIS optical and collocated NLDN properties of LIS lightning flashes. The collocation routine assumes that LIS flashes are considered "parents" with single or multiple NLDN "children" even though, due to the strict criteria

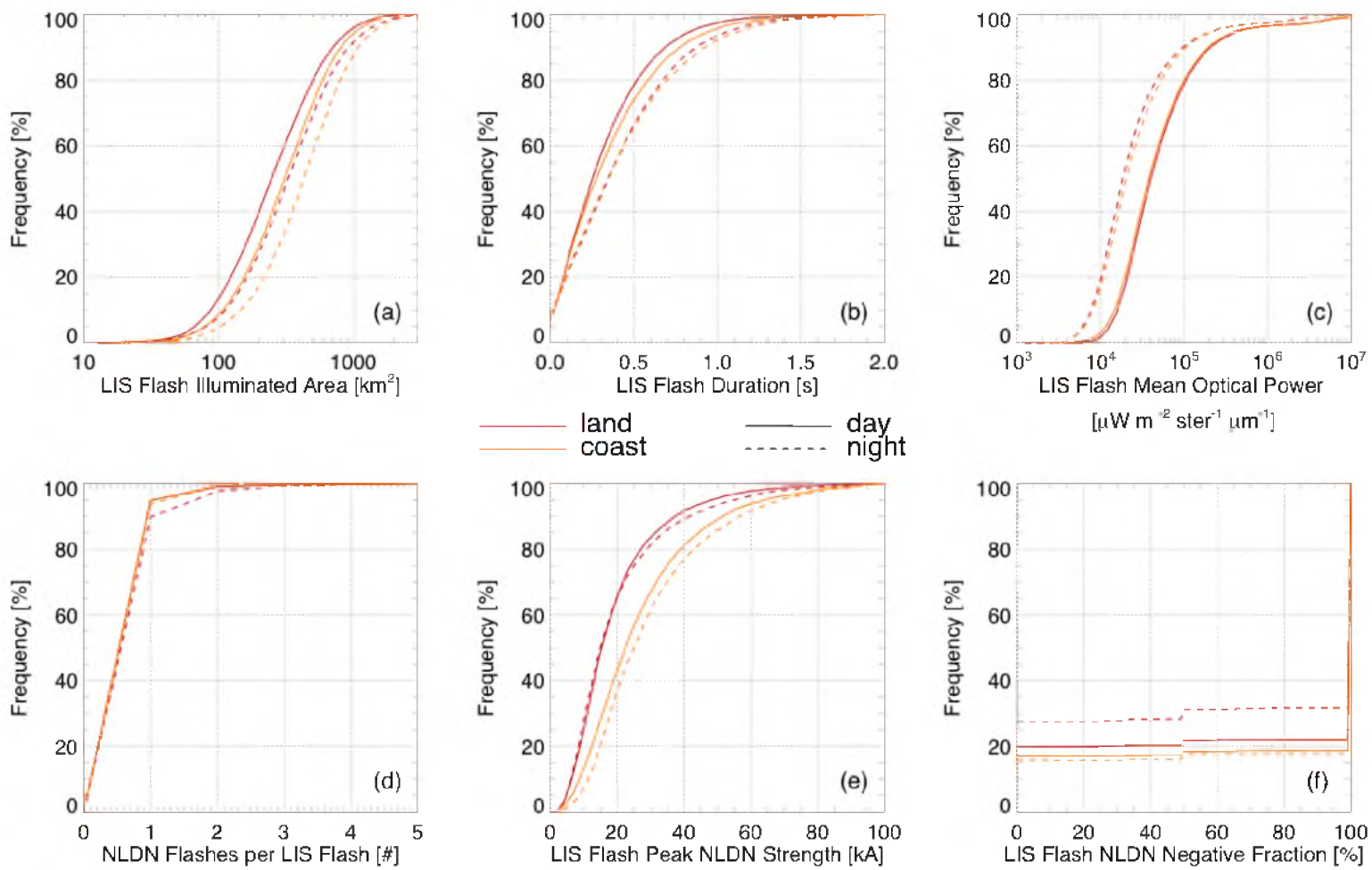

Fig. 4.1. CDFs of LIS and NLDN properties of collocated flashes. Properties include LIS flash illuminated area (a), LIS parent duration (b), LIS flash mean optical power (c), the number of NLDN collocations per LIS flash (d), peak NLDN child stroke strength (e), and the fraction of negative NLDN collocations to the LIS flash (f) categorized by terrain type and LIS sensitivity regime.

employed for the collocation process, most LIS flash parents have only a single child NLDN stroke. Collocated flashes are separated by the sensitivity regime and terrain type of the parent LIS flash. Panels a, b, and c show the statistics of the optical properties of each collocated LIS flash. Some of the same trends of Chapter 3 can be observed. As before, nighttime flashes are larger, longer lasting, and can be less optically bright than flashes observed during the day for land and coastal flashes using the same partitioning scheme employed for LIS observations. Also, coastal flashes seem to be larger and longer lasting than flashes over land. Optical powers do not vary between land and coast, however, only between day and night.

The bottom three panels in Fig. 4.1 show the properties of the collocated NLDN child flashes. A vast majority of collocated LIS flashes (90% for nighttime land flashes, 95% for all other groups) have only one NLDN child stroke due to the strict criteria used in the collocation routine. Additionally, more than 99% of all collocations have less than four child NLDN strokes (Fig. 4.1d). The strength of NLDN breakdown for each collocation seems to vary significantly by region and slightly by LIS sensitivity regime (Fig. 4.1e). Coastal flashes seem to be associated with significantly stronger breakdowns than flashes over land. The median land-based flash has a NLDN-reported strength of just 15 kA compared to nearly 25 kA over the coast. This result may signify a characteristic difference between land and coastal ocean flashes, or it may be due to the limitations of the network including difference in signal propagation between land (more attenuation) and ocean (less attenuation). Even though the collocated flash sample takes care to omit flashes that are not well resolved by the NLDN (with location errors greater than the size of a 5 km LIS pixel), triangulation uncertainty is not the only limitation of looking at

offshore data. Since there are no NLDN stations over the coastal ocean, the further offshore a weak stroke occurs, the less likely it will be detected by the network. Consequently, the coastal portion of the collocated sample likely does not include as many weak strokes as over land and is therefore likely biased towards strong breakdowns that can be detected with reasonable accuracy further away. However, this caveat only applies for strokes that are far offshore. Since there are many NLDN stations right along the coastline, strokes that occur at least within the typical grid spacing of land-based NLDN stations from shore would likely be just as easily detected by the network as flashes over land, even if their triangulation location accuracies may be less due to fewer stations detecting the stroke. Alternatively, since less of the signal is attenuated as it propagates over the ocean, this effective range might be slightly greater than the sensor spacing over land.

The last panel of Fig. 4.1 shows the negative fraction of the collocated NLDN strokes for LIS flashes. Since most collocations are one-to-one (Fig. 4.1d), most flashes are either entirely negative (20% of daytime land flashes) or entirely positive (58% of daytime land flashes) rather than being a collection of positive and negative NLDN strokes (2% of daytime land flashes). The fact that most flashes are of negative polarity over the US in this subset is consistent with the raw dataset and with literature (Orville et al. 2011). In general, there are about 3% more positive polarity flashes over land during the day (and 11% more at night) compared to coastal flashes. This distribution is better illustrated in Table 4.1. Nearly three in four flashes, overall for all times of day and terrains, are entirely negative polarity in the sample, while 22% are positive polarity, and nearly 3% are of mixed polarity. These mixed polarity flashes often consist of one

Table 4.1. Fractions of LIS flashes that have only positive collocated NLDN strokes, only negative collocated NLDN strokes, and NLDN strokes of both polarities for different terrain categories and times of day.

Time of Day	Terrain	Positive NLDN Collocations (%)	Negative NLDN Collocations (%)	Mixed NLDN Collocations (%)
All	all	22.5	74.7	2.8
	land	24.4	72.4	3.1
	coast	17.9	80.2	1.9
Day	all	19.5	78.7	1.8
	land	20.3	77.6	2.1
	coast	17.7	81.0	1.3
Night	all	24.1	72.4	3.4
	land	27.9	67.9	4.2
	coast	16.1	82.0	1.9

positive polarity flash and one negative polarity flash, and they are most frequent at night over land, where they account for over 4% of the overall sample.

However, the true benefit of collocating LIS and NLDN data is not to look at each sensor, independently. The true benefit of this effort is to be able to examine LIS and NLDN properties together and see if they may relate to one another. Figure 4.2 shows one-dimensional histograms of NLDN child strength for various LIS optical parent flash properties. Results are shown for all sensitivity regimes since NLDN parameters were shown to primarily vary by terrain rather than time of day. The strength of the NLDN stroke may be related to any number of the optical characteristics of the resulting flash of illumination ranging from brightness (stronger strokes mean more optical energy) to illuminated area (more optical energy, then, means larger illuminated areas) to even duration (IC strokes, which are weaker than CG strokes, may last longer).

Of the optical parameters in Fig. 4.2, however, the only one that is shown to vary significantly and consistently with collocated peak NLDN strength is parent flash illuminated area (Fig. 4.2a). Flashes that illuminate large areas are nearly twice as strong as flashes that are very small over both land and coastal ocean regions. Flash duration (Fig. 4.2b) and brightness (Fig. 4.2c and d), on the other hand, show only small changes in the NLDN strength statistics between typical ranges of short-lived or dim flashes and long-lived or bright flashes. The key exception is flashes with extreme maximum radiances (the top 5% in Fig. 3.1) whose collocated NLDN strength statistics suddenly jump by nearly 7 kA over land and less for coastal flashes, possibly due to the relatively small sample size of coastal bright flashes. A similar spike is not present in optical power statistics, but flashes with exceptionally bright events have already been shown to be

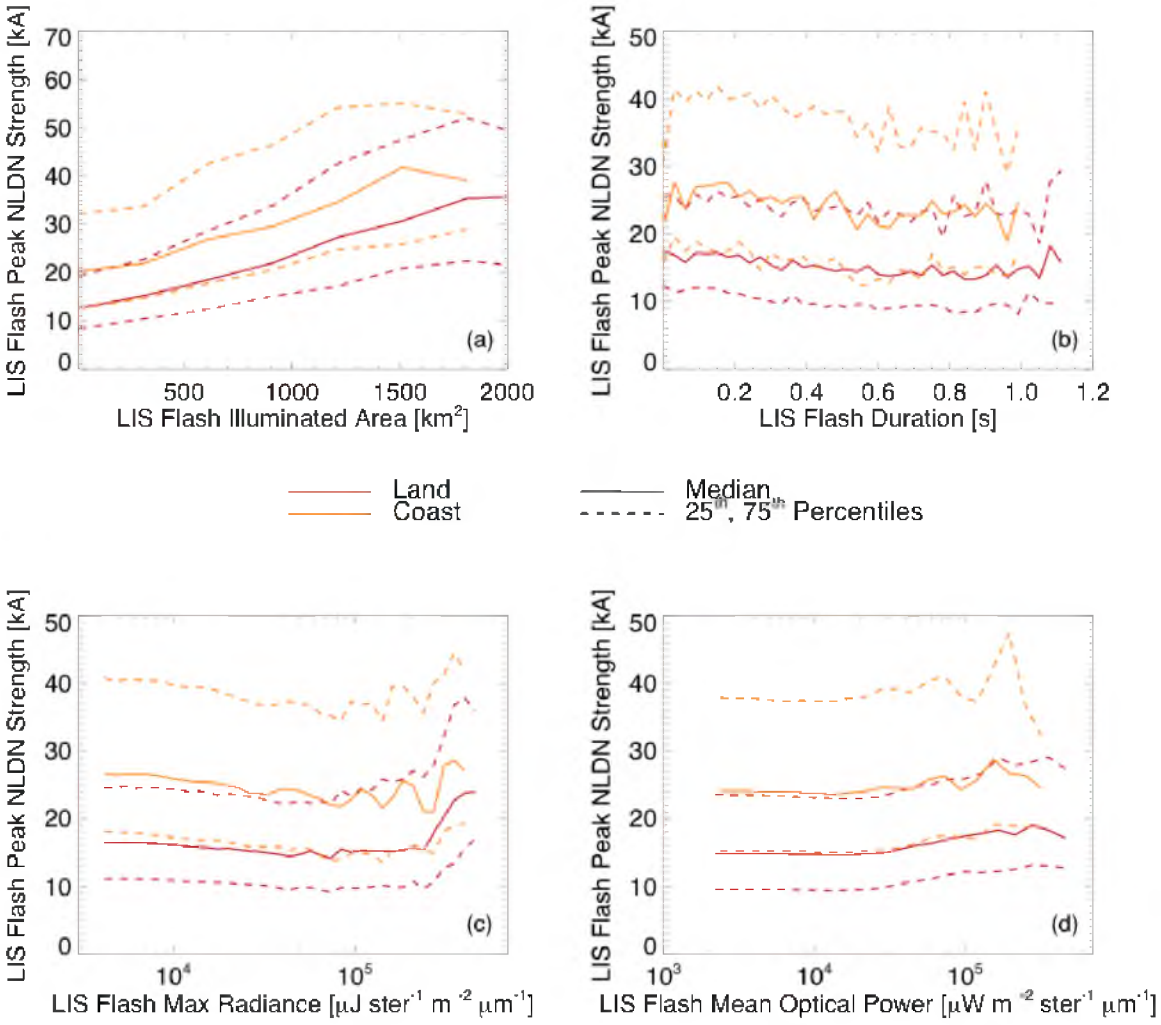

Fig. 4.2. Two dimensional CDFs of LIS flash peak NLDN collocated stroke strength and LIS flash illuminated area (a), duration (b), maximum event radiance (c), and mean optical power (d).

"special" (Section 3.3.3).

What Fig. 4.2 shows is that the characteristics of the electrical breakdown influence the observed illuminated area of the flash, but do not play much of a role in determining its duration or optical brightness in most cases. This idea runs counter to what was seen in the observations and computer simulations of lightning flashes in the previous chapter where flash illuminated area and maximum event radiance were shown to be intimately related. If flash area is related to collocated NLDN strength and flash maximum brightness is related to area, then flash maximum brightness *should* be related to collocated NLDN strength as well. But, this is simply not what observations indicate. In fact, if anything, the statistics for NLDN strength *decrease* for flashes with increasing maximum radiances up until exceptional values are reached where sample sizes are small and may be biased. Viewing medium considerations fail to explain this trend because if the viewing medium is sufficient to allow large flashes to be observed (e.g., stratiform precipitation where large flashes often occur), it will also not inhibit bright event pixels at the discharge location from being seen. Radiative considerations alone do not explain these results.

Instead, the third proposed factor that may control the optical footprints of lightning flashes could be the source: the structure of the electrical breakdown. It should be no surprise that CG and IC flashes look different to the LIS. They look very different to the casual observer on the ground. CG flashes are often point-to-point discharges between the lowest cloud layers and the surface, while IC flashes spread horizontally as airborne charge regions interact. CG flashes were also shown to be much stronger than IC flashes (Fig. 2.7b) for both land and coastal terrain. However, there are not enough

LIS/NLDN collocations with CG/IC information, making it difficult to see whether this could explain how large flashes can be stronger, but not brighter.

One way of potentially looking at CG/IC differences is by using flash polarity. According to Fig. 2.7a, 80% of IC flashes are of positive polarity, while 90% of CG flashes are of negative polarity. Because of this, if the relationship between flash area and NLDN strength holds for both negative and positive polarities, it may indicate that IC flashes may explain larger flashes resulting from stronger discharges.

Figure 4.3 looks at the relationship between LIS area and collocated NLDN strength using a slightly different approach. The color contour represents probability density functions (PDFs) for flashes of varying footprint areas rather than one-dimensional box plots, and the peak probabilities for both the negative and positive branches of the figure are shown (thick line) along with sample density (thin line contours). Flash areas are also represented using a logarithmic scale rather than the linear scale shown before. This figure shows that the shift of the statistics towards stronger discharges for larger flashes holds for both positive and negative polarity flashes. Even though the positive branch does not have as many samples, the maximum probabilities do seem to diverge, meaning that the trend in Fig. 4.2a may not just be due to flash type.

However, there are many problems with this statement. First and foremost, while the NLDN easily detects CG flashes, it has difficulty detecting IC flashes, causing CG flashes to dominate the NLDN sample despite being less common, overall. Second, all this shows is that this trend holds for both positive and negative flashes; it does not actually say anything about CG or IC flashes. In order to see if this is actually what may be occurring, Fig. 4.4 shows the relationships between collocated NLDN strength and

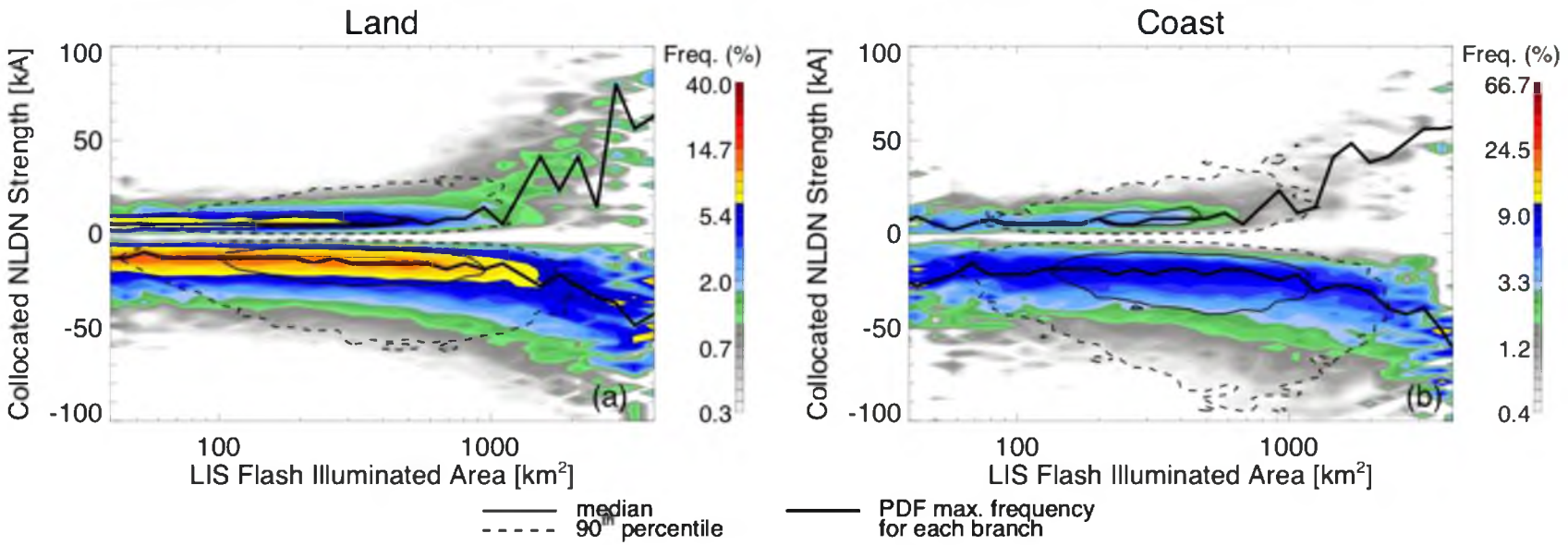

Fig. 4.3. Histogram distributions (colored contour) of NLDN stroke strength for flashes of various LIS illuminated areas over land (a) and over the coastal ocean (b). The integrated sum of the contour for each LIS illuminated area bin is 100%. Two peak probability curves (thick lines) —one for positive polarity flashes and one for negative polarity flashes—as well as two-dimensional histograms of sample density (thin lines) are overlain.

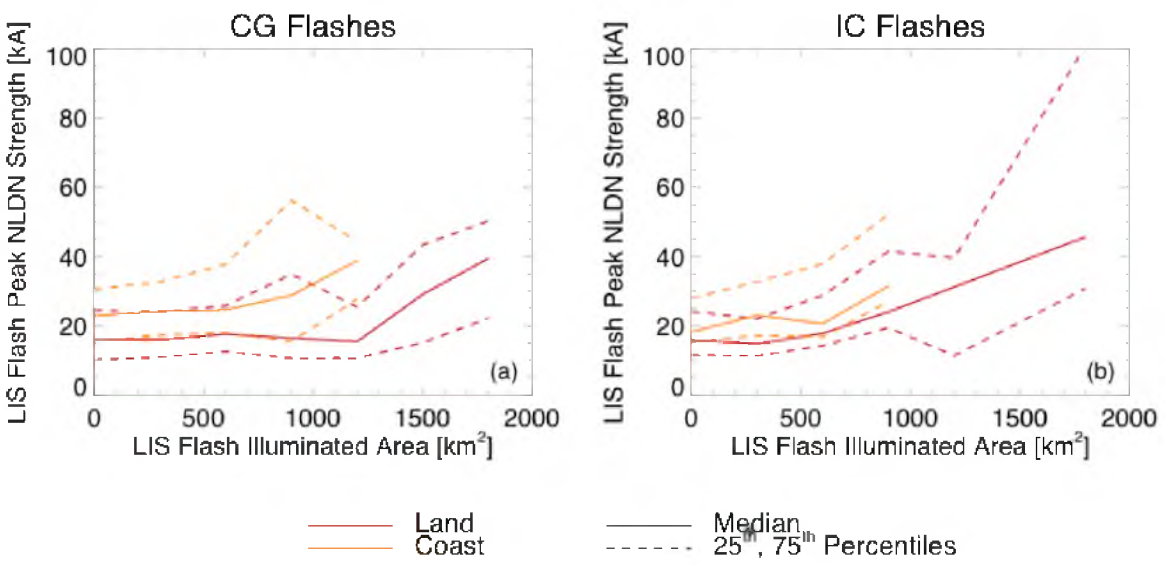

Fig. 4.4. Two-dimensional CDFs of LIS flash peak NLDN collocated stroke strength and LIS flash illuminated area for CG (a) and IC (b) flashes.

flash illuminated area for the very limited sample of collocated flashes with CG/IC information. It is important to use discretion when examining this figure because many of the bins on the right side of the figure only have 5–10 flashes, producing very weak statistics. However, a clear difference is visible between NLDN-identified CG flashes and IC flashes. The statistics of CG flashes do not appear to change with illuminated area throughout most of the domain. A 100 km^2 flash over land is just as likely to have an NLDN strength of 20 kA than a flash that is 500 km^2. The statistics of IC flashes, however, tend towards stronger NLDN strengths for flashes greater than 250 km^2 in area. While these statistics may not be robust until the sample size can be increased, they provide direct evidence that supports the idea of an electrical breakdown component in determining the illuminated area of an IC flash that is not present for CG. The reason for this is possibly that IC breakdowns over large distances that would illuminate extremely large areas require more energy to overcome the resistance of the air in between charge regions. Therefore, the enormous area illuminated by the flash is explained by breakdown strength, even when it is not explained by radiance or cloud medium properties.

Additional support for the idea that breakdown structure can determine the optical characteristics of the flash comes from examining LIS mean properties of single-stroke (all CG flashes and 40% of IC flashes) and multistroke flashes (60% of IC flashes) in Table 4.2. Like flash polarity, multiplicity is not a perfect indicator of whether the flash is CG or IC, but it does allow statistics to be computed using more of the collocated sample. Multistroke IC flashes are much larger, on average, than single-stroke flashes, exceeding their mean illuminated area by 60–80 km^2. Multistroke flashes also last a few milliseconds longer than single stroke flashes, but only have one-fourth the mean optical

Table 4.2. Mean LIS optical properties for single-stroke and multistroke collocated NLDN flashes.

Mean LIS Property	Terrain	Single-Stroke Collocated Flashes	Multiple-Stroke Collocated Flashes
Illuminated Area (km^2)	land	407.9	491.1
	coast	515.8	578.2
Duration (s)	land	0.36	0.42
	coast	0.40	0.45
Mean Power (μW m^{-2} $ster^{-1}$ μm^{-1})	land	423 108	115 142
	coast	435 530	103 639
Min:Max Event Radiance Ratio	land	23.0	19.1
	coast	29.8	22.8

power of single-stroke flashes. Radiance ratios are also slightly less for multistroke flashes. This shows that compared to their IC counterparts, CG flashes are smaller and shorter lasting yet much brighter.

Differences between storm regions with CG and IC flashes have been noted (e.g., Rutledge and MacGorman 1988; Carey et al. 2005; among others) by observing lightning in specific thunderstorm cases. A robust, collocated, NLDN and TRMM dataset make it possible to examine lightning flashes in different regions of storms on a statistical scale and see how they compare. Figure 4.5 shows mean NLDN strengths for flashes categorized by convective and stratiform fractions. Collocated NLDN strengths over land typically average around 20 kA for convective and anvil flashes, but stratiform flashes seem to have abnormally high mean NLDN pulse strengths, typically between 30 and 40 kA. This is consistent with the results in Chapter 3 and Fig. 4.2, in that stratiform flashes have been demonstrated to be comparably larger than their convective counterparts, meaning that they should be stronger, as well, following the results from this chapter. Both stratiform and anvil flashes seem to have greater strengths than primarily convective flashes over coastal regions. This result is not as strong, however, given the relatively small sample size for coastal and anvil flashes.

Figure 4.6 shows the mean negative fractions of different categories of flashes over land and coastal regions. Negative NLDN strokes account for 40–60% of LIS flashes with high stratiform fractions over land and coastal regions, compared to 70% for mostly convective flashes and more than 90% for mostly anvil flashes. Positive polarity stratiform flashes are well known (e.g., Rutledge and MacGorman 1988), so it is not surprising that primarily stratiform flashes are the most likely category to be associated

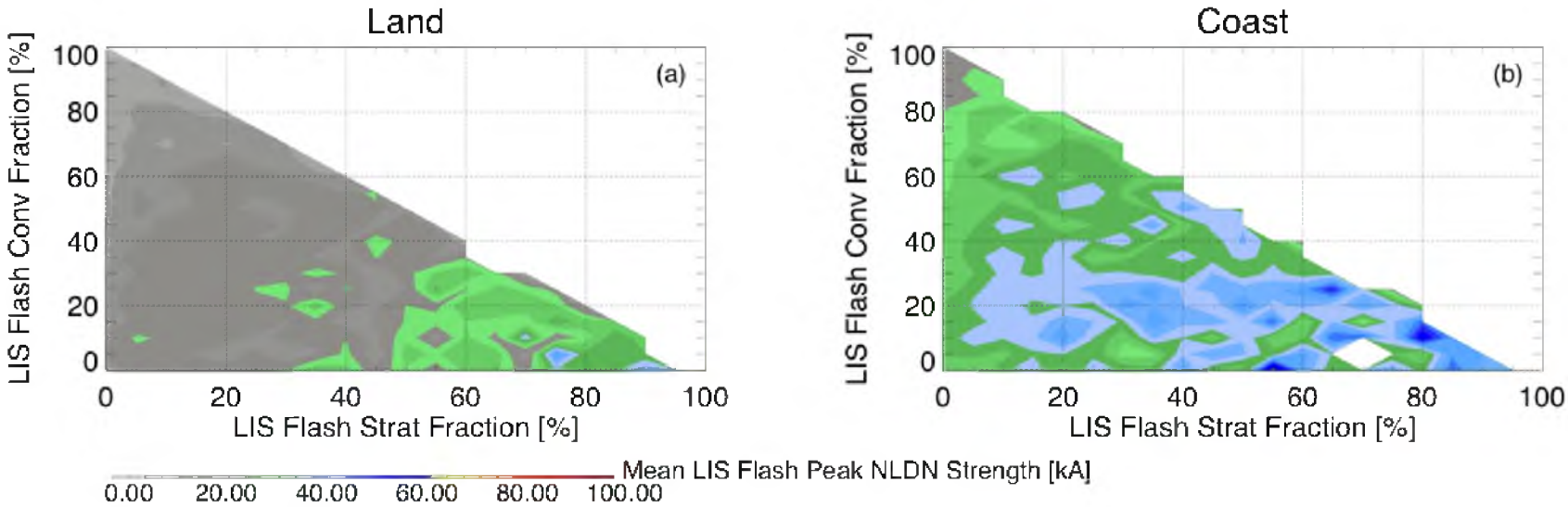

Fig. 4.5. Mean collocated NLDN strengths for flashes categorized by LIS flash footprint convective fraction (y axis) and LIS flash footprint stratiform fraction (x axis) plotted for each terrain type.

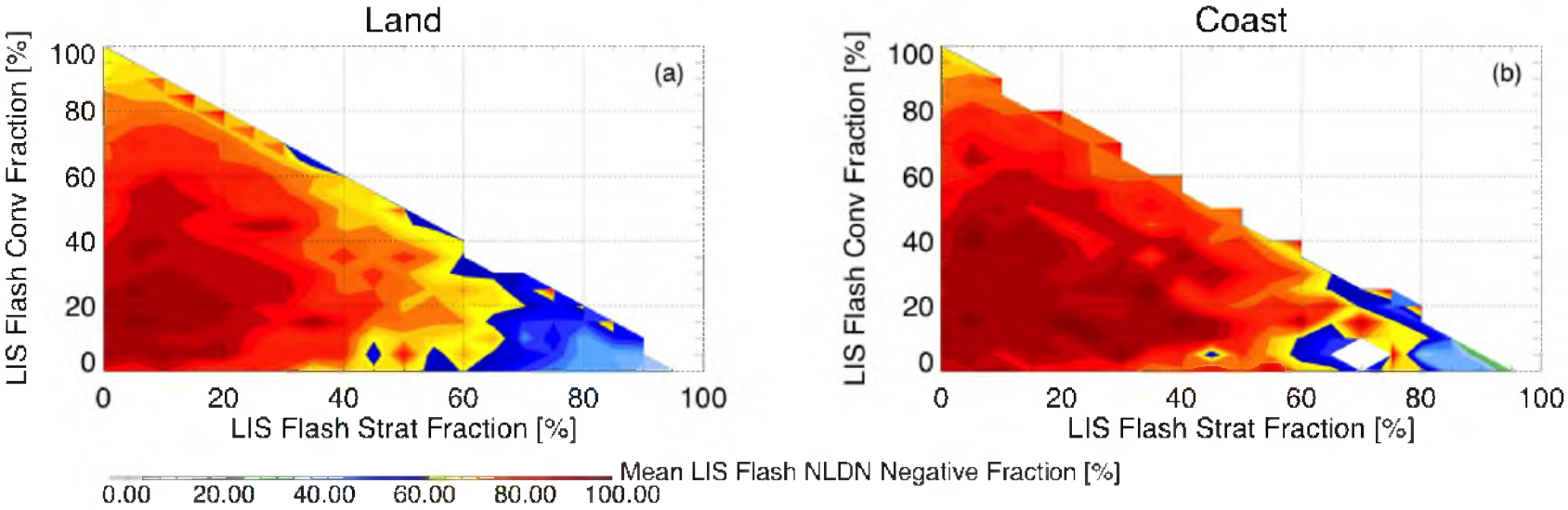

Fig. 4.6. Mean collocated NLDN negative stroke fraction for LIS flashes categorized by footprint convective fraction (y axis) and footprint stratiform fraction (x axis) plotted for each terrain type.

with positive lightning.

4.2 An NLDN Perspective of Exceptionally Bright Flashes

In the previous chapter, flashes with highly radiant pixels were proposed to be the result of flashes occurring right at the edge of convective regions, possibly interacting with anvil charge, and so-called upward lightning in the terminology of Krehbiel et al. (2008) that includes bolts from the blue, which are thought to initiate via the same processes as upward lightning. While it is impossible to determine with certainty that these types of flashes are responsible for the extreme flash statistics, it may be possible to use NLDN parameters to determine whether upward discharges *could* be involved and, if so, which types of upward discharges are most consistent with the statistics.

Typical thunderstorms acquire a slight negative charge imbalance, but in the instants after a negative CG stroke lowering negative charge to the ground, the charge imbalance switches to positive, enhancing the electric fields in the upper levels of the storm. If charging continues, then the electrical potential can become strong enough to initiate positive discharges out the top of the storm. Three types of upward lightning phenomenon are studied in Krehbiel et al. (2008): blue jets, gigantic jets, and bolts from the blue. Their modeling results indicate that blue jets occur as a result of an electrical breakdown between the uppermost charge region of a thunderstorm and the screening layer immediately above the cloud top. Gigantic jets, in contrast, begin as normal upward-directed IC lightning flashes between the midlevel charge region and an upper level charge region without a corresponding screening layer above, allowing the discharge to continue out the top of the cloud.

Bolts from the blue are thought to start off in the same way as gigantic jets in normally electrified storms, but instead of the negative breakdown propagating through the upper level positive charge region and out the top of the storm, the breakdown exits the side of the cloud and is redirected downward, terminating at the surface. Bolts from the blue can strike targets dozens of kilometers from the parent storm and, for that reason, can be particularly dangerous. According to their simulations, this can occur when the upper level charge layer is depleted with respect to the midlevel charge layer, and a screening layer of inferred positive charge is present along the side of the thundercloud to "guide" the negative breakdown channel back down towards the ground. In the absence of a lateral positive screening layer, bolts from the blue would continue upwards to form gigantic jets (Krehbiel et al. 2008).

It is reasonable to expect that these features might show up in the LIS dataset at some level since gigantic jets at least are relatively common in tall convective towers in the tropics (Pasko et al. 2002), but since they occur by and large outside of the cloud layer, it is difficult to imagine how they might be identified. Lyons et al. (2003) include numerous photographs of blue jets that appear as bright streamers out the tops of ordinary thunderstorms. These discharges are substantially brighter than their adjacent cloud layers, though multiple examples have illumination below the cloud top from the in-cloud section of the breakdown channel. Each of these pictures was taken from the ground, allowing the observer to see the vertical extent of the event. If a jet like these were observed by LIS, the picture would be much different. The jet would be represented by a single bright dot in the middle of a broader illuminated region if viewed from above, resulting in extreme radiance ratios not seen in other types of flashes. The major issue

with hypothesizing that jets could be consistent with flashes that explain these statistics is whether they would be observed by LIS. Blue jets are named for their signature color, and it remains to be seen whether they would emit strongly enough at 777.5 nm to be detectable by LIS. However, blue jets are not the only phenomena that might be consistent with these trends. Any electrical event that propagates out the top or side of the cloud could be characterized in the same way, including bolts from the blue, cloud-to-air discharges, and lightning superbolts (Turman 1977). Using what is known about these types of upward discharges, it may be possible to use NLDN observations to test whether this idea could explain these statistics or if extremely bright flashes are just the result of regular lightning flashes that are near the edge of convection.

Figure 4.7 shows the overall distribution of LIS collocated flashes in the LIS-NLDN dataset characterized by flash illuminated area and max:min radiance ratio for land and coastal flashes. As before, most collocated LIS flashes are rather small and have relatively low radiance ratios, but the overall shape of the distribution can be characterized by the same two branches: a lower branch along the x-axis, representing dim flashes of varying sizes, and an upper branch along the upper boundary of the distribution representing the brightest flashes for a given illuminated area. There are also differences in the distributions between land and the coastal ocean as observed previously, with coastal flashes being more likely to have large illuminated areas. However, since diurnal sensitivity is not taken into account in this figure, this is due to both coastal ocean flashes being larger by nature and the effect of LIS sensitivity on observed flash illuminated area.

Average collocated NLDN strengths are shown in Fig. 4.8. As before, there is a

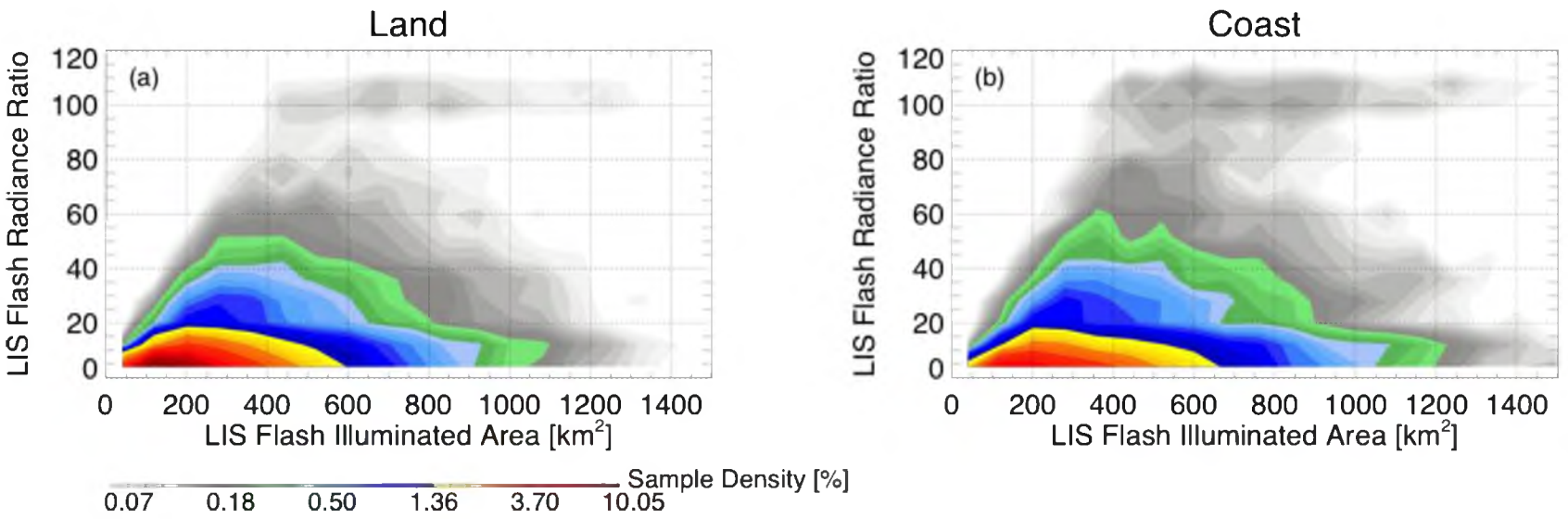

Fig. 4.7. Two-dimensional histograms of collocated flashes categorized by LIS flash illuminated area (x axis) and LIS flash event max:min radiance ratio (y axis) plotted for each terrain type.

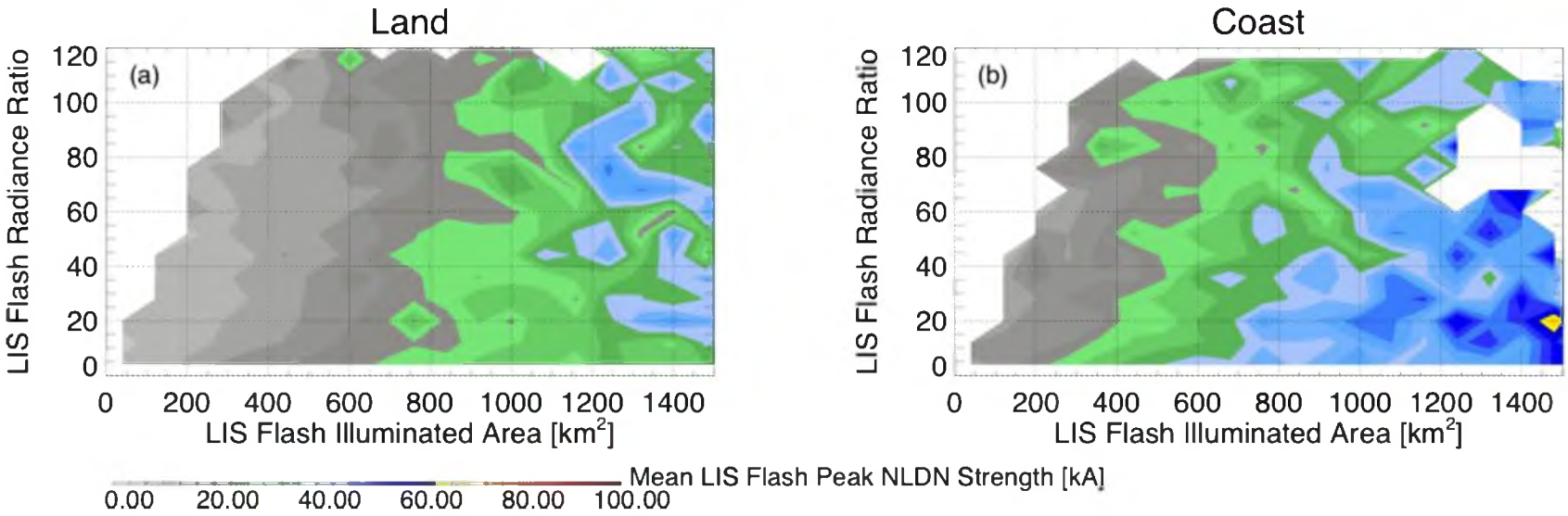

Fig. 4.8. Two-dimensional histograms of collocated flash peak NLDN strength categorized by LIS flash illuminated area (x axis) and LIS flash event max:min radiance ratio (y axis) plotted for each terrain type.

distinct horizontal gradient in NLDN strength between small flashes with mean strengths of 20 kA and large flashes with NLDN strengths nearing 40 kA over land and 60 kA over the coastal ocean. NLDN strength is not a strong function of radiance ratio as it is for illuminated area, but there is some tilt to the contours for coastal flashes, though not over land. Of course, coastal flashes may be subject to some bias induced by the diminishing detection efficiency offshore, and the sample sizes of these bins are relatively small, so this may not be a real trend. Particularly bright flashes are not particularly different than flashes with lower radiance ratios in this figure, however. Suspect upward discharges in this sample would not be dramatically stronger or weaker than typical flashes, if they were present in these statistics.

Figure 4.9 shows the mean fractions of single-stroke flashes in each bin of the distribution. Particularly dim flashes along the lower branch of Figs. 3.26 through 3.29 in the nomenclature of the previous chapter are usually not single-stroke flashes. Up to 80% of these flashes are multistroke IC flashes, regardless of illuminated area. In fact, large lower branch flashes are probably examples of spider lightning, given their size and relatively low radiance. In contrast, extremely bright upper branch flashes are typically single-stroke flashes. These could be CG or IC flashes since all CG flashes are single-stroke and 40% of IC flashes are single-stroke. However, given the NLDN bias towards detecting CG flashes, upper branch flashes are probably either CG flashes (including bolts from the blue) or the upward discharge analog of CG flashes (blue jets and gigantic jets). If these flashes are mostly CG flashes, then these results would favor upward discharges over anvil flashes and boundary convective flashes, which could both be types of IC flashes. Unfortunately, CG/IC NLDN partitioning is not available for enough of the

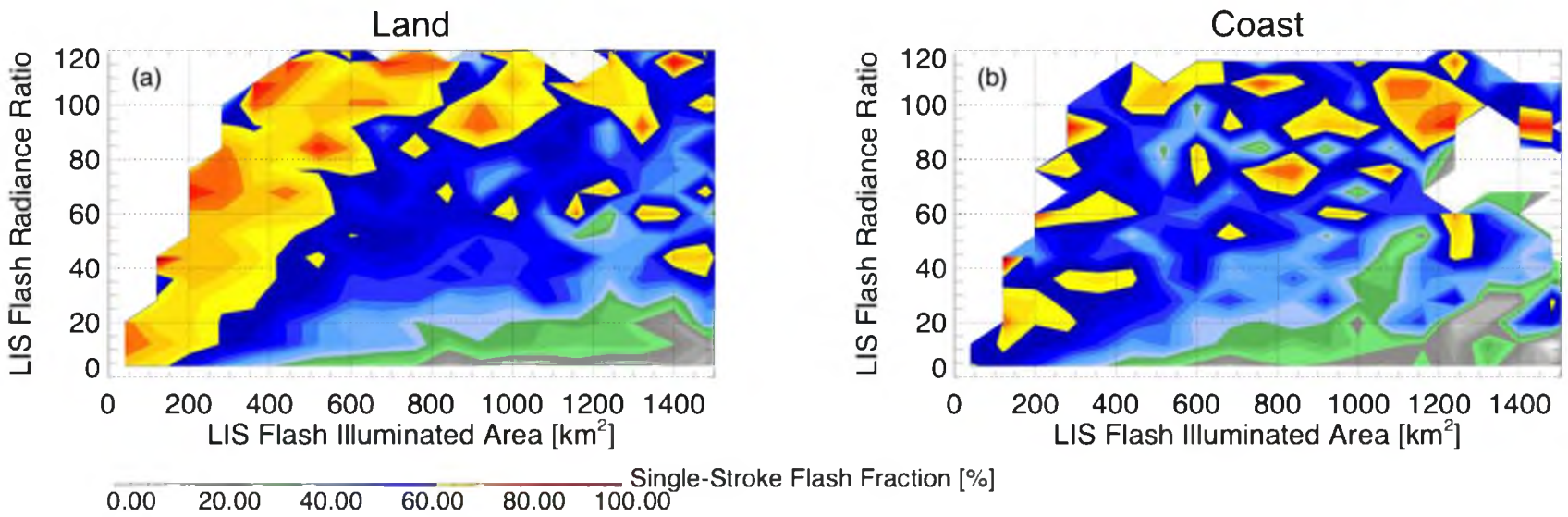

Fig. 4.9. Two-dimensional histograms of the fractions of single-stroke collocated NLDN flashes categorized by LIS flash illuminated area (x axis) and LIS flash event max:min radiance ratio (y axis) plotted for each terrain type.

collocated sample to be able to make such a claim.

Finally, Fig. 4.10 shows the fraction of negative flashes in each bin. As with the previous figure, there is a distinct contrast between the brightest and dimmest flashes. Particularly dim lower branch flashes are mostly negative lightning flashes, despite being largely stratiform flashes. This is consistent with spider lightning flashes, which occur near the end of the life cycle of a storm when the polarity of the storm is inverted (Mazur et al. 2012). On the other hand, brighter upper branch flashes are much more often to be of positive polarity than typical lightning flashes, indicating that the upper region of positive charge is accessed more frequently, as it would be with positive blue jets (Krehbiel et al. 2008). With the exception of the top of the figure where sample size is an issue, nearly half the flashes in the upper branch are positive and half are negative. This means that if this branch contained mostly upward discharges, both positive (blue jets) and negative (bolts from the blue, gigantic jets) could be accounted for in these statistics. However, without a better way of examining these flashes in this current study, there is not much more that can be said other than that it makes sense that flashes with particularly bright pixels could be upward or extracloud discharges, but more information is needed to verify that this is the case or whether typical flashes that illuminate the cloud region in particular ways is to blame.

4.3 Summary

In this chapter, the properties of NLDN strokes collocated with LIS optical flashes were used to examine whether the breakdown properties of lightning play a role in determining the optical properties of flashes, to verify the unique properties of

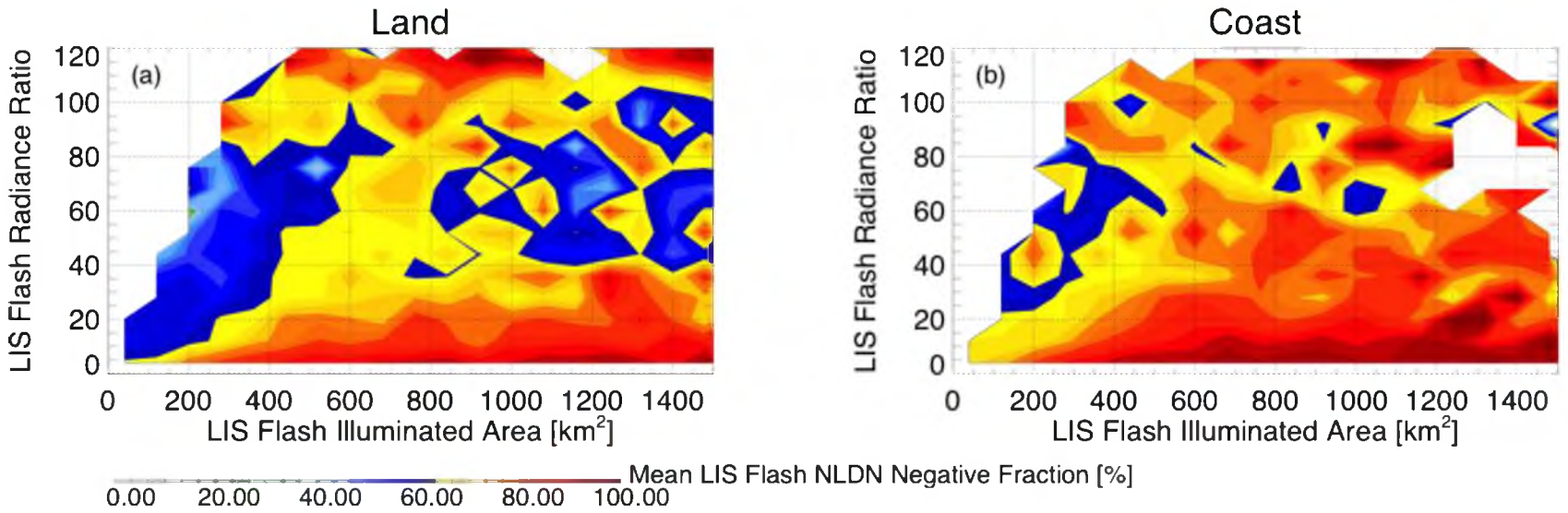

Fig. 4.10. Two-dimensional histograms of the fractions of negative collocated NLDN flashes categorized by LIS flash illuminated area (x axis) and LIS flash event max:min radiance ratio (y axis) plotted for each terrain type.

stratiform lightning, and to look into what makes lightning flashes with exceptionally radiative events unique. Breakdown strength was shown to vary with the illuminated area of the flash, but not any of the other optical properties outside of the maximum radiances of extreme event radiance cases. CG flashes were shown to be small, bright, and short-lasting while IC flashes were shown to be comparably large, dim, and slightly longer lasting. The illuminated area of IC flashes (and not necessarily CG flashes) may be a predictable function of breakdown strength, but more data are needed to verify this trend. Stratiform flashes were shown to have positive polarities more often than any other categories. Finally, the electrical properties of extreme event radiance flashes were examined, and particularities of exceptionally bright flashes may be indicative of upward discharges, but additional work is needed to clarify this result. However, it may be possible to classify some examples of spider lightning using these results.

CHAPTER 5

RELATIONSHIPS BETWEEN OBSERVATIONS OF ELECTRIC FIELDS AND MICROWAVE BRIGHTNESSES TAKEN OVER ELECTRIFIED CLOUDS

The final chapter of this study looks at observations of electric fields over charged clouds that perform an essential charging function of the Global Electric Circuit (GEC; Williams et al. 2009). The goal of this chapter is to use collocated observations of high-altitude electric fields taken above electrified clouds by the Lightning Instrument Package (LIP) and microwave brightness temperatures observed by the Advanced Microwave Precipitation Radiometer (AMPR) to study the driving force of the GEC and see if it is possible to reconstruct electric fields above electrified clouds using only microwave observational proxies.

The basic principle behind this potential relationship is that ice plays a key role in cloud electrification (Takahashi 1978). Since 37 GHz and 85 GHz passive microwave observations are sensitive to column-integrated ice water path (Vivekanandan et al. 1991), the stronger the microwave signal (brightness temperature depression), the more ice that is present, the more collisions there may be to initiate charge separation, and the stronger the observed electric field may be. If such a relationship between uncommon high-altitude aircraft observed electric footprints of charged clouds and common passive microwave observations could be found, an algorithm could be developed to derive the

electrical characteristics above storms around the world using satellite measurements such as from the TRMM TIMI, making it possible to quantify the Wilson current "batteries" of the GEC with more detail than previous studies (e.g., Blakeslee et al. 1999; Bailey et al. 2007; Williams 2009; Liu et al. 2010; Mach et al. 2011).

This chapter is divided into three sections. First, coincident observations of aircraft-level electric fields and AMPR observations will be discussed. Then, a method for finding such a relationship will be proposed. Lastly, the performance of this algorithm will be assessed for a number of cases.

5.1 Collocated LIP and AMPR Observations

The collocation of LIP and AMPR observations is not simple. Each dataset has a different series of caveats, including aircraft behavior, missing data, and artifacts, which can significantly bias the resulting combined dataset. The intricacies of the collocation routine employed in this study are described in detail in Chapter 2. Perhaps the most important step in preparing the sample is the removal of LIP artifacts. Since the focus on this study is looking at the quasi-steady state electric fields of electrified clouds, electric field spikes from lightning flashes and other sources such as aircraft charging must be removed from the record so that only storm-induced perturbations remain.

Figure 5.1 shows the microwave brightness temperatures at 37 GHz and 85 GHz of a convective system over land observed in the Brazilian Amazon as part of TRMM-LBA (a,b) and the change in the electric field caused by the storm as at the aircraft location as the NASA ER-2 aircraft flew overhead (c,d). This is a particularly useful case since the AMPR's limited 30–40 km swath width captured the entire system, the aircraft

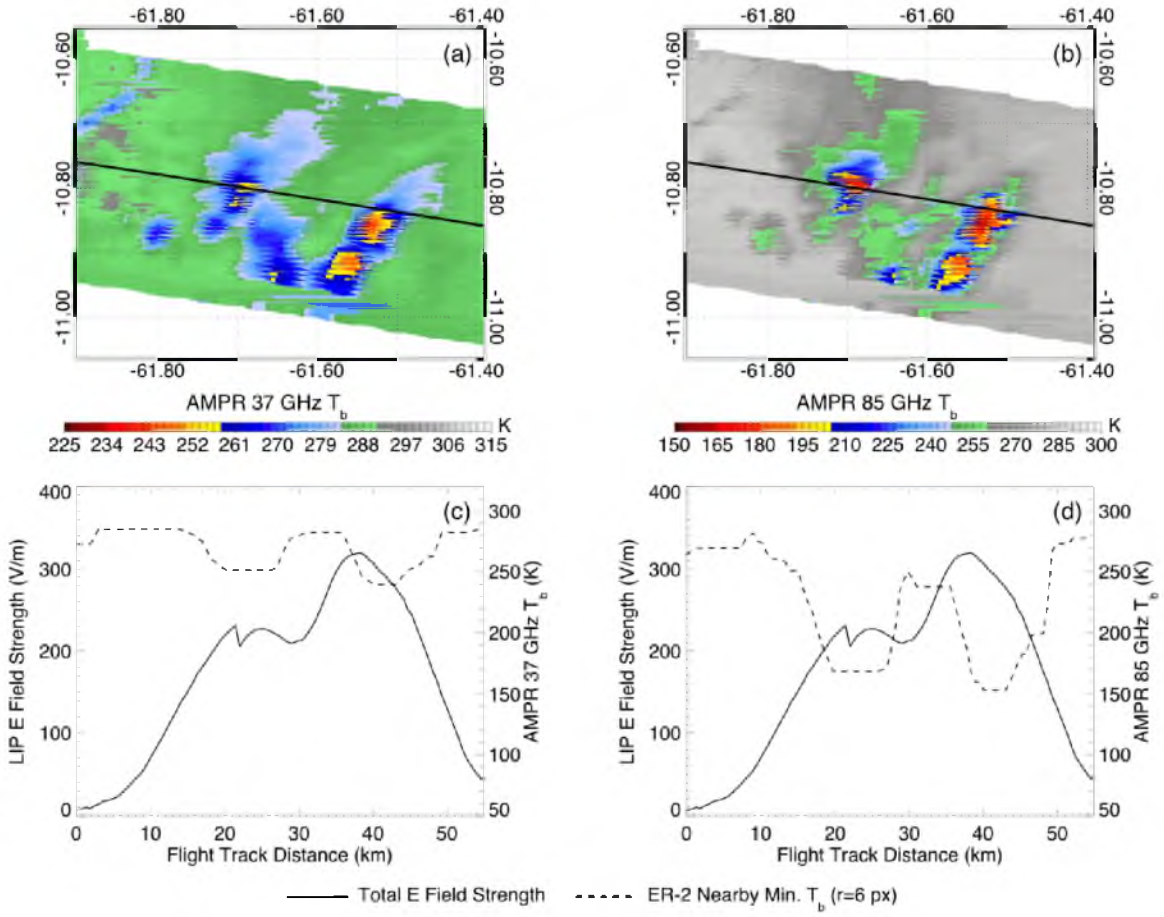

Fig. 5.1. AMPR observations above a storm over land. AMPR 37 GHz (a) and 85 GHz (b) brightness temperatures (contour) are shown as well as the ER-2 flight track (solid line). Nearby minimum 37 GHz (c) and 85 GHz (d) brightness temperatures relative to the ER-2 flight track and LIP-observed total electric field strength are also shown.

is flying level at cruising altitude and not turning, there is no interference from lightning, and there are no missing datapoints in the record. Many other cases suffer from one, if not multiple, of these caveats, making it necessary to take care when looking for relationships between AMPR and LIP observations.

In this case, as the aircraft approaches a convective region (illustrated in the top two panels by the black line of the ER-2 flight track and the bottom two panels as the distance along that track), the resulting drop in observed brightness temperatures is accompanied by an increase in the observed LIP electric field strength. As the aircraft approaches the first cell, the 37 GHz minimum AMPR brightness temperature within 6 pixels of aircraft nadir drops to around 260 K as the observed electric field strength increases to 235 V m^{-1}. Between cells, the brightness temperatures increase and the electric field decreases before approaching the second convective region, where the electric field increases once more as the brightness temperatures once again fall. The same trend occurs with 85 GHz observations in panel (d).

From this case, alone, it would seem that there is something to this idea that passive microwave brightness temperature valleys and LIP electric field peaks may be related, and that finding a statistical relationship between AMPR and LIP observations may be straightforward. However, not all cases are as clear as the one shown in Fig. 5.1. Figure 5.2 shows a completely different case, observed off the coast of Costa Rica during TCSP when the ER-2 was flying over a mature and dissipating, yet still electrically active nocturnal MCS. The most striking feature of this case is that the color scale appears to be inverted at 37 GHz (Fig. 5.2a). This, however, is no error in the plotting program RGB table. Even though 85 GHz observations (Fig. 5.2b) appear to be normal and 37 GHz

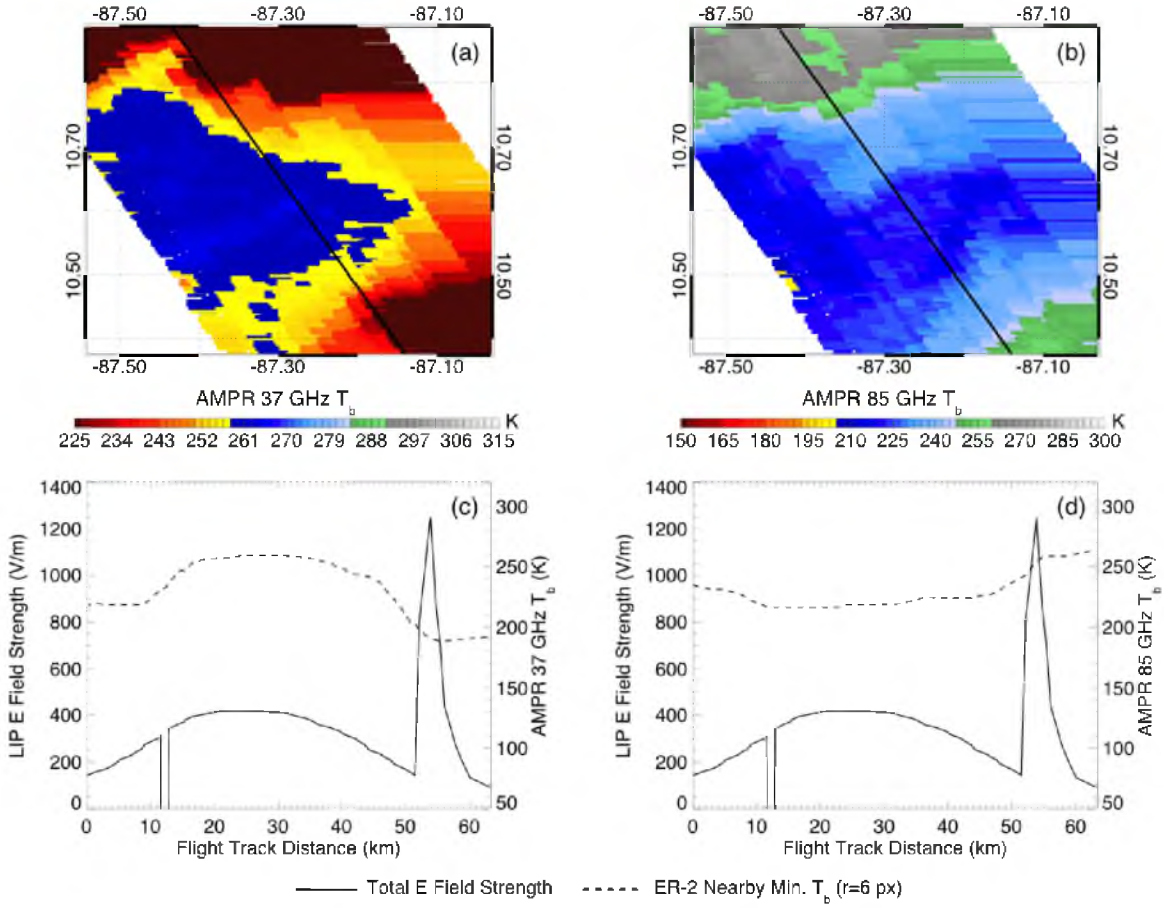

Fig. 5.2. AMPR observations above an offshore electrified cloud. AMPR 37 GHz (a) and 85 GHz (b) brightness temperatures (contour) are shown as well as the ER-2 flight track (solid line). Nearby minimum 37 GHz (c) and 85 GHz (d) brightness temperatures relative to the ER-2 flight track and LIP-observed total electric field strength are also shown.

looks fine over land in Fig. 5.1a, 37 GHz brightness temperatures see the ocean as extremely cold. This is a caveat that is not seen when looking at TRMM data since Polarization Corrected Temperatures (PCTs) filter out this effect using both the horizontal and vertical polarizations combined. However, AMPR does not have dedicated observations for each polarization, making such a simple solution fleeting, at best.

This is not the only issue with the case in Fig. 5.2, however. Unlike the land case in Fig. 5.1, which showed some small, convective features, in this case the ER-2 flew over a broad and ambiguous cloud region that may be more stratiform in nature and is considerably larger than the AMPR swath. Despite a lack of obvious convection at 85 GHz, this overpass saw a broad region of electric fields exceeding 400 V m^{-1}, almost 100 V m^{-1} greater than the peak electric field in the previous case. Not only that, but there is a small region of missing LIP data early on in the event and an unexplained spike up past 1,200 V m^{-1} near the end of the overflight. Since this spike occurs as the aircraft is leaving the cloud region and there are no strong convective features anywhere within the swath that could explain that sudden event, its presence must either be due to a very strong connective region outside the swath (very unlikely due to the relatively small duration over which it has an effect on the observed electric field, but definitely an issue for other cases), contamination from lightning that the lightning removal algorithm was unable to filter out, or an artifact in the data collection system. The latter two are possible since the algorithm only looks for short duration oscillations in the observed electric field. If a lightning flash is particularly long lasting or many flashes occur in rapid succession or the flash is far enough away so that the resulting oscillations are not strong enough, there is a chance that the algorithm will consider it to be an "electrified cloud

feature" and skip over it.

Of these issues, perhaps the greatest obstacle to constructing a method of modeling LIP electric fields using AMPR observation is the land/ocean issue. Passive microwave brightness temperature depressions become meaningless if the environment looks similar to the most intense convection. Unfortunately, for most of the field campaigns used in this analysis, shown in Table 2.1, most datapoints are taken over offshore coastal regions, while most observations over land—where this effect is not an issue—come from a single field campaign, TRMM-LBA.

These differences between 37 GHz and 85 GHz are particularly prominent in the two dimensional histograms shown in Fig. 5.3 between ER-2 nadir AMPR brightness temperatures and LIP electric field strengths. The 37 GHz distribution, shown in Fig. 5.3a, is separated into two segments: one centered at 170 K and the other centered at 270 K. The former is entirely made up of datapoints over water, and, despite most samples showing observed electrical fields less than 10 V m^{-1} (fair-weather between clouds), the sample does include a substantial number of storm-scale datapoints greater than 100 V m^{-1} that would hinder the investigation. The second maximum, on the right side of the figure, contains both the entire subset of datapoints over land as well as many coastal and oceanic datapoints away from the edges of electrified clouds. Electric fields for datapoints with nadir AMPR brightness temperatures greater than 250 K range from 1 V m^{-1} to more than 1,000 V m^{-1}.

Unlike 37 GHz, the two-dimensional histogram between 85 GHz nadir brightness temperatures and observed electric field strengths does not have a left branch like the one in Fig. 5.3a. In fact, the distribution looks almost like a radar cross-section of a

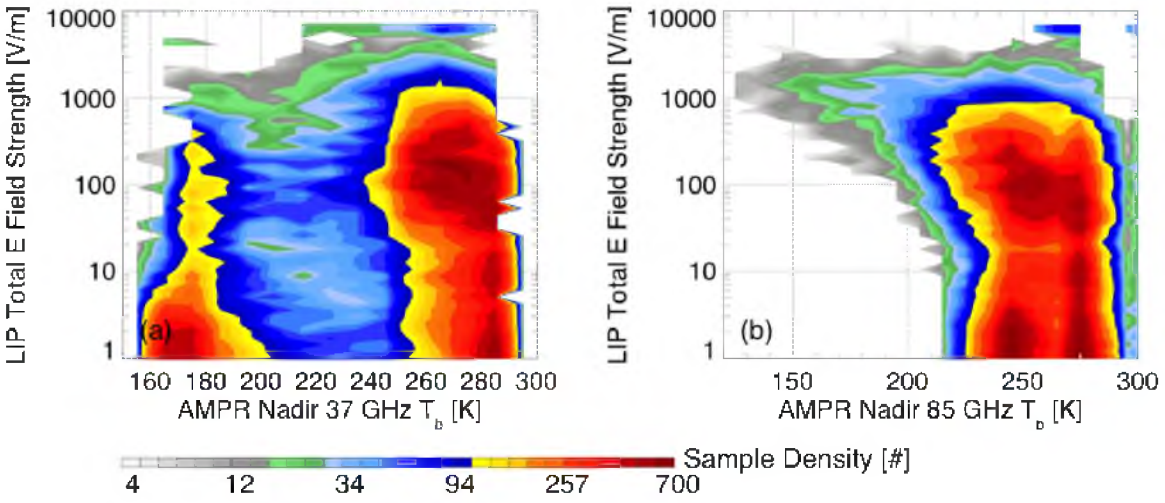

Fig. 5.3. Two-dimensional histogram showing the distribution of datapoints over the coastal ocean with various LIP total electric field strengths and AMPR nadir 37 GHz (a) and 85 GHz (b) brightness temperatures.

convective anvil, with a smaller variance in LIP-observed electric field strength for cold 85 GHz AMPR brightness temperatures than for warmer brightness temperatures. Clouds with 200 K or lower 85 GHz T_bs, for instance, almost always have strong electric fields greater than 100 V m^{-1}, compared to 250 K clouds, which span the entire range of possibilities.

Despite the lack of the "cold ocean" artifact at 37 GHz, land/ocean differences are present in this distribution as well. This can be seen by comparing Fig. 5.4, showing just the AMPR brightness temperature/LIP electric field distributions over land, with Fig. 5.3, showing the general distributions. Unlike Fig. 5.3a, Fig. 5.4a does not have the oceanic left branch and even shows some of the same "anvil" shape that the 85 GHz distribution had in Fig. 5.3b. Also, the bulk of the 85 GHz land distribution in Fig. 5.4b is concentrated towards warmer nadir brightness temperatures compared to the general distribution in Fig. 5.3b. This could very well mean that if there is a relationship between AMPR 85 GHz brightness temperatures and LIP electric field strengths, it may be different between land and ocean, but the complications introduced by ocean backgrounds compared to land make it substantially more desirable to create a land-based relationship, first, and then attempt to adapt it for use over the ocean. For this reason, the search for such a relationship in the next section will begin with land-based data, the bulk of it coming from TRMM-LBA, which will then be validated for the entire sample—land, ocean, and coast, and all four field campaigns.

There is still one aspect that must be addressed before moving on to such a search. Even the land distribution for 85 GHz in Fig. 5.4b shows a substantial range in observed electric field strength for the same AMPR nadir brightness temperature: a 270 K AMPR

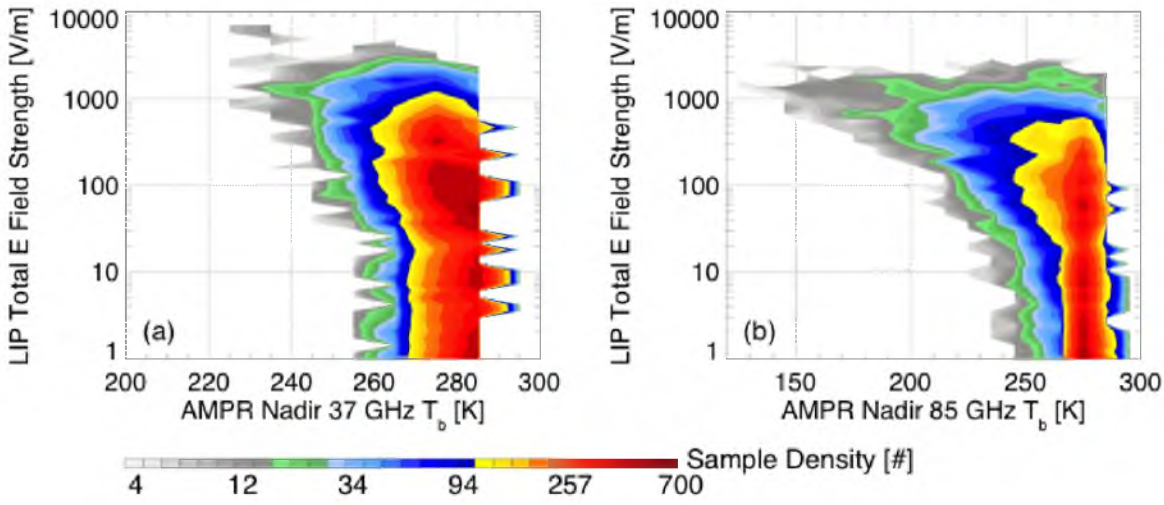

Fig. 5.4. Two-dimensional histogram showing the distribution of datapoints over land with various LIP total electric field strengths and AMPR nadir 37 GHz (a) and 85 GHz (b) brightness temperatures over land.

pixel may occur with a LIP reading of 1 V m^{-1} or 100 V m^{-1} with an almost equal probability. How do we know that it is even possible to relate one parameter to the other? To answer this question, it is important to remember that electric field strength is not just dependent on a single source. That source could mean multiple charged particles, all contributing to the net electric field, or, in this context, multiple AMPR bins filled with charged ice particles influencing the reading taken by the LIP.

In order to demonstrate how nearby AMPR pixels can explain much of this variance, instead of showing a two-dimensional histogram, Fig. 5.5 shows takes the minimum AMPR brightness temperatures of all pixels within 9 pixels of nadir for each datapoint rather than just the nadir observation and then displays the mean value for each bin in Fig. 5.4. For example, for datapoints with nadir 85 GHz brightness temperatures of 250 K and observed electric field strengths of 1 V m^{-1}, the average brightness temperature within 9 pixels of nadir is also close to 250 K. That means that there are no nearby convective sources of charge that could increase the observed electric field for an average pixel located in that bin of the figure. However, moving up to nadir 250 K pixels with 1,000 V m^{-1} observed electric fields, despite the fact that that nadir pixel may read 250 K, on average, there are pixels colder than 180 K within 9 pixels of that datapoint, or, in other terms, convective sources of charge just a few kilometers away, resulting in such a high reading for a relatively warm nadir brightness temperature. This effect results in an overall slanting of the contours in Fig. 5.5. Many of these pixels have much stronger electric fields than their relatively warm brightness temperatures would suggest due to the three-dimensional nature of charging. For this reason, nadir brightness temperature is not a sufficient metric for exploring relationships between AMPR and LIP observations. So,

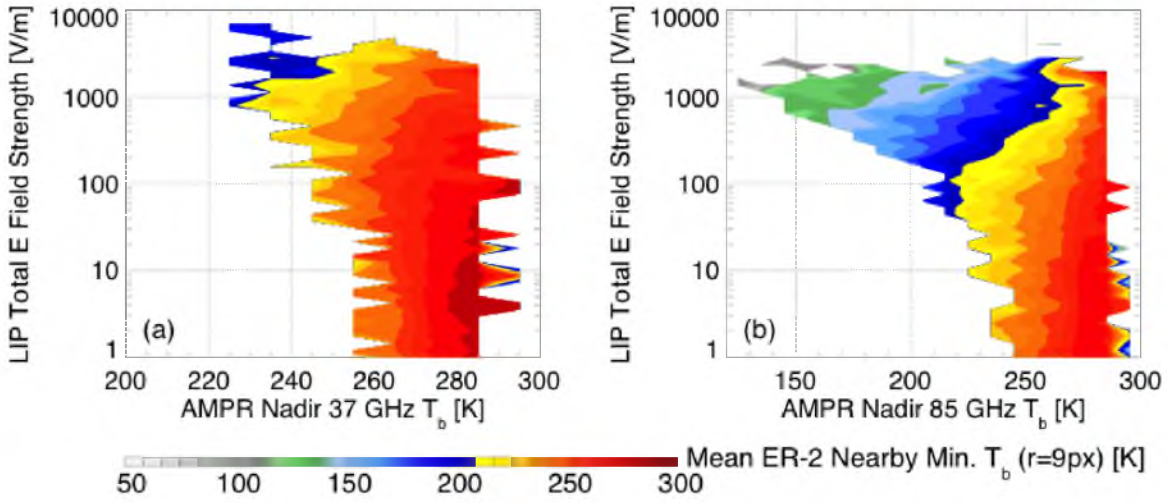

Fig. 5.5. Two-dimensional histogram showing the mean nearby minimum AMPR brightness temperature (within a 9 pixel radius) of datapoints over land with various LIP total electric field strengths and AMPR nadir 37 GHz (a) and 85 GHz (b) brightness temperatures.

what then is a good metric? In order to answer that, it is necessary to consider the fundamental problem at hand.

5.2 Derivation of AMPR Electric Field Proxy

Consider an ordinary thunderstorm with an abundance of ice and supercooled liquid water, such as the one shown in Fig. 5.6. The electrical structure of a mature thunderstorm is quite complex. The noninductive charging mechanism and the storm's internal wind field sets up a complicated three-dimensional electrical structure within the storm, consisting of pockets of sizable amounts of positive and negative charge. Complicating things further, this accumulation of charged particles within the heart of the storm leads opposite polarity ions to gather along its boundaries, resulting in the development of significant screening layers along its flanks. The resulting accumulation of charge might end up looking something like in Fig. 5.6.

Estimating the electric field at any location inside or even nearby a storm like this would be no easy task, as every charged particle—every piece of graupel, every raindrop, every piece of dust—contributes to the net electric field at a given location following Coulomb's law. Each charged particle depicted in the Fig. 5.6 insert would contribute

$$\left|E_i(Q_i, r_i)\right| = \frac{k_e|Q_i|}{r_i^2} \tag{5.1}$$

to the net electric field (E_i) at an arbitrary point, where Q_i is the charge on each particle, r_i is its distance from the observer and k_e is Coulomb's constant. The overall net electric field can be determined by summing over each of these charge source contributions in

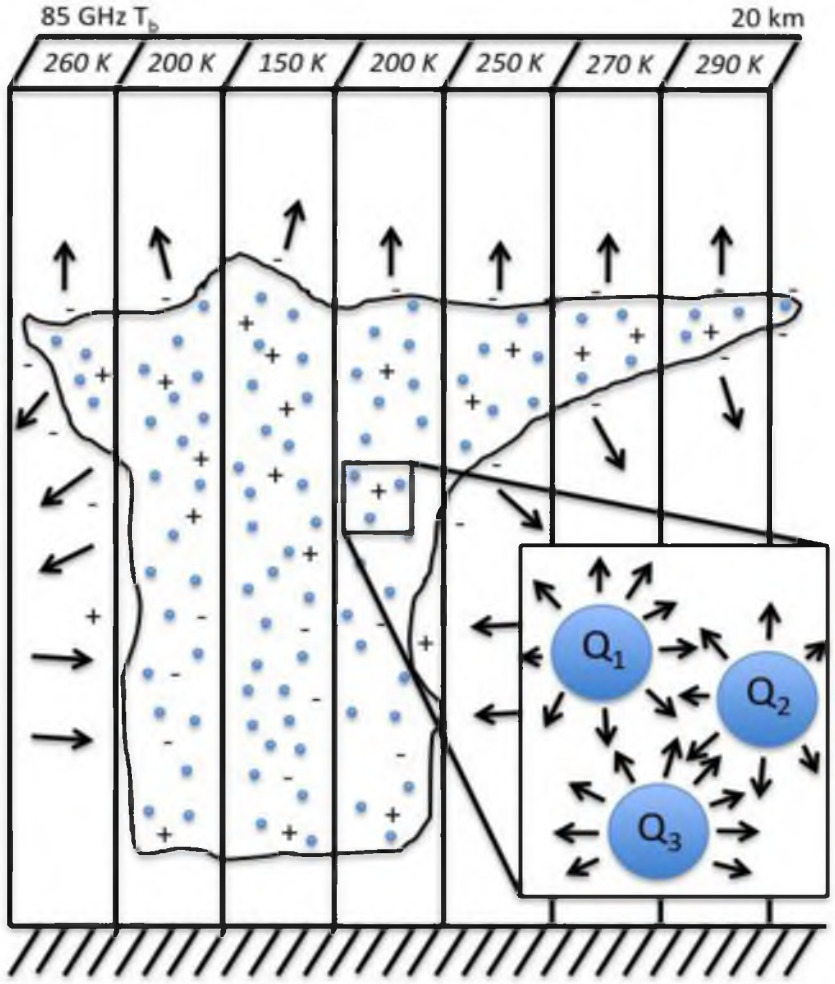

Fig. 5.6. Conceptual diagram of the electrical structure and 85 GHz brightness temperatures of a thunderstorm as well as the net electric field along its perimeter.

three-dimensional space. As it flew around the boundaries of a storm, a remote controlled plane carrying a test positive charge might feel a force outward as it rose up under the anvil, inward as it passed by the middle region of negative charge, downward as it flew below the anvil, and upward as it flew above the storm, following the arrows indicating the net electric field vector orientations.

Microwave brightness temperatures at 37 GHz and 85 GHz may indicate the abundance of ice, but they are, by nature, column integrated values. It would be impossible for any AMPR overflight to derive the three-dimensional electric field throughout the storm. The 85 GHz brightness temperatures listed across the top of the figure reduce the distribution of charged ice particles throughout the storm structure in Fig. 5.6 to just one number that characterizes the amount of ice in each column, but this is not necessarily a problem. If there is significant distance between the storm and the observer, the intricacies of the small-scale electric field variations become less important, and the net effect is all that really matters.

If the storm in Fig. 5.6 is observed from far enough above, its effective electrical structure seen from above can be simplified to that of Fig. 5.7, consisting of a single charge source in each bin that characterizes the net charge of all of the charged particles within that column. Unlike the previous figure, Fig. 5.7 shows electric field orientations and relative strengths at the aircraft location. Since Wilson currents rely on only the charge available for interacting with the ionosphere above, not charge participating in internal processes within the cloud or interacting with the ground, this "black box" view of an electrified cloud from above is consistent with the goals of this chapter in creating a method of studying this driving force of the GEC. Assuming that the amount of ice is

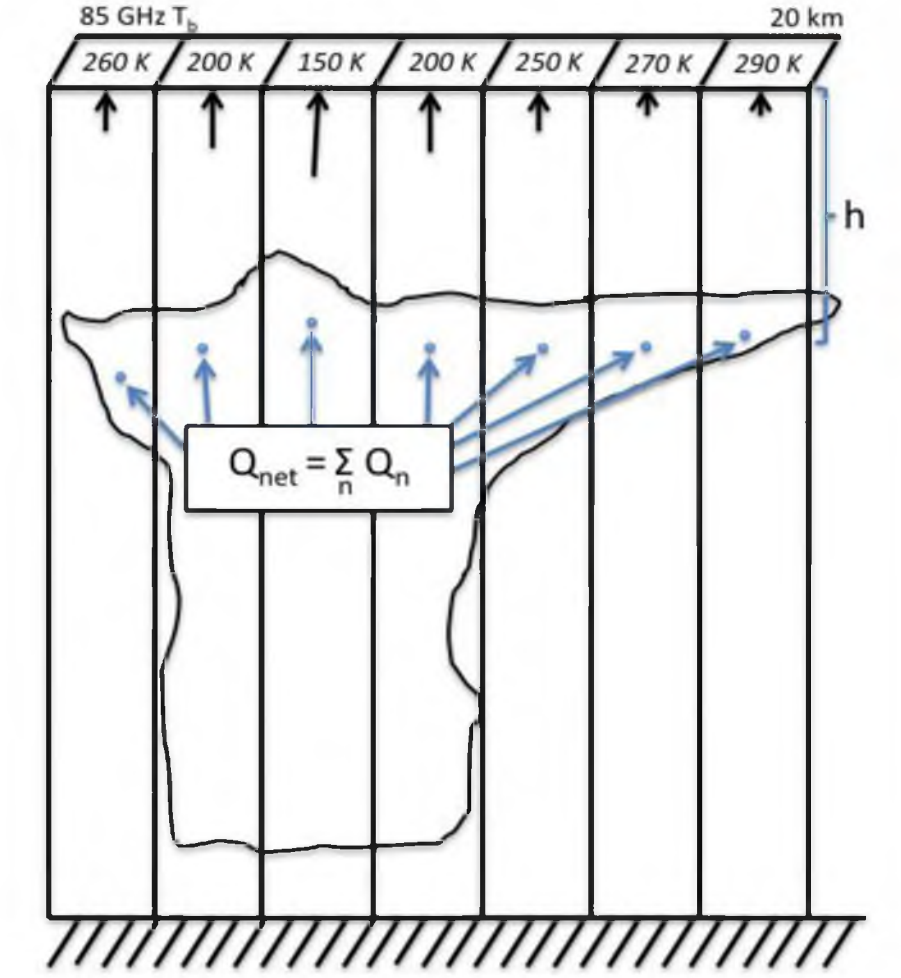

Fig. 5.7. Conceptual diagram of the net electrical structure as seen from above and 85 GHz Tbs of a thunderstorm as well as aircraft-observed electric field vectors.

the limiting factor in charge generation in this scenario and that the effective amount of charge available to produce Wilson currents for a given concentration of column ice is predictable following some distribution and that this charge region can be represented by some effective height, it may be possible to characterize this relationship using real-world microwave brightness temperature and electric field observations.

In terms of ER-2 observations, such an approach would characterize the most relevant charge region for generating Wilson currents as a distribution of individual net charges at each bin in the AMPR domain. Relative quantities of ice and charge can be approximated using AMPR brightness temperatures, while the distances of each charge relative to the aircraft can be calculated using the geospatial coordinates of each AMPR bin. This information can then be fed into Coulomb's law in order to derive a proxy for the total electric field vector induced by the overflown cloud. However, while the horizontal locations of each of these net effective charges are known, the vertical distance between the effective altitude of the relevant charge layer and the aircraft (h in Fig. 5.7) is not. Previous studies have assigned constant altitudes for each charge layer within a thunderstorm (Driscoll et al. 1992; Mach et al. 2009), but this method does not take into account variations in storm height and intensity. For example, a 15 km upper level charge layer height makes no sense for a shallow oceanic system that is only 12 km tall. While this method may be satisfactory for statistical studies, it can lead to substantial errors when trying to recreate electric fields above individual electrified clouds due to Coulomb's law's r-squared relationship.

A slightly better method would be to choose an effective charge height that is a function of the microwave brightness temperature at a given location. This approach

would be able to satisfy convective cells with differing convective strengths. TRMM observations are once again used to create such a relationship. Figure 5.8 shows two-dimensional histograms between coincident PR and TMI measurements, but with a few additional assumptions. First, the effective charge height is assumed to be the 30 dBZ echo top height. This is completely arbitrary, and likely incorrect in some circumstances, but it does yield a decent range of heights that make sense for this algorithm. The second assumption is that brightness temperatures and PCTs are interchangeable. This is not exactly true, but since both parameters vary over similar ranges (and since PCTs are valid over land and ocean), this assumption is also helpful for the purposes of creating this algorithm. Finally, the third assumption is that the median 30 dBZ echo top height is representative of most instances of an observed coincident PCT of a certain value. In reality, there is a significant amount of variance in these observations from convective, stratiform, and anvil clouds, isolated convection, MCSs and hurricanes, et cetera, and the median only represents a small fraction of these scenarios.

These three assumptions lead to the creation of lookup tables for effective charge height from observed values of microwave brightness temperatures for each terrain type and frequency of interest shown as black lines in Fig. 5.8. Each line runs from low effective charge heights of around 6–8 km for warm observed brightness temperatures to over 14 km for the strongest convective pixels. Variations between these two extremes are roughly described as a linear relationship for 85 GHz observations and a logarithmic relationship for 37 GHz. These distributions highlight the substantial potential for error in these estimates. Even though there are many pixels over land with 15 km echo top heights and 250 K 85 GHz PCTs, the lookup table will always yield effective charge

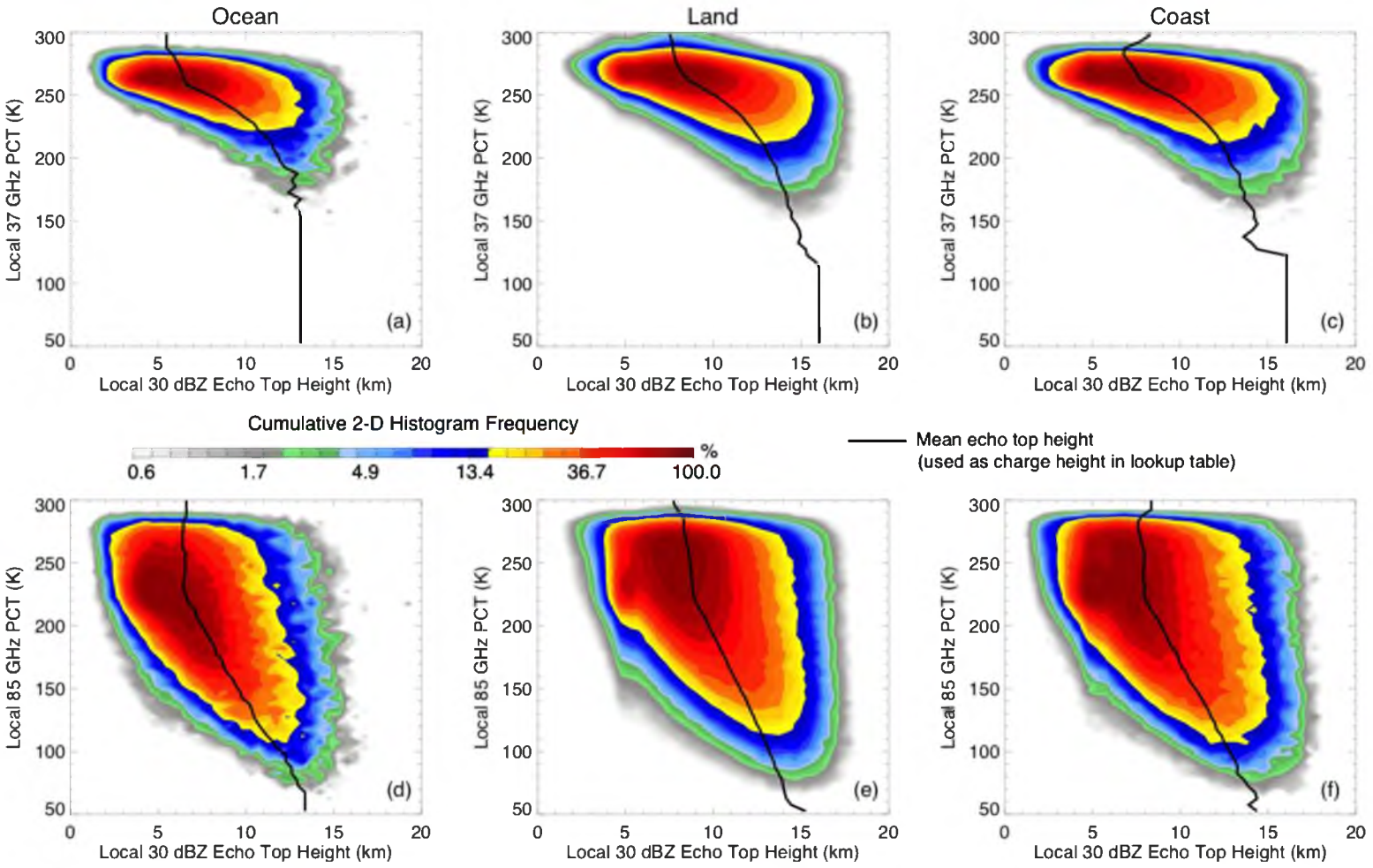

Fig. 5.8. Two dimensional histograms of TRMM PR 30 dBZ echo top height and coincident 37 GHz PCT (a,b,c) and 85 GHz PCT (d,e,f) for land, ocean, and coastal regions across the globe. The lookup table for charging height from AMPR Tb is drawn as a solid line based on the median 30 dBZ echo top height for a given PCT and terrain type.

heights of just 6 km. Based on the range of values, these relationships are likely most often valid for convective cores and least representative of stratiform or nonraining anvil regions. Future work will seek a better lookup table, perhaps by classifying the dominant precipitation type, but these assumptions at least give a starting point for determining the validity of such an approach in creating an algorithm that can predict electric fields from passive microwave observations.

Once the locations of the net charge sources relative to the aircraft are known, approximating the electric field vectors observed by the aircraft at each point becomes possible through a straight-forward integration using Coulomb's law. This process is shown in the schematic diagram in Fig. 5.9, which is an expanded version of Fig. 2.3. Starting from where Fig. 2.3 left off, the algorithm takes the collocated AMPR-LIP dataset and the new TRMM-based effective charge height lookup table and works to create the AMPR Electric Field Proxy variable (EFP), which is defined throughout the AMPR domain. EFP values for AMPR datapoints at aircraft nadir are then tuned to actual electric field strengths observed by the LIP using a statistical model. Estimated electric fields tuned to observations are then calculated for the entire AMPR domain, culminating in a reconstruction of the entire electric field footprint of electrified clouds.

Since observations of cloud charge content are not available, it is necessary to examine charge accumulation using a proxy variable that may relate to charge accumulation. Using the previously described line of reasoning, passive microwave signals at 37 GHz and 85 GHz are assumed to be related to charge accumulation, such that

$$\left|Q_{net\ i}\right| = f\left(T_{b\ i}\right) \tag{5.2}$$

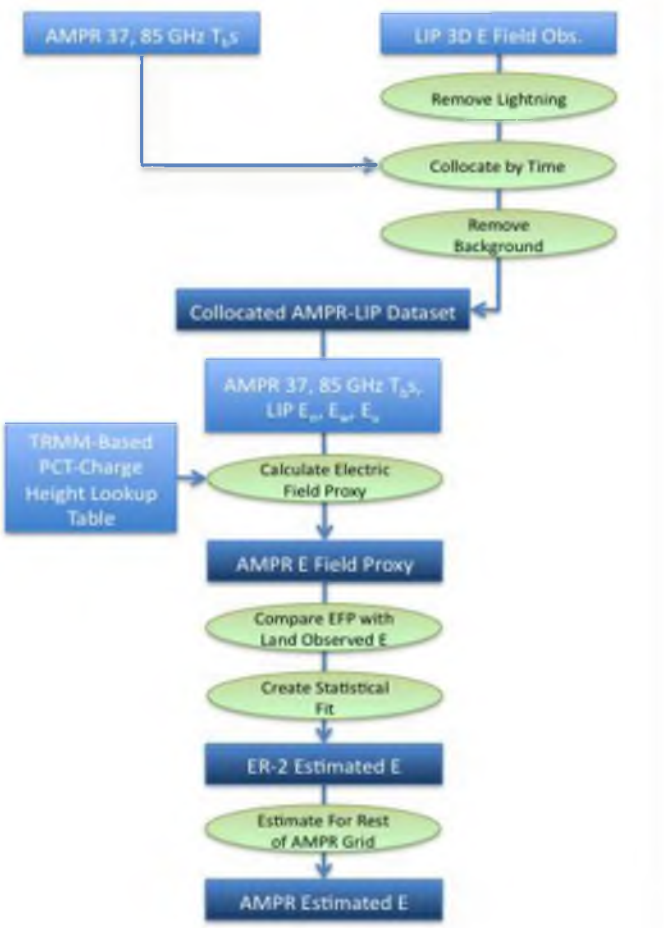

Fig. 5.9. Schematic diagram of AMPR/LIP data processing resulting in AMPR Estimated Electric Fields.

where $Q_{net\,i}$ is the net charge content of the *i*th AMPR bin and $T_{b\,i}$ is the 37 GHz or 85 GHz brightness temperature of the bin. Substituting this approximation into Eq. 5.1 changes Coulomb's law into

$$|E_i(r_i)| = \frac{f(T_{b_i})}{r_i^2} \tag{5.3}$$

Since $f(T_{b\,i})$ is an arbitrary function, k_e is folded into the numerator, simplifying the expression. The components of the overall electric field vector, ($\vec{E}$), in Earth-relative coordinates is determined by summing this expression over each component of the distance vector, $\vec{r}$:

$$E_w = \sum_i \frac{r_{wi}}{|r_{wi}|} \frac{f(T_{b_i})}{r_{wi}^2} \tag{5.4}$$

$$E_n = \sum_i \frac{r_{ni}}{|r_{ni}|} \frac{f(T_{b_i})}{r_{ni}^2} \tag{5.5}$$

$$E_u = \sum_i \frac{r_{ui}}{|r_{ui}|} \frac{f(T_{b_i})}{r_{ui}^2} \tag{5.6}$$

where

$$\vec{r} = r_w \cdot \hat{w} + r_n \cdot \hat{n} + r_u \cdot \hat{u} \tag{5.7}$$

The overall electric field vector in Earth-relative coordinates can then be written as

$$\dot{E} = E_w \cdot \hat{w} + E_n \cdot \hat{n} + E_u \cdot \hat{u} \tag{5.8}$$

The actual function $f(T_{b\,i})$ that defines the electric field proxy is still unknown, but it is assumed that it is an indirect relationship where Q_i increases with decreasing $T_{b\,i}$. Since there are no observations of cloud charge available, it becomes necessary to employ a guess-and-check solution to determine $f(T_{b\,i})$ where an arbitrary function will be specified for $f(T_{b\,i})$ for use in the calculations, and then the results will be compared with observations and then corrected using a statistical model. Any function can be used for this technique as a starting point, but for the purposes of this study, a quadratic relationship between brightness temperature depression and charge content is chosen such that

$$f(T_b) = \left(T_{b\,env} - T_b\right)^2 \tag{5.9}$$

where $T_{b\,env}$ corresponds to the clear-air microwave brightness temperature. Brightness temperature depression from an environmental open-air value is used in lieu of raw brightness temperatures because it is a better measure of microwave signal strength and because it would likely vary directly, as opposed to indirectly, with cloud charge content. A higher-order polynomial is chosen to highlight the differences between low and high electric field proxy values.

Applying this relationship to Coulomb's law in Eq. 5.3 defines electric field proxy as

$$|pE_i(r)| = \frac{\left(T_{b\,env} - T_{b\,i}\right)^2}{r_i^2} \tag{5.10}$$

for a given AMPR pixel. The electric field proxy vector is determined by integrating Eq. 5.10 over the entire AMPR domain for each given ER-2 aircraft location following Eqs. 5.4–5.6, resulting in the full electric field proxy vector in Earth-relative coordinates

$$\overrightarrow{pE} = pE_w \cdot \hat{w} + pE_n \cdot \hat{n} + pE_u \cdot \hat{u} \tag{5.11}$$

An example calculation of electric field proxy is shown in Fig. 5.10. In this scenario, there is a cold convective core to the northeast of the aircraft and clear air to the southwest, resulting in a southwest-northeast brightness temperature depression gradient. Plugging these values into the electric field proxy equations yields the values in Fig. 5.10b. Even though the most intense convection is located under the far northeast pixel, because Coulomb's law is a strong function of distance, the strongest contribution to the observed electric field at the ER-2's location would actually be from the northern center pixel.

Electric field proxy values are not true values of electric field. They have units of $K^2\ km^{-2}$, not $V\ m^{-1}$, and lack any sort of theoretical basis other than a basic idea that they might be related somehow. To see if this is true, electric field proxy values and electric field observations over land are plotted simultaneously as a two-dimensional histogram in Fig. 5.11. As it turns out, electric field proxy values and actual observed electric fields correlate rather well, especially for 85 GHz observations (Fig. 5.11b). Because of this, it

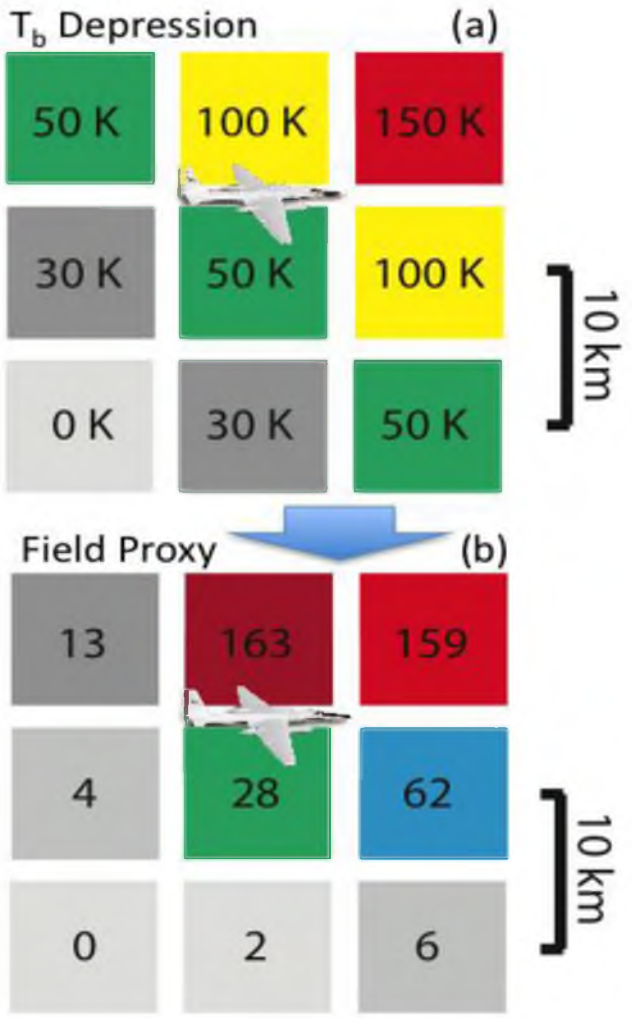

Fig. 5.10. Sample calculations of E Field Proxy from AMPR Tb Depressions. Tb depressions are shown in (a) and the magnitudes of EFP contributions from each bin relative to the aircraft location are shown in (b).

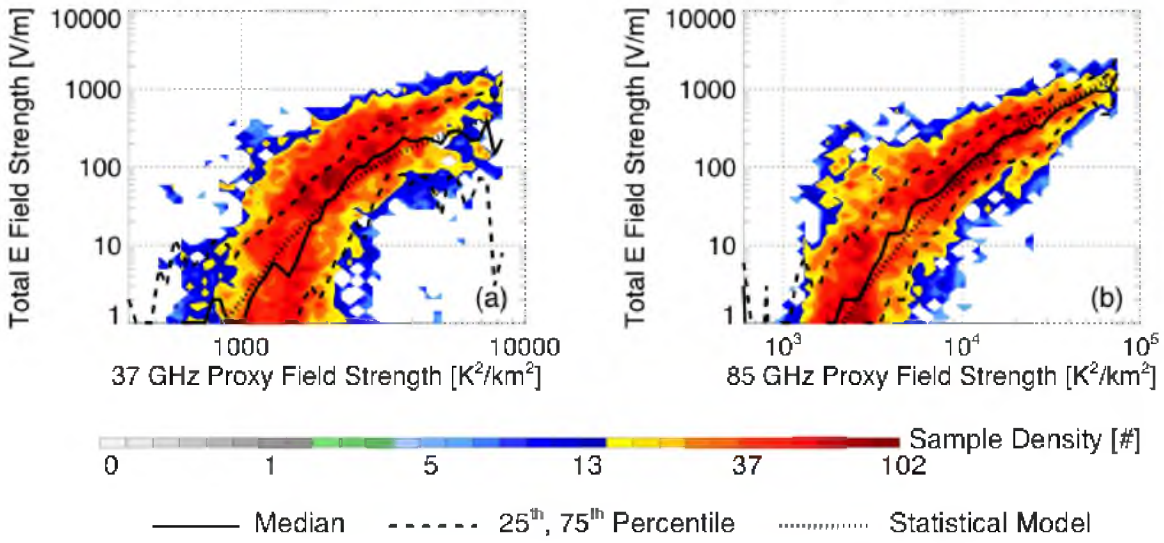

Fig. 5.11. Two-dimensional histogram showing between LIP total electric field strengths and 37 GHz (a) and 85 GHz (b) proxy electric field strengths over land. One-dimensional box plots for various proxy field strengths are shown (solid, dashed) as well as a statistical model fit line (dotted).

is possible to construct a transfer model between these two quantities that explains most observations. Statistical models are constructed that approximate the median electric field observations for different ranges of electric field proxy

$$\left|E_{est.\ 37GHz}\right| = \begin{cases} \exp\left(-95.77 + 22.87 * x_{37GHz} - 1.29 * x_{37GHz}^{\ 2}\right) & x_{37GHz} < 8.29 \\ \exp\left(-6.61 + 1.42 * x_{37GHz}\right) & x_{37GHz} \geq 8.29 \end{cases} \tag{5.12}$$

$$\left|E_{est.\ 85GHz}\right| = \begin{cases} \exp\left(-49.89 + 9.35 * x_{85GHz} - 0.39 * x_{85GHz}^{\ 2}\right) & x_{85GHz} < 10.60 \\ \exp\left(-5.43 + 1.13 * x_{85GHz}\right) & x_{85GHz} \geq 10.60 \end{cases} \tag{5.13}$$

where

$$x = \ln\left(\left|\overrightarrow{pE}\right|\right) \tag{5.14}$$

and E_{est} corresponds to actual AMPR-based estimates of observed electric fields.

Oceanic transfer models are not as clear and consistent, however. Figure 5.12 shows two-dimensional histograms between electric field proxy and observed electric field strength for coastal ocean and open ocean datapoints. Unsurprisingly, the 37 GHz histogram does not have any form of clear shape. The cold ocean surface leads to extreme values of electric field proxy, regardless of the observed electric field strength. However, the 85 GHz oceanic histogram also lacks the distinct, concentrated distribution that was prevalent in Fig. 5.11b. Much of this spread is due to another aforementioned LIP caveat: the limited width of the sensor's swath. Oceanic storms, particularly hurricanes like those studied in CAMEX-3, CAMEX-4, and TCSP, where much of the oceanic data come from, are much larger than 40 km across, and therefore the AMPR cannot be used to

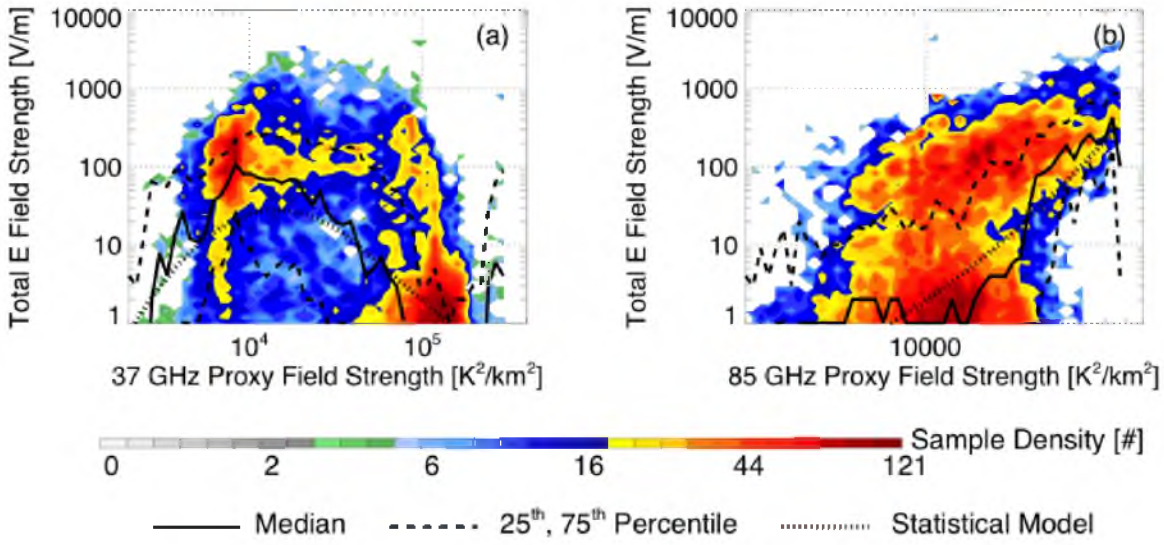

Fig. 5.12. Two-dimensional histogram showing between LIP total electric field strengths and 37 GHz (a) and 85 GHz (b) proxy electric field strengths over offshore coastal regions. One-dimensional box plots for various proxy field strengths are shown (solid, dashed) as well as a statistical model fit line (dotted).

accurately estimate electric fields above these larger storms. Because of these caveats, the land-based model described in Eqs. 5.12 and 5.13 will be used to estimate electric fields over all terrain regions.

This procedure is followed for every LIP datapoint, using all nearby AMPR pixels at each datapoint, within a reasonable range. The current version of the algorithm uses a grid box of roughly 40 km by 30–40 km to determine the electric field proxy values and AMPR-estimated electric fields for each LIP datapoint along the ER-2 flight track. Vector magnitudes, orientation angles (relative to East), and inclination angles are recorded. The major caveat in comparing the orientation of derived and observed vectors is that this procedure assumes that the relevant charge region is always entirely positive. Intervening negative charge regions and intense screening layers can lead to significant disagreement.

The overall performance of this algorithm is assessed using two-dimensional histograms of observed and AMPR-estimated electric field strengths over land in Fig. 5.13. Median and quartile values of observed electric field strength for a given AMPR-estimate are also shown. Because of the filtering routines described in Chapter 2, observations less than 20 V m^{-1} may be subject to a considerable amount of uncertainty. In general, both the 37 GHz model and the 85 GHz model show some agreement with observations, as seen by the color contours near the 1:1 line in each panel.

There are some deviations, however. The 37 GHz routine often overestimates observations for lower electric field strengths and underestimates strongest electric fields given the large number density above the line, but also overestimates strong electric fields, overall, as seen by the histograms. The 85 GHz routine more closely mirrors

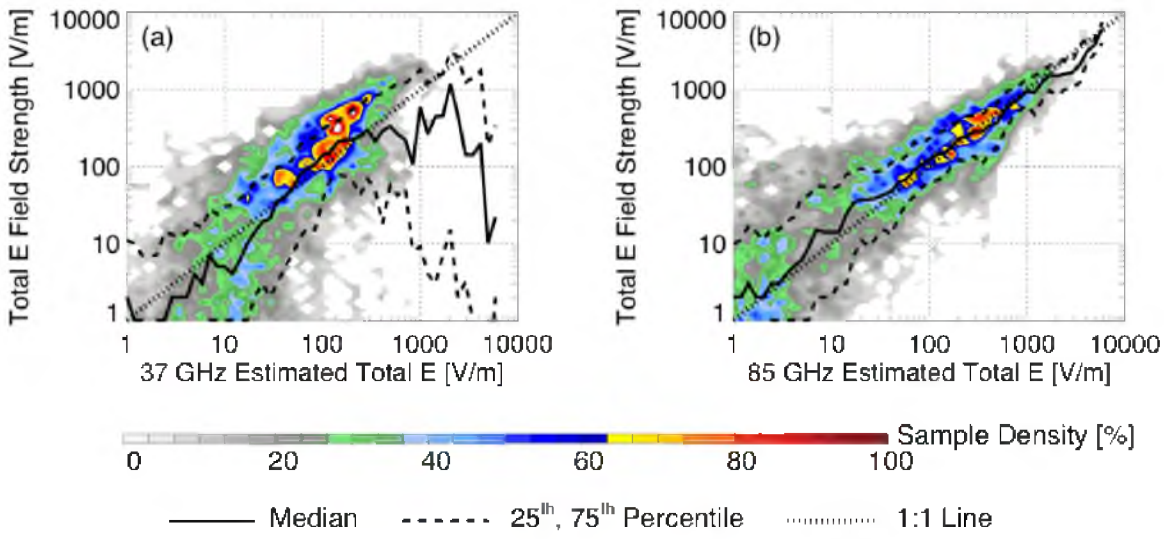

Fig. 5.13. Validity of the statistical model fit between 37 GHz (a) and 85 GHz (b) proxy field strengths and estimated electric field strength over land shown as a two-dimensional histogram between observed total electric field strengths and estimated electric field strengths. One-dimensional box plots for various estimated electric field strengths are shown as well as a 1:1 line between the two parameters.

observations, as a whole, as seen by the median line remaining close to the 1:1 line throughout the domain, but there are still significant numbers of datapoints that either overestimate or underestimate observations, particularly for weaker electric field values.

Much of the spread in the 85 GHz estimate can be explained by two scenarios: missed cases and false alarms. Missed events are concentrated near the y-axis and correspond to cases with strong electric fields but weak 85 GHz microwave signals, resulting in weak electric field estimates. This scenario is more common than the false alarm scenario and includes cases where the ER-2 aircraft was flying near convection that was not captured within the ER-2 swath. In these cases, the LIP field mills would detect the presence of nearby electrified clouds, but the AMPR sensor may be only seeing clear air. A second, less common, situation that leads to missed events is the case of lightning contamination. The lightning filter is not perfect, so some lightning artifacts get through. In these cases, the lightning signal would show strong electric fields, often above 100 V m^{-1}, even when the ER-2 is flying over fair-weather clouds or clear air. Both of these kinds of cases have been observed, and a few will be shown in the next section.

The other scenario that likely accounts for much of the error in the 85 GHz estimate is from false alarm cases. Cases that fall into this category account for much of the spread on the underside of the 85 GHz distribution. These cases are categorized as having strong electric field estimates with observations that are weak in comparison. These cases are often the result of assumptions and caveats within the algorithm, particularly stemming from the effective height of the charge layer. Since Coulomb's law is a strong function of distance between the charge source and the observer, if the algorithm assumes that the charge source is a couple of kilometers closer to the observer

than it should be, then the routine would report much stronger electric field estimates than it really should, even if every other assumption inherent in the algorithm were correct. Cases where this is the likely cause of the discrepancy between estimates and observations have been found and will be shown in the next section, as well.

To put some numbers on how well each routine is performing, overall, Table 5.1 shows the distribution of datapoints estimated within certain error ranges, overestimated, or underestimated by each model. For example, very few datapoints are predicted correctly by each model within 10% error (0.3%), with slightly more predicted well by the 37 GHz model (4%) or the 85 GHz model (6%). The 85 GHz model was more likely to underestimate (53%) than overestimate (41%) by more than 10% error, while the reverse was true for the 37 GHz model.

Increasing the threshold to 50%, just over 30% of the datapoints are predicted by the 85 GHz model, while 21% are predicted by the 37 GHz model. Those fractions increase drastically when the allowed errors reach 100%. Now, the 85 GHz model predicts almost 3 out of every 4 datapoints within the allowed error range (a factor of 2), while the 37 GHz model predicts 60% of the observations. Now, both models, when they do miss their targets, exclusively overestimate the observed values. Finally, when the threshold is increased to 1,000%, or an order of magnitude, the 85 GHz model predicts 92% of the observations, while the 37 GHz model predicts 80%. Clearly, there is still room for improvement, but consider what this is showing: using only 85 GHz passive microwave observations and despite many significant assumptions, it is possible to reconstruct the electric field above a storm within a factor of two of the observed value nearly three-fourths of the time.

Table 5.1. Distributions of estimated electric field strength categorized by allowed error thresholds.

Threshold			Distribution			
10%			85 GHz			
			Within	Under	Over	Total
		Within	0.3%	1.9%	1.9%	4.1%
	37 GHz	Under	3.3%	36.6%	6.6%	46.5%
		Over	2.4%	14.4%	32.5%	49.3%
		Total	6.0%	52.9%	41.0%	100%
50%			85 GHz			
			Within	Under	Over	Total
		Within	10.3%	6.4%	5.1%	21.8%
	37 GHz	Under	9.9%	23.3%	0.8%	34.0%
		Over	9.9%	7.8%	26.5%	44.2%
		Total	30.1%	37.5%	32.4%	100.0%
100% (factor of 2)			85 GHz			
			Within	Under	Over	Total
		Within	55.8%	0.0%	4.2%	60.0%
	37 GHz	Under	0.0%	0.0%	0.0%	0.0%
		Over	18.0%	0.0%	22.0%	40.0%
		Total	73.8%	0.0%	26.2%	100.0%
1,000% (order of magnitude)			85 GHz			
			Within	Under	Over	Total
		Within	79.4%	0.0%	0.7%	80.1%
	37 GHz	Under	0.0%	0.0%	0.0%	0.0%
		Over	12.8%	0.0%	7.1%	19.9%
		Total	92.2%	0.0%	7.8%	100.0%

Another way of looking at model errors is to pick an allowed error level and examine how datapoints from different field campaigns, terrain classifications, and types of clouds compare with observations. Table 5.2 and Table 5.3 show this type of comparison for an allowed error level of 100% or a factor of two. Open ocean observations are not shown due to the limited number of samples. Overall, the 37 GHz estimate (Table 5.2) correctly predicts the electric field to within this margin 12% of the time, including both land and ocean observations. It is much more likely to overestimate electric fields by a significant margin (75%) than underestimate them (12%). Median errors using 37 GHz data are over 6,000%, or more than an order of magnitude difference between estimates and observations. This can be attributed to the "cold" ocean surface at 37 GHz, as discussed previously, and causes field campaigns that take place mostly over the ocean (CAMEX-3, CAMEX-4, TCSP) to be subject to tremendous errors (even up to 700 000%) compared to field campaigns over land (TRMM-LBA). Despite this caveat, the 37 GHz routine predicts strong convective overflight electric fields one-third of the time to within a factor of two over the coastal ocean, increasing to 40% for events with significant LIP electric field observations (> 100 V m^{-1}). The 37 GHz routine predicts the observed electric fields over land for overflights of both weak (85 GHz observations between 230 K and 260 K) and strong (85 GHz observations < 220 K) convective intensity clouds between 35–40% of the time to within the specified margin.

Compared to the 37 GHz routine estimates, the 85 GHz estimates (Table 5.3) are at least as accurate, if not more accurate, in every category. The 85 GHz routine predicts observed electric fields to within factor of two 40–50% of the time for every category with LIP observations exceeding 100 V m^{-1}. This measure of algorithm performance

Table 5.2. Overall performance of the 37 GHz electric field estimation algorithm in terms of percent error. Median percent errors and fractions of datapoints within a factor of 2 of observations, underestimating by more than a factor of 2 and overestimating by more than a factor of 2, are shown for various categories. Shower clouds and convection are classified by 85 GHz brightness temperatures (230–260 K: likely shower clouds; < 220 K: likely convection). Performance is assessed for all datapoints (including clear air) and for only observations with significant electric fields (> 100 V/m).

	Median |Error|	|Error| < 100%	Error < -100%	Error > 100%
All data	6,066.3 %	12.2 %	12.6 %	75.2 %
> 100 V/m	252.6 %	26.9 %	29.0 %	44.0 %
CAMEX 3	17 536.5 %	8.9 %	3.1 %	88.0 %
> 100 V/m	225.7 %	29.2 %	8.8 %	62.0 %
CAMEX 4	768 612.0 %	2.0 %	0.5 %	97.5 %
> 100 V/m	1,460.2 %	13.9 %	2.3 %	83.8 %
TCSP	49 414.5 %	4.3 %	3.0 %	92.7 %
> 100 V/m	521.1 %	18.8 %	12.5 %	68.8 %
TRMM LBA	233.4 %	29.3 %	39.8 %	30.9 %
> 100 V/m	183.7 %	32.2 %	66.2 %	1.6 %
Land				
Shower clouds	167.1 %	35.0 %	35.9 %	29.1 %
> 100 V/m	134.2 %	40.3 %	53.2 %	6.4 %
Convection	128.9 %	41.8 %	45.7 %	12.4 %
> 100 V/m	128.9 %	41.7 %	47.1 %	11.2 %
Coastal Ocean				
Shower clouds	740, 369.0 %	3.6 %	0.4 %	96.0 %
> 100 V/m	493.8 %	18.9 %	2.3 %	78.9 %
Convection	181.4 %	33.9 %	4.8 %	61.3 %
> 100 V/m	135.7 %	41.2 %	5.8 %	53.1 %

Table 5.3. Overall performance of the 85 GHz electric field estimation algorithm in terms of percent error. Median percent errors and fractions of datapoints within a factor of 2 of observations, underestimating by more than a factor of 2 and overestimating by more than a factor of 2, are shown for various categories. Shower clouds and convection are classified by 85 GHz brightness temperatures (230–260 K: likely shower clouds; < 220 K: likely convection). Performance is assessed for all datapoints (including clear air) and for only observations with significant electric fields (> 100 V/m).

	Median |Error|	|Error| < 100%	Error < -100%	Error > 100%
All data	642.2 %	22.9 %	19.3 %	57.9 %
> 100 V/m	111.5 %	47.1 %	34.5 %	18.4 %
CAMEX 3	1,253.8 %	17.2 %	11.5 %	71.2 %
> 100 V/m	134.4 %	42.1 %	23.9 %	34.0 %
CAMEX 4	3,841.0 %	13.5 %	12.1 %	74.4 %
> 100 V/m	150.7 %	39.8 %	52.6 %	7.6 %
TCSP	1,591.6 %	17.4 %	18.1 %	64.4 %
> 100 V/m	109.9 %	47.4 %	44.7 %	7.9 %
TRMM LBA	151.2 %	40.3 %	34.5 %	25.1 %
> 100 V/m	84.3 %	54.5 %	35.5 %	10.0 %
Land				
Shower clouds	87.8 %	53.1 %	12.6 %	34.3 %
> 100 V/m	56.1 %	68.2 %	17.5 %	14.4 %
Convection	57.5 %	68.6 %	7.2 %	24.2 %
> 100 V/m	56.2 %	69.5 %	7.4 %	23.2 %
Coastal Ocean				
Shower clouds	6,971.1 %	13.1 %	4.2 %	82.6 %
> 100 V/m	84.6 %	54.9 %	21.4 %	23.8 %
Convection	177.3 %	35.0 %	9.5 %	55.6 %
> 100 V/m	127.4 %	42.3 %	11.5 %	46.2 %

improves significantly to nearly 70% over land for both strong and weak convective overflights. The cloud type that gives the 85 GHz estimate the most trouble, however, is general oceanic weak convective clouds, where it significantly overestimates the observed electric field 82% of the time.

Statistical approaches like this give an overall view of how well the algorithm performs as a whole and indicates where it can be improved, but in order to gain a better understanding of when the models work well and when the models could use some improvement, it is necessary to look at how the passive microwave electric field estimation algorithm handles some actual real-world cases.

5.3 Case Study

The key benefit of having such a robust dataset is that there are plenty of different kinds of storms to choose from to validate AMPR-estimated electric fields. A sensible starting point is a case that has already been discussed. Figure 5.14 shows the estimated electric field strengths using both the 37 GHz and 85 GHz model estimates for the Amazonian land-based case shown at the beginning of this chapter in Fig. 5.1. Since this case is almost entirely captured by the AMPR swath, the electric field estimates shown in Fig. 5.1a and b would not likely be affected by other nearby electrified clouds. Estimates using both frequencies agree that the overall electric field pattern consists of a maximum over the middle of the stronger convective line and a plateau reaching out to the isolated weaker convective cell. The maximum happens to be located over the region of strongest convection, but that is not necessarily the case. Since both convective areas in the line contribute to the perceived electric field vector, particularly in the Earth-relative up

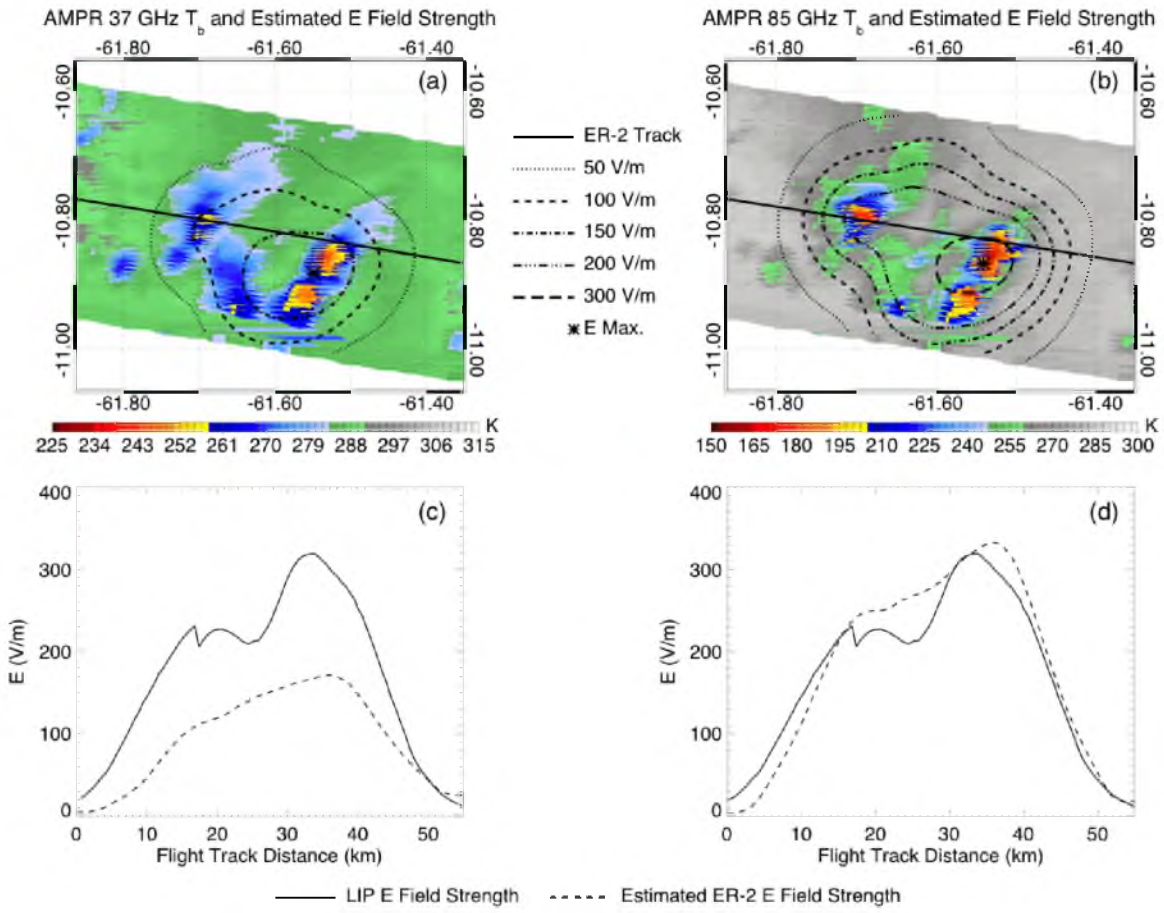

Fig. 5.14. AMPR observations and estimated electric fields of the same storm over land shown in Fig. 5.11. AMPR 37 GHz (a) and 85 GHz (b) brightness temperatures (contour), estimated electric field strengths (line contours), and the ER-2 flight track (solid line) are shown. A comparison of observed and estimated electric field strengths along the flight track is also shown in (c) and (d).

direction, it stands to reason that in a multicell feature, electric fields may sometimes be greatest between cells, where the observer can feel the effects of both separate electrified clouds due to the short distance between cell, rather than over one cell or the other.

There is quite the disagreement between the peak magnitudes of the estimated electric fields between the two models, however, which is easily seen in Fig. 5.14c and d. While the 37 GHz model estimates the peak electric field along the ER-2 flight track at 160 V m^{-1}, the 85 GHz model estimates electric fields just over 300 V m^{-1}. Based on observations, it would appear that the 85 GHz model does rather well in this case, closely resembling the observed electric field both in timing and peak amplitudes, while the 37 GHz model underestimates the observed electric field considerably. Looking back to Table 5.1 in the previous section, this case would outperform the norm for the 85 GHz model, with most datapoints lying within a few percent of the observed value, much less than the factor of two threshold used previously.

Despite its strengths in this case, one area where the 85 GHz model does not perform well is between the individual cell and the convective line. Observations show a true plateau between the two regions of convection and even a slight decrease on the backside of the isolated cell, while the model levels off momentarily before starting to increase once more under the influence of the convective line. It is difficult to say why this is the case. It could come from the fact that the model does not take into account complex charge structures with areas of both positive and negative polarity, or it could be due to deficiencies in assumed charge height. Nevertheless, even these datapoints fall well within the factor-of-two threshold discussed before.

Throughout this chapter, the 85 GHz model has been shown to outperform the 37

GHz model in many cases, but that does not mean that the 37 GHz model is necessarily inferior. After all, while the 85 GHz model can account for almost three in four datapoints within a factor of two, the 37 GHz can still estimate 60% of the sample over land with the same threshold of accuracy. The primary difference between the two frequencies, aside from the "cold water" issue with 37 GHz, is the sizes of ice particles each is sensitive to. Applying the same model to all storms implies that the same cocktail of ice particles is responsible for the same amount of charge accumulation across the board. That is not necessarily the case. Figure 5.15 shows another TRMM-LBA example where the 37 GHz model outperforms the 85 GHz model. This case also takes place over land, so the "cold water" does not contaminate the estimates. Both models perform well in this example, but the 37 GHz only underestimates the observed peak electric field by 20 V m^{-1} and captures the timing of the event nearly perfectly, while the 85 GHz model overestimates by nearly 50 V m^{-1} and feels the electric field's presence almost 5 km sooner along the flight track than the LIP. Interestingly, the 85 GHz does wind up simulating the end of the event nicely, despite being out of phase initially.

Both of these cases seem to do a decent job at reconstructing the LIP record with reasonable accuracy, but they are also both land cases. The ocean is fundamentally different than land, and it is entirely possible that these models, particularly the 37 GHz model, may not be able to properly characterize electric fields over ocean storms. Figure 5.16 shows an example ocean case observed over the Caribbean. This case is a simple linear feature with 85 GHz brightness temperatures dipping just below 200 K and 37 GHz brightness temperatures colder than 250 K along the edge and reaching 250 K in the interior of the cloud. Naturally, the cold nature of the ocean wreaks havoc on the 37 GHz

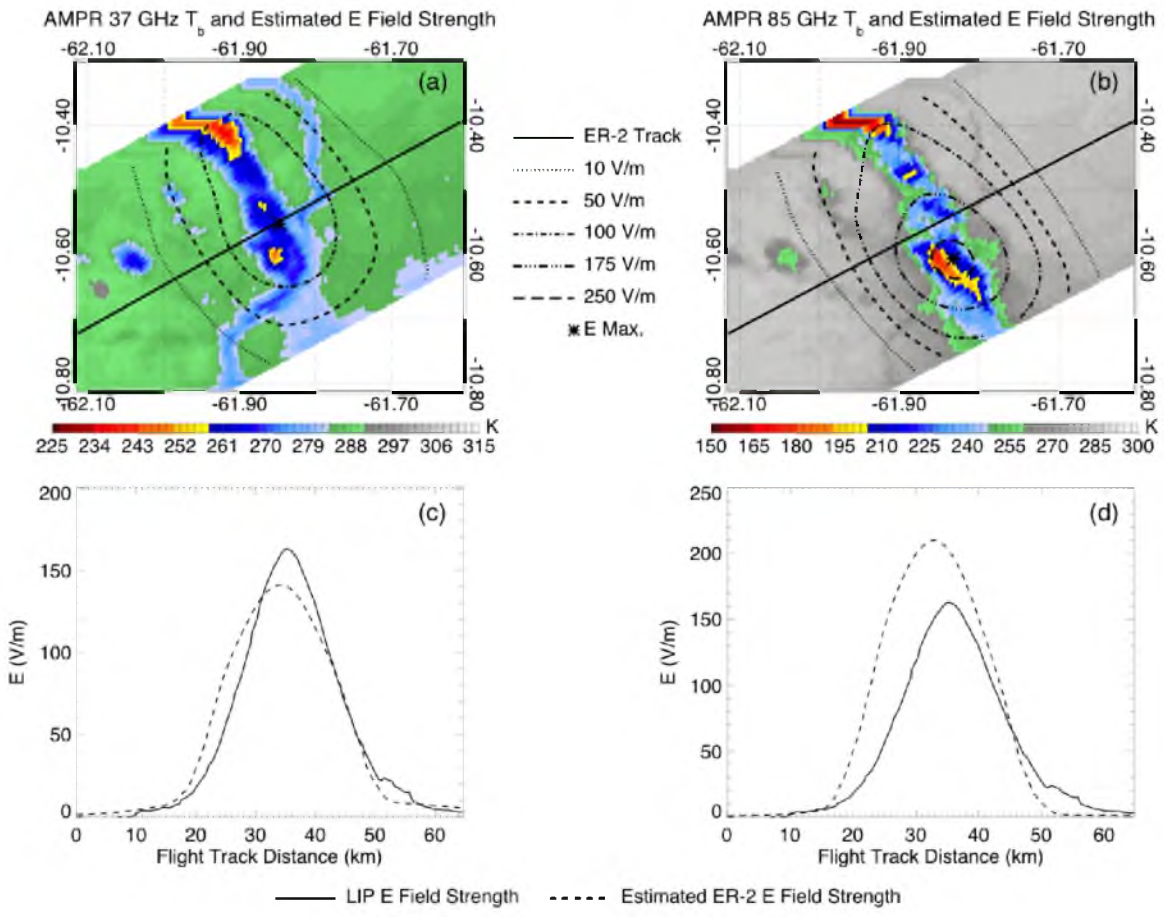

Fig. 5.15. AMPR observations and estimated electric fields above a storm over land. AMPR 37 GHz (a) and 85 GHz (b) brightness temperatures (contour), estimated electric field strengths (line contours), and the ER-2 flight track (solid line) are shown. A comparison of observed and estimated electric field strengths along the flight track is also shown in (c) and (d).

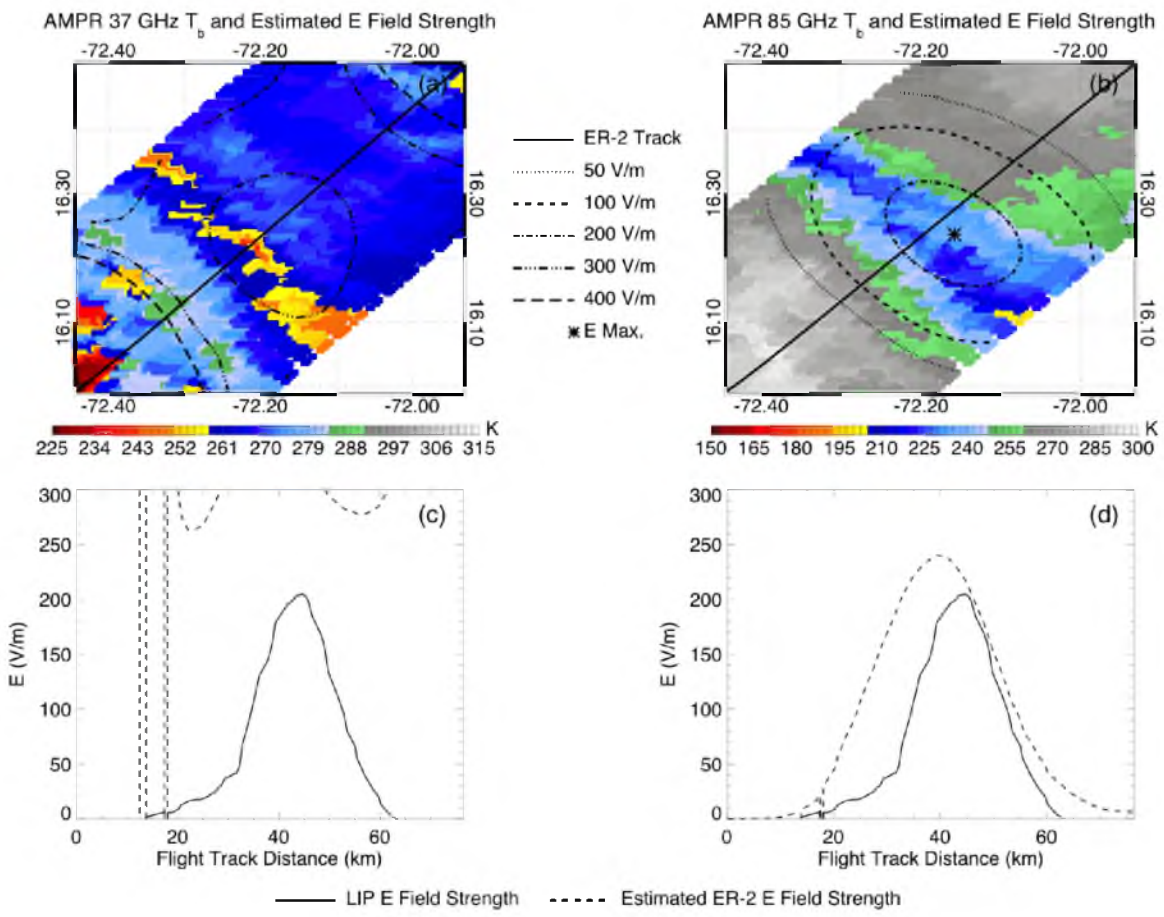

Fig. 5.16. AMPR observations and estimated electric fields above an offshore coastal cloud. AMPR 37 GHz (a) and 85 GHz (b) brightness temperatures (contour), estimated electric field strengths (line contours), and the ER-2 flight track (solid line) are shown. A comparison of observed and estimated electric field strengths along the flight track is also shown in (c) and (d).

model, producing electric field estimates exceeding 400 V m^{-1} over clear air, dropping rapidly to under 300 V m^{-1} closer to the interior, and rising again past 300 V m^{-1} near the strongest brightness temperatures.

This is not the only reason reconstructed charge structure over the storm looks unusual, however. Unlike the previous figures, which contained most of the electrified storm within the AMPR swath, in this case it is clear that there are electrified clouds outside of the AMPR field of view that the models are not detecting. This results in closed electric field contours around the center of the image, even with the 85 GHz model. Because of this, the level of confidence in the observed electric field decreases outward across the AMPR swath away from aircraft nadir, particularly with MCSs, stratiform clouds, or any other broad precipitation feature that cannot be well captured by the AMPR. Still, despite this hindrance, the 85 GHz model does do a good job at reconstructing the LIP observations along the flight track (Fig. 5.16d). As the aircraft flies from the northeast heading southwest, it initially overestimates the observed electric field—likely due to the outward extending region of 250 K on the right side of the figure. This flanking feature appears to be part of the storm's trailing stratiform region. The fact that it does not affect the observed electric field as much as it does the estimated electric field from the 85 GHz model could be a sign that the model overestimates charge accumulation of oceanic stratiform regions.

Despite overestimating the electric field initially, the 85 GHz model does manage to capture the aircraft's departure from over the storm rather well. Even the amplitude of this event is only off by 40 V m^{-1}, or 20%. It would seem that the 85 GHz model could work with ocean cases, at least for some types of storms. Figure 5.17 shows another

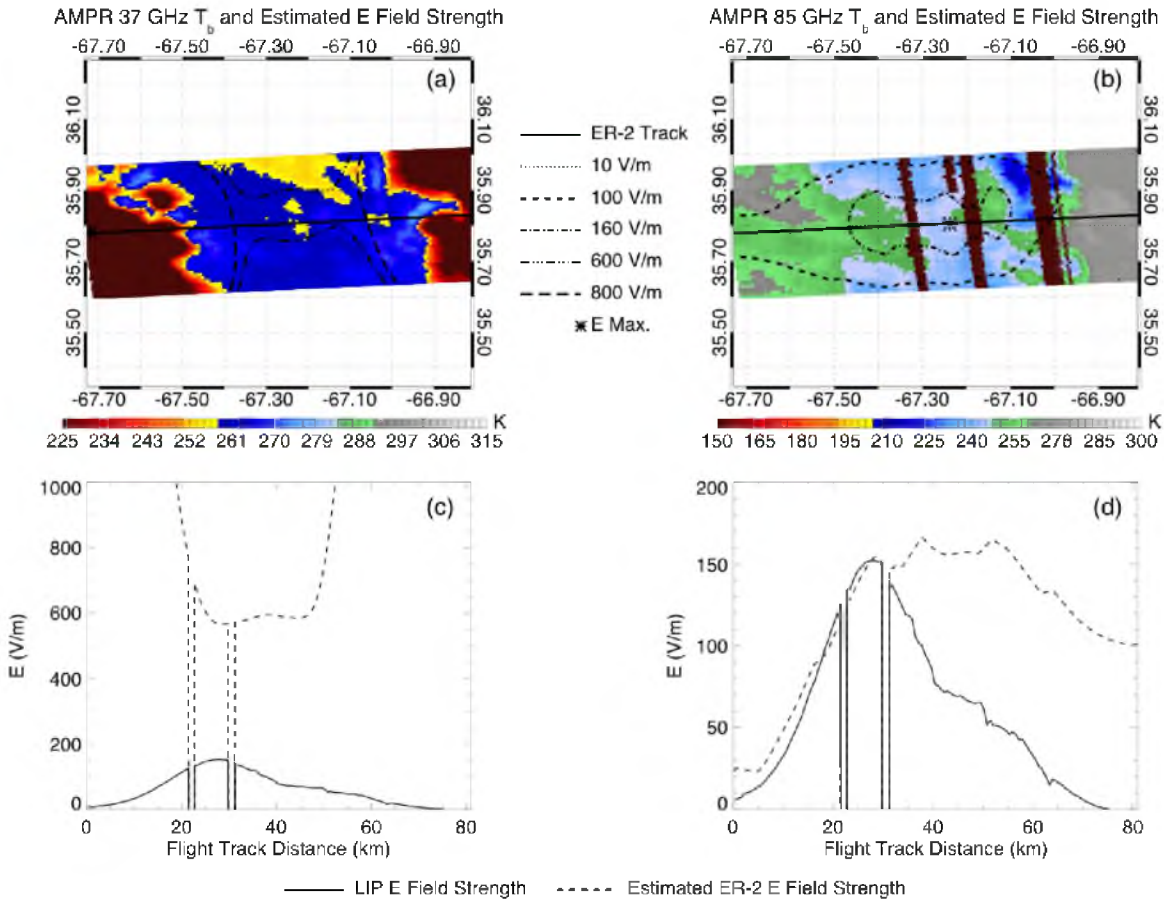

Fig. 5.17. AMPR observations and estimated electric fields above an offshore MCS. AMPR 37 GHz (a) and 85 GHz (b) brightness temperatures (contour), estimated electric field strengths (line contours), and the ER-2 flight track (solid line) are shown. A comparison of observed and estimated electric field strengths along the flight track is also shown in (c) and (d).

oceanic storm, this time a very clean cross section of a leading line trailing stratiform MCS that was observed over the Atlantic Ocean during CAMEX-4 as the ER-2 was returning from taking observations of Hurricane Erin. At 37 GHz, the data are quite complex, but 85 GHz clearly shows the ER-2 flying across a 210 K convective line on the right and into its trailing stratiform region as it headed west, despite a few bad scans, which were discarded.

Once more, since the width of this case far exceeds the AMPR swath width, the resulting 85 GHz estimated electric field contours form closed contours, but nevertheless, the flight track estimates follow the actual LIP observations as the ER-2 approaches the storm, even reproducing the correct peak amplitude of 150 V m^{-1} for the convective part of the event. However, the estimate diverges from observations when the aircraft crosses into the oceanic stratiform region. While the 85 GHz model keeps the estimates at around 150 V m^{-1}, the actual observed electric field quickly drops below 75 V m^{-1} before tapering off completely. This case provides more evidence that while the 85 GHz model works reasonably well over land and ocean convection, it completely overestimates electric fields over oceanic stratiform rain. There are three potential reasons for this. One, the model assumes an effective charge height that is too high (too close to the aircraft). Two, it overestimates the amount of ice for a given brightness temperature. Or three, there is a strong shielding layer above the stratiform cloud that blocks the electric field from being detected. It is likely that all three of these issues play a role. Future work will be required to identify stratiform precipitation using microwave observations, and then formulating a separate stratiform model for land and oceanic cases.

Fig. 5.18 shows the electric field estimates of the TCSP offshore weakening

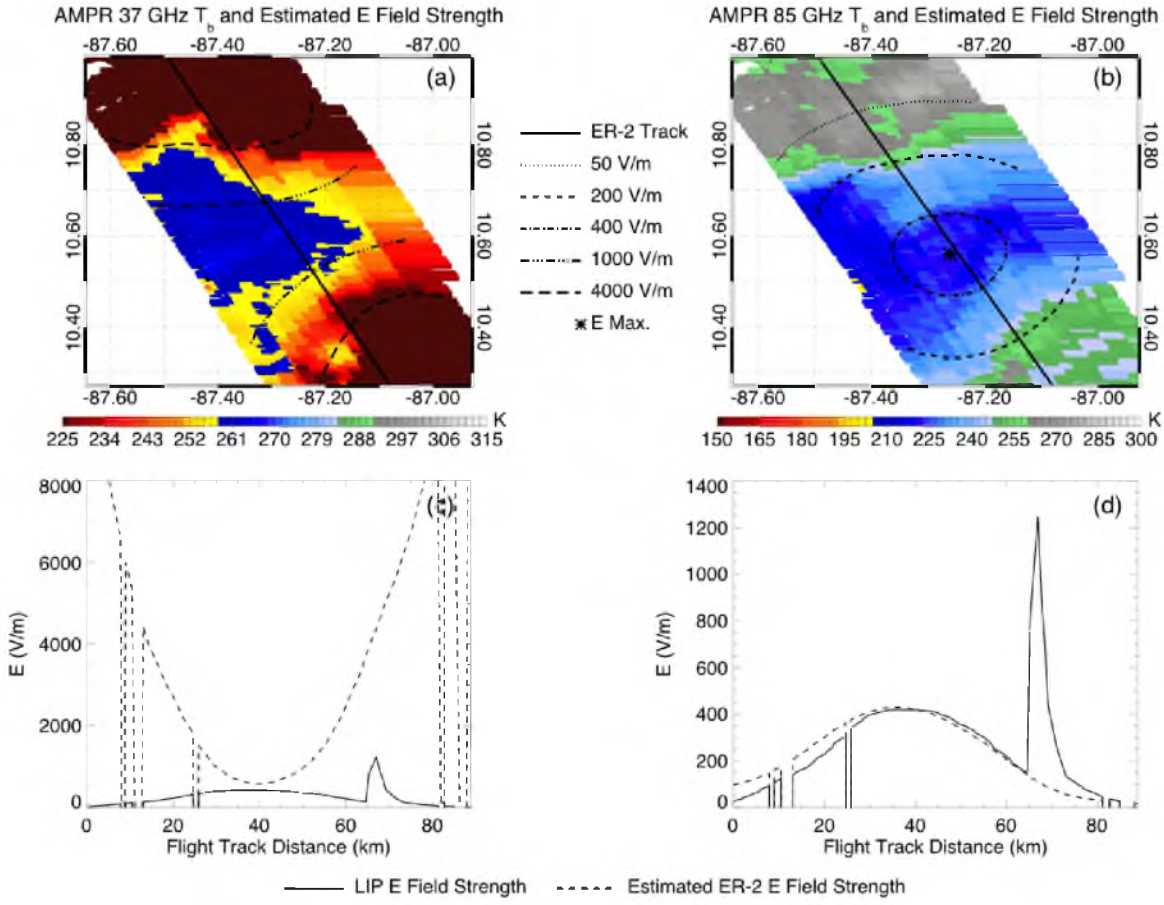

Fig. 5.18. AMPR observations and estimated electric fields above an offshore coastal storm. AMPR 37 GHz (a) and 85 GHz (b) brightness temperatures (contour), estimated electric field strengths (line contours), and the ER-2 flight track (solid line) are shown. A comparison of observed and estimated electric field strengths along the flight track is also shown in (c) and (d).

nocturnal MCS case shown in Fig. 5.2. The 37 GHz model for this case produces a parabola shape electric field estimate that actually is close (within 100 V m^{-1}) to the observed peak. One potential reason for this is that this oceanic storm is considerably large and since electric field strength depends on distance squared, central pixels within the storm may not be affected by the cold ocean surface at 37 GHz. The 85 GHz model fares much better in this case. Despite not being entirely captured by the AMPR swath, the model agrees very well with the LIP observations along the flight track. The fact that the estimate does not show any sort of increase near the observed electric field spike near the end of the overflight and that this MCS had high observed lightning flash rates provides more evidence that it was the result of a lightning artifact, not some odd convective feature.

Now that a few "normal" cases have been examined, it may be interesting to look at some unusual cases. The first few cases have all taken place when the ER-2 was flying straight, over an electrified cloud, but what would happen if the aircraft were performing a banked turn? Since the AMPR is mounted in a fixed position, if the aircraft does turn, it rotates with the aircraft, seeing further out and at shallower angles. As the field of view rotates, it also oversamples certain areas, possibly resulting in overestimates of electric field strength. Figure 5.19 shows such a case where the ER-2 turned left while over an Atlantic storm. At both 37 GHz and 85 GHz, the upper right corner of the AMPR swath is reporting very cold brightness temperatures, or considerably reduced radiative flux, possibly due to those bins being orientated above the horizon. Since most datapoints of note come from stretches of the ER-2 record where the aircraft is flying straight, no effort is made in the model to correct for a turning aircraft. These pixels would appear to be a

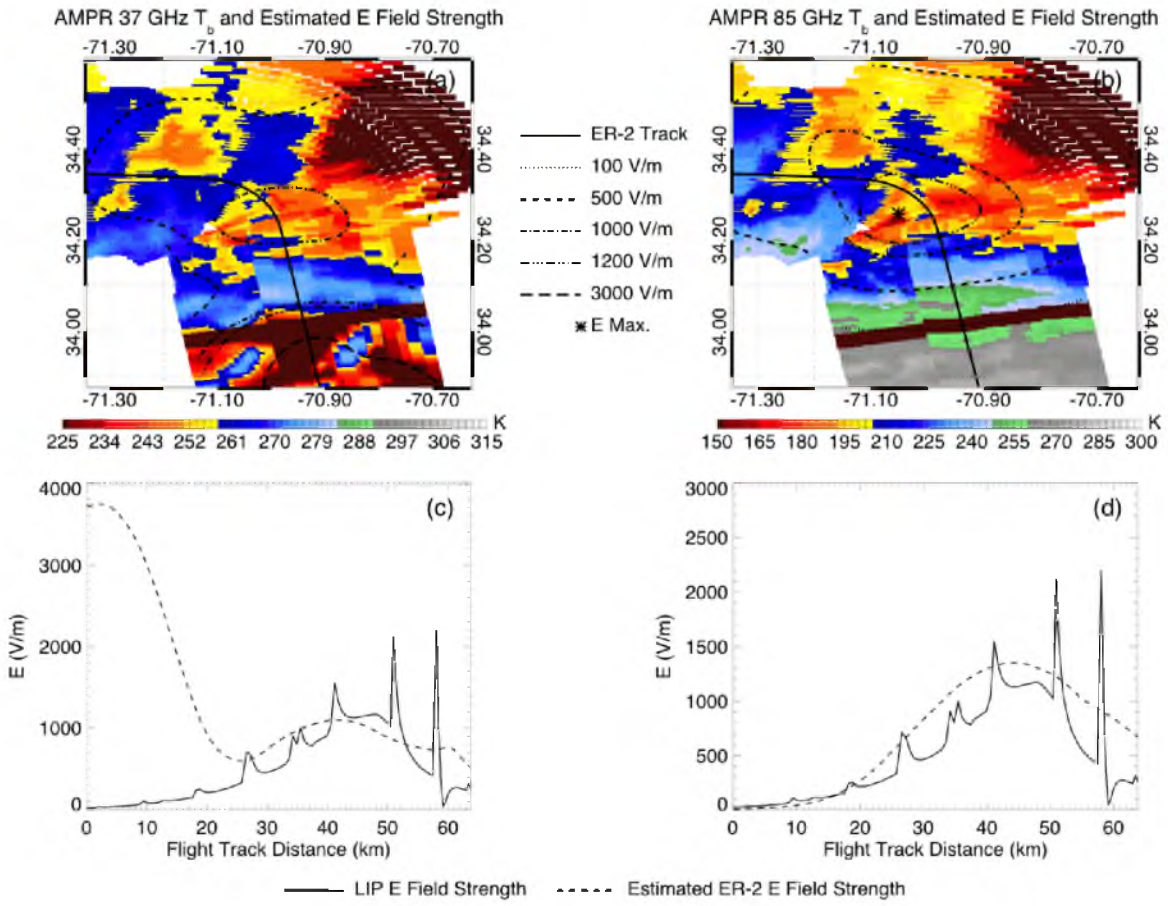

Fig. 5.19. AMPR observations and estimated electric fields above an offshore coastal storm featuring a banked turn. AMPR 37 GHz (a) and 85 GHz (b) brightness temperatures (contour), estimated electric field strengths (line contours), and the ER-2 flight track (solid line) are shown. A comparison of observed and estimated electric field strengths along the flight track is also shown in (c) and (d).

very strong storm, but given the increased recorded distance from the aircraft of these pixels in the AMPR record, the estimates may be saved by the fact that their effect is reduced by a factor of distance squared. Looking at the lower half of the figure, this would appear to be the case. Despite some lightning contamination, the 37 GHz and 85 GHz models decently reproduce the timing and amplitude of the observed event. By studying additional cases like this, it would appear that banking and turning does not seem to be a significant source of error in these results.

One of the more interesting cases where the models failed to perform is shown in Fig. 5.20. This particular case occurs over land where the ER-2 aircraft flew above and alongside a strong, large Amazonian convective system during TRMM-LBA. Even though both models have the timing of the event down, neither can reproduce the nearly 2,500 V m^{-1} peak electric field observed by the LIP, nor do they seem to do a good job at recreating the smaller-scale oscillations caused by the individual nearby convective cells. One reason for this could be lightning activity, but it does not help that this event is only half captured by the AMPR, meaning that there is likely more convection outside of the AMPR FOV influencing the observed electric field. Given the intensity of the event, the tallest towers are likely only a few kilometers below the ER-2, perhaps calling into question the "net effect is what matters at such a distance" assumption. It is also likely that the effective charge height is higher than assumed in the model, which is why the model does not estimate as strong of an electric fields as observations. This case is particularly interesting because it illustrates many of the ways and scenarios in which the model may fail to live up to observations.

Finally, while the previous cases have had more typical thunderstorm structures,

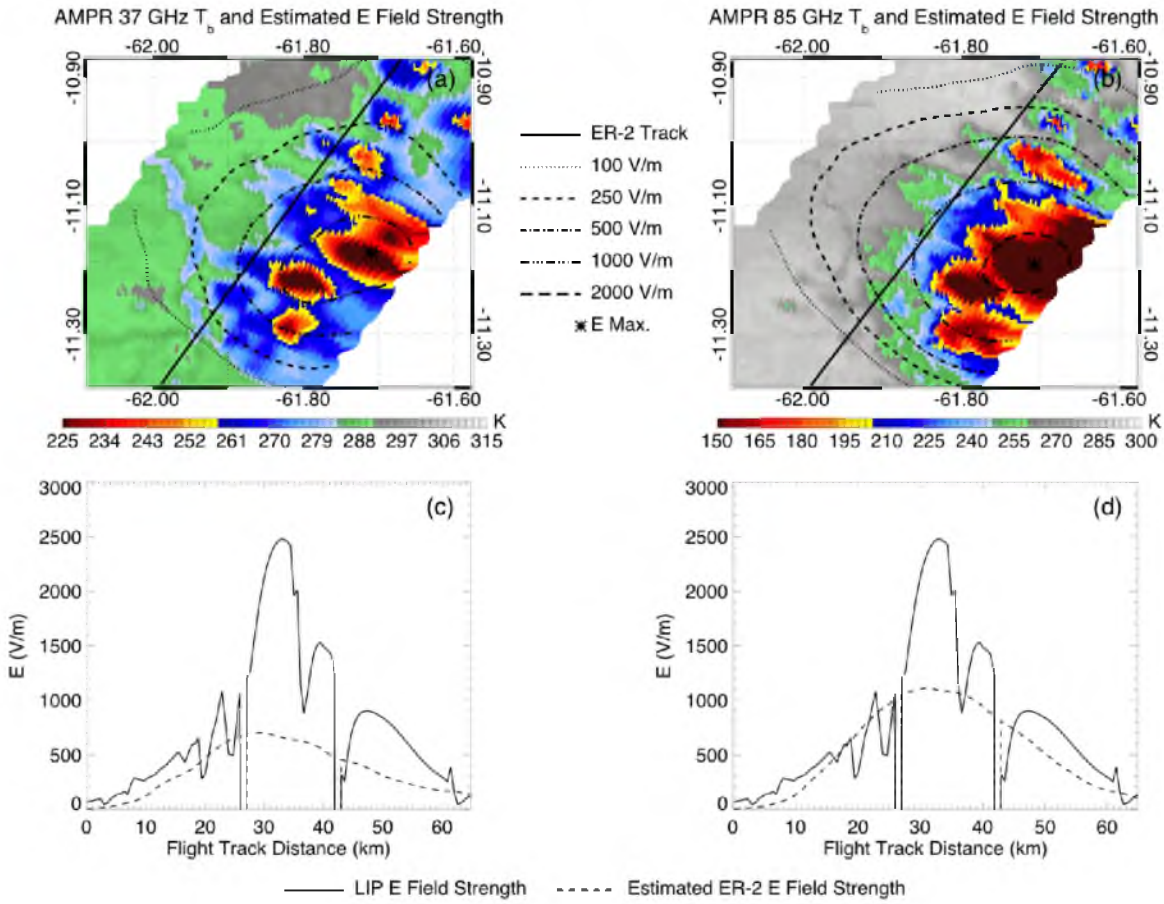

Fig. 5.20. AMPR observations and estimated electric fields above a storm over land. AMPR 37 GHz (a) and 85 GHz (b) brightness temperatures (contour), estimated electric field strengths (line contours), and the ER-2 flight track (solid line) are shown. A comparison of observed and estimated electric field strengths along the flight track is also shown in (c) and (d).

the last case, shown in Fig. 5.21, is an overpass of Hurricane Emily in 2005 when it was in the Caribbean. In this particular case, the ER-2 aircraft flew over the eye of the storm, capturing only a fraction of the convection in the inner core. Because of this, and because of lightning activity within the storm, the 85 GHz estimated electric fields form an interesting pattern. Despite the lack of observations outside of the AMPR swath, what appears to be a "donut hole" above the eye can still be observed in the AMPR estimates. As for the flight track electric fields, since the hurricane is over water, the 37 GHz model does not quite capture the event, but the 85 GHz at least gets the timing right for the most part, despite missing the peak intensity. The observations have a significant amount of missing data, but the southwest eye wall appears to have a stronger electric field than the northeast eye wall (assuming that the spike in the data is due to lightning contamination). The 85 GHz estimate, on the other hand, shows the opposite trend, with the northeastern eye wall having slightly higher electric fields than the other. The 85 GHz model could obviously stand to be improved to better handle hurricane cases due to the lack of coverage of the AMPR sensor and assumptions about the effective charge height in these cases. Future work will focus on correcting the model for all sorts of complex cases with the aim of creating an algorithm that performs well over all types of storms and can characterize the electrical characteristics of electrified clouds across the globe.

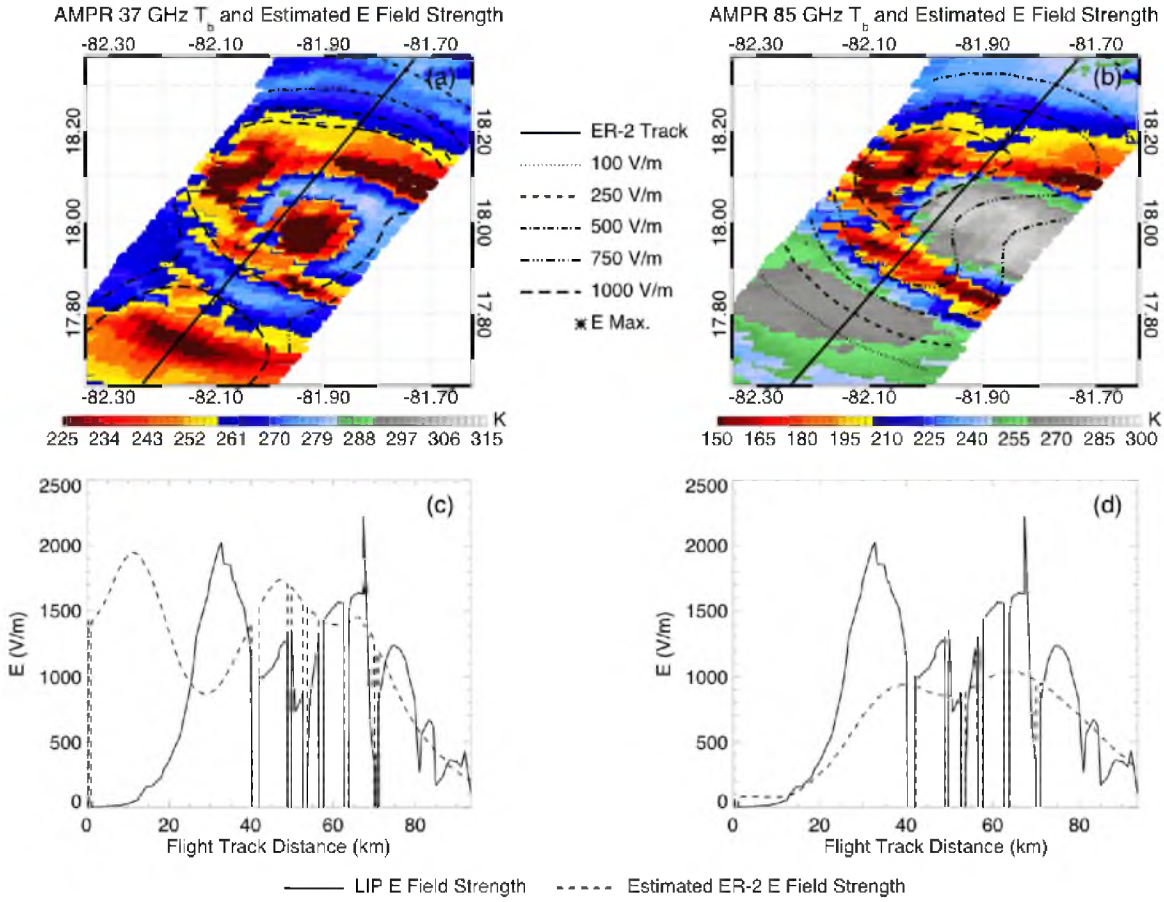

Fig. 5.21. AMPR observations and estimated electric fields above Hurricane Emily in the Caribbean. AMPR 37 GHz (a) and 85 GHz (b) brightness temperatures (contour), estimated electric field strengths (line contours), and the ER-2 flight track (solid line) are shown. A comparison of observed and estimated electric field strengths along the flight track is also shown in (c) and (d).

CHAPTER 6

SUMMARY

The primary purpose of this study is to develop a deeper understanding of properties of lightning and the intricate relationship between atmospheric charge separation and storm structure. Lightning flashes over the ocean were shown to be significantly larger and brighter than flashes observed over land, while coastal flashes were shown to be longer lasting than the other terrain types by optical observations (TRMM LIS). The question then became, why. Is there something special about oceanic convection that often leads to larger and brighter flashes, or are these flashes just more easily observed due to the weaker nature of convection over the ocean?

The perceived optical properties of lightning seem to depend on three factors: the radiative energy of the flash, the state of the viewing medium, the structure of the electrical breakdown. Any of these three factors can then by affected by the properties of the parent storm. First, the radiative energy of the flash has been shown to be an important factor in determining the optical flash characteristics. High correlation coefficients have been observed between flash radiance and illuminated area in a number of scenarios, implying that in many cases the brightness of the flash plays a major role in determining its apparent size. The nature of the viewing medium also plays a role as the apparent brightness of a flash often depends on how thick the cloud layer is and how

much radiance may be scattered and redistributed so that it is not detected from above. Additionally, the strength of the LF radio impulses from the breakdown and flash illuminated area have been shown to be related. Relationships with radio impulse strength have not been observed for other optical parameters, including radiance, and this relationship between sferic strength and area may only exist for IC flashes. These factors imply that the optical footprint of a lightning flash depends additionally on the strength of the breakdown and possibly the horizontal extent of the discharge.

At the same time, the properties of the parent storm on the whole seem to influence the optical properties of LIS flashes as well. Even though strong convective areas scatter away the most radiance, resulting in a potential reduction of flash area and observed brightness, the statistics for systems with only small, dim, and short-lived flashes prefer weak storms, while storms with exceptionally large, bright, and long lasting flashes tend to be stronger and larger with higher flash counts.

Finally, coincident comparison of high-altitude electric field strengths and passive microwave observations has led to the construction of a retrieval algorithm that is capable of consistently predicting electric field strengths above convective clouds both over land and over the ocean using only 85 GHz passive microwave observations as input. This algorithm needs some improvement, however, before it can be applied to a global dataset, particularly in how it handles stratiform cloud regions. Despite this setback, its results show promise, and future work will continue to develop this algorithm and eventually apply it to satellite passive microwave observations across the globe. The ultimate goal is to estimate the global Wilson currents generated by electrified clouds and help quantify the current source of the global electric circuit.

REFERENCES

Abarca, S. F., K. L. Corbosiero, and T. J. Galarneau Jr., 2010: An evaluation of the Worldwide Lightning Location Network (WWLLN) using the National Lightning Detection Network (NLDN) as ground truth, *J. Geophys. Res.*, **115**, D18206, doi:10.1029/2009JD013411.

Awaka, J., T. Iguchi, and K. Okamoto, 1998: Rain type classification algorithm. *Measuring Precipitation from Space*, **3,** 213–224.

Awaka, J., T. Iguchi, and K. Okamoto, 2009: TRMM PR standard algorithm 2A23 and its performance on bright band detection, *J. Meteor. Soc. Japan*, **87a**, 31–52.

Bateman, M. G., M. F. Stewart, R. J. Blakeslee, S. J. Podgorny, H. J. Christian, D. M. Mach, J. C. Bailey, and D. Daskar, 2007: A low- noise, microprocessor-controlled, internally digitizing rotating- vane electric field mill for airborne platforms, *J. Atmos. Oceanic Technol.*, **24**, 1245–1255, doi:10.1175/JTECH2039.1.

Battan, L. J., 1964: Some observations of vertical velocities and precipitation sizes in a thunderstorm. *J. Appl. Meteor.*, **3,** 415–420.

Betz, H. D., K. Schmidt, P. Oettinger, and M. Wirz, 2004: Lightning detection with 3-D discrimination of intracloud and cloud-to-ground discharges. *Geophys. Res. Lett.*, **31,** L11108, doi:10.1029/2004GL019821.

Biter, C. J., and P. N. Johnson, 1982: Sunday Creek—The CCOPE operations center. *Bull. Amer. Meteor. Soc.*, **63**, 482–486.

Boccippio, D. J., W. Koshak, R. Blakeslee, K Driscoll, D. Mach, D. Buechler, W. Boeck, H. J. Christian, and S. J. Goodman, 2000: The Optical Transient Detector (OTD): Instrument characteristics and cross-sensor validation. *J. Atmos. Oceanic Tech.*, **17,** 441–458.

Boccippio, D. J., W. Koshak, and R. Blakeslee, 2002: Performance assessment of the Optical Transient Detector and Lightning Imaging Sensor. Part I: Predicted diurnal variability. *J. Atmos. Oceanic Tech.*, **19,** 1318–1332.

Brooks, C. E. P., 1925: The distribution of thunderstorms over the globe. *Geophys.*

Memo, **3,** No. 24, 147–164.

Braun, S. A., R. Kakar, E. Zipser, G. Heymesfield, C. Albers, S. Brown, S. L. Durden, S. Guimond, J. Halverson, A. Heymsfield, S. Ismail, B. Lambrigtsen, T. Miller, S. Tanelli, J. Thomas, and J. Zawislak, 2013: NASA's genesis and rapid intensification (GRIP) field experiment. *Bull. Amer. Meteor. Soc.*, **94,** 3, 345–363.

Brown, K. A., P. R. Krehbiel, C. B. Moore, and G. N. Sargent, 1971: Electrical screening layers around charged clouds. *J. Geophys. Res.,* **76**, 2825–2835.

Brown, R. A., 1992: Initiation and evolution of updraft rotation within an incipient supercell thunderstorm. *J. Atmos. Sci.*, **49**, 1997–2031.

Brunning, E. C., W. D. Rust, T. J. Schuur, D. R. MacGorman, P. R. Krehbiel, and W. Rison, 2007: Electrical and polarimetric radar observations of a multicell storm in TELEX. *Mon. Wea. Rev.*, **135**, 2525–2544.

Carey, L. D., and S. A. Rutledge, 2000: The relationship between precipitation and lightning in tropical island convection: a C-band polarimetric study. *Mon. Wea. Rev.*, **128**, 2687–2710.

Carey, L. D., M. J. Murphy, T. L. McCormick, and N. W. S. Demetriades, 2005: Lightning location relative to storm structure in a leading-line, trailing-stratiform mesoscale convective system. *J. Geophys. Res.,* **110,** D03105.

Cecil, D. J., S. J. Goodman, D. J. Boccippio, E. J. Zipser, and S. W. Nesbitt, 2005: Three years of TRMM precipitation features. Part I: Radar, radiometric, and lightning characteristics. *Mon. Wea. Rev.*, **133**, 543–566.

Cecil, D. J., D. R. Buechler, and R. J. Blakeslee, 2014: Gridded lightning climatology from TRMM-LIS and OTD: Dataset description. *J. Atmos. Res.*, **135–136**, 404-414.

Christian, H. J., and S. J. Goodman, 1987: Optical observations of lightning from a high-altitude airplane. *J. Atmos. Oceanic Tech.*, **4,** 701–711.

Christian, H. J., R. J. Blakeslee, D. J. Boccippio, W. L. Boeck, D. E. Buechler, K. T. Driscoll, S. J. Goodman, J. M. Hall, W. J. Koshak, D. M. Mach, and M. F. Stewart, 2003: Global frequency and distribution of lightning as observed from space by the Optical Transient Detector. *J. Geophys. Res.* **108**, 4005–4020.

Christian, H. J., R. J. Blakeslee, and S. J. Goodman, 2000: Lightning Imaging Sensor (LIS) for the International Space Station. *AIP Conf. Proc.,* **504**, 423, 2000, doi: 10.1063/1.1302515.

Christian, H. J., and coauthors, 1994: Algorithm Theoretical Basis Document (ATBD) for the Lightning Imaging Sensor (LIS). NASA, 53 pp.

Church, C. R., 1966: The electrification of hail. Ph.D. thesis, University of Durham, 55–57.

Davis, M. H., M. Brook, H. Christian, B. G. Heikes, R. E. Orville, C. G. Park, R. G. Roble, and B. Vonnegut, 1983: Some scientific objectives of a satellite-borne lightning mapper. *Bull. Amer. Meteor. Soc.*, **64,** 114–119.

Deierling, W., and W. A. Peterson, 2008: Total lightning activity as an indicator of updraft characteristics. *J. Geophys. Res.,* **113,** doi: 10.1029/2007JD009598.

Deierling, W., W. A. Peterson, J. Latham, S. Ellis, and H. J. Christian, 2008: The relationship between lightning activity and ice fluxes in thunderstorms. *J. Geophys. Res.,* **113,** doi: 10.1029/2007JD009700.

Dotzek, N., R. M. Rabin, L. D. Carey, D. R. MacGorman, T. L. McCormick, N. W. Demetriades, M. J. Murphy, and R. L. Holle, 2005: Lightning activity related to satellite and radar observations of a mesoscale convective system over Texas on 7-8 April 2002. *Atmos. Res.* **76**, 127–166.

Driscoll, K. T., R. J. Blakeslee, and M. E. Baginski, 1992: A modeling study of the time-averaged electric currents in the vicinity of isolated thunderstorms. *J. Geophys. Res.,* **97,** D11, 11 535–11 551.

Driscoll, K. T., R. J. Blakeslee, and W. J. Koshak, 1994: Time-averaged current analysis of a thunderstorm using ground-based measurements. *J. Geophys. Res.,* **99,** D5, 10 653–10 661.

Dye, J. E., M. G. Bateman, H. J. Christian, E. Defer, C. A. Grainger, W. D. Hall, E. P. Krider, S. A. Lewis, D. M. Match, F. J. Merceret, J. C. Willett, and P.T. Willis, 2007: Electric fields, cloud microphysics, and reflectivity in anvils of Florida thunderstorms. *J. Geophys. Res.*, **112,** D11215.

Elster, J., and H. Geitel, 1913: Zur Influenztheorie der Niederschlagselektrizität. *Phys. Z.*, **14**, 1287.

Ely, B. L., R. E. Orville, D. C. Lawrence, and C. L. Hodapp, 2008: Evolution of the total lightning structure in a leading-line, trailing-stratiform mesoscale convective system over Houston, Texas. *J. Gephys. Res.*, **113,** doi:10.1029/2007JD008445.

Goodman, S. J., and H. J. Christian, 1988: A comparison of the optical pulse characteristics of intracloud and cloud-to-ground-lightning as observed above clouds. *J. Appl. Meteor.*, **27,** 1369–1381.

Grenet, G., 1947:Essai d'explication de la charge électrique des nuages d'orages. *Extrait Ann. Geophys.*, **3**, 306.

Halverson, J., M. Black, S. Braun, D. Cecil, M. Goodman, A. Heymsfield, G. Heymsfield, R. Hood, T. Krishnamurti, G. McFarquhar, M. J. Mahoney, J. Molinari, R. Rogers, J. Turk, C. Velden, D.-L. Zhang, E. Zipser, and R. Kakar, 2007: NASA's tropical cloud systems and processes experiment. *Bull. Amer. Meteor. Soc.*, **88,** 6, 867–882.

Halverson, J., and T. Rickenbach, 2002: Environmental characteristics of convective systems during TRMM-LBA. *Mon. Wea. Rev.*, **130,** 1,493–1,509.

Hendon, H., and K. Woodberry, 1993: The diurnal cycle of tropical convection. *J. Geophy. Res.*, **98**, 16 623–16 637.

Heymsfield, A. J., C. Schmitt, A. Bansemer, C. H. Twohy, 2010: Improved representation of ice particle masses based on observations in natural clouds. *J. Atmos. Sci.*, **67,** 10, 3303–3318.

Hood, R. E., D. J. Cecil, F. J. LaFontaine, R. J. Blackeslee, D. M. Mach, G. M. Heymsfield, F. D. Marks Jr., E. J. Zipser, and M. Goodman, 2006: Classification of tropical oceanic precipitation using high-altitude aircraft microwave and electric field measurements. *J. Atmos. Sci.*, **63,** 218–233.

Iguchi, T., T. Kozu., R. Meneghini, J. Awaka, and K. Okamoto, 2000: Rain-profiling algorithm for the TRMM precipitation radar. *J. Appl. Meteor.*, **39,** 2038–2052.

H. Iwabuchi, 2006: Efficient Monte Carlo methods for radiative transfer modeling. *J. Atmos. Sci.* **63**, 2324–2339.

Jacobson, A. R., R. Holzworth, J. Harlin, R. Dowden, E. Lay, 2006: Performance assessment of the World Wide Lightning Location Network (WWLLN), using the Los Alamos Sferic Array (LASA) as ground truth. *J. Atmos. Oceanic Technol.*, **23**, 1082–1092.

Jayaratne, E. R., C. P. R. Saunders, and J. Hallet, 1983: Laboratory studies of the charging of soft hail during ice crystal interactions. *Quart. J. Roy. Meteor. Soc.*, **109,** 609–630.

Jennings, S. G., 1975: Charge separation due to water droplet and cloud droplet interactions in an electric field. *Quart. J. Roy. Meteor. Soc.,* **101**, 227–234.

Jonas, P. R., 1990: Observations of cumulus cloud entrainment. *Atmos. Res.,* **25**, 105–127.

Kaker, R., M. Goodman, R. Hood, and A. Guillory, 2006: Overview of the convection

and moisture experiment (CAMEX). *J. Atmos. Sci.*, **63,** 5–18.

Krehbiel, P. R., J. A. Riousset, V. P. Pasko, R. J. Thomas, W. Rison, M. A. Stanley, and H. E. Edens, 2008: Upward electrical discharges from thunderstorms. *Nature,* **1**, 233–237.

Keighton, S. J., H. B. Bluestein, and D. R. MacGorman, 1991: The evolution of a severe mesoscale convective system: cloud-to-ground lightning location and storm structure. *Mon. Wea. Rev.,* **119**, 1533–1556.

Koshak, W. J., R. J. Solakiewicz, R. J. Blakeslee, S. J. Goodman, H. J. Christian, J. M. Hall, J. C. Bailey, E. P. Krider, M. G. Bateman, D. J. Boccippio, D. M. Mach, E. W. McCaul, M. F. Stewart, D. E. Buechler, W. A. Petersen, D. J. Cecil, 2007: North Alabama lightning mapping array (LMA): VHF source retrieval algorithm and error analyses. *J. Atmos. Oceanic Technol.*, **21**, 4, 543–558.

Koshak, W. J., E. P. Krider, N. Murray, and D. J. Boccippio, 2007: Lightning charge retrievals: dimensional reduction, LDAR constraints, and a comparison with LIS satellite data. *J. Atmos. Oceanic Technol.*, **24**, 1817–1838.

Krider, E. P., R. C. Noggle, and M. A. Uman, 1975: A gated, wideband magnetic direction finder for lightning return strokes. *J. Appl. Meteor.*, **14,** 3, 252–256.

Krider, E. P., R. C. Noggle, A. E. Pifer, and D. L. Vance, 1980: Lightning direction-finding systems for forest fire detection. *Bull. Amer. Meteor. Soc.*, **61,** 9, 980–986.

Kuhlman, K. M., D. R. MacGorman, M. I. Biggerstaff, and P. R. Kreibiel, 2009: Lightning initiation in the anvils of two supercell storms. *Geophys. Res. Lett.*, **36**, L07802.

Kummerow, C., W. Barnes, T. Kozu, J. Shiue, and J. Simpson, 1998: The Tropical Rainfall Measuring Mission (TRMM) sensor package. *J. Atmos. Oceanic Technol.*, **15**, 809–817.

Lang, T. J., S. A. Rutledge, and K. C. Wiens, 2004: Origins of positive cloud-to-ground lightning in the stratiform region of a mesoscale convective system. *Geophys. Res. Lett.*, **31,** doi: 10.1029/2004GL019823.

Lang, T. J., and S. A. Rutledge, 2008: Kinematic, microphysical, and electrical aspects of an asymmetric bow-echo mesoscale convective system observed during STEPS 2000. *J. Geophys. Res.*, **113**, D8, doi: 10.1029/2006JD007709.

Larsen, H. R., and E. J. Stansbury, 1974: Association of lightning flashes with precipitation cores extending to height 7 km. *J. Atmos. Terr. Phys.*, **36,** 1547–1553.

Latham, D., 1991: Lightning flashes from a prescribed fire-induced cloud. *J. Geophys. Res.*, **96**, 17 151–17 157.

Lay, E. H., R. H Holzworth, C. J. Rodger, J. N. Thomas, O. Pinto Jr., and R. L. Dowden, 2004: WWLL global lightning detection system: Regional validation study in Brazil. *Geophys. Res. Lett.*, **31,** doi: 10.1029/2003GL018882.

Lay, E. H., A. R. Jacobson, R. H. Holzworth, C. J. Rodger, and R. L. Dowden, 2007: Local time variation in land/ocean lightning flash density as measured by the World Wide Lightning Location Network, *J. Geophys. Res.*, **112**, D13111, doi:10.1029/2006JD007944.

Lewis, E. A., R. B. Harvey, and J. E. Rasmussen, 1960: Hyperbolic direction finding with sferics of transatlantic origin. *J. Geophys. Res.,* **65,** 1879–1905.

Liu, C., E. J. Zipser, D. J. Cecil, S. W. Nesbitt, and S. Sherwood, 2008: A cloud and precipitation feature database from 9 years of TRMM observations. *J. Appl. Meteor. Climate*, **47**, 2712–2728. doi:10.1175/2008JAMC1890.

Liu, C., and E. J. Zipser, 2008: Diurnal cycles of precipitation, clouds, and lightning in the tropics from 9 years of TRMM observations. *Geophys. Res. Lett.*, **35**, doi: 10.1029/2007GL032437.

Liu, C., D. Cecil, and E. J. Zipser, 2011: Relationships between lightning flash rates and passive microwave brightness temperatures at 85 and 37 GHz over the tropics and subtropics. *J. Geophys. Res.*, **116**, D23108, doi: 10.1029/2011JD016463.

Liu, C., D. Cecil, and E. J. Zipser, 2012: Relationships between lightning flash rates and radar reflectivity vertical structures in thunderstorms over the tropics and subtropics. *J. Geophys. Res.*, **117,** 2156–2202.

Lund, N. R., D. R. MacGorman, T. J. Schuur, M. I. Biggerstaff, and W. D. Rust, 2009: Relationships between lightning location and polarimetric radar signatures in a small mesoscale convective system. *Mon. Wea. Rev.,* **137**, 4151–4170.

MacClement, W. D., and R. C. Murty, 1978: VHF direction finder studies of lightning. *J. Appl. Meteor.,* **17,** 786–795.

Mach, D. M., H. J. Christian, R. J. Blackeslee, D. J. Boccippio, S. J. Goodman, and W. L. Boeck, 2007: Performance assessment of the Optical Transient Detector and Lightning Imaging Sensor. *J. Geophys. Res.,* **112**, D09210.

Mach, D. M., R. J. Blakeslee, M. G. Bateman, and J. C. Bailey, 2009: Electric fields, conductivity, and estimated currents from aircraft overflights of electrified clouds. *J. Geophys. Res.*, **114**, D10204, doi:10.1029/2008JD011495.

Mach, D. M., R. J. Blakeslee, M. G. Bateman, and J. C. Bailey, 2010: Comparisons of total currents based on storm location, polarity, and flash rates derived from high-altitude aircraft overflights, *J. Geophys. Res.*, **115**, D03201, doi:10.1029/2009JD012240.

Mach, D. M., R. J. Blakeslee, and M. G. Bateman 2011: Global electric circuit implications of combined aircraft storm electric current measurements and satellite-based diurnal lightning statistics, *J. Geophys. Res.*, **116**, D05201, doi:10.1029/2010JD014462.

Mach, D. M., and W. J. Koshak, 2003: General matrix inversion technique for the calibration of electric field sensor arrays on aircraft platforms. Preprints, *12th Int. Conf. on Atmospheric Electricity*, Versailles, France, International Commission on Atmospheric Electricity, 207–210.

MacGorman, D. R., W. D. Rust, T. J. Schuur, M. I. Biggerstaff, J. M. Straka, C. L. Ziegler, E. R. Mansell, E. C. Brunning, K. M. Kuhlman, N. R. Lund, N. S. Biermann, C. Payne, L. D. Carey, P. R. Krehbiel, W. Rison, K. B. Eack, and W. H. Beasley, 2008: TELEX the thunderstorm electrification and lightning experiment. *Bull. Amer. Meteor. Soc.*, **89,** 7, 997–1013.

Marshall, J. S., and S. Radhakant, 1978: Radar precipitation maps as lightning indicators. *J. Appl. Meteorol.*, **17,** 206–212.

Marshall, T. C., W. D. Rust, W. P. Winn, and K. E. Gilbert, 1989: Electrical structure in two thunderstorm anvil clouds. *J. Geophys. Res.*, **94,** 2171–2181.

Marshall, T. C., and W. D. Rust, 1993: Two types of vertical electrical structures in stratiform precipitation regions of mesoscale convective systems. *Bull. Amer. Meteor. Soc.*, **74,** 2159–2170.

Marshall, T. C., M. Stolzenburg, P. R. Krehbiel, N. R. Lund, and C. R. Maggio, 2009. Electrical evolution during the decay stage of New Mexico thunderstorms, *J. Geophys. Res.*, **114**, D02209, doi: 10.1029/2008JD010637.

Martell, E. A., 1984: Ion pair production in convective storms by radon and its radioactive decay products. *Proc. 8th Int. Conf on Atmospheric Electricity,* Albany, NY, Amer. Meteor. Soc., 67–71.

Mazur, V., X. Shao, and P. R. Krehbiel, 2012: "Spider" lightning in intracloud and positive cloud-to-ground flashes. *J. Geophys. Res.*, **103**, D16, 19 811–19 822.

Miller, S., and H. Urey, 1959: Organic compound synthesis on the primitive earth, *Science*, **130,** 3370, 245–251.

Moore, C. B., 1977: An assessment of thunderstorm electrification mechanisms.

Electrical Processes in Atmospheres, N. Dolezalek and R. Reiter, Eds., Steinkopff, 333–352.

Moore, C. B., B. Vonnegut, B. A. Stein, and H. J. Survilas, 1960: Observations of electriflcation and lightning in warm clouds. *J. Geophys. Res.,* **65**, 1907–1910.

Murty, R. C., and W. D. MacClement, 1973: VHF direction finder for lightning location. *J. Appl. Meteor.,* **12,** 1401–1045.

Nesbitt, S. W., and E. J. Zipser, 2003: The diurnal cycle of rainfall and convective intensity according to three years of TRMM measurements. *J. Climate,* **16**, 1456–1475.

Norinder, H., 1953: Long-distance location of thunderstorms. *Thunderstorm Electricity*, H. R. Byers, Univ. Chicago Press, 276–327.

Oetzel, G. N., and E. T. Pierce, 1969: VHF technique for locating lightning. *Radio Sci.,* **4,** 199–201.

Orville, R. E., and D. W. Spencer, 1979: Global lightning flash frequency. *Mon. Wea. Rev.,* **107,** 934–943.

Orville, R. E., and R. W. Henderson, 1986: Global distribution of midnight lightning: September 1977 to August 1978. *Mon. Wea. Rev.,* **114,** 2640–2653.

Orville, R. E., 2008: Development of the National Lightning Detection Network. *Bull. Amer. Meteor. Soc.*, **89,** 182–190.

Pasko, V. P., M. A. Stanley, J. D. Matthews, U. S. Inan, and T. G. Wood, 2002: Electrical discharge from a thundercloud top to the lower ionosphere. *Nature,* **416**, 152–154.

Petersen, W. A., H. J. Christian, and S. A. Rutledge, 2005: TRMM observations of the global relationship between ice water content and lightning. *Geophys. Res. Lett.*, **32,** L14819, doi: 10.1029/2005GL023236.

Peterson, M. J., 2011: Satellite and ground based observations of lightning flashes in the stratiform and anvil regions of convective systems. M.S. thesis, University of Utah, 139 pp.

Peterson, M. J., and C. Liu, 2011: Global statistics of lightning in anvil and stratiform regions over the tropics and subtropics observed by TRMM, *J. Geophys. Res.*, **116**, D23, doi: 10.1029/2011JD015908.

Peterson, M. J., and C. Liu, 2013: Characteristics of lightning flashes with exceptional illuminated areas, durations, and optical powers and surrounding storm properties in the tropics and inner subtropics, *J. Geophys. Res.*, **118**, 11 727–11 740, doi:

10.1002/jgrd.50715.

Poelman, D. R., W. Schulz, and C. Vergeiner, 2013: Performance characteristics of distinct lightning detection networks covering Belgium. *J. Atmos. Oceanic Tech.*, **30,** 942–951.

Reynolds, S. E., M. Brook, and M. F. Gourley, 1957; Thunderstorm charge separation. *J. Meteor.*, **14**, 426–437.

Rudlosky, S. D., and D. T. Shea, 2013: Evaluating WWLLN performance relative to TRMM/LIS. *Geophys. Res. Lett.,* **40**, 2344–2348, doi:10.1002/grl.50428.

Rutledge, S. A., and D. R. MacGorman, 1988: Cloud-to-ground lightning activity in the 10-11 June 1985 mesoscale convective system observed during the Oklahoma-Kansas PRESTORM project. *Mon. Wea. Rev.*, **116**, 1393–1408.

Saunders, C. P. R., W. D. Keith, and R. P. Mitzeva, 1991: The effect of liquid water content on thunderstorm charging. *J. Geophys. Res.,* **96,** 11 007–11 017.

Schuur, T. J., and S. A. Rutledge, 2000: Electrification of stratiform regions in mesoscale convective systems. Part II: Two-dimensional numerical model simulations of a symmetric MCS. *J. Atmos. Sci.*, **57,** 1983–2006.

Shackford, C. R., 1960: Radar indications of a precipitation-lightning relationship in New England thunderstorms. *J. Meteor.,* **17,** 15–19.

Sonnenfeld, R. G., J. D. Battles, G. Lu, and W. P. Winn, 2006: Comparing E field changes aloft to lightning mapping data. *J. Geophys. Res.*, **111**, D20209, doi:10.1029/2006JD007242.

Spencer, R. W., H. G. Goodman, and R. E. Hood, 1989: Precipitation retrieval over land and ocean with the SSM/I: Identification and characteristics of the scattering signal. *J. Atmos. Oceanic Tech.*, **6,** 254–273.

Stolzenburg, M., T.C. Marshall, W. D. Rust, and B.F. Smull, 1994: Horizontal distribution of electrical and meteorological conditions across the stratiform region of a mesoscale convective system. *Mon. Wea. Rev.*, **122,** 1777–1797.

Stolzenburg, M., T.C. Marshall, and P. R. Krehbiel, 2010: Duration and extent of large electric fields in a thunderstorm anvil cloud after the last lightning. *J. Geophys. Res.*, **115**, D19202, doi:10.1029/2010JD014057.

Takahashi, T., 1978: Riming electrification as a charge generation mechanism in thunderstorms. *J. Atmos. Sci.,* **35,** 1536–1548.

Takayabu, Y. N., 2006: Rain-yield per flash calculated from TRMM PR and LIS data and

its relationship to the contribution of tall convective rain. *Geophys. Res. Lett.*, **33**, L18705, doi:10.1029/2006GL027531.

Thomas, R. J., P. R. Krehbiel, W. Rison, S. J. Hunyady, W. P. Winn, T. Hamlin, and J. Harlin, 2004: Accuracy of the Lightning Mapping Array. *J. Geophys. Res.*, **109,** doi: 10.1029/2004JD004549.

Toracinta, E. R., D. J. Cecil, E. J. Zipser, and S. W. Nesbitt, 2002: Radar, passive microwave, and lightning characteristics of precipitating systems in the tropics. *Mon. Wea. Rev.*, **130**, 802–824.

Turnam, B. N., 1977: Detection of lightning superbolts. *J. Geophys. Res.*, **82**, 2566–2568.

Ushio, T., K. T. Driscoll, S. Heckman, D. J. Boccippio, W. J. Koshak, and H. J. Christian, 1999: Initial comparison of the Lightning Imaging Sensor (LIS) with Lightning Detection and Ranging (LDAR). *Proc. 11th Int. Conf. on Atmospheric Electricity,* Guntersville, AL, NASA, 738–741.

Vaughan, O. H. Jr., 1990: Mesoscale lightning experiment (MLE): a view of lightning as seen from space during the STS-26 mission. NASA Technical Memorandum (NASA TM-103513), 70 pp.

Vonnegut, B., 1953: Possible mechanism for the formation of thu rıderstorm electricity. *Bull. Amer. Meteor. Soc.*, **34**, 378–381.

Vonnegut, B., 1963: Some facts and speculations concerning the origin and role of thunderstorm electricity. *Meteor. Monogr.*, **5**, 224–241.

Vonnegut, B., 1983: Deductions concerning accumulations of electrified particles in thunderstorms based on electric field changes associated with lightning. *J. Geophys. Res.*, **88,** C6, 3911–3912.

Vonnegut, B., O. H. Vaughan Jr., M. Brook, and P. K. Krehbiel, 1985: Mesoscale observations of lightning from space shuttle. *Bull. Amer. Meteor. Soc.*, **66**, 20–29.

Vonnegut, B., O. H. Vaughan Jr., and M. Brook, 1989: Nocturnal photographs taken from a U-2 airplane looking down on tops of clouds illuminated by lightning. *Bull. Amer. Meteor. Soc.*, **70**, 1263–1271.

Wacker, R. S., and R. E. Orville, 1999a: Changes in measured lightning flash count and return stroke peak current after the 1994 U.S. National Lightning Detection Network upgrade: 1. Observations, *J. Geophys. Res.*, **104**, 2151–2158.

Wacker, R. S., and R. E. Orville, 1999b: Changes in measured lightning flash count and return stroke peak current after the 1994 U.S. National Lightning Detection Network upgrade: 2. *Theory, J. Geophys. Res.*, **104**, 2159–2162.

Watson-Watt, R. A., and J. F. Herd, 1926: An instantaneous direct-reading radio goniometer. *J. Inst. Elec. Engrs.*, **64**, 611–622.

Watson-Watt, R. A., J. F. Herd, and L. H. Bainbridge-Bell, 1933: Applications of the cathode ray oscillograph in radio research. His Majesty's Stationery Office, 290 pp.

Williams, E.R., 2005: Lightning and climate: a review. *Atmos. Res.,* **76,** 272–287.

Williams, E.R., and G. Sátori, 2004: Lightning, thermodynamic and hydrological comparison of the two tropical continental chimneys. *J. Atmos. Sol. Terr. Phys.*, **66**, 1213–1231.

Wilson, C. T. R., 1920:Investigation on lightning dischargesand on the electric field of thunderstorms. *Phil. Trans. Roy. Soc. Ser. A,* **221**, 73–115.

Wilson, C. T. R., 1929:Some thundercloud problems. *J. Franklin Inst.,* **208**, 1–12

Winn, W. P., W. A. Amai, A. M. Blyth, and J. E. Dye, 1986: Downdrafts at the tops of thunderclouds. Preprint, *Conf on Cloud Physics,* Snowmass, CO. Amer. Meteor. Soc., J253–J255.

Wormell, T. W., 1953: Atmospheric electricity: some recent trends and problems. *J. Roy. Meteor. Soc.,* **79**, 3.

Xu, W., E. Zipser, C. Liu, and H. Jiang, 2010: On the relationships between lightning frequency and thundercloud parameters of regional precipitation systems. *J. Geophys. Res.*, **115,** doi:10.1029/2009JD013385.

Zajac, B. A., and S. A. Rutledge, 2001: Cloud-to-ground lightning activity in the contiguous United States from 1995 to 1999. *Mon. Wea. Rev.*, **129**, 999–1019.

Zipser, E. J., D. J. Cecil, C. Liu, S. W. Nesbitt, and D. P. Yorty, 2006: Where are the most intense thunderstorms on earth? *Bull. Amer. Meteor. Soc.*, **87**, 1057–1071.